Secondary beams obtained through the interaction of 95 MeV/u ^{36}Ar ions with various targets

R. Bimbot, T. Benfoughal, M. Mirea, C. Cabot, F. Clapier, O. Sorlin, C. Stephan, P. Roussel-Chomaz, R. Anne, Dominique Bazin, et al.

18 octobre 1996

IPNO-DRE-96-18

Secondary beams obtained through the interaction of 95 MeV/u ^{36}Ar ions with various targets

R. Bimbot, T. Benfoughal, M. Mirea, C. Cabot, F. Clapier, O. Sorlin, C. Stéphan, P. Roussel-Chomaz, R. Anne, D. Bazin, M. Lewitowicz, M.F. Saint-Laurent et al

SECONDARY BEAMS OBTAINED THROUGH THE INTERACTION OF 95 MeV/u ^{36}Ar IONS WITH VARIOUS TARGETS

R.Bimbot, T.Benfoughal, M.Mirea[a], C.Cabot, F.Clapier, O.Sorlin, C.Stéphan, P.Roussel-Chomaz[b], R.Anne[b], D.Bazin[b], M.Lewitowicz[b], M.F.Saint-Laurent[b], P.Delbourgo-Salvador[c], T.Ethvignot[c], J.E.Sauvestre[c], J.L.Sida[e], R.Freeman[e], P.Aguer[f], A.Lefebvre[f], G.Farès[g], A.Hachem[g]

Institut de Physique Nucléaire, CNRS-IN2P3, 91406 - Orsay Cedex, France
[a] *Institut de Physique Atomique, Bucarest, Roumanie*
[b] *GANIL, BP 5027, 14021 - Caen Cedex, France*
[c] *CE Bruyères-le-Châtel, BP 12, 91680 - Bruyères-le-Châtel, France*
[d] *CE Saclay, DAPNIA, 91191 - Gif/Yvette Cedex, France*
[e] *CRN, BP 20, 67037 - Strasbourg Cedex, France*
[f] *CSNSM, Université Paris Sud, 91405- Orsay Cedex, France*
[g] *Université de Nice, Laboratoire Radiochimie, 06034 - Nice Cedex, France*

Abstract:

An ongoing program is developed using the GANIL-facilities in order to determine the experimental yields for secondary beams produced through projectile fragmentation. In this work, an experimental systematics for all the isotopes detected in the peripheral collisions of 95 MeV/u ^{36}Ar ions with various targets covering a wide range of atomic numbers (Be, Ni, Ta) is presented. A short comparison with the theoretical predictions given by two usual numeric codes (LISE and INTENSITY) is also given.

1. INTRODUCTION

Beams of radioactive isotopes have known an increasing interest during the last ten years. Since the very first attempts to produce and use such beams, which were reported at the early meetings concerning radioactive nuclear beams, this field of research revealed very promising and many experiments using such projectiles have been performed [1,2]. The interest of such secondary beams is not only for the study of the fundamental properties of nuclear matter, but also for application purposes (as in fields like biology, atomic physics, astrophysics or solid state physics).

Two methods can be used for the production of radioactive beams:
i) the production of radioactive nuclei at rest followed by their ionization and acceleration.
ii) The direct production of secondary beams through projectile fragmentation followed by the selection of the isotopes of interest. This method is more powerful at higher energies and will concern us in the remaining of this paper.

Despite the fact that many experiments have now been performed with radioactive beams produced by the projectile fragmentation process, this production method, especially at the Fermi energies, has not been experimentally studied in a systematic way. In this range of energies, one operates at the midway of the transition from dissipative mechanisms to an abrasion process.

A detailed explanation of some aspects of these phenomenon is still unsatisfactory. It is why a great effort must be still done to develop experimental systematics in order to obtain reliable estimations of fragmentation cross sections. So, an ongoing program is established using the Ganil facilities, including the LISE spectrometer [3], to determine the yields for different isotopes emerging from collision reactions at Fermi energies. These values will be further used to state the optimum conditions for the production of a given isotope and for a better understanding of the reaction mechanisms.

Experiments involving ^{12}C, ^{13}C [4], ^{36}Ar [5] (at different energies) ^{58}Ni and ^{65}Cu have already been performed. The aim of this contribution is to present some experimental results obtained using the ^{36}Ar primary beam at 95 MeV/nucleon.

2. EXPERIMENTAL TECHNIQUES

The experimental techniques used to produce radioactive beams through projectile fragmentation have already been described in ref. [6]. The radioactive ions produced from the interaction of the fast projectiles with the target nuclei are emitted forward with a velocity close to that of the exiting beam and with a narrow angular distribution. These favourable kinematics conditions lead to the possibility of a practically direct transport of the beam towards the magnetic spectrometer which can select a given isotope corresponding to its magnetic rigidity. The experimental set-up is sketched in Fig. 1. Due to the finite acceptance of the spectrometer, the velocity of the fragments is distributed around its average value and beams with slightly different energies are transmitted together. In the focal dispersive plane of the first magnet, a slit selects the secondary beams according to their magnetic

rigidity:

$$B\rho = 0.1438 \frac{A}{Q} \left(\frac{E}{A}\right)^{\frac{1}{2}} \quad (1)$$

The width of the slits defines the total momentum acceptance $\Delta B\rho/B\rho$. Due to the finite value of this acceptance, beams of slightly different magnetic rigidities are transmitted together. This means that, for a given isotope (a given A/Q value), the energy resolution $\Delta E/E$ will be relatively poor. On the other hand, for a given velocity value, several beams of slightly different A/Q values will get through the spectrometer. In the present work, the width was set at ± 10 mm, the spectrometer at zero degree relative to the primary beam direction and the angular acceptance at its maximum value (± 17 mrad in both planes).

The primary beam intensity I_0 was measured by a secondary emission monitor calibrated using a Faraday cup. The isotopic composition of the secondary beam was analyzed with a silicon telescope detector placed at the achromatic focus of the spectrometer. The telescope serves also to measure the intensity I of the secondary beam. The secondary emission detectors have been intensively studied and are known to deliver a current of intensity i_0 proportional to that of the monitored beam, so that $I_0 = \ constant \ \times i_0$. This property is kept over a wide range of intensities and this was very useful in the present study due to the fact that some measurements had to be performed at very low intensities (outside the work domain of the Faraday cup).

As mentioned before, the counting rate and the identification of the isotopes from the secondary beam was performed using a telescope of two silicon detectors (of 300 and 1000 μm in thickness and area equal to 300 mm^2) placed at the achromatic focus. The range of some ions exceeded the total thickness of these detectors. Therefore, for the identification, the well known $\Delta E - TOF$ method was applied. The GANIL acquisition system was used to record the data.

The experimental program implied the use of a set of targets characterized by various atomic numbers (Z_2) and different thicknesses. So, targets realized from Be, Ni and Ta were used to cover a wide range in Z_2. For a given element, three target thicknesses were used. Typically, the thin targets corresponded to an energy loss of about (1-5)% by the incident beam, the medium ones to about (20-25)% and the thick ones to more than 35%. The characteristics of the targets involved in these measurements are given in table 1. Here, B_0 denotes the values of the magnetic field inside the dipoles associated to the magnetic rigidity of the ^{36}Ar beam after its slowing-down inside the target. The values of the primary beam are calculated [7] at the exit point of the target.

3. EXPERIMENTAL PROCEDURE

At the beginning of the experiment, it was checked that the detector telescope intercepted the totality of the secondary beam. Therefore, as a first step, we compared the size of the detector aperture with that of the beam spot, visualized using a multiwire ionization chamber placed in the neighbouring of the detector. As a second step, it was verified that small changes in the horizontal and vertical positions of this beam spot (variations obtained with the aid of the steerers) did not influence significantly the detector counting rate.

For a given $B\rho$ and a given target (i.e. for each run), when the primary beam intensity was measured, the in-beam insertion of the secondary emission detector induced additional production of radioactive isotopes. Under these circumstances, it was not possible to record simultaneously the intensity of the primary and that of the secondary beams. Therefore, the following procedure was adopted. In the first stage of each run, the secondary emission detector was inserted and the value of the intensity signal was read on the associated picoamperemeter. Then, the secondary emission detector was taken off the beam and the counting rate I_s of the detector was recorded during a short period of time (10 or 20 s). Immediately after, the secondary emission detector was inserted again to check that the primary beam intensity was unchanged. If this intensity has varied significantly, this measurement was repeated. In this way, a measurement of the ratio I_s/I_0 could be obtained independently of the bidimensional recording performed using the acquisition system, and for which is was difficult to acces to absolute production rates, because of the acquisition dead time and of the fluctuations of the beam intensities received by the target during the spectra acquisition. Finally, the $\Delta E - TOF$ distribution was recorded on a magnetic tape during a time period long enough to obtain good statistics. The number of events in each peak $N(A,Z)$ divided by the total number of events in the whole spectrum N_{tot} was used to calculate the secondary beam production according to the relation:

$$\frac{I(A,Z)}{I_0} = \frac{N(A,Z)}{N_{tot}} \frac{I_s}{I_0} \tag{2}$$

Measurements were performed in a large range of the spectrometer magnetic rigidity (1.6-3.2 Tm) with a step equals to 0.1 Tm. However, the values which selected the main charge states of the primary beam were avoided.

4. EXPERIMENTAL RESULTS

The main scope of the present paper is to offer an experimental systematics of production yields (together with the respective differential cross section) for the large amount of secondary beams produced in the collision reactions of a primary

beam of 95 MeV/u- ^{36}Ar with different targets in a wide range of Z_2. Moreover, a short comparison with the predictions of the LISE and INTENSITY codes is presented without extensive comments.

In figure 2(a), the intensity of the total current due to the secondary beams divided by that of the ^{36}Ar projectiles for the three Be targets is presented versus the parameter B/B_0 which is the most appropriate for comparison purposes because it takes into account some slowing-down effects in the target. Indeed, when B/B_0=1, the value of the magnetic field corresponds to the magnetic rigidity of the primary beam. For each target, the value of the thickness is plotted on the graph in mg/cm^2 units. In the figure 2(b), the differential cross section, which depends on the spectrometer acceptance, is computed. It is known that the angular distributions of the projectile-like fragments are very forward peaked. Even for the finite acceptance of the spectrometer, the values of the currents could be used to obtain good estimations of the differential cross sections. At first sight, a general behaviour could be extracted from these pictures. Generally, the yields must have a proportional dependence with the target thickness and therefore should correspond to a constant differential cross section. But, at the same time, there is an increase of the dispersion in energy which leads to the loss of some particles due to the limited energy acceptance of the spectrometer. Despite the fact that the differential cross section is almost unchanged, for the thick target the yield is smaller than for the medium one. The same behaviour is still present on the next two figures (figure 3(a-b) and figure 4(a-b)) where the same observables are plotted for the Ni and Ta targets, respectively. So, as a conclusion, to obtain greatest yields, the target with medium thickness is more appropriate and for accurate determination of the differential cross section the thin one must be preferred.

A comparison of the total yields obtained with the three thinnest targets of each material is presented in figures 5(a-b). Despite the lower value of the differential cross section, the Be target is the best choice when larger intensities of the secondary beams are desired. This is obviously due to the larger number of collision centers (density of nuclei) which characterizes this material. Also, an effect due to the target is easy to be observed on these figures. The targets with larger Z_2 (which in the same time are more neutron rich) are more convenient to produce isotopic beams with higher N/Z.

In figures 6(a to p), the isotopic yields of different secondary beams produced with the Be target of 44.5 mg/cm^2 are plotted separately for different elements. Two horizontal and two vertical scales are used to represent both the yields and the differential cross sections versus the magnetic rigidity and the ratio B/B_0. The dashed lines are plotted to guide the eyes and to offer a rapid estimation of the

values of the yields between two experimental points.

The mass number values are mentioned in the vicinity of some curves to indicate the concerned isotopes. The other mass numbers could be identified keeping in mind that the peaks of the isotopes with positive isospin ($N > Z$) are situated towards the right side of the figure (where the ratio B/B_0 has values greatest than 1) and the peaks of the isotopes with negative isospin ($N < Z$) are situated towards the left side of the figure. This rule is also valid for the figures 7(a to p) to 14(a to p) where the yields due to the other targets are plotted.

Two remarks can be made. On one hand, mostly for the thicker targets, the number of experimental points measured in the region around the value of $B/B_0 \approx 1$ is very small (situation requested in order to avoid the high intensities due to the $^{36}Ar^{18+}$ primary beam charge states). That leads to a loss of precision when the yields are estimated in these ranges of energies. However, this restriction is not too severe, as this region corresponds to beams close to or corresponding to the stability line. On the other hand, at some energies, the bidimensional analyzer threshold value was high enough to cut the record of some events incoming from Li and Be isotopes.

Some trends can be extracted from these pictures. Firstly, the mean velocity corresponding to the maxima of the peaks is always slightly lower and very close to that of the primary beam. Also, the linear momentum widths are narrower for elements with A close to the mass number A_0 of the projectile. The width of the spectra increase smoothly when moving away from the mass of the projectile. This is partly due to the reaction mechanism, and partly to the effect of the target thickness on the momentum of the exiting products (see ref. [2]). Furthermore, the spectra are asymmetric. The isotopes with $Z \leq Z_0/2$ (Z_0 being the atomic number of the projectile) show more pronounced tails towards the low energies (that means for smaller values of B/B_0), a phenomenon which denotes a dissipative mechanism. Such an asymmetry is not observed for higher energies, as is mentionned in ref [8]. Note also that, for fragments with Z greater than Z_0, which can only be produced through nuclear transfers from target to projectiles, the production decreases rapidly. Only a small number of K and Ca isotopes are observed and the associated cross sections are low. These results are not presented here. Finally, the yields increase proportionally with the target thickness up-to a certain value of the thickness (optimum thickness). Afterwards, the maxima of the yields decrease.

The last series of figures (15a to 15a-f) presents a sampling of comparisons of the experimental data with the predictions of the codes LISE and INTENSITY. These codes, which are described in detail in ref. [9] and [10] rely on the same parameter-

ization concerning the reaction cross sections. They take into account the reaction kinematics and the spectrometer characteristics to calculate its transmission yield.

Two remarks can be made concerning this comparison between calculated and experimental results. Firstly the shape of the curves is not reproduced, as the codes lead to gaussian shapes whereas the experimental curves exhibit a low energy tail.

Secondly, the maximum production yield is relatively well reproduced for secondary beams close to stability, but the calculations strongly overestimate the production both for neutron rich and neutron deficient isotopes, and the disagreement increases when the observed isotope get further from the stability line. It can reach one order of magnitude, for example, for ^9C production.

We thank the GANIL crew for their cooperation, and E. Davanture for her help in preparing the manuscript.

REFERENCES

[1] I. Tanihata et al., Phys. Rev. Lett. **55**, 2676 (1985), Phys. Lett. **162B**, 217 (1985).

[2] R. Bimbot et al., Z. Phys. **A322**, 443 (1985).

[3] R. Anne et al., Nucl. Instr. and Meth. **A257**, 215 (1987).

[4] R. Bimbot et al., to be published.

[5] P. Delbourgo Salvador et al., Int. Rept. of CEA/CE Bruyères-le-Châtel, Service de Physique et Techniques Nucléaires, DO.0051/PTN-643/95 (4 août 1995).

[6] R. Bimbot, Int. Symposium RIKEN-IN2P3, Shimoda, Japan, 1987.

[7] F. Hubert et al., At. Data. Nucl. Data. Tab. **46**, 1, 1 (1990).

[8] R. Dayras et al., Nucl. Phys. **A460**, 299 (1986).

[9] D. Bazin et O. Sorlin, code LISE, GANIL, Caen.
D. Bazin, Thèse d'Université, GANIL T-87.01.
O. Sorlin, Thèse d'Université, Orsay, IPNO-T-91-04.

[10] J.A. Winger et al, Nucl. Instr. and Methods in Phys. Res. **B70**, 380 (1992).

TABLE 1: Characteristics of the targets.

Nature of the target	Thickness (mg/cm^2)	B_0 (T)	Primary beam exit energy (MeV)	$\frac{\Delta E}{E}$ %
Be	44.5	1.41	92.52	2.61
Be	360	1.2312	73.05	23.11
Be	540	1.0998	60.08	36.76
Ni	32	1.416	93.48	1.6
Ni	451	1.224	71.44	24.8
Ni	706	1.1198	55.27	41.82
Ta	133	1.3897	90.38	4.86
Ta	578	1.24	79.82	19.14
Ta	920	1.095	57.96	38.99

FIGURE CAPTION

Figure 1: Sketch of the experimental setup.

Figure 2: Total production yields (a) and differential cross section (b) as fonction of the ratio B/B_0 for the three Be targets.

Figure 3: Total production yields (a) and differential cross section (b) as fonction of the ratio B/B_0 for the three Ni targets.

Figure 4: Total production yields (a) and differential cross section (b) as fonction of the ratio B/B_0 for the three Ta targets.

Figure 5: Total production yields (a) and differential cross section (b) as fonction of the ratio B/B_0 for the three thin targets.

Figure 6(a to p): Production yields and differential sections for all the elements (Ar to Li) identified in the secondary beam for the Be thin target (44.5 mg/cm^2).

Figure 7(a to p): Production yields and differential sections for all the elements (Ar to Li) identified in the secondary beam for the Be medium target (360 mg/cm^2).

Figure 8(a to p): Production yields and differential sections for all the elements (Ar to Li) identified in the secondary beam for the Be thick target (540 mg/cm^2).

Figure 9(a to p): Production yields and differential sections for all the elements (Ar to Li) identified in the secondary beam for the Ni thin target (33 mg/cm^2).

Figure 10(a to p): Production yields and differential sections for all the elements (Ar to Li) identified in the secondary beam for the Ni medium target(451 mg/cm^2).

Figure 11(a to p): Production yields and differential sections for all the elements (Ar to Li) identified in the secondary beam for the Ni thick target (706 mg/cm^2).

Figure 12(a to p): Production yields and differential sections for all the elements (Ar to Li) identified in the secondary beam for the Ta thin target (133 mg/cm^2).

Figure 13(a to p): Production yields and differential sections for all the elements (Ar to Li) identified in the secondary beam for the Ta medium target(578 mg/cm^2).

Figure 14(a to p): Production yields and differential sections for all the elements (Ar to Li) identified in the secondary beam for the Ta thick target (920 mg/cm^2).

Figure 15(a to af): Comparison of the experimental yields to the predictions of the codes LISE and INTENSITY.

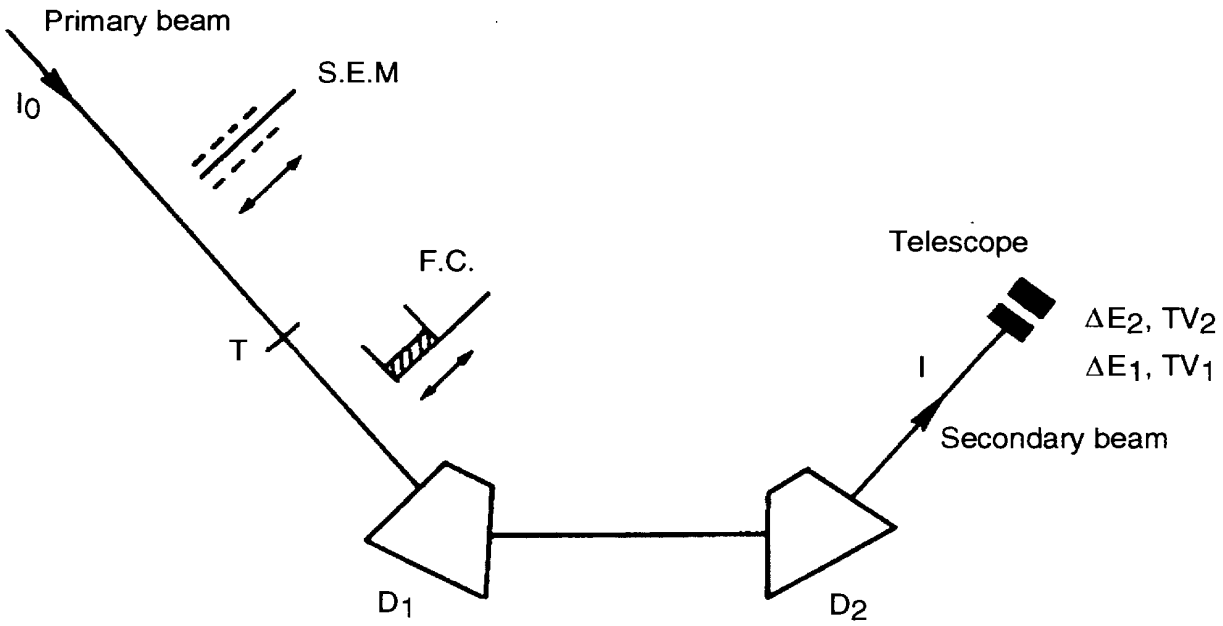

LISE Spectrometer

I_0	: Primary beam intensity
S.E.M.	: Insertable secondary emission monitor
T	: Target
F.C.	: Insertable Faraday cup
D_1,D_2	: Dipoles
I	: Secondary beam intensity
ΔE_1, ΔE_2	: Energy loss in the detectors 1 and 2 (diodes)
TV_1,TV_2	: Time of flight mesured in the detectors 1 and 2

Fig.1: Experimental set-up

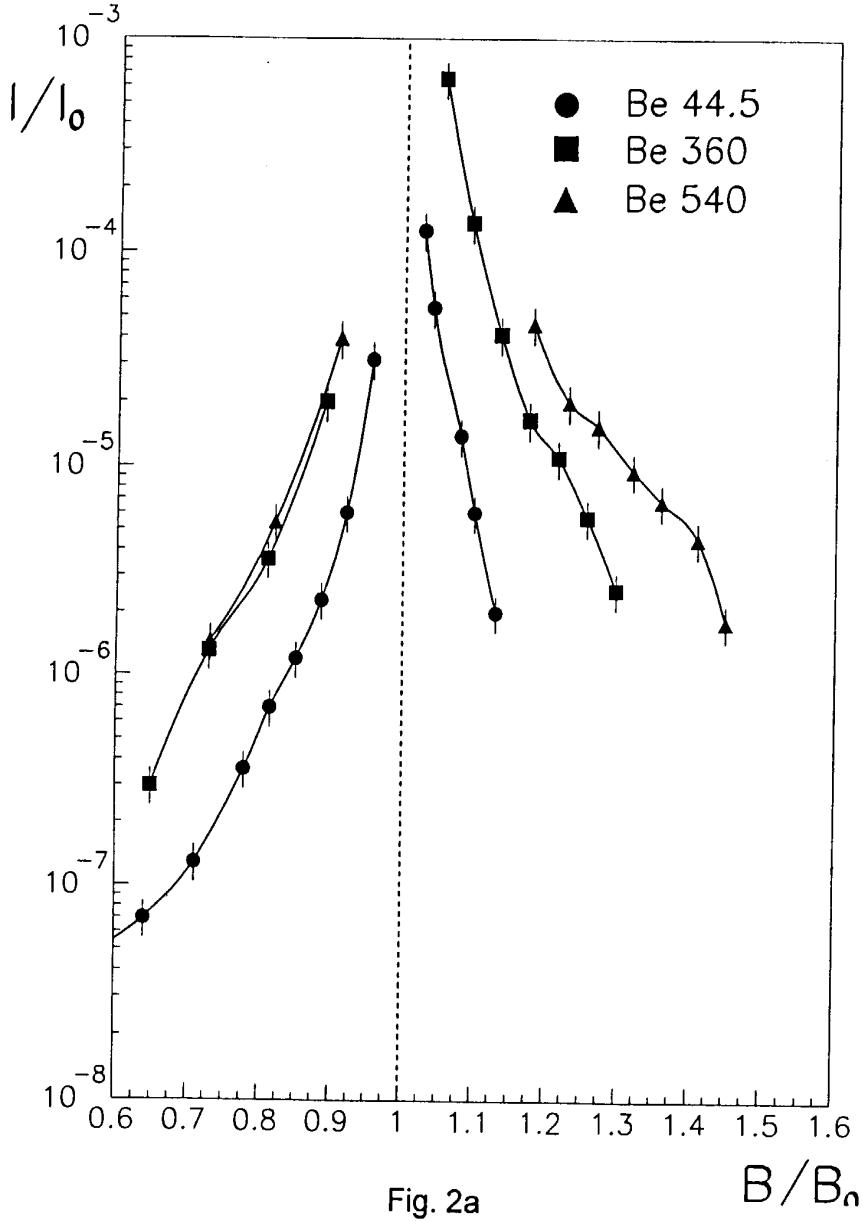
I/I0
Be 44.5
Be 360
Be 540
B/B0

Fig. 2a

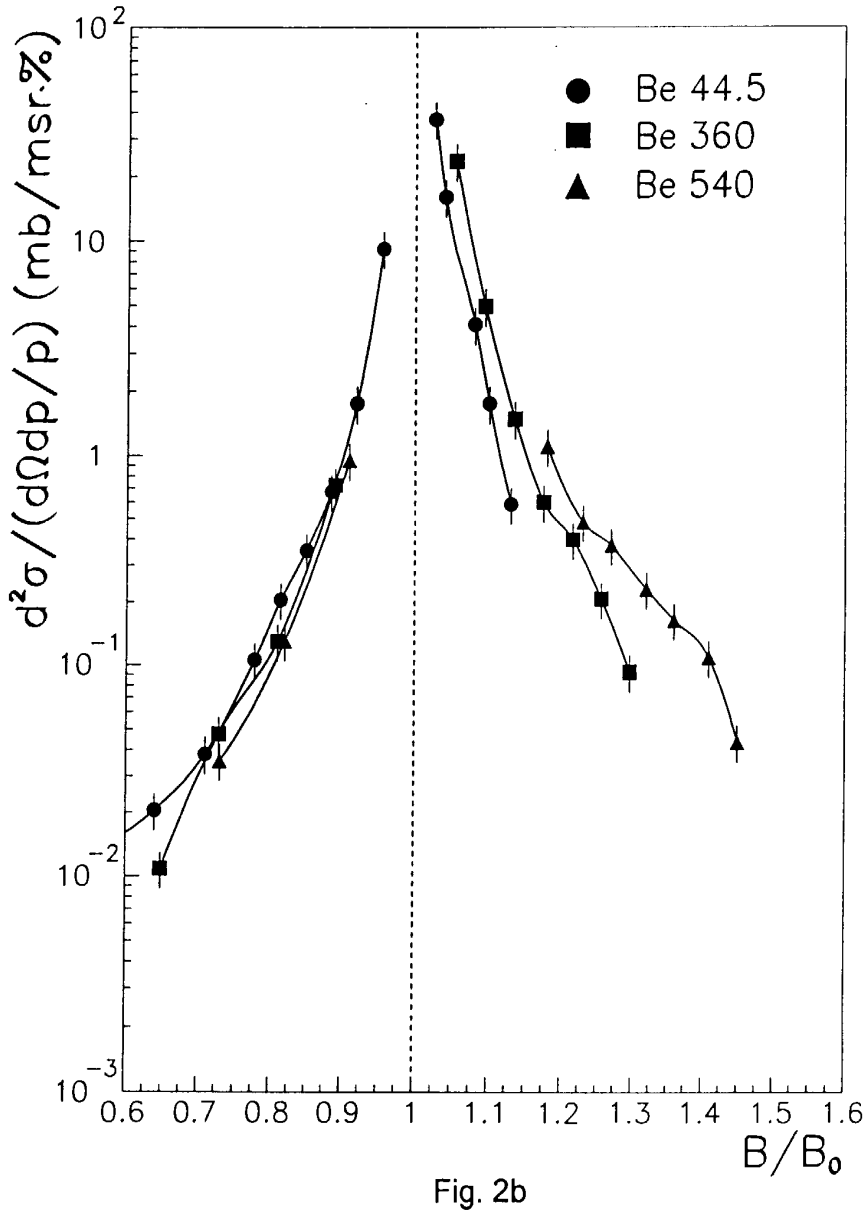
d²σ/(dΩdp/p) (mb/msr·%)
Be 44.5
Be 360
Be 540
B/B0

Fig. 2b

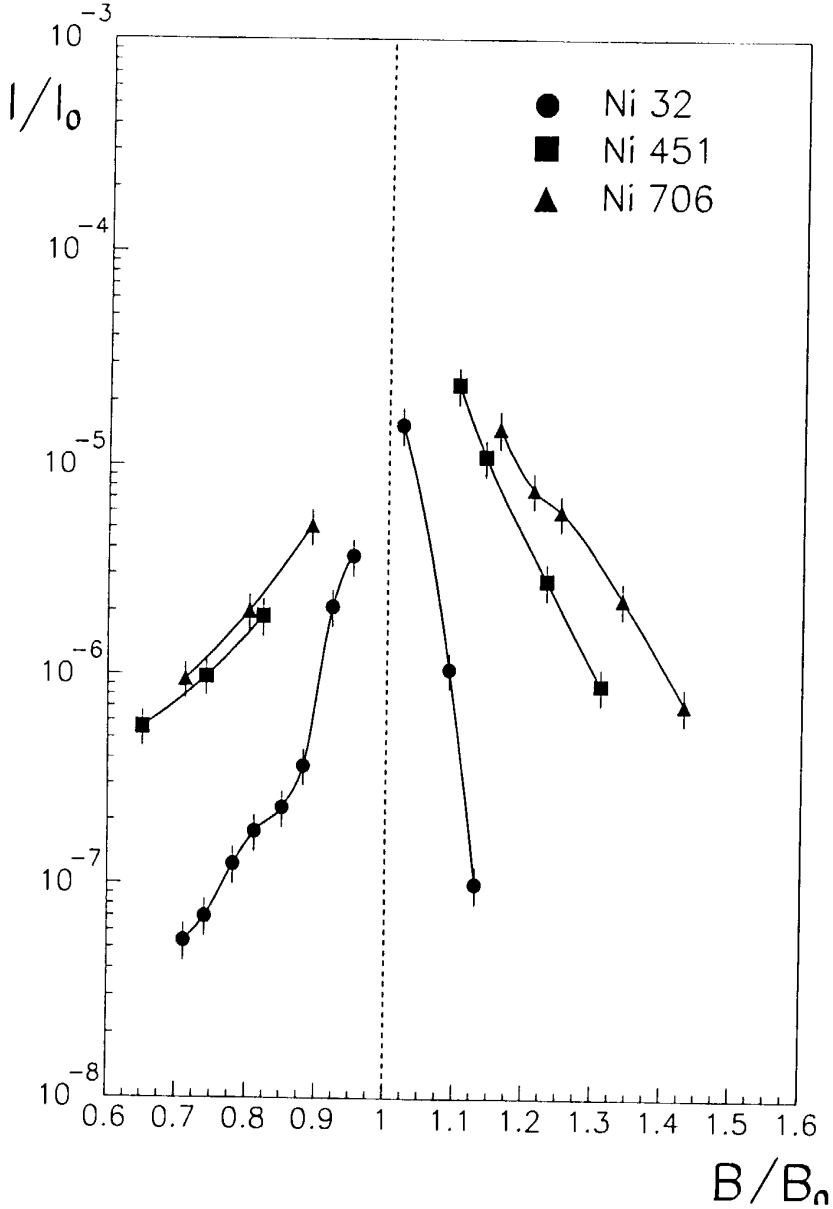
10^{-3}
I/I_0
10^{-4}
10^{-5}
10^{-6}
10^{-7}
10^{-8}
Ni 32
Ni 451
Ni 706
0.6 0.7 0.8 0.9 1 1.1 1.2 1.3 1.4 1.5 1.6
B/B_0

Fig. 3a

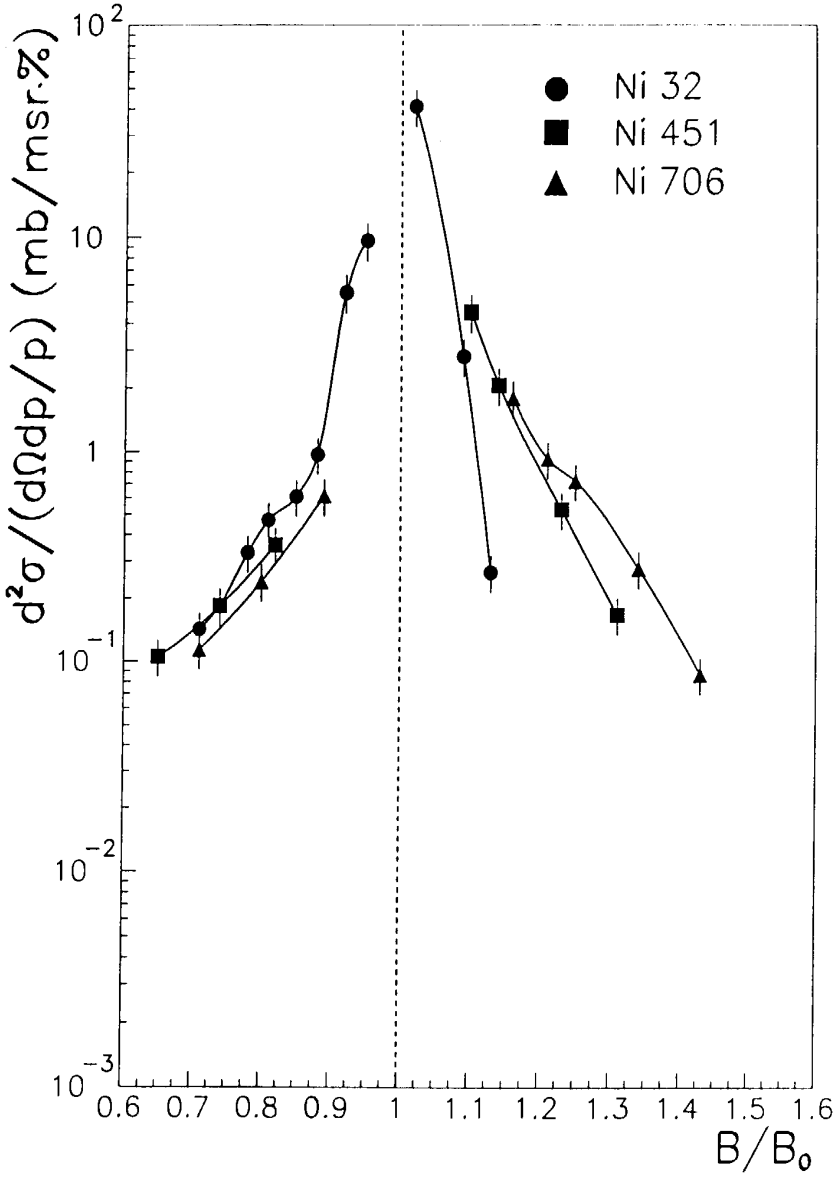
10^2
$d^2\sigma/(d\Omega dp/p)$ (mb/msr·%)
10
1
10^{-1}
10^{-2}
10^{-3}
Ni 32
Ni 451
Ni 706
0.6 0.7 0.8 0.9 1 1.1 1.2 1.3 1.4 1.5 1.6
B/B_0

Fig. 3b

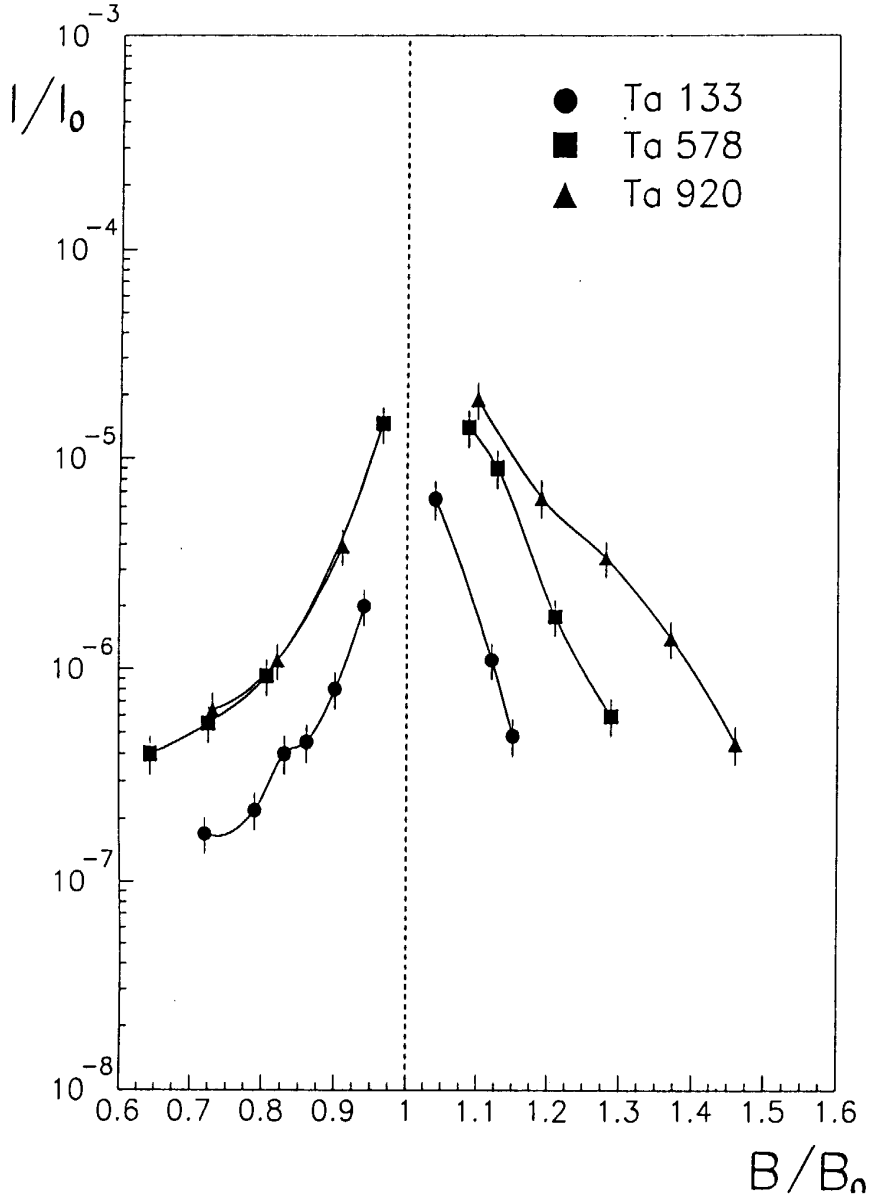
10^{-3}
I/I_0
10^{-4}
10^{-5}
10^{-6}
10^{-7}
10^{-8}
Ta 133
Ta 578
Ta 920
0.6 0.7 0.8 0.9 1 1.1 1.2 1.3 1.4 1.5 1.6
B/B_0

Fig. 4a

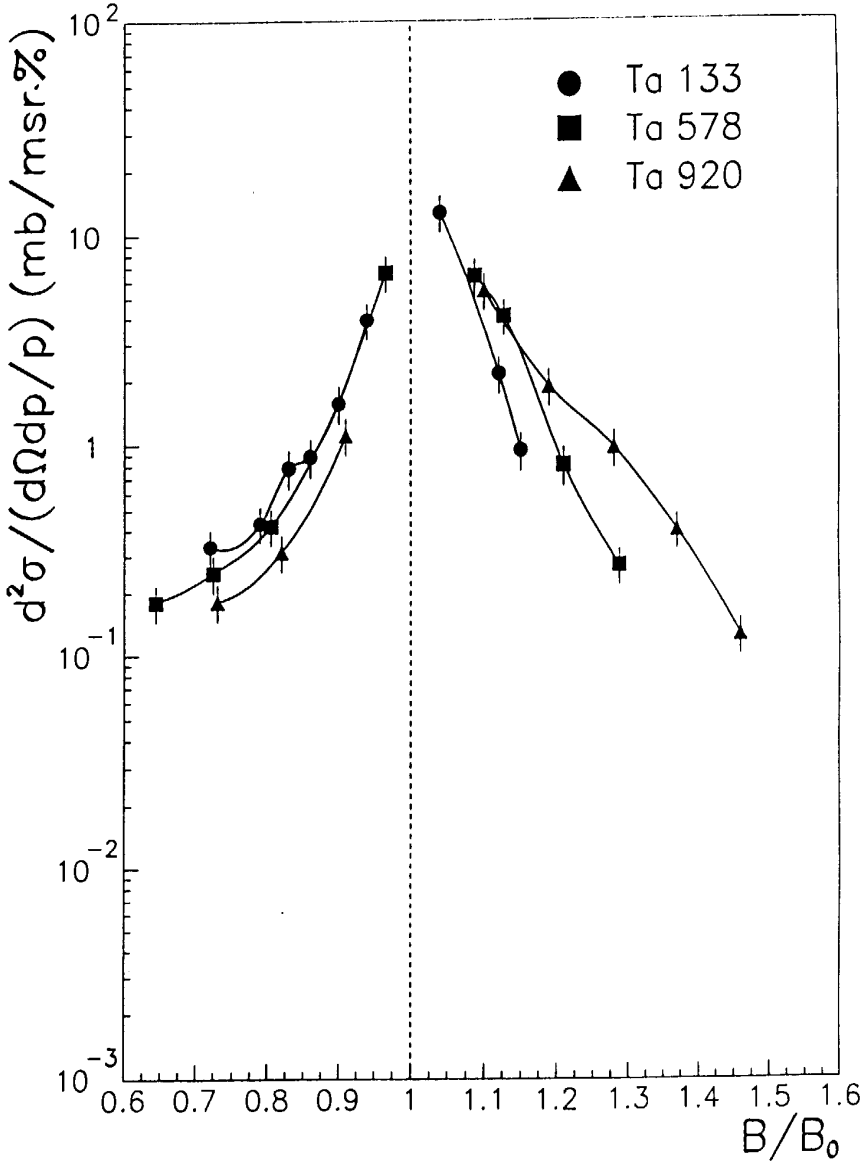
10^{2}
$d^2\sigma/(d\Omega dp/p)$ (mb/msr.%)
10
1
10^{-1}
10^{-2}
10^{-3}
Ta 133
Ta 578
Ta 920
0.6 0.7 0.8 0.9 1 1.1 1.2 1.3 1.4 1.5 1.6
B/B_0

Fig. 4b

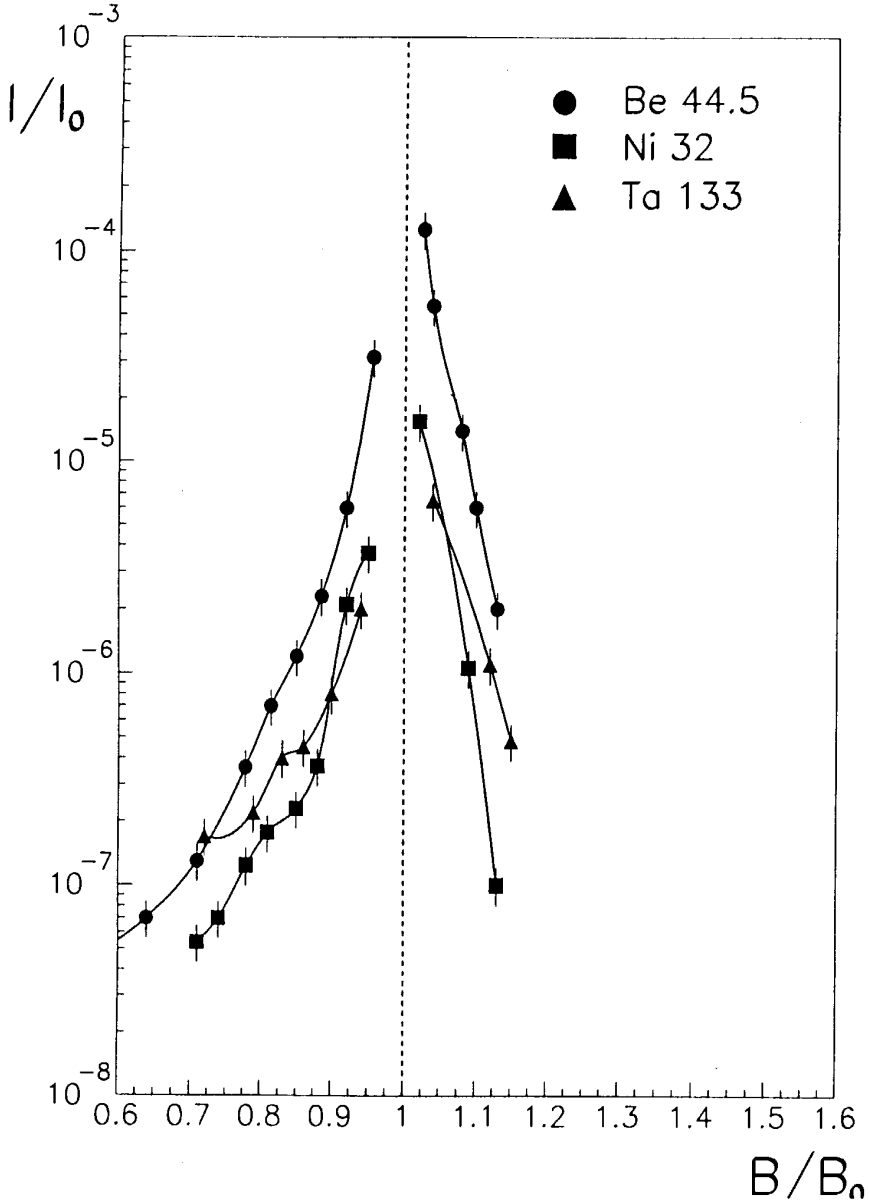
10^{-3}
I/I_0
10^{-4}
10^{-5}
10^{-6}
10^{-7}
10^{-8}
Be 44.5
Ni 32
Ta 133
0.6 0.7 0.8 0.9 1 1.1 1.2 1.3 1.4 1.5 1.6
B/B_0

Fig. 5a

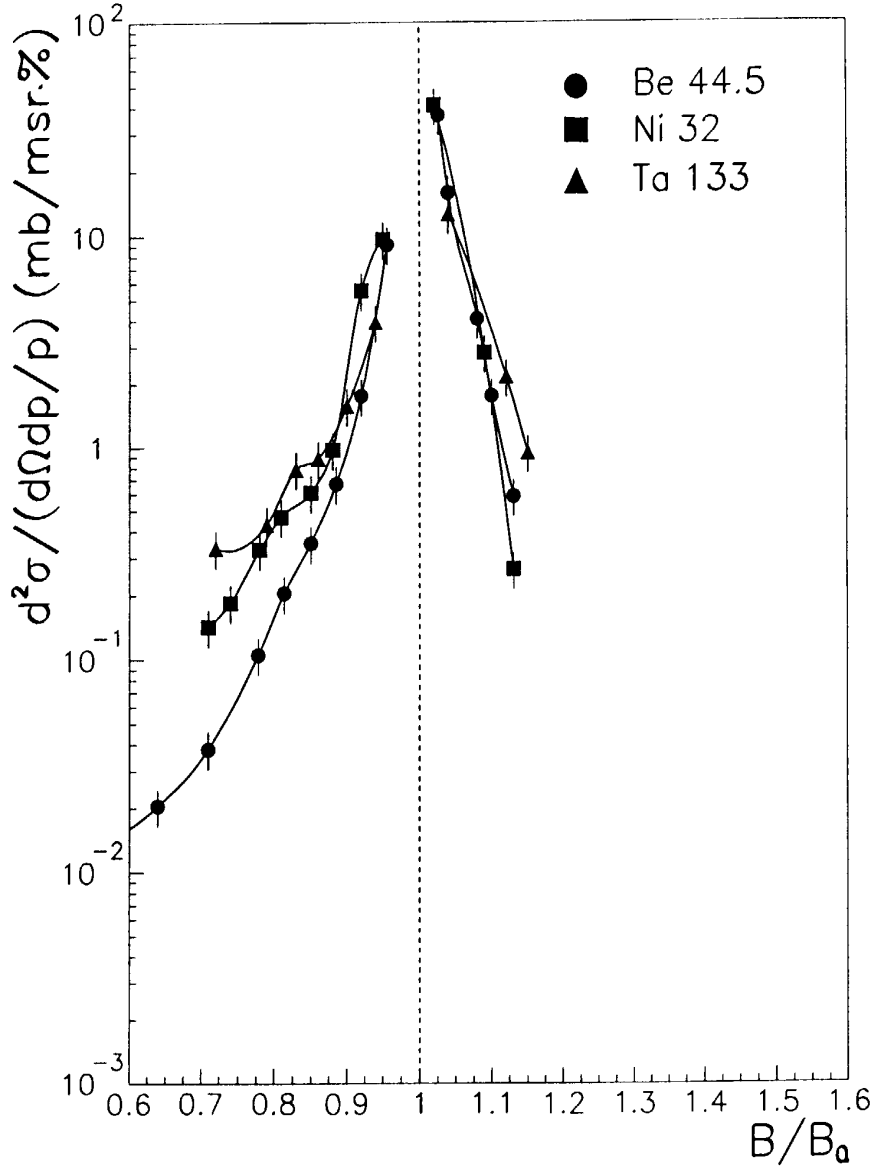
10^2
$d^2\sigma/(d\Omega dp/p)$ (mb/msr.%)
10
1
10^{-1}
10^{-2}
10^{-3}
Be 44.5
Ni 32
Ta 133
0.6 0.7 0.8 0.9 1 1.1 1.2 1.3 1.4 1.5 1.6
B/B_0

Fig. 5b

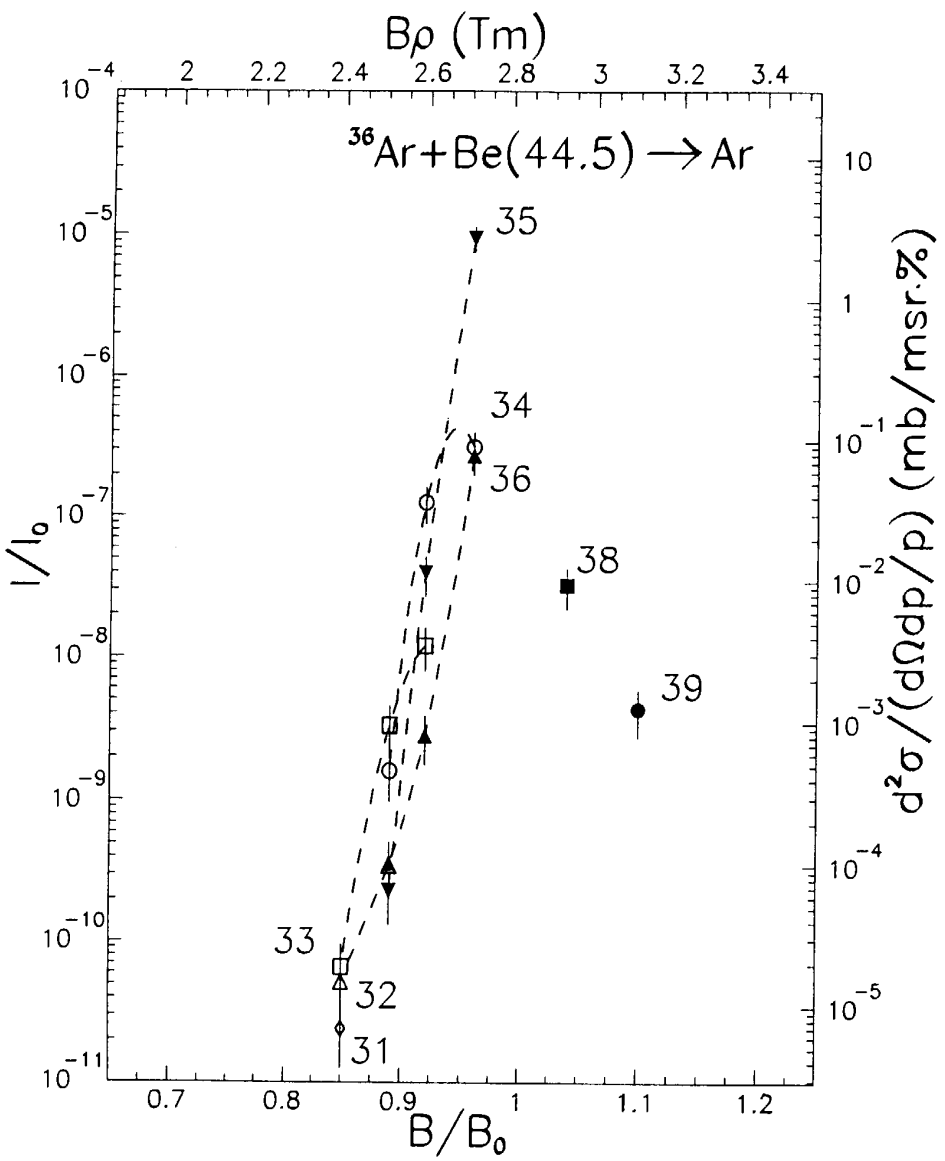
Bρ (Tm)
^{36}Ar+Be(44.5) → Ar
35
34
36
38
39
33
32
31
I/I$_0$
d^{2}σ/(dΩdp/p) (mb/msr.%)
B/B$_0$

Fig. 6a

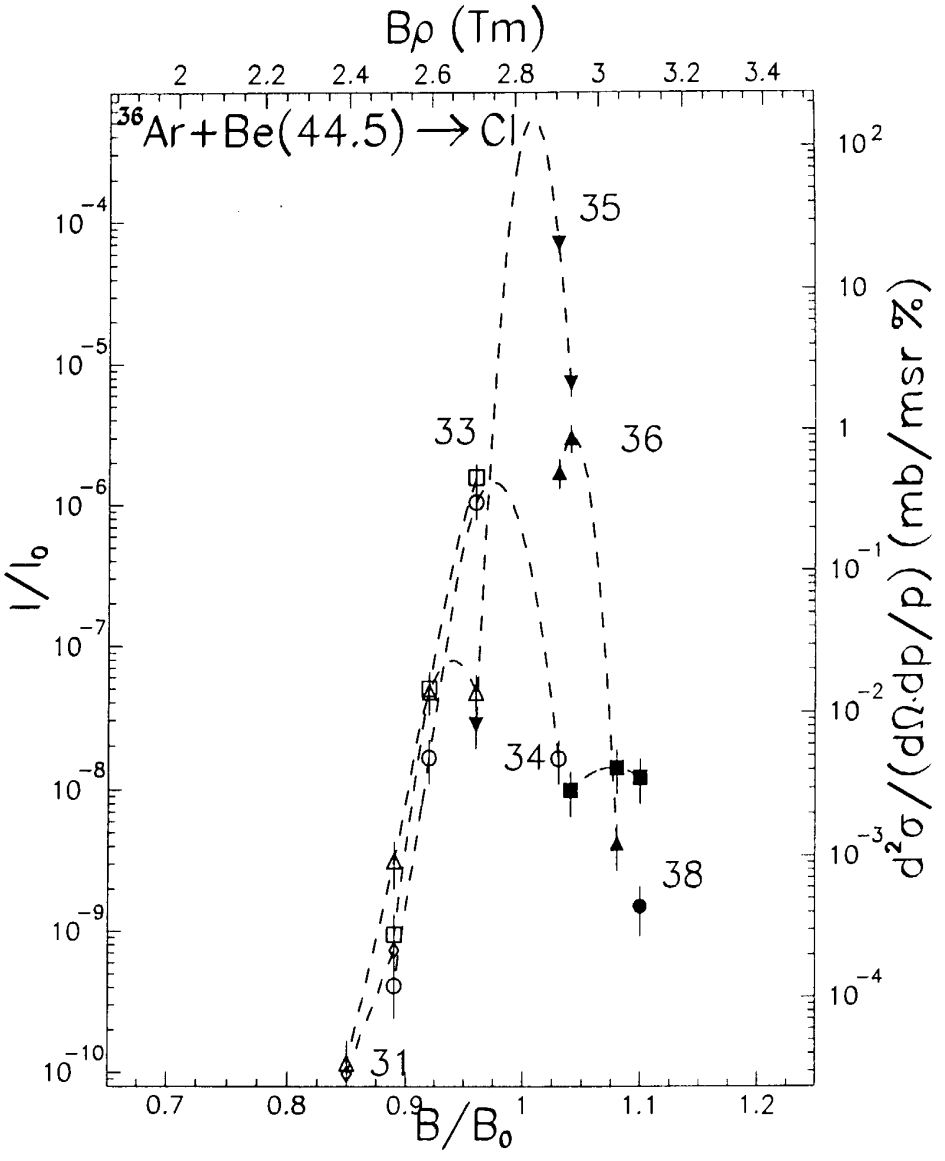
Bρ (Tm)
^{36}Ar+Be(44.5) → Cl
35
33
36
34
38
31
I/I$_0$
d^{2}σ/(dΩ·dp/p) (mb/msr %)
B/B$_0$

Fig. 6b

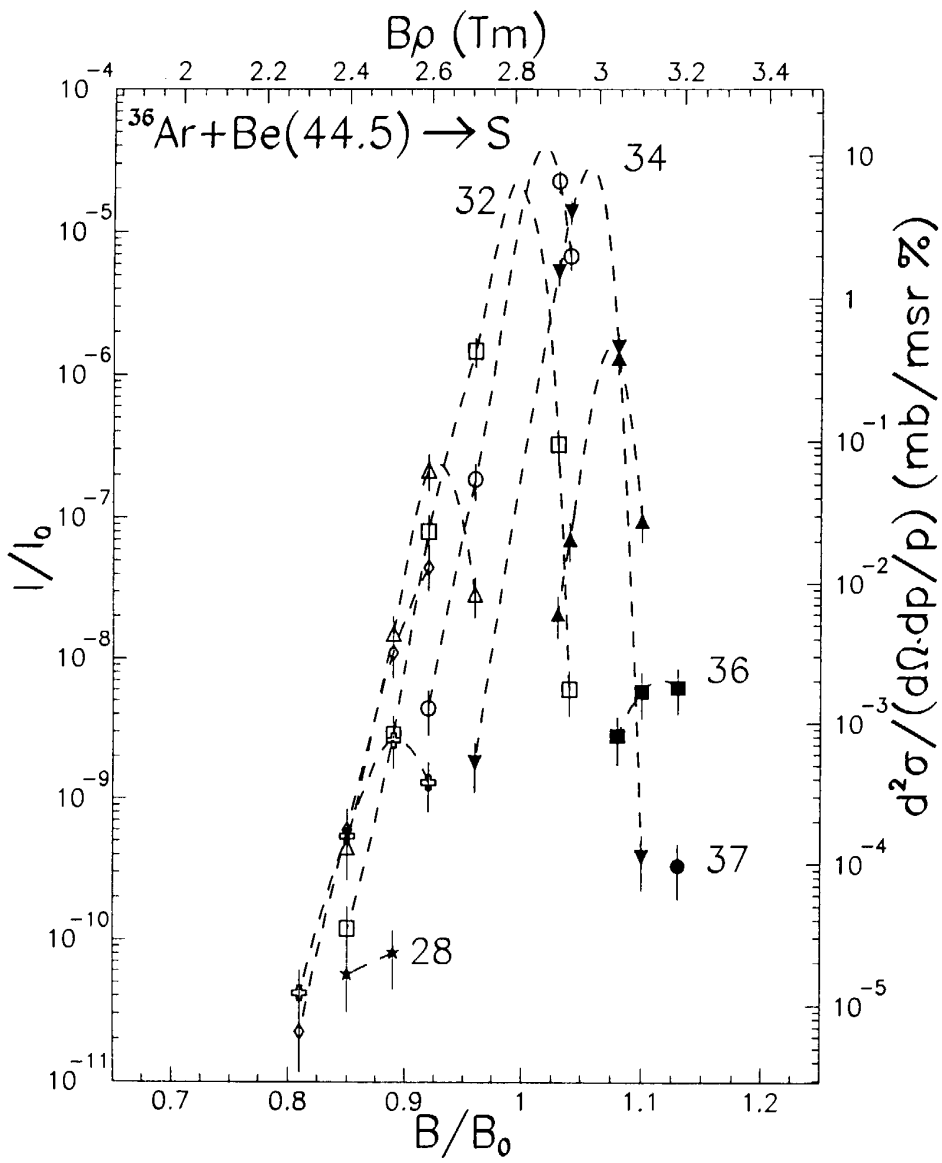
Bρ (Tm)
^{36}Ar+Be(44.5) → S
I/I$_0$
d^{2}σ/(dΩ·dp/p) (mb/msr %)
B/B$_0$
28
32
34
36
37

Fig. 6c

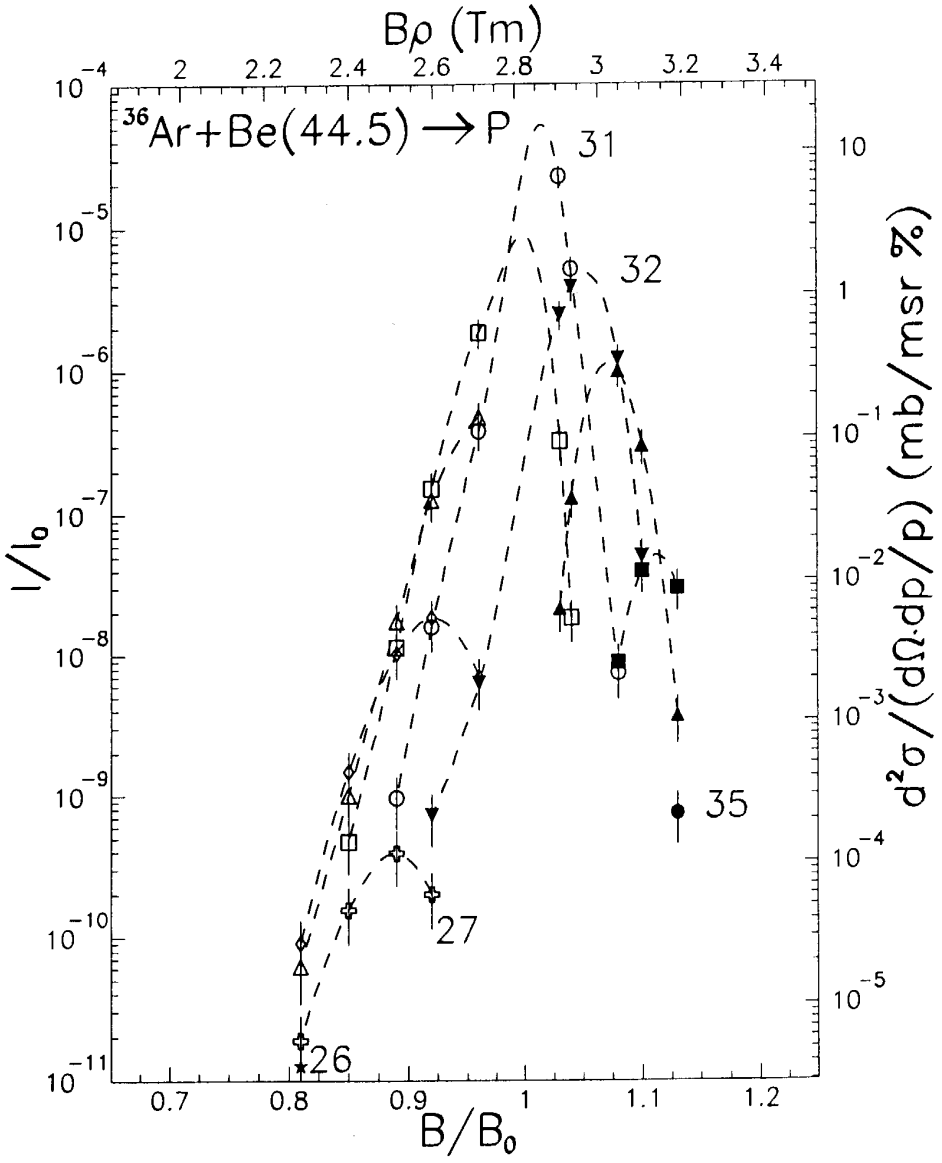
Bρ (Tm)
^{36}Ar+Be(44.5) → P
I/I$_0$
d^{2}σ/(dΩ·dp/p) (mb/msr %)
B/B$_0$
26
27
31
32
35

Fig. 6d

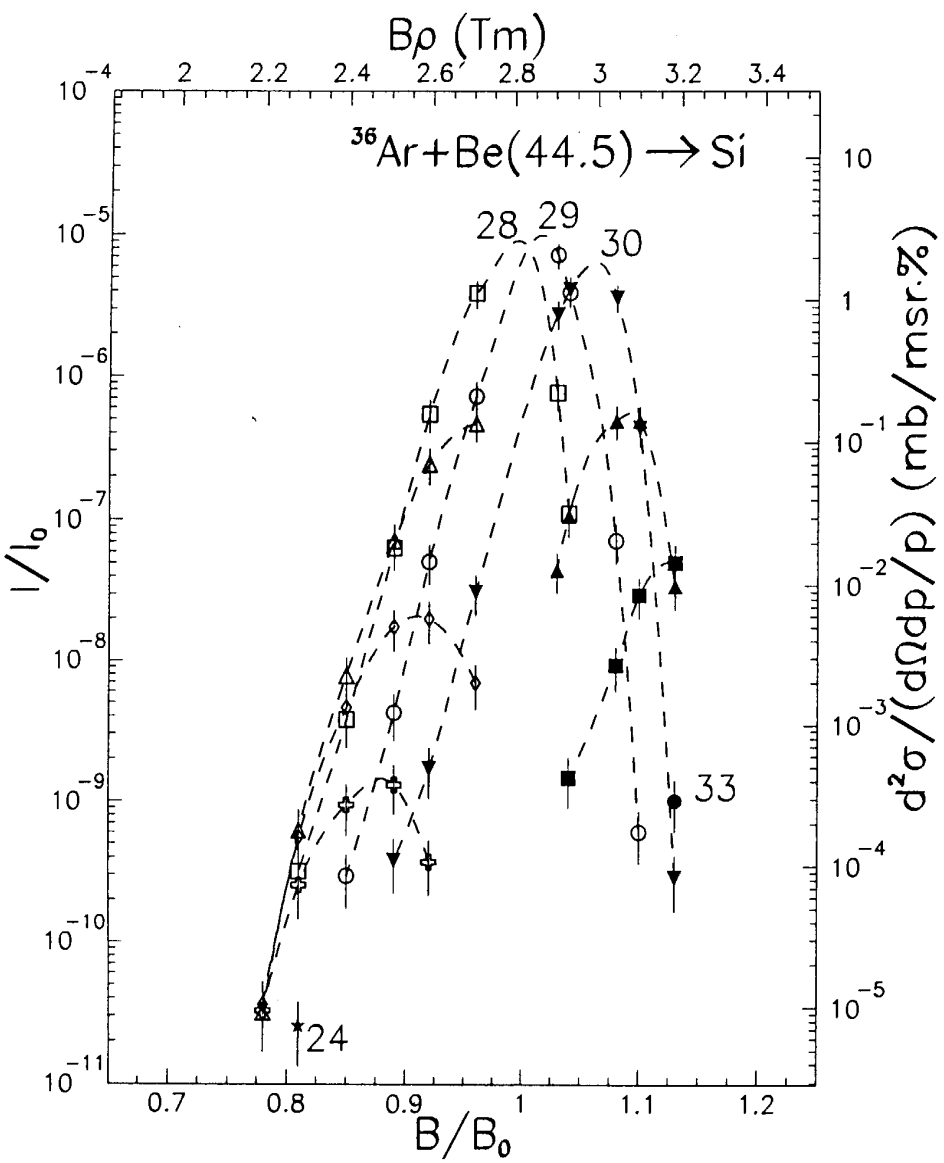
Bρ (Tm)
2
2.2
2.4
2.6
2.8
3
3.2
3.4
^{36}Ar+Be(44.5) → Si
28
29
30
33
24
I/I$_0$
d^{2}σ/(dΩdp/p) (mb/msr.%)
B/B$_0$
0.7
0.8
0.9
1
1.1
1.2

Fig. 6e

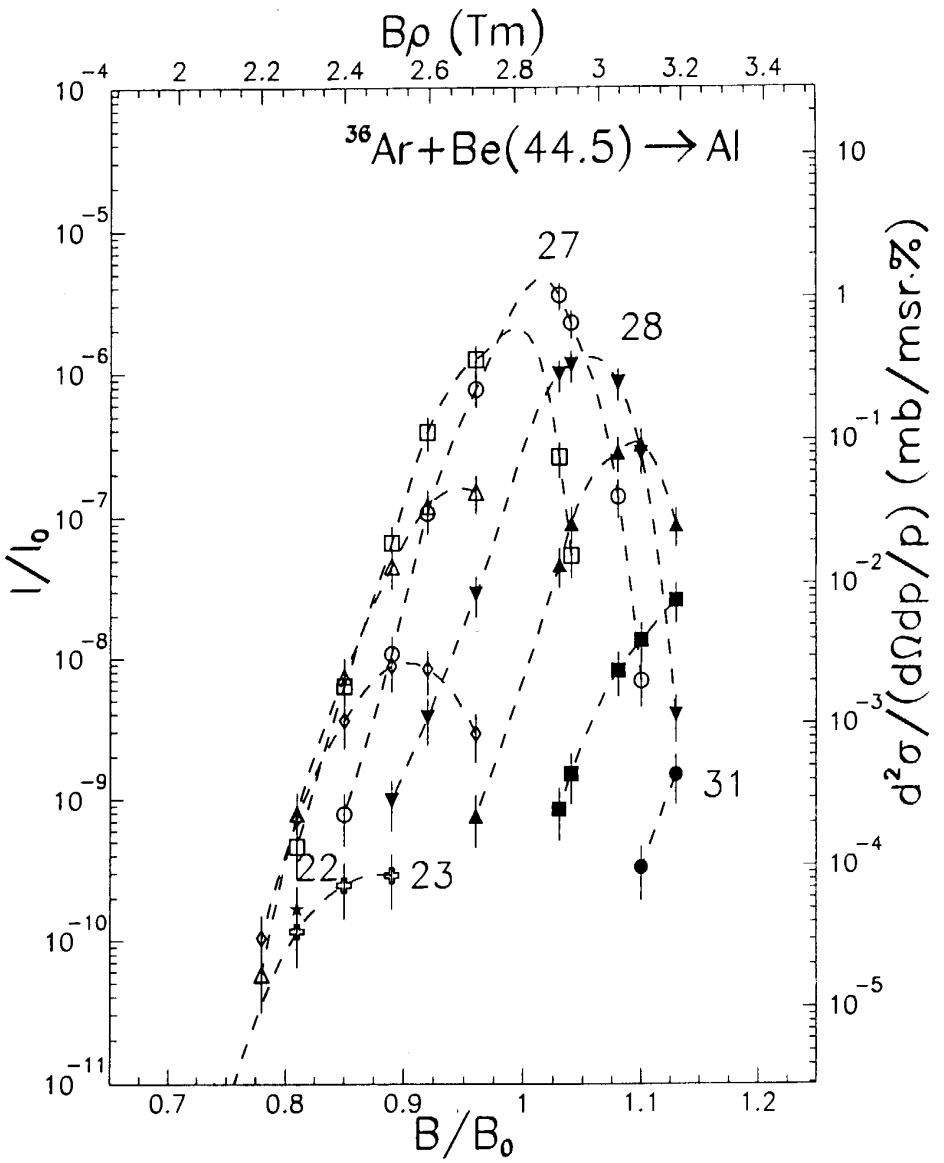
Bρ (Tm)
2
2.2
2.4
2.6
2.8
3
3.2
3.4
^{36}Ar+Be(44.5) → Al
27
28
31
22
23
I/I$_0$
d^{2}σ/(dΩdp/p) (mb/msr.%)
B/B$_0$
0.7
0.8
0.9
1
1.1
1.2

Fig. 6f

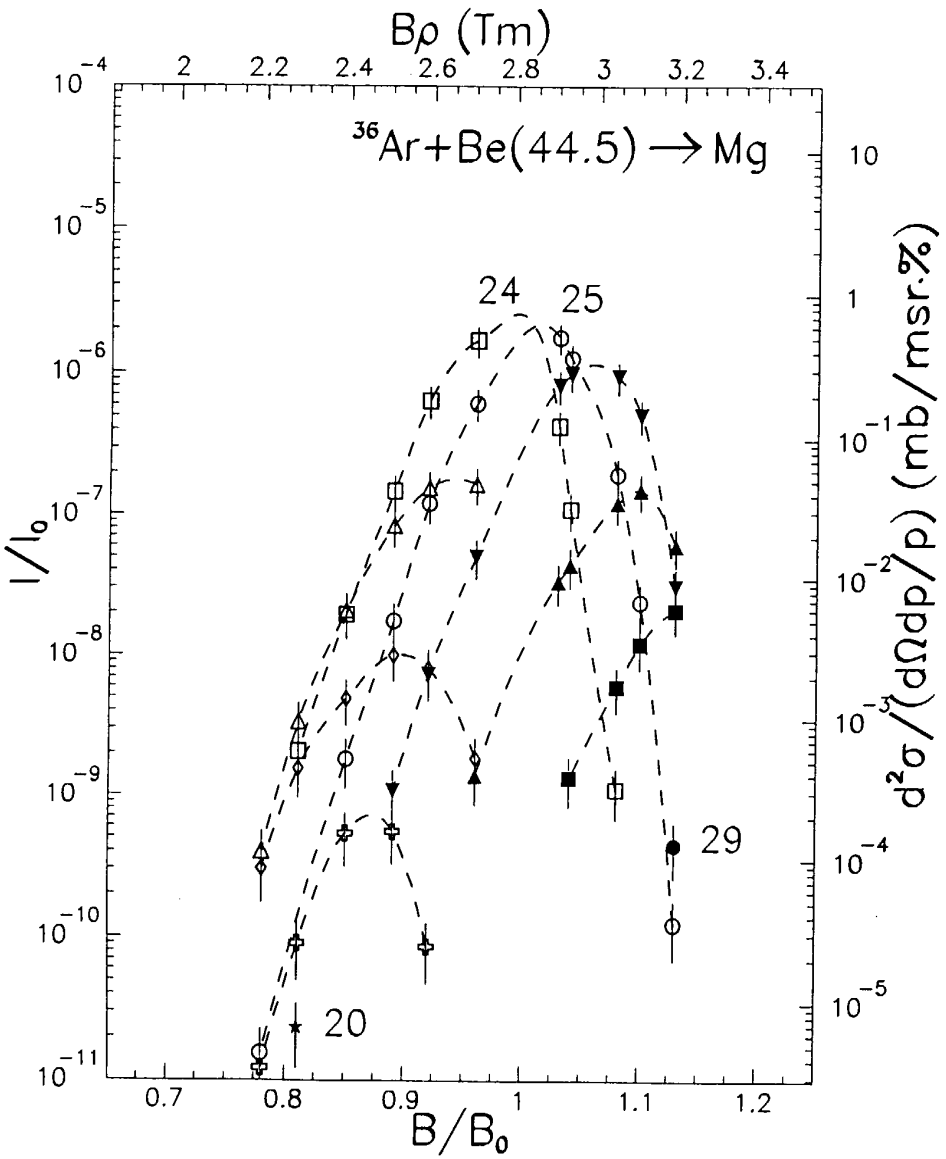
Bρ (Tm)
^{36}Ar+Be(44.5) → Mg
I/I$_0$
d^{2}σ/(dΩdp/p) (mb/msr.%)
B/B$_0$
20
24
25
29

Fig. 6g

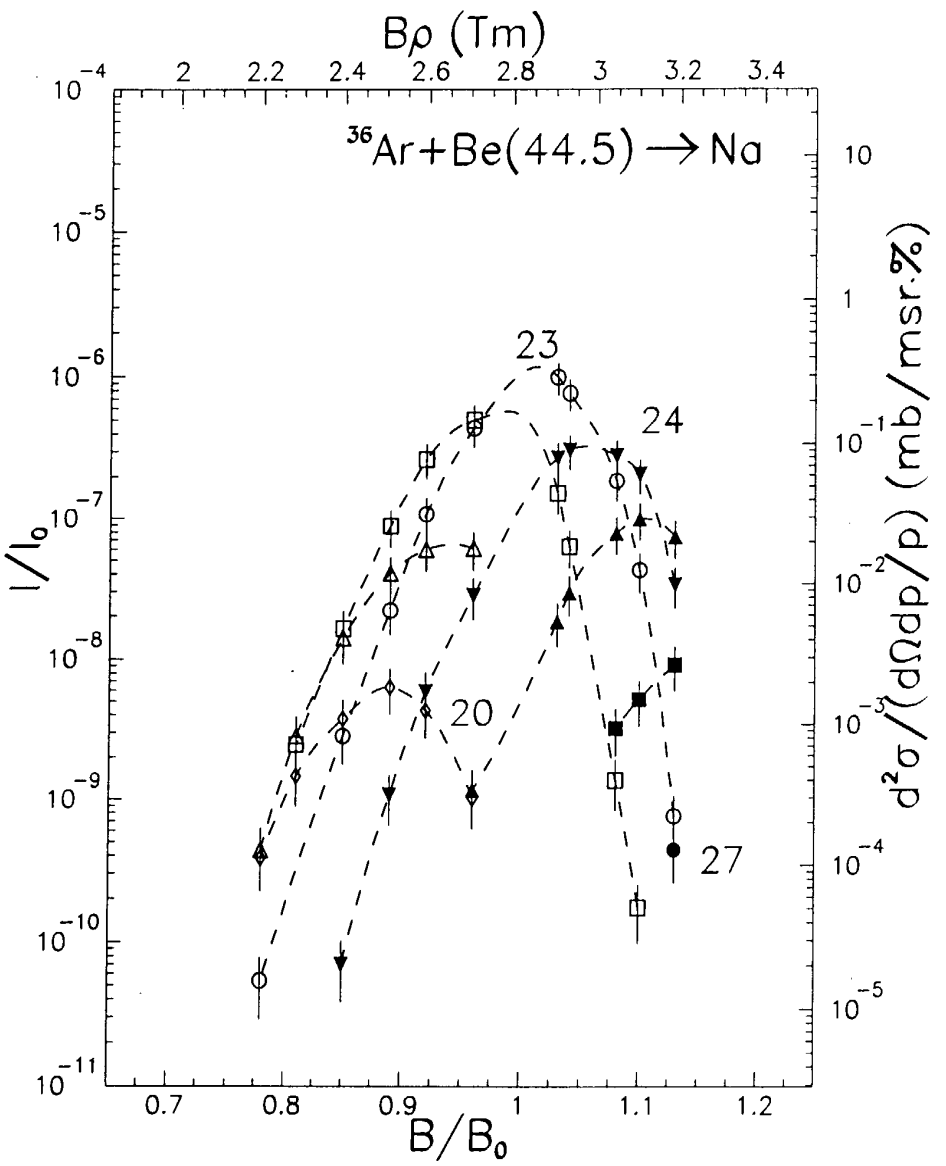
Bρ (Tm)
^{36}Ar+Be(44.5) → Na
I/I$_0$
d^{2}σ/(dΩdp/p) (mb/msr.%)
B/B$_0$
20
23
24
27

Fig. 6h

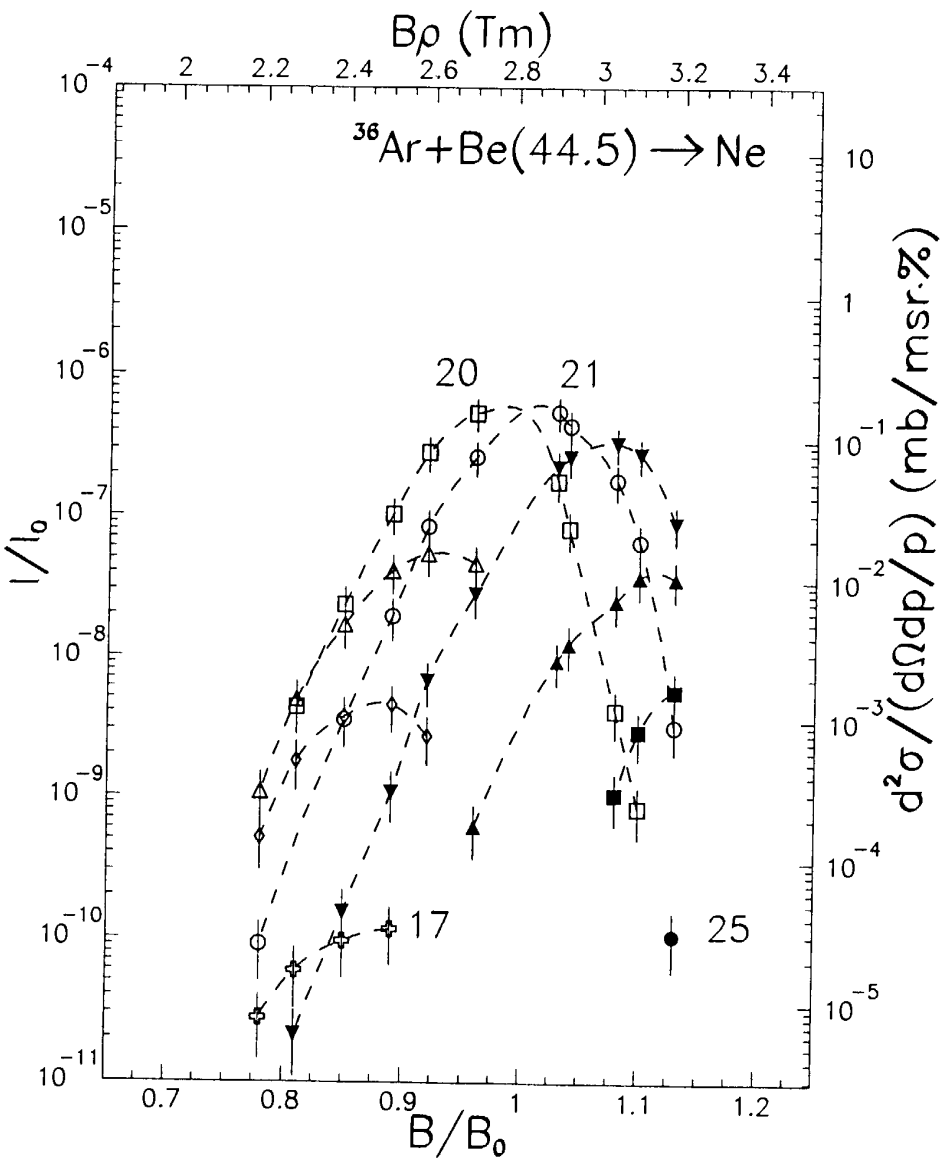
Bρ (Tm)
^{36}Ar+Be(44.5) → Ne
20
21
17
25
I/I$_0$
d^{2}σ/(dΩdp/p) (mb/msr.%)
B/B$_0$

Fig. 6i

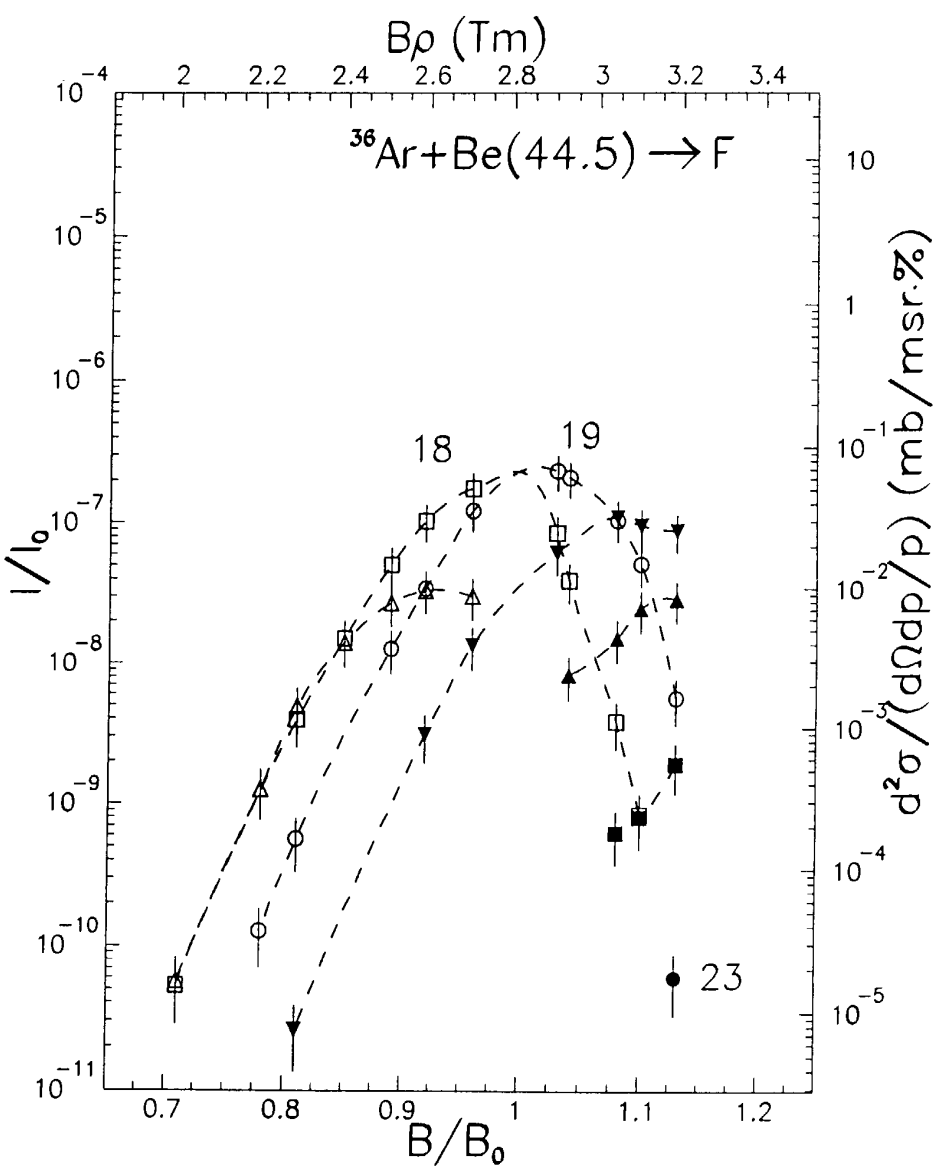
Bρ (Tm)
^{36}Ar+Be(44.5) → F
18
19
23
I/I$_0$
d^{2}σ/(dΩdp/p) (mb/msr.%)
B/B$_0$

Fig. 6j

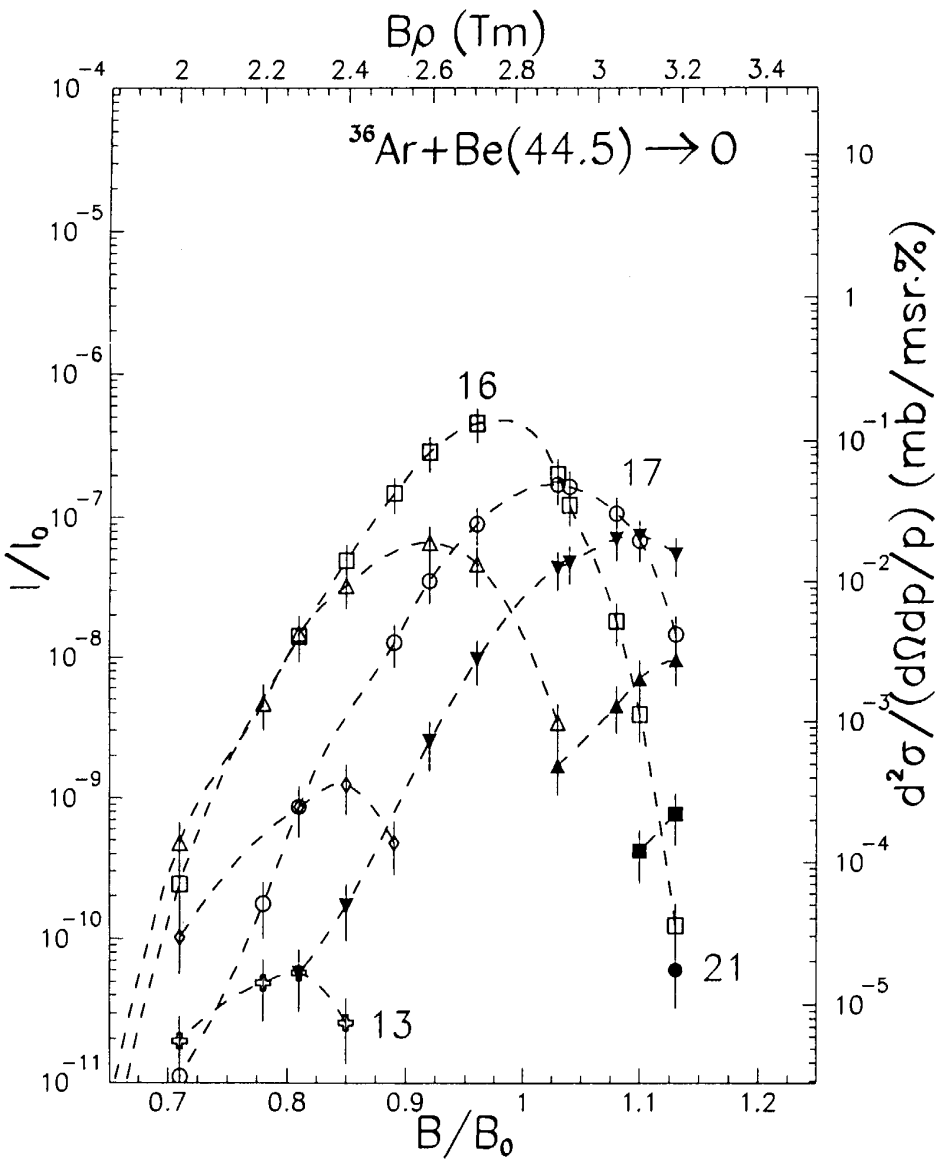
Bρ (Tm)
2
2.2
2.4
2.6
2.8
3
3.2
3.4
^{36}Ar+Be(44.5) → O
16
17
21
13
I/I$_0$
d^{2}σ/(dΩdp/p) (mb/msr·%)
B/B$_0$
0.7
0.8
0.9
1
1.1
1.2

Fig. 6k

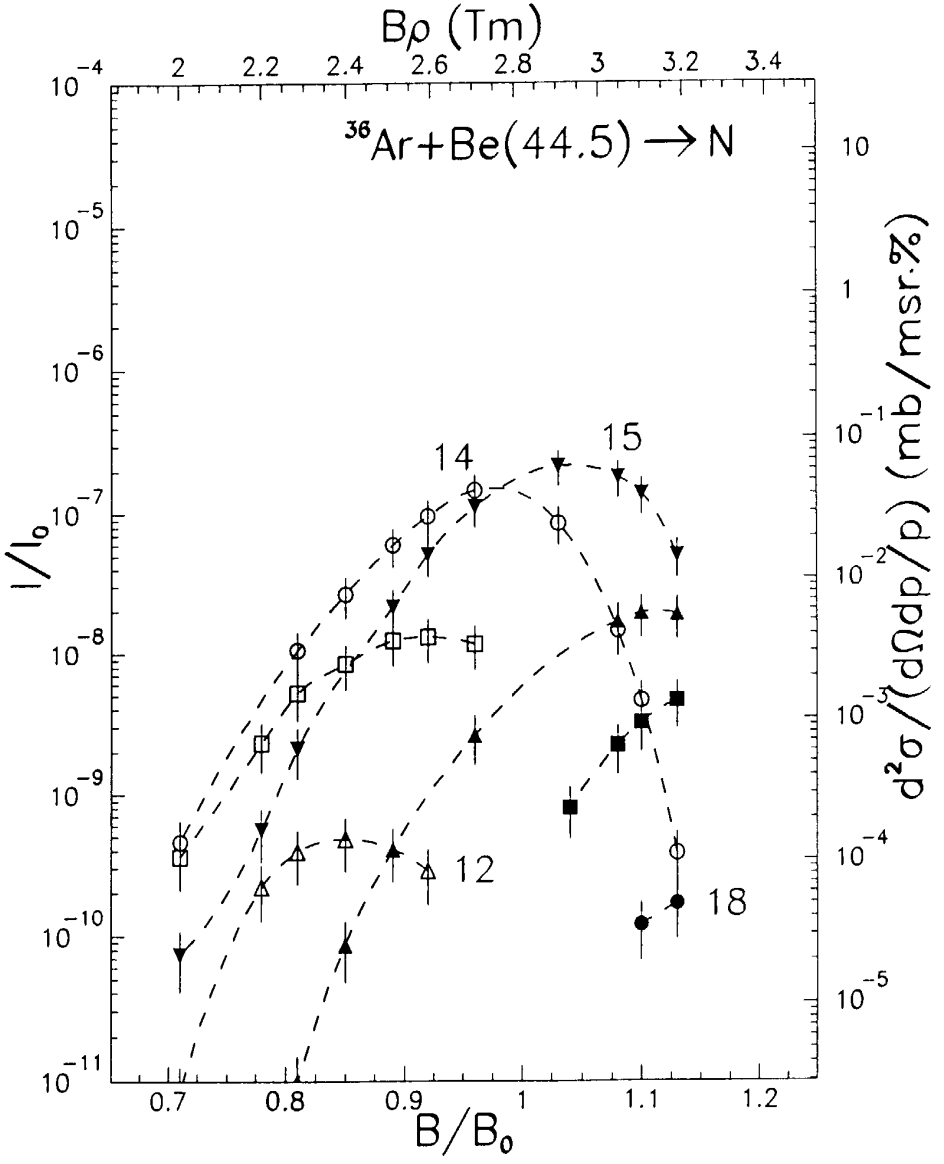
Bρ (Tm)
2
2.2
2.4
2.6
2.8
3
3.2
3.4
^{36}Ar+Be(44.5) → N
14
15
12
18
I/I$_0$
d^{2}σ/(dΩdp/p) (mb/msr·%)
B/B$_0$
0.7
0.8
0.9
1
1.1
1.2

Fig. 6l

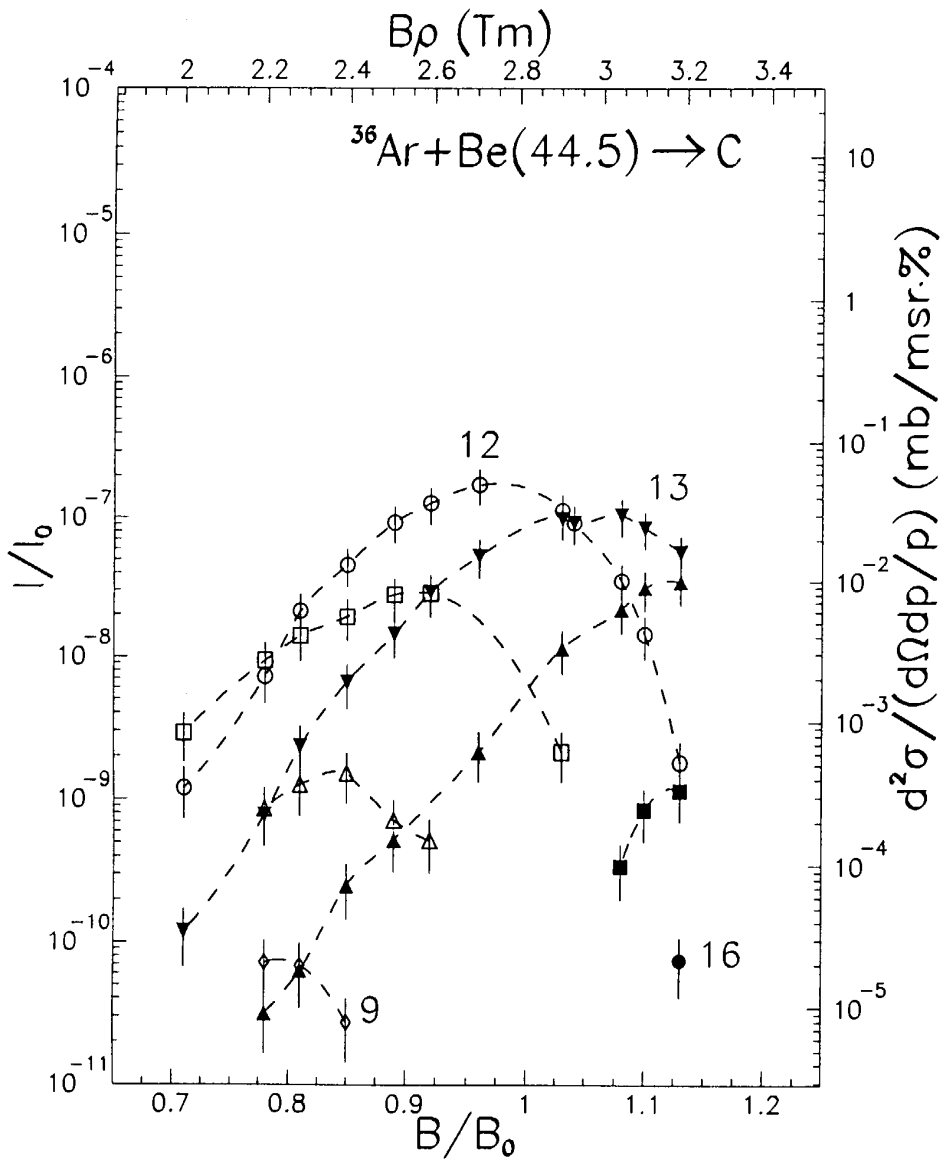
Bρ (Tm)
^{36}Ar+Be(44.5) → C
I/I$_0$
d^{2}σ/(dΩdp/p) (mb/msr·%)
B/B$_0$
12
13
9
16

Fig. 6m

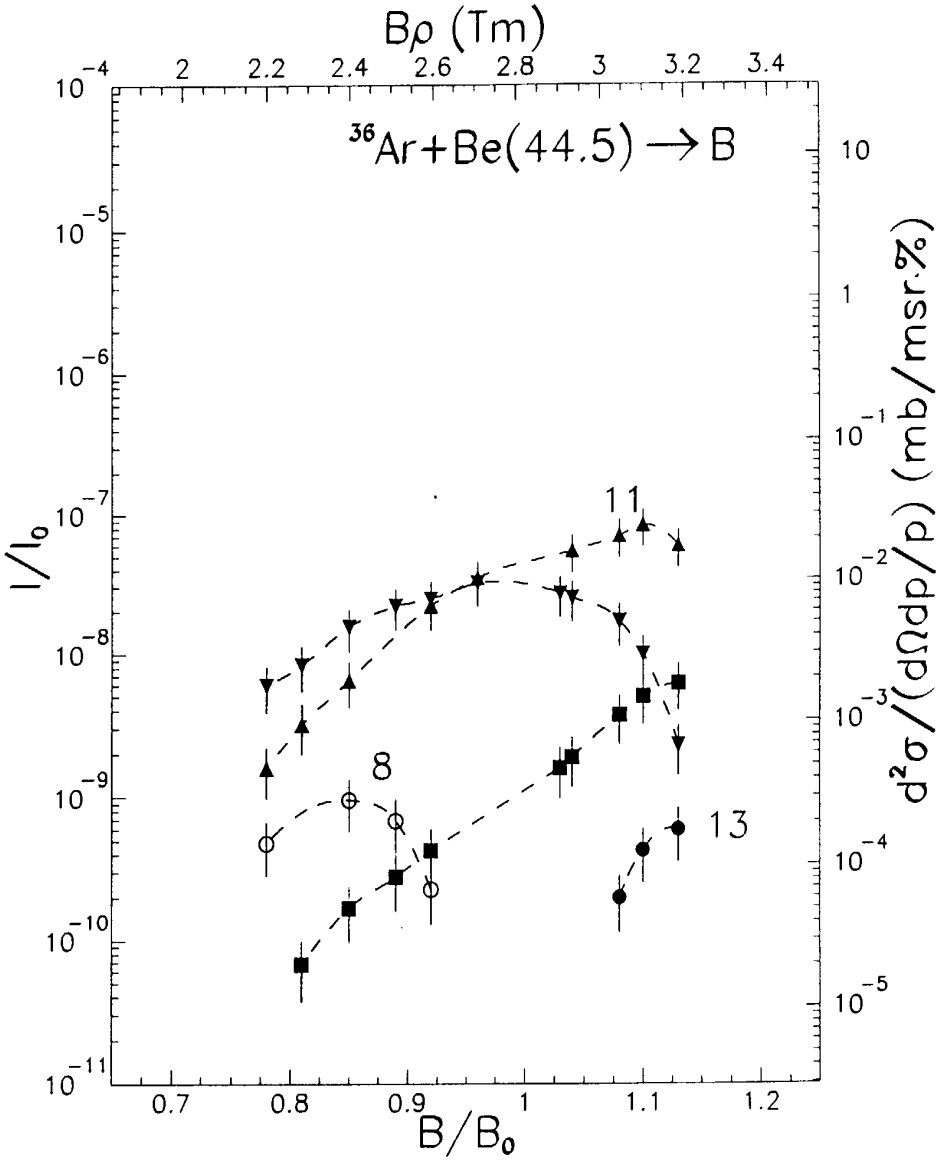
Bρ (Tm)
^{36}Ar+Be(44.5) → B
I/I$_0$
d^{2}σ/(dΩdp/p) (mb/msr·%)
B/B$_0$
11
8
13

Fig. 6n

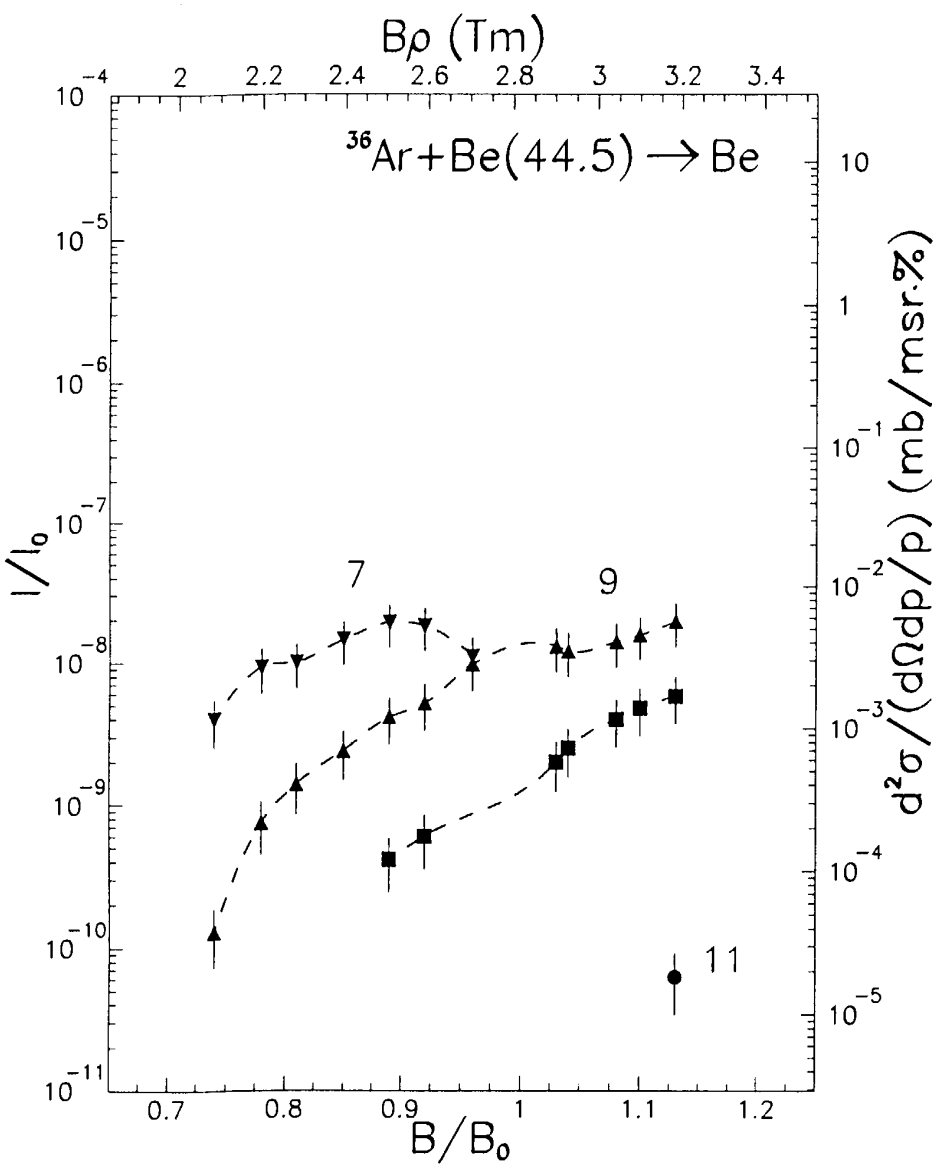
Bρ (Tm)
^{36}Ar+Be(44.5) → Be
I/I$_0$
d^{2}σ/(dΩdp/p) (mb/msr.%)
B/B$_0$
7
9
11

Fig. 6o

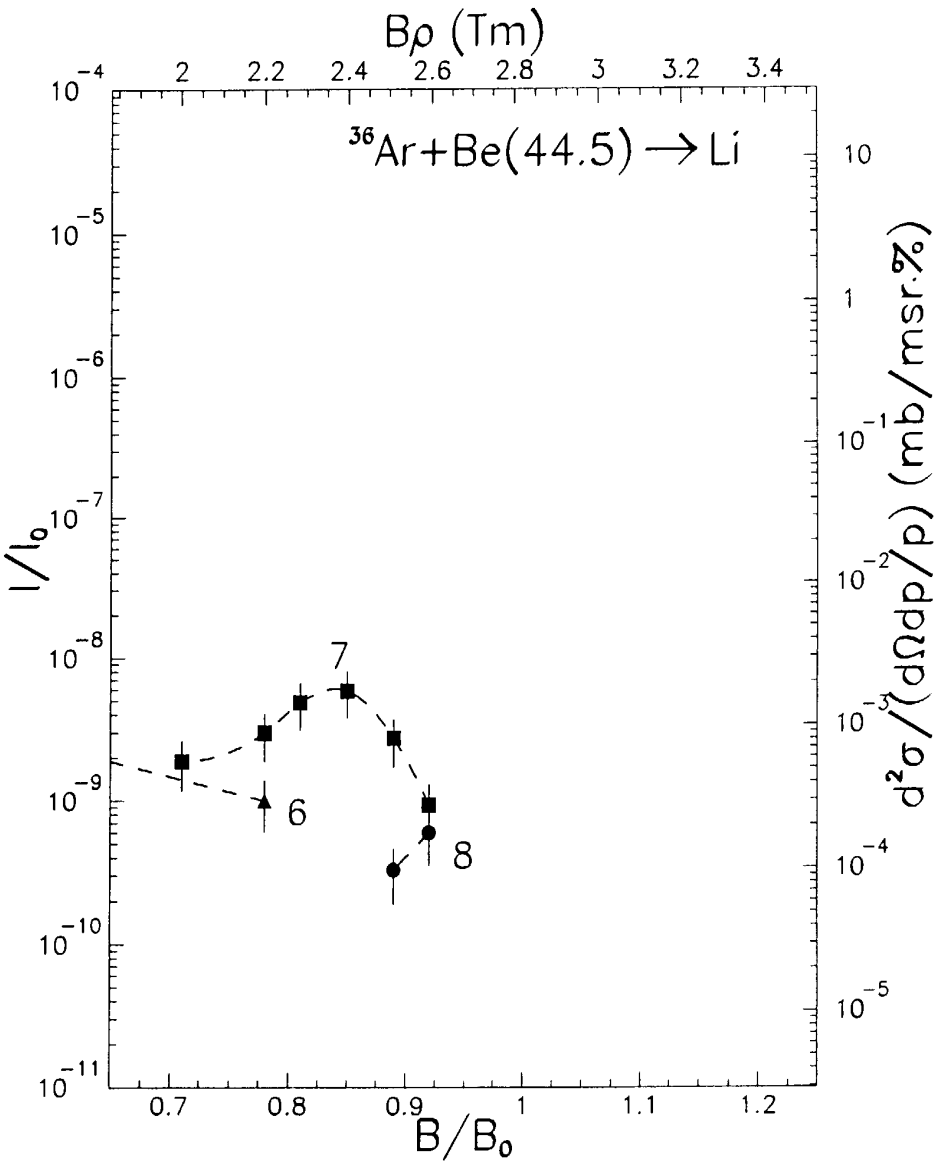
Bρ (Tm)
^{36}Ar+Be(44.5) → Li
I/I$_0$
d^{2}σ/(dΩdp/p) (mb/msr.%)
B/B$_0$
6
7
8

Fig. 6p

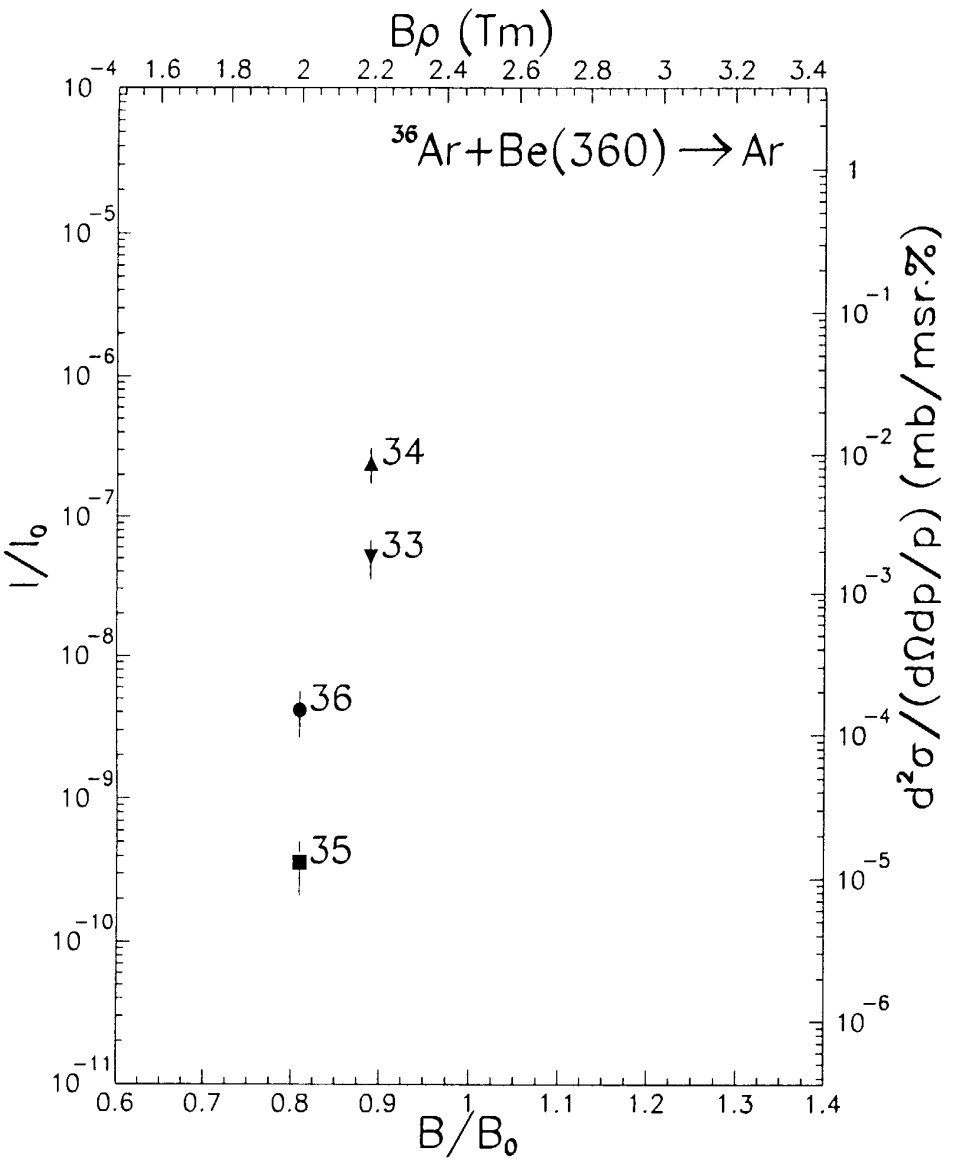
Bρ (Tm)
^{36}Ar+Be(360) → Ar
I/I$_0$
d^{2}σ/(dΩdp/p) (mb/msr·%)
B/B$_0$
34
33
36
35

Fig. 7a

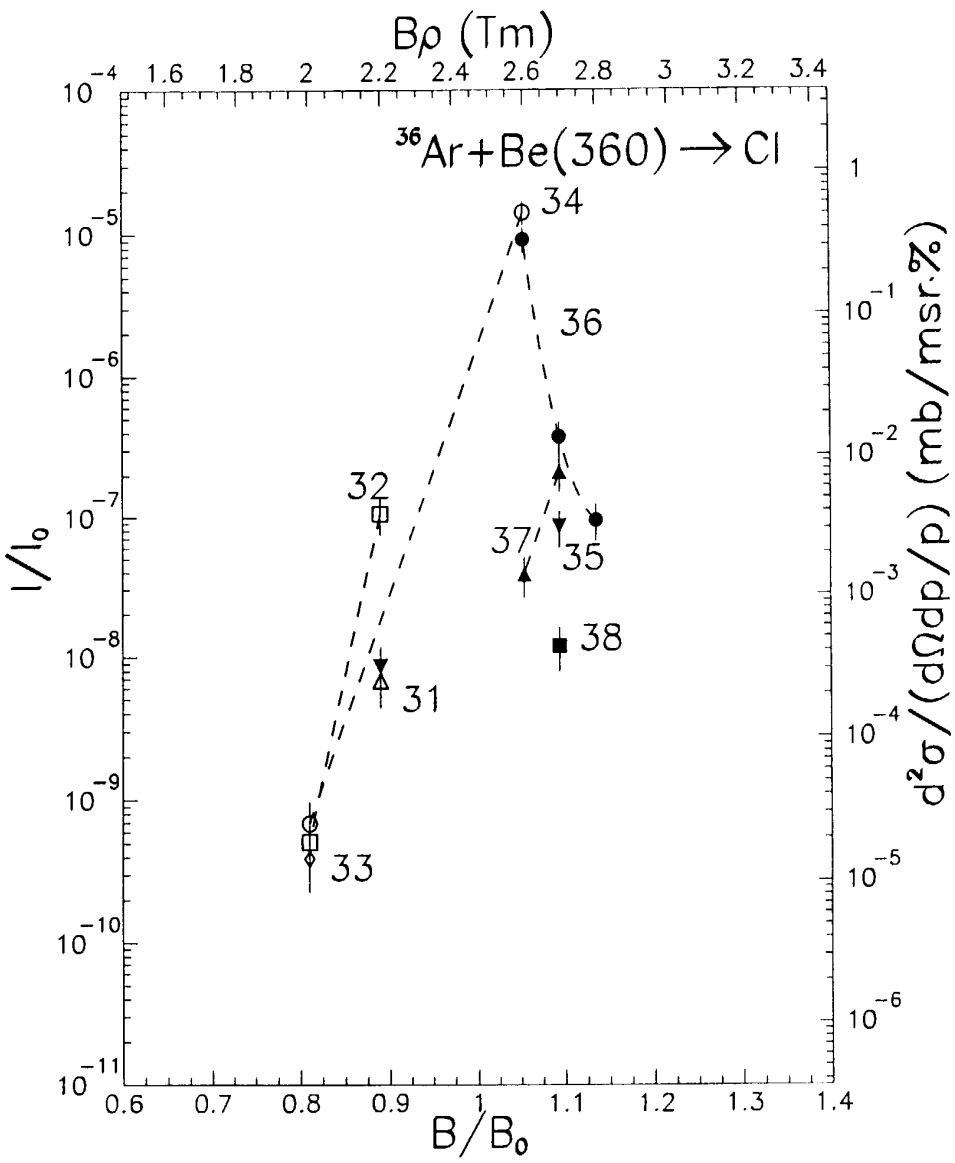
Bρ (Tm)
^{36}Ar+Be(360) → Cl
I/I$_0$
d^{2}σ/(dΩdp/p) (mb/msr·%)
B/B$_0$
34
36
32
37
35
38
31
33

Fig. 7b

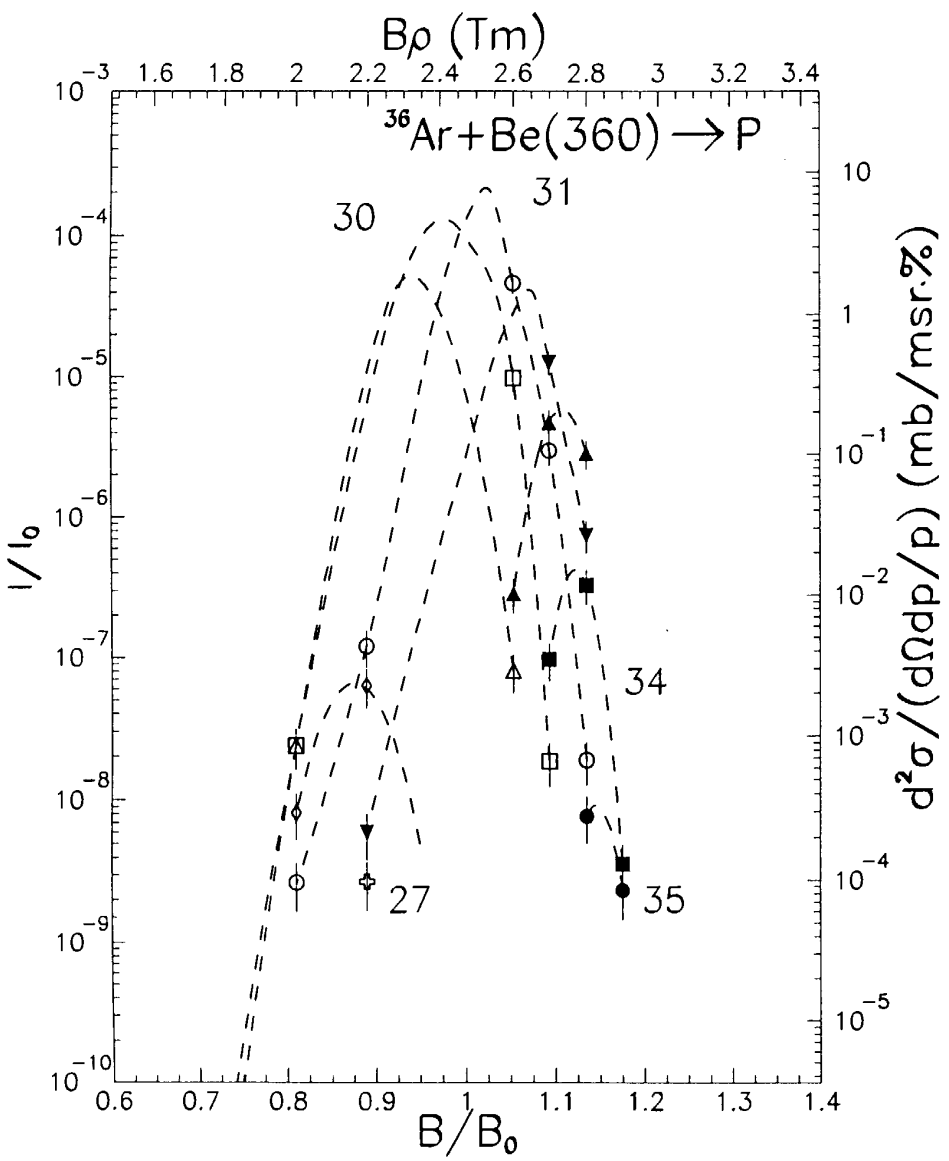
Bρ (Tm)
^{36}Ar+Be(360) → P
30
31
34
27
35
I/I$_0$
d^{2}σ/(dΩdp/p) (mb/msr·%)
B/B$_0$

Fig. 7c

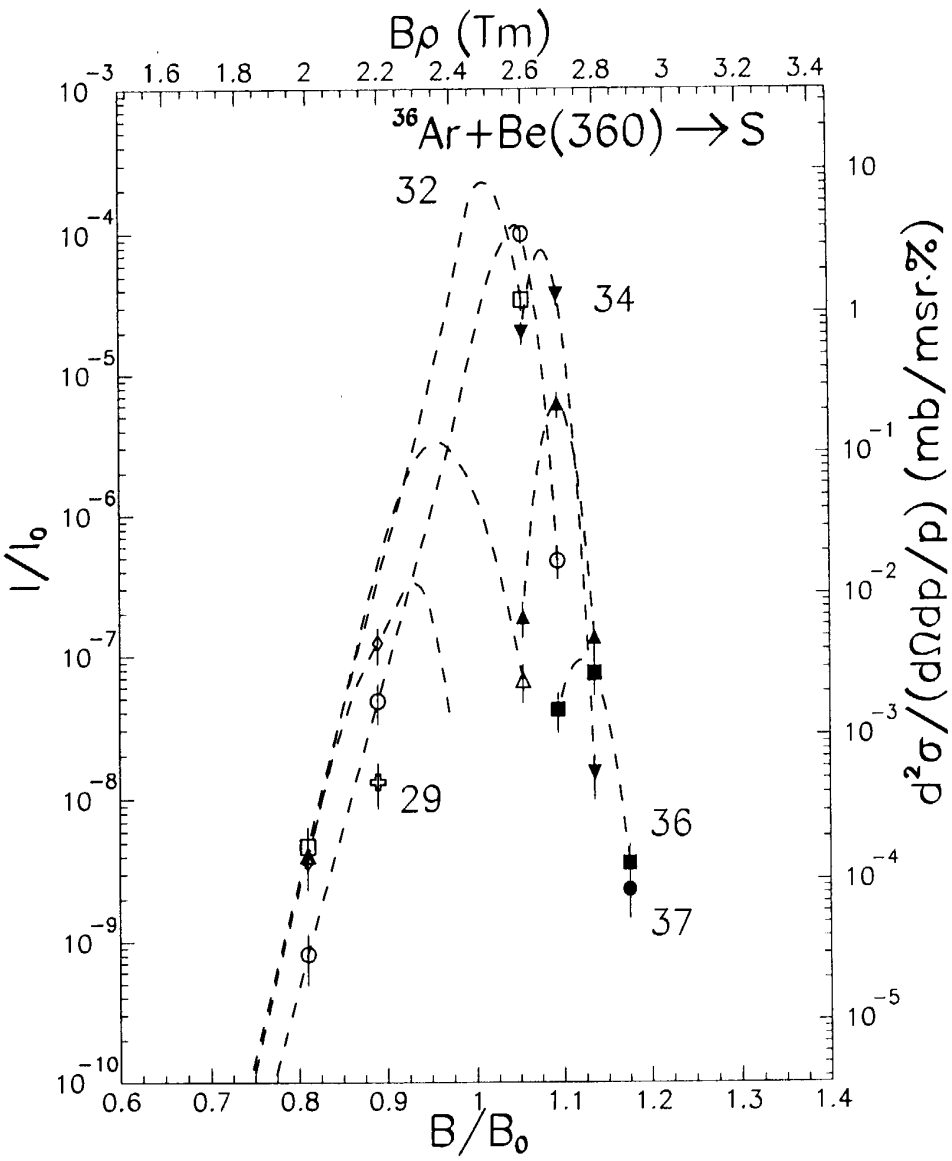
Bρ (Tm)
^{36}Ar+Be(360) → S
32
34
29
36
37
I/I$_0$
d^{2}σ/(dΩdp/p) (mb/msr·%)
B/B$_0$

Fig. 7d

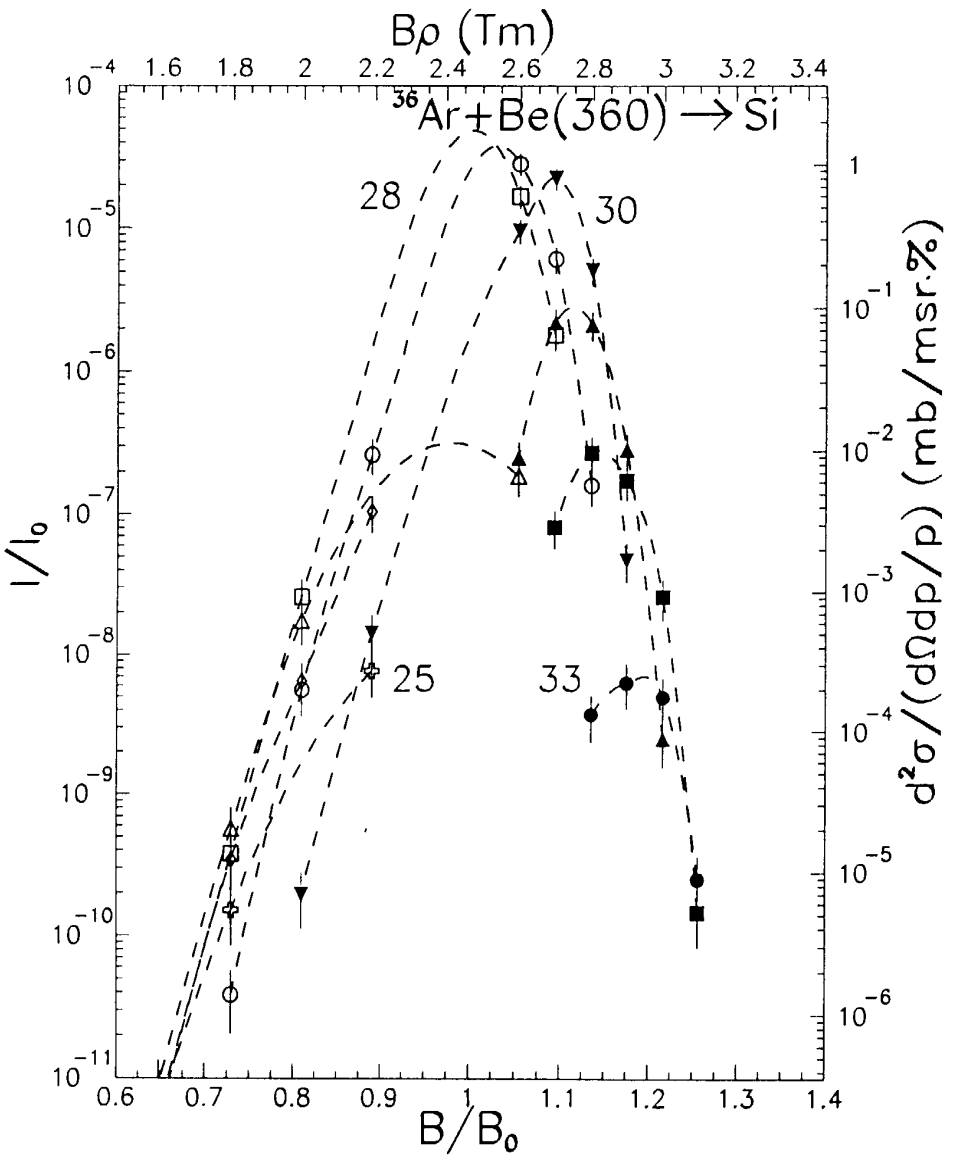
Bρ (Tm)
^{36}Ar+Be(360) → Si
28
30
25
33
I/I$_0$
B/B$_0$
d^{2}σ/(dΩdp/p) (mb/msr·%)

Fig. 7e

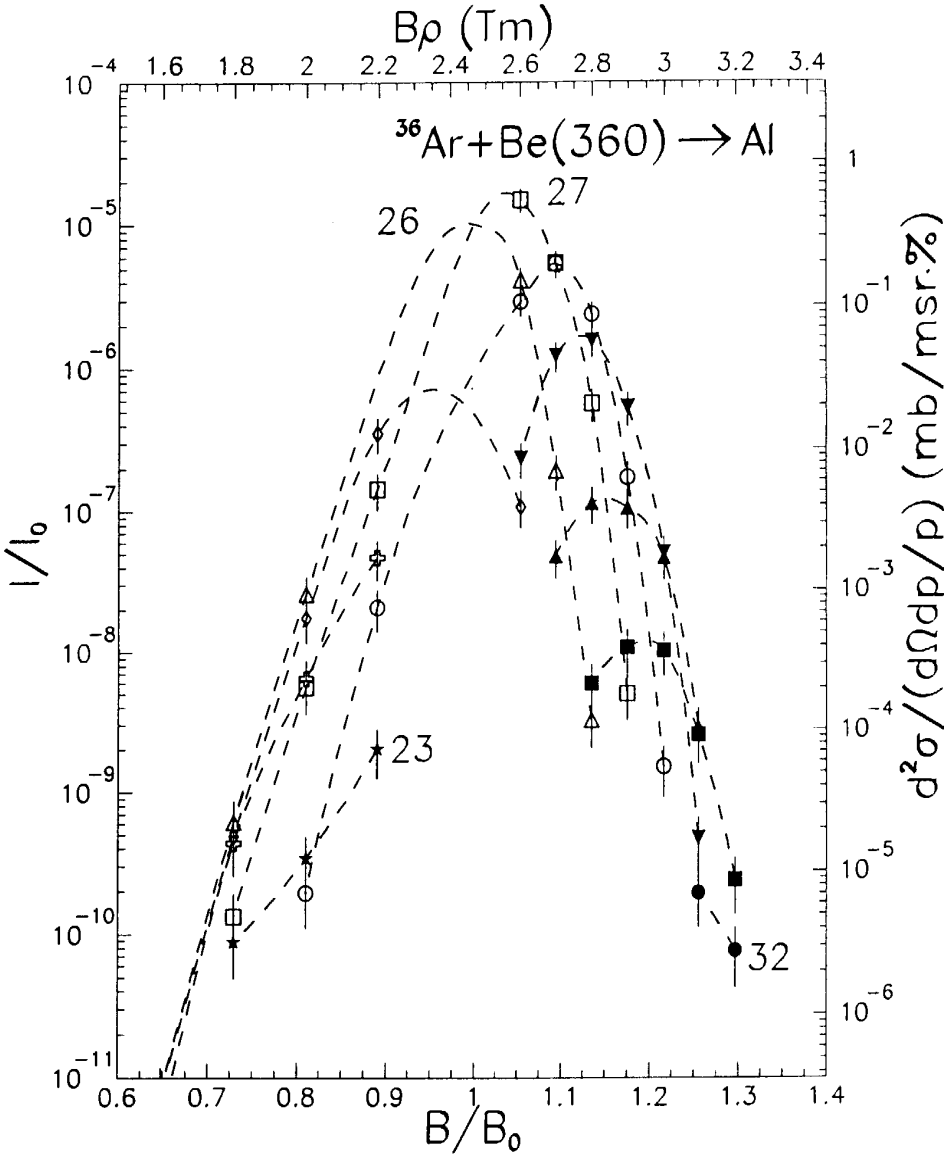
Bρ (Tm)
^{36}Ar+Be(360) → Al
26
27
23
32
I/I$_0$
B/B$_0$
d^{2}σ/(dΩdp/p) (mb/msr·%)

Fig. 7f

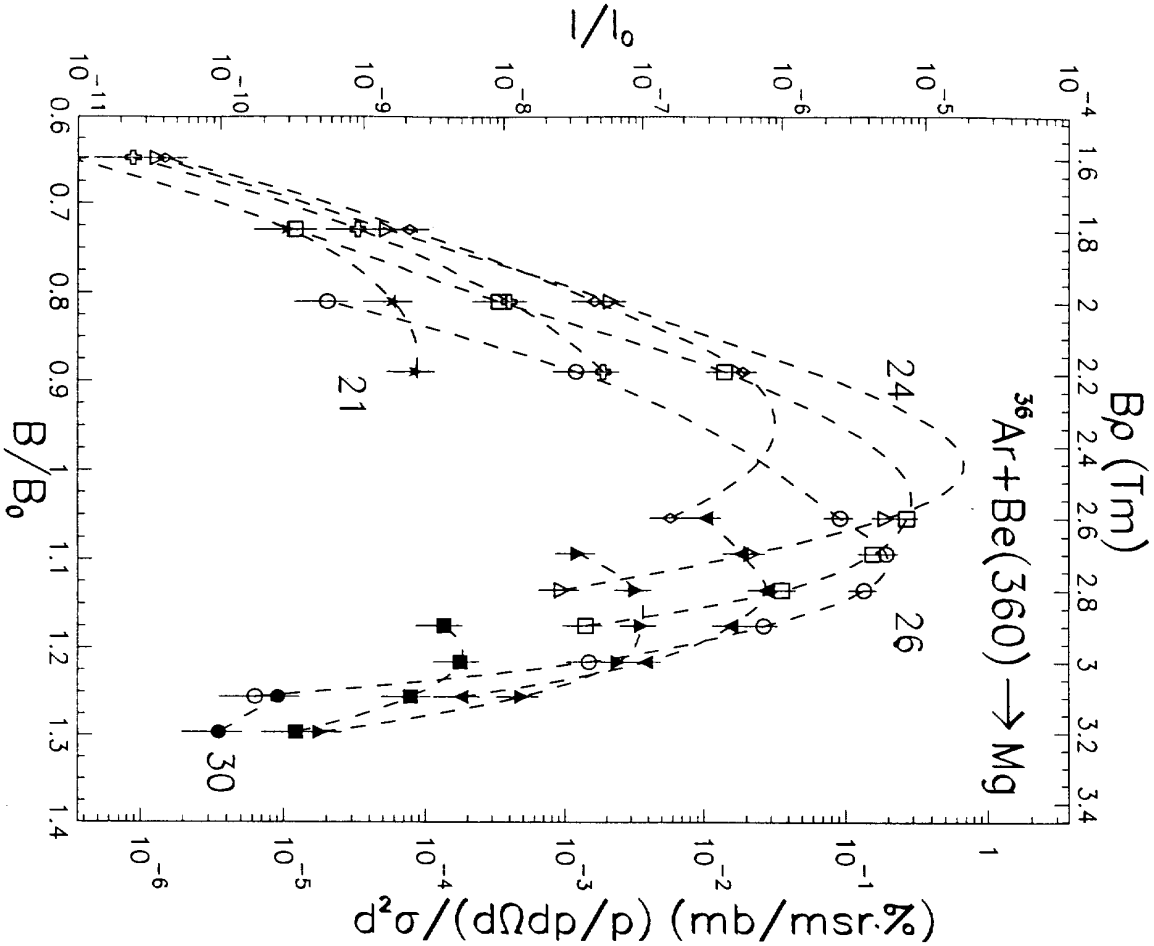
^{36}Ar+Be(360) → Mg
Bρ (Tm)
B/B$_0$
I/I$_0$
d^{2}σ/(dΩdp/p) (mb/msr.%)
21
24
26
30

Fig. 7g

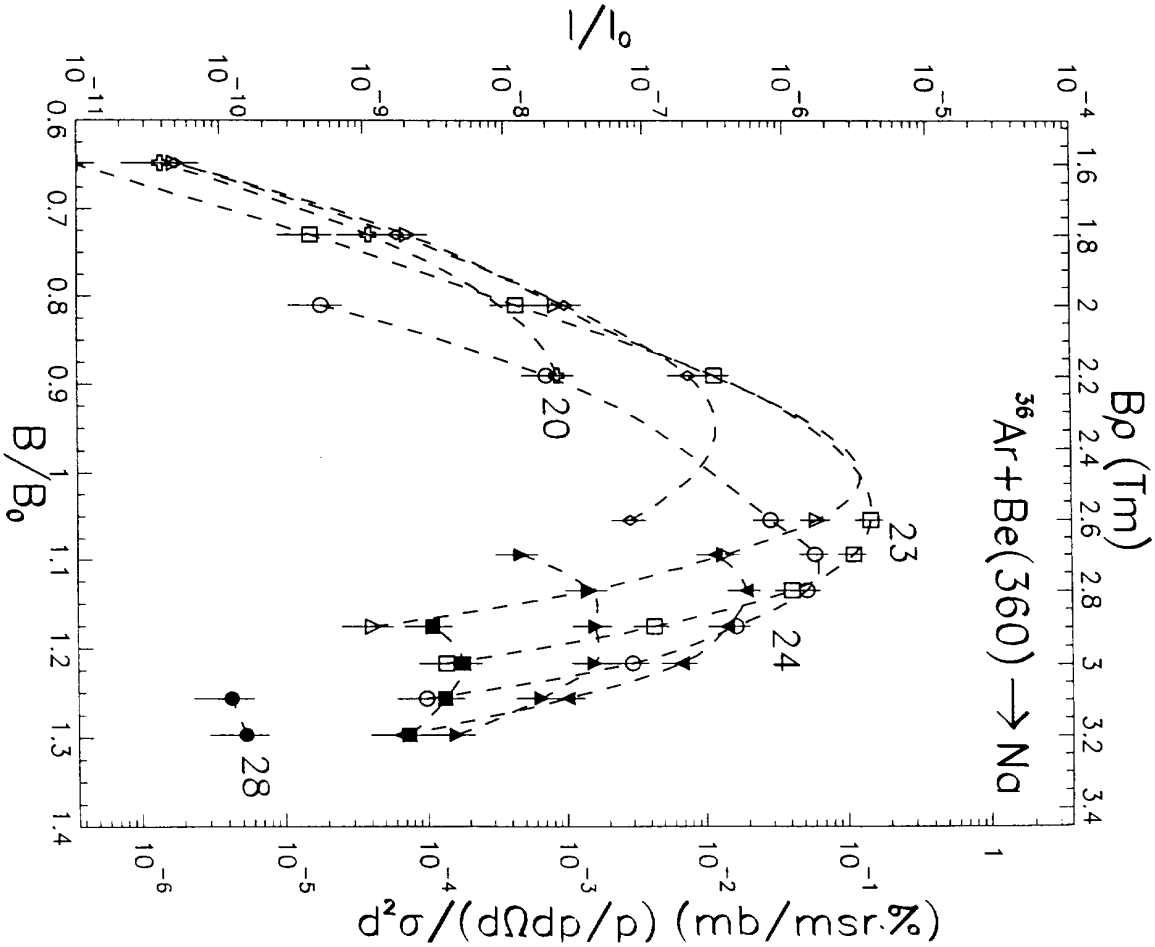
^{36}Ar+Be(360) → Na
Bρ (Tm)
B/B$_0$
I/I$_0$
d^{2}σ/(dΩdp/p) (mb/msr.%)
20
23
24
28

Fig. 7h

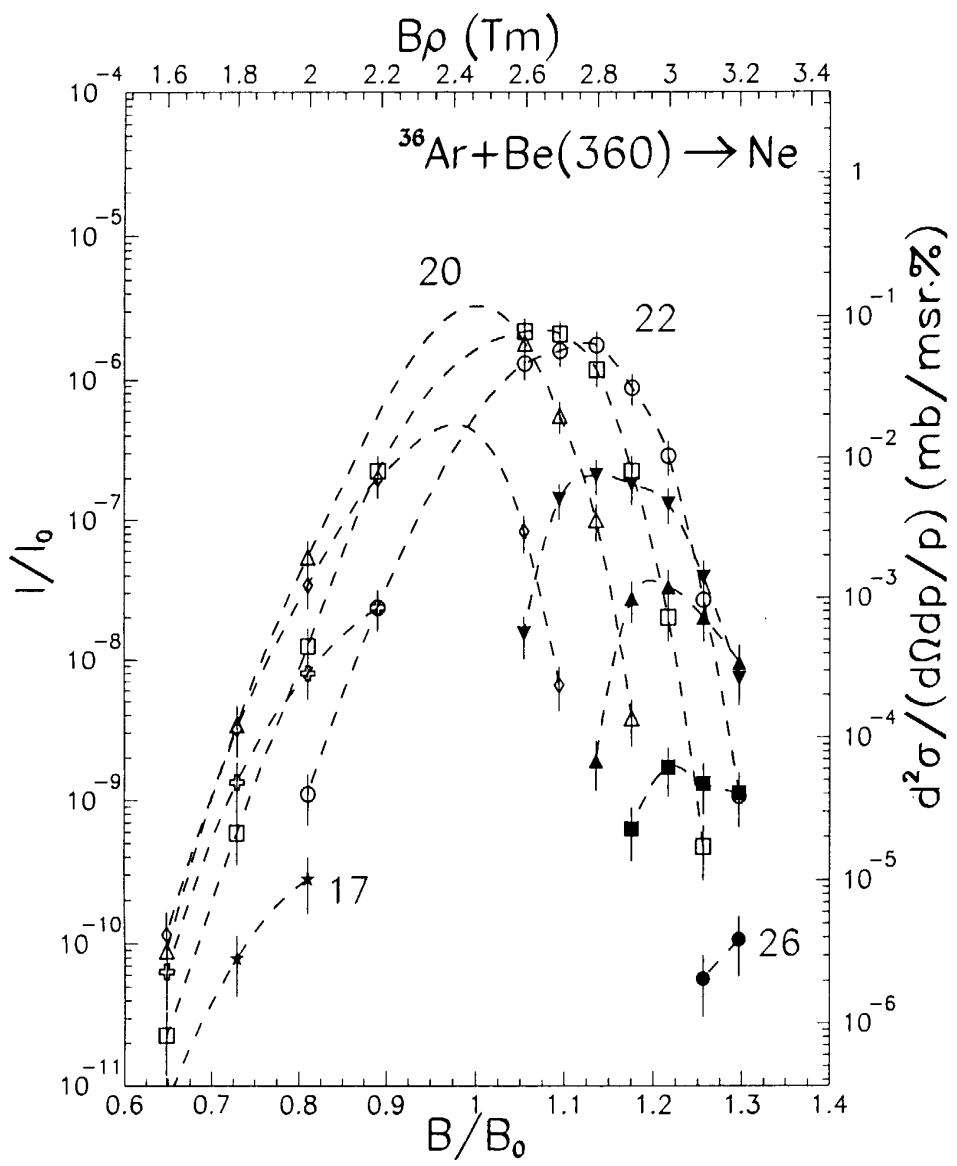
Bρ (Tm)
^{36}Ar+Be(360) → Ne
20
22
17
26
I/I$_0$
d^{2}σ/(dΩdp/p) (mb/msr·%)
B/B$_0$

Fig. 7i

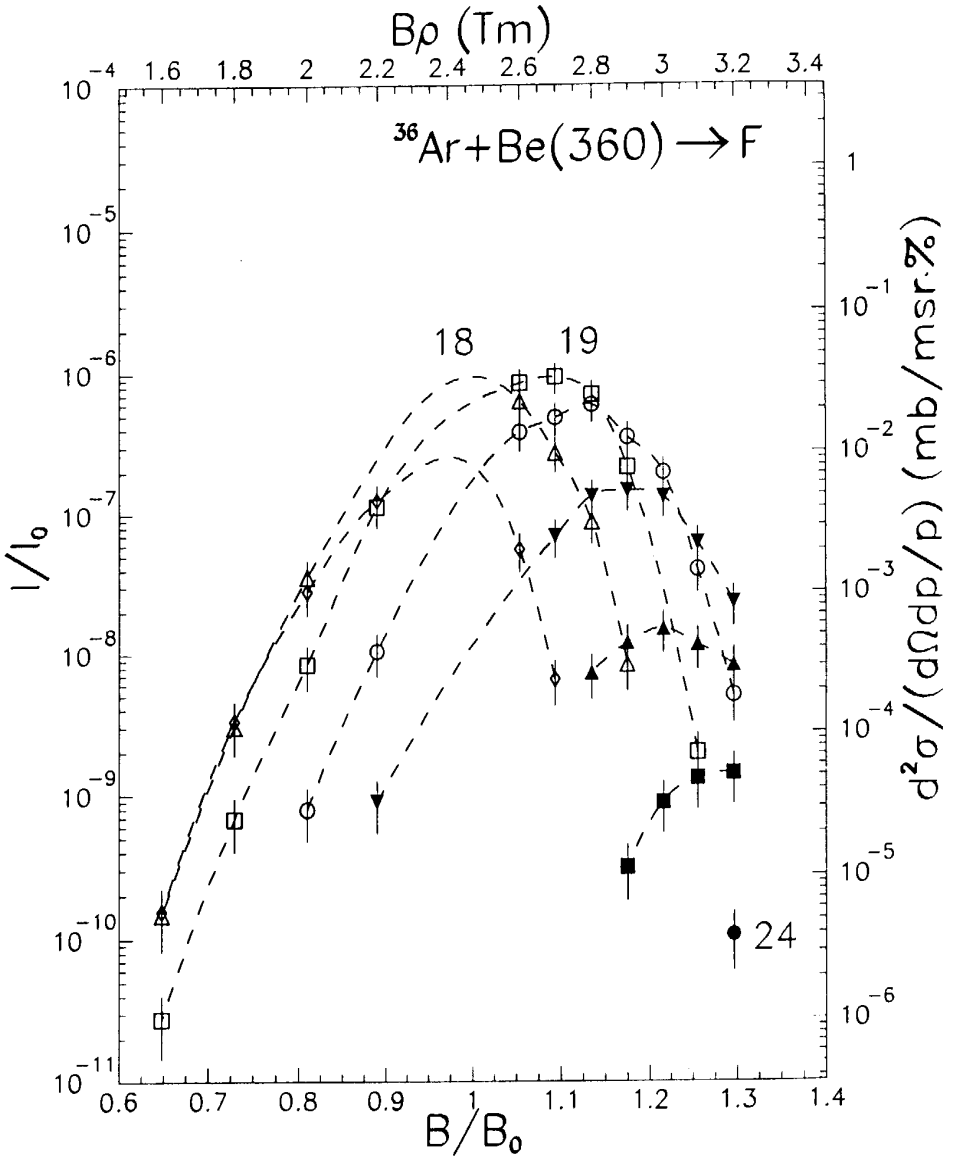
Bρ (Tm)
^{36}Ar+Be(360) → F
18
19
24
I/I$_0$
d^{2}σ/(dΩdp/p) (mb/msr·%)
B/B$_0$

Fig. 7j

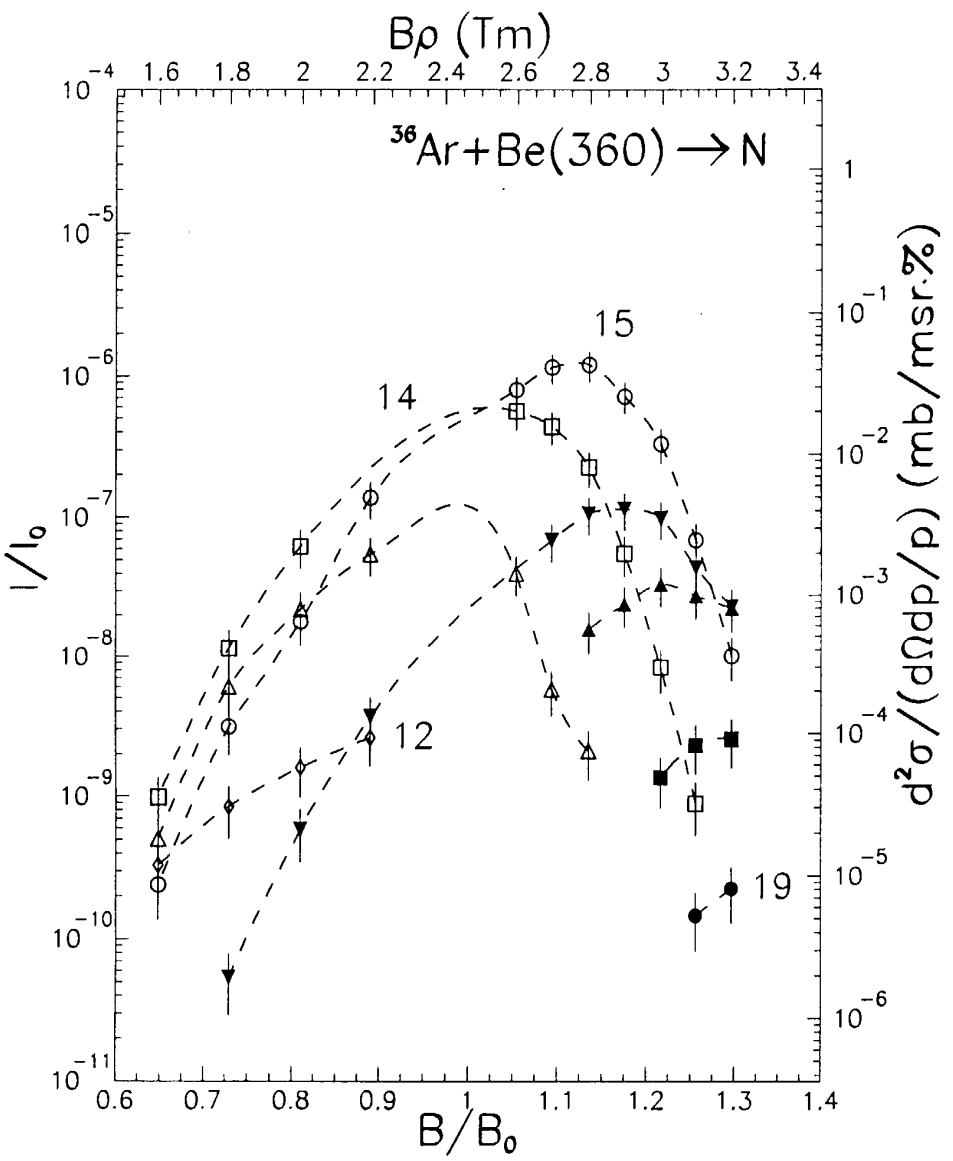
Bρ (Tm)
^{36}Ar+Be(360) → N
I/I$_0$
d^{2}σ/(dΩdp/p) (mb/msr·%)
B/B$_0$
12
14
15
19

Fig. 7k

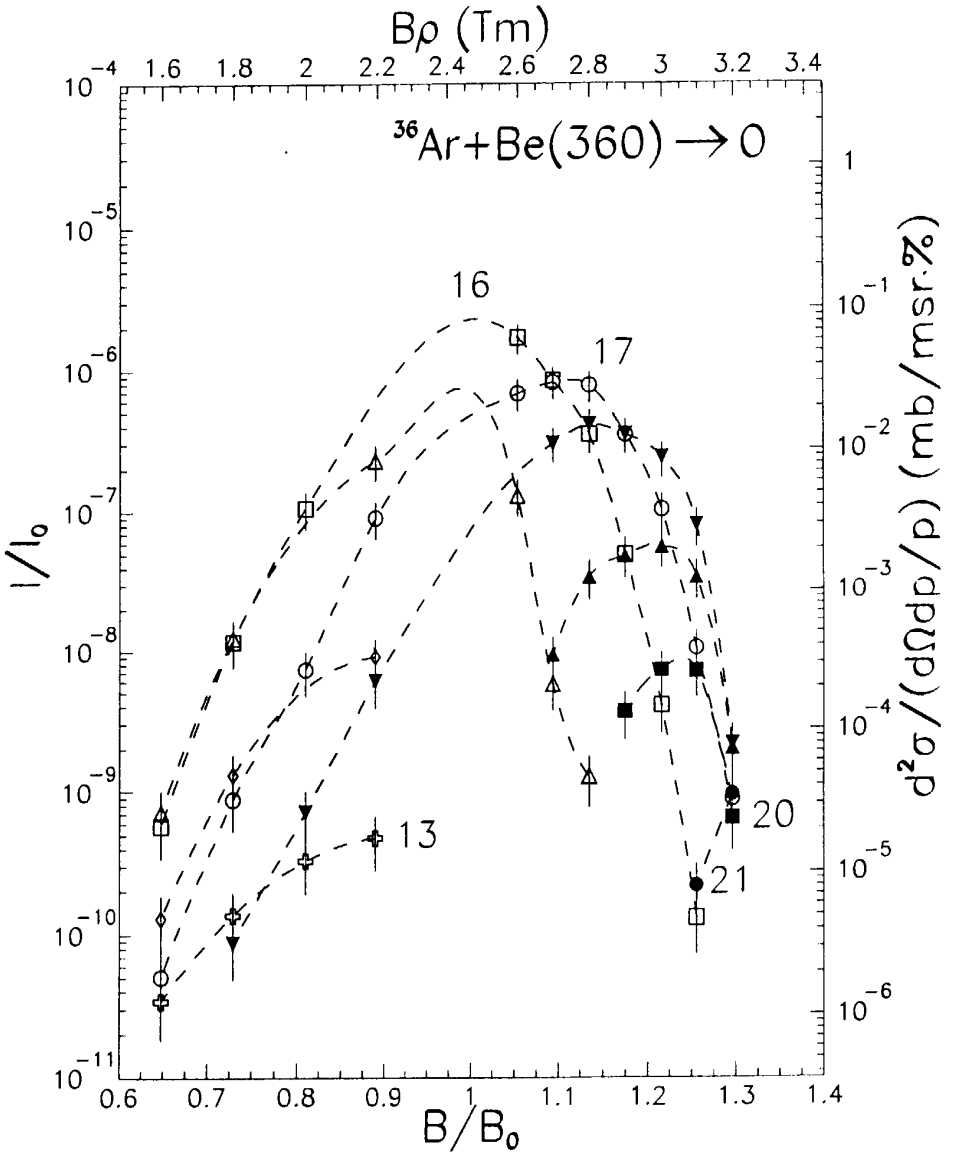
Bρ (Tm)
^{36}Ar+Be(360) → O
I/I$_0$
d^{2}σ/(dΩdp/p) (mb/msr·%)
B/B$_0$
13
16
17
20
21

Fig. 7l

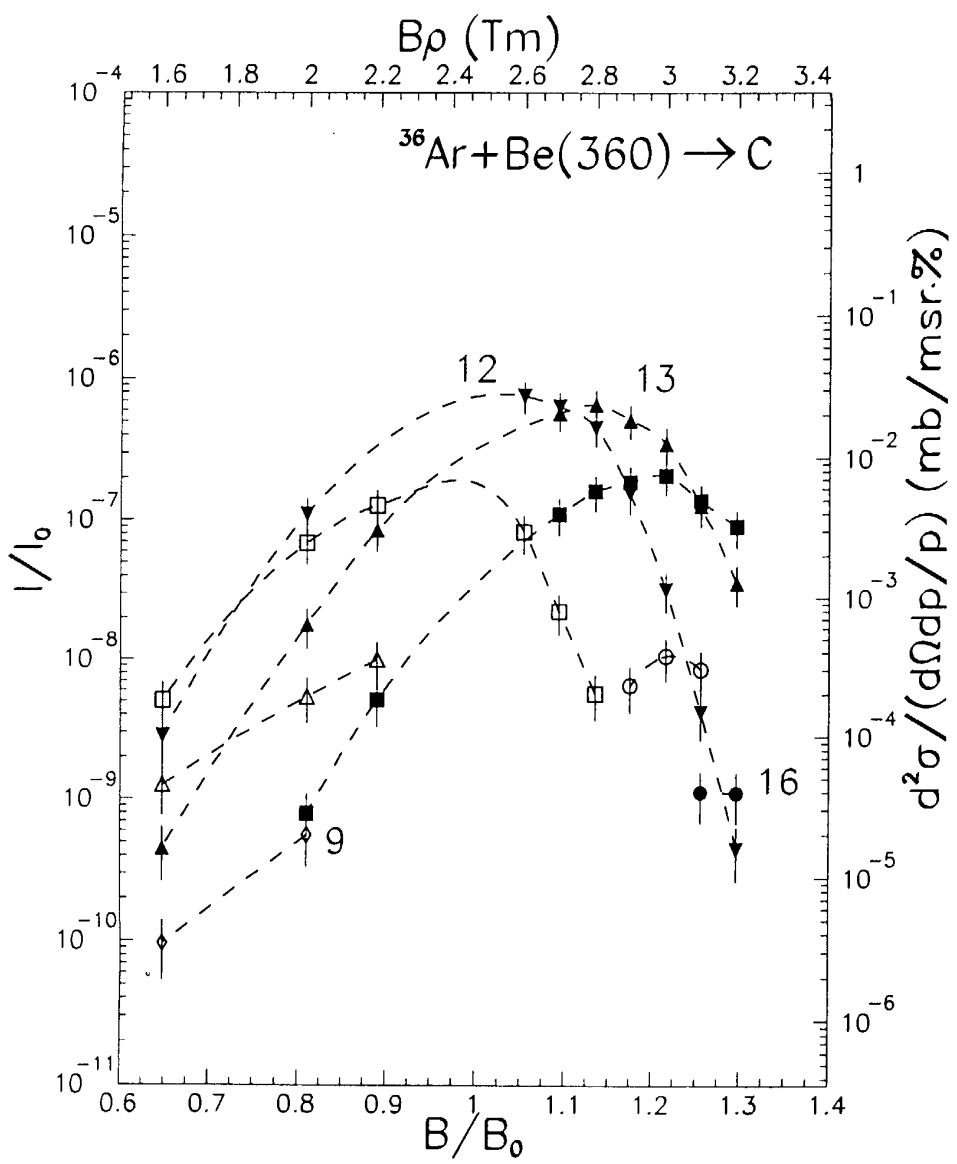
Bρ (Tm)
1.6 1.8 2 2.2 2.4 2.6 2.8 3 3.2 3.4
^{36}Ar+Be(360) → C
12
13
16
9
I/I$_0$
d^{2}σ/(dΩdp/p) (mb/msr·%)
B/B$_0$
0.6 0.7 0.8 0.9 1 1.1 1.2 1.3 1.4

Fig. 7m

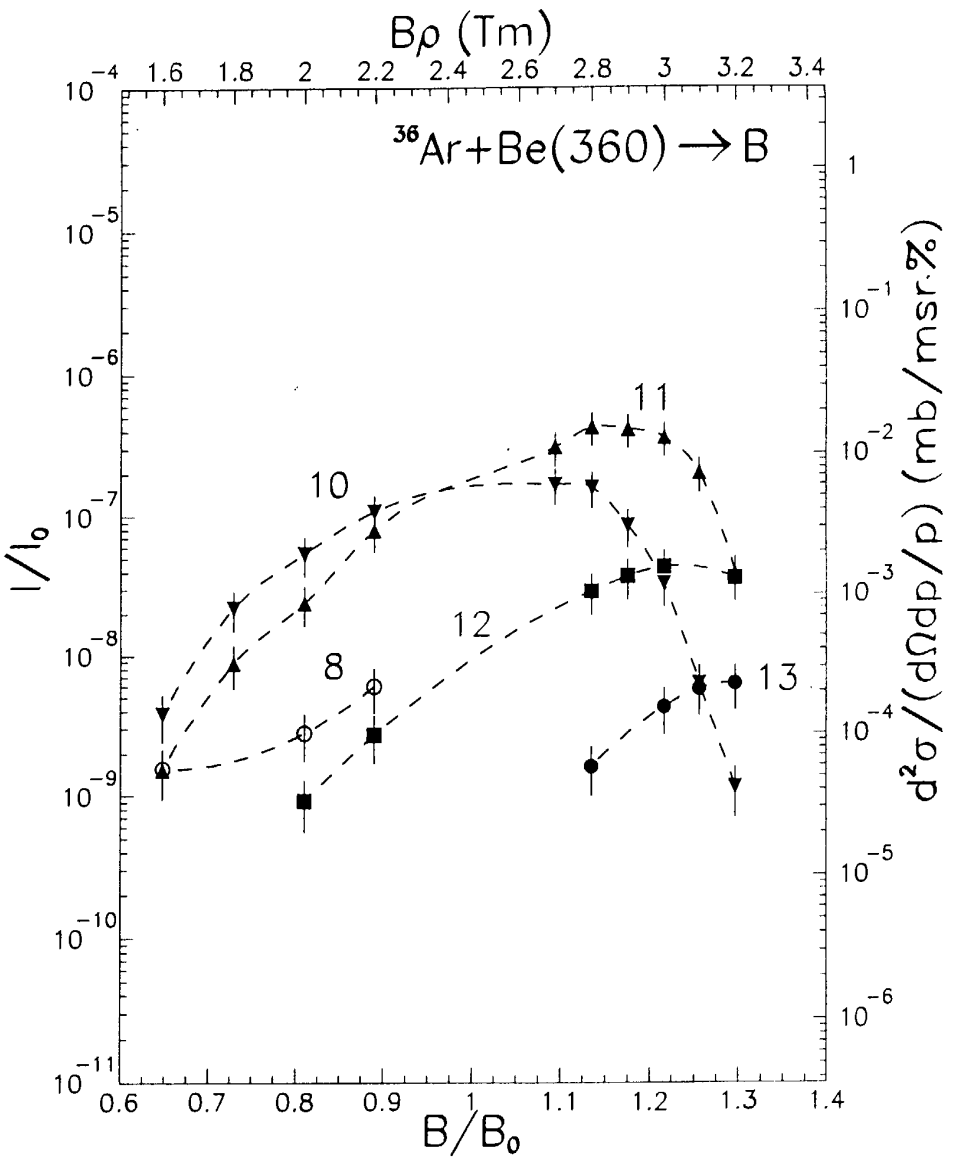
Bρ (Tm)
1.6 1.8 2 2.2 2.4 2.6 2.8 3 3.2 3.4
^{36}Ar+Be(360) → B
11
10
12
8
13
I/I$_0$
d^{2}σ/(dΩdp/p) (mb/msr·%)
B/B$_0$
0.6 0.7 0.8 0.9 1 1.1 1.2 1.3 1.4

Fig. 7n

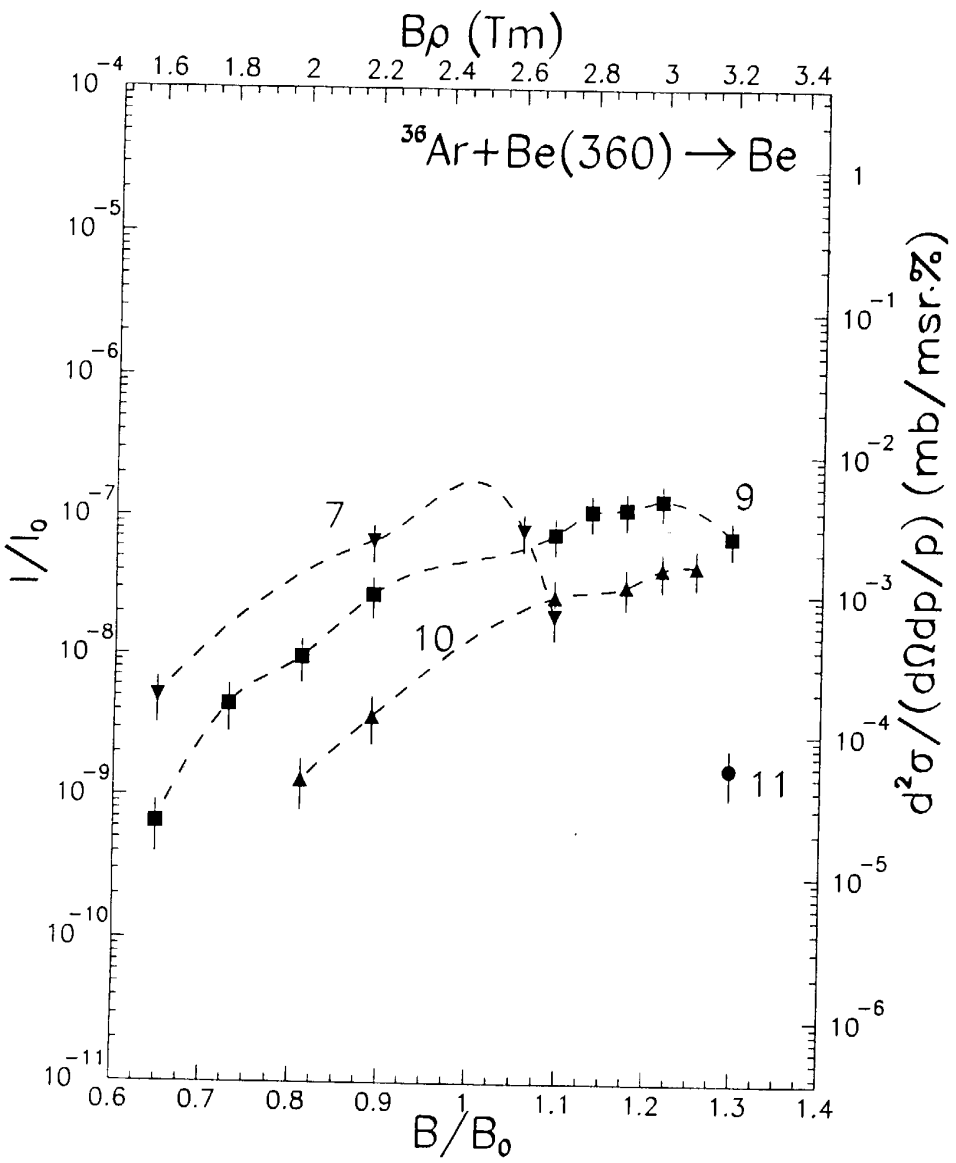
Bρ (Tm)
^{36}Ar+Be(360) → Be
I/I$_0$
d^{2}σ/(dΩdp/p) (mb/msr.%)
B/B$_0$
7
9
10
11

Fig. 7o

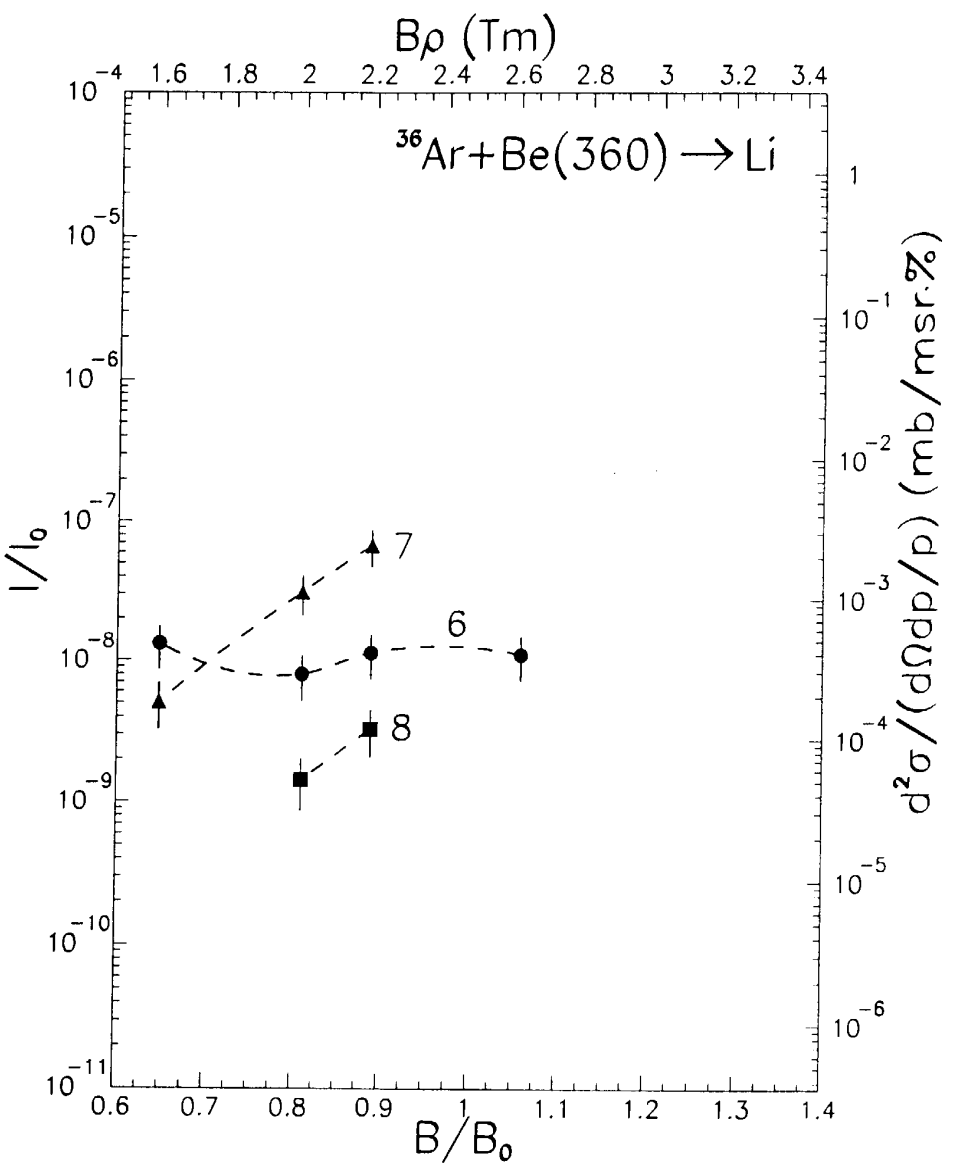
Bρ (Tm)
^{36}Ar+Be(360) → Li
I/I$_0$
d^{2}σ/(dΩdp/p) (mb/msr.%)
B/B$_0$
7
6
8

Fig. 7p

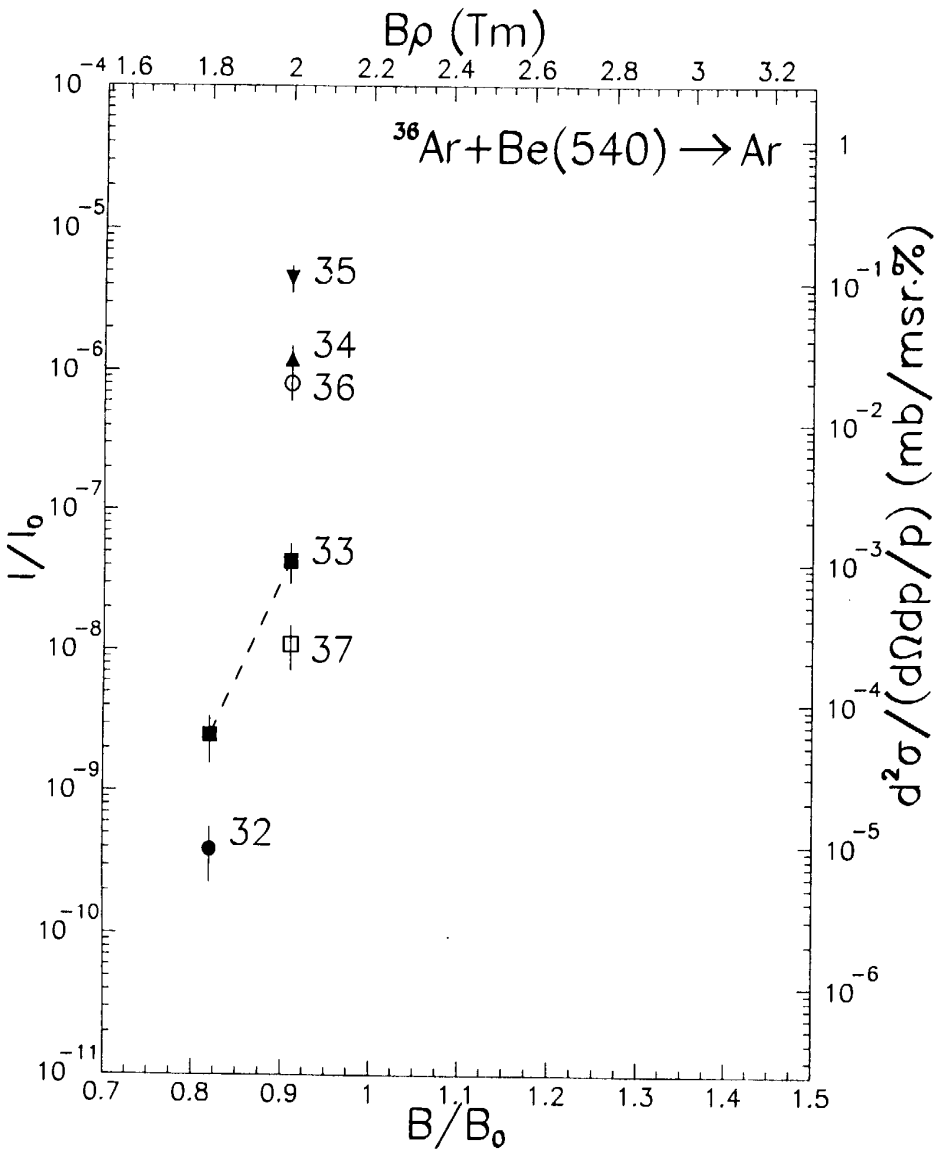
Bρ (Tm)
^{36}Ar+Be(540) → Ar
35
34
36
33
37
32
I/I$_0$
d^{2}σ/(dΩdp/p) (mb/msr·%)
B/B$_0$

Fig. 8a

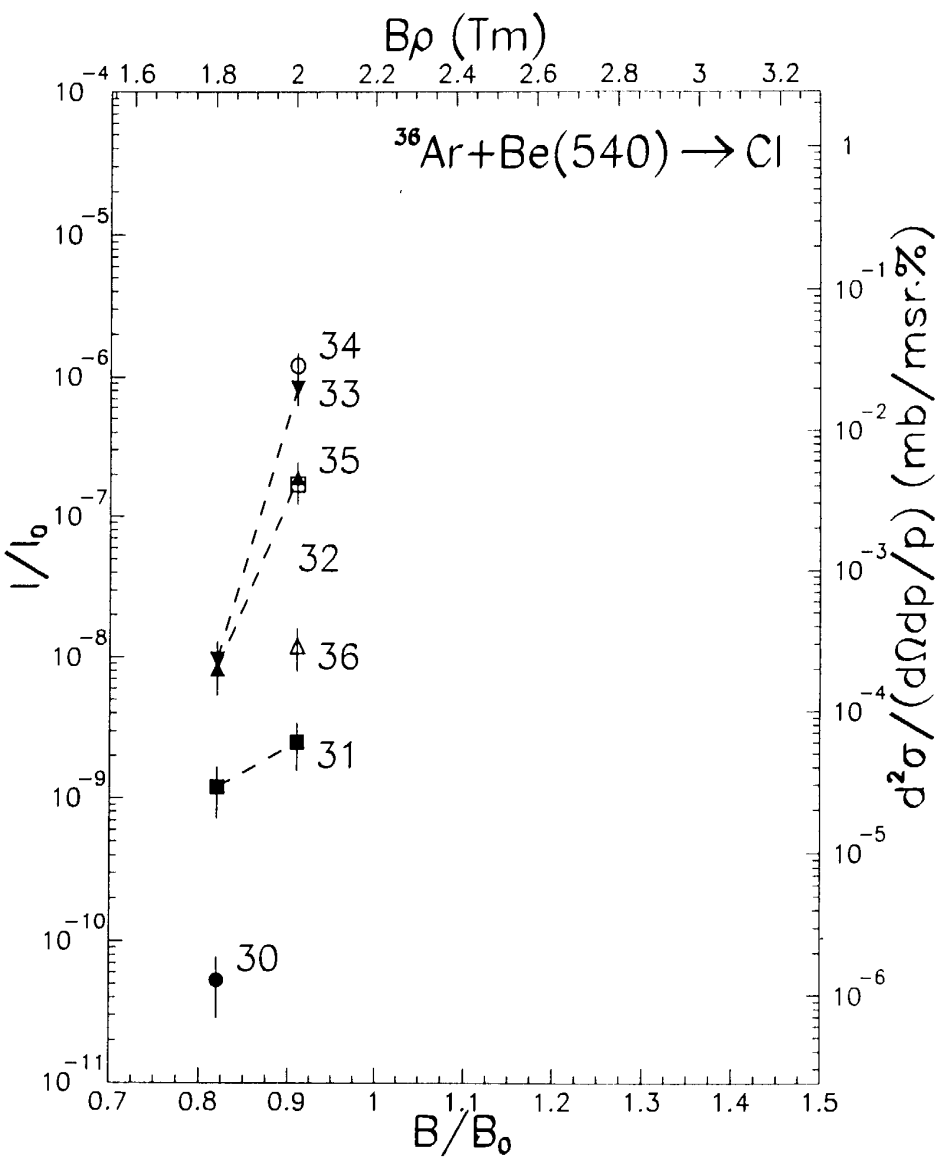
Bρ (Tm)
^{36}Ar+Be(540) → Cl
34
33
35
32
36
31
30
I/I$_0$
d^{2}σ/(dΩdp/p) (mb/msr·%)
B/B$_0$

Fig. 8b

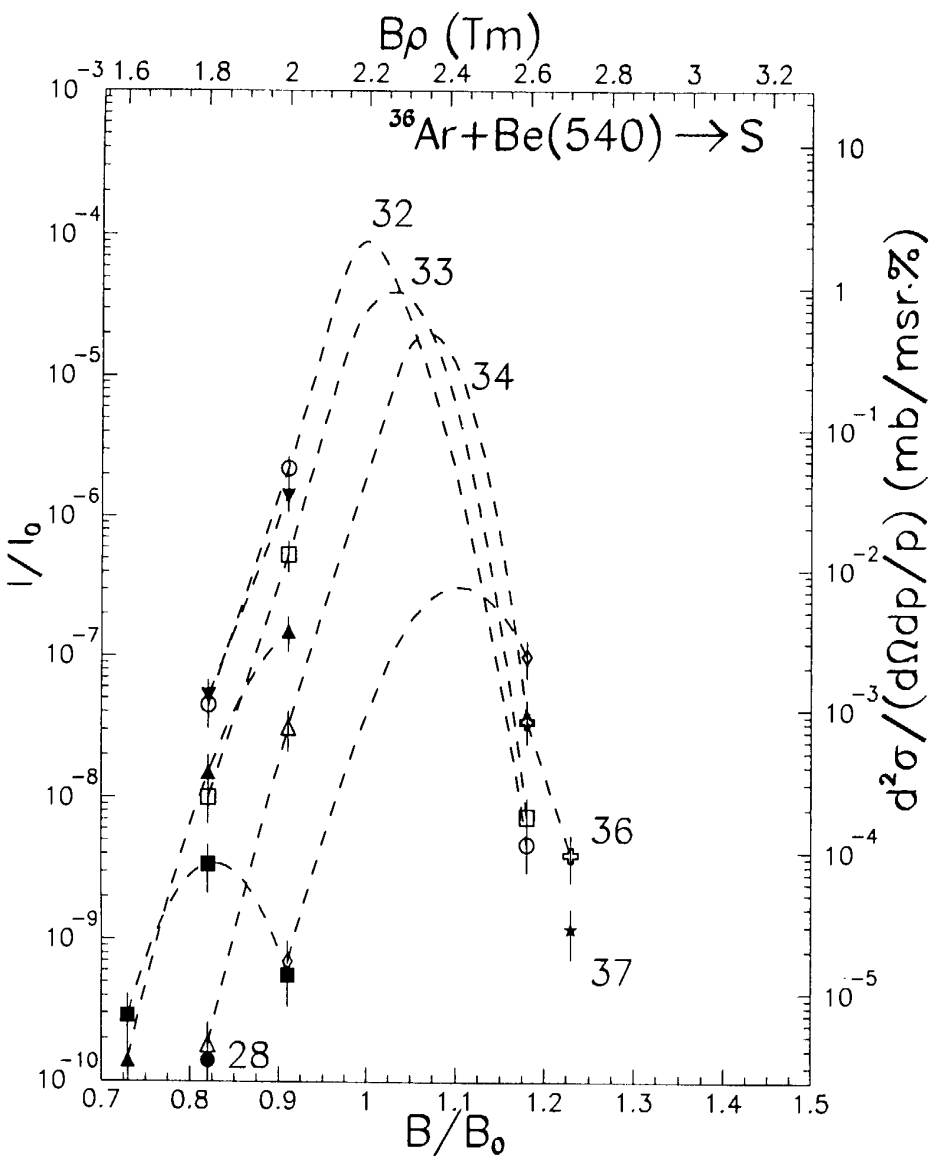
Bρ (Tm)
^{36}Ar+Be(540) → S
32
33
34
36
37
28
I/I$_0$
d^{2}σ/(dΩdp/p) (mb/msr·%)
B/B$_0$

Fig. 8c

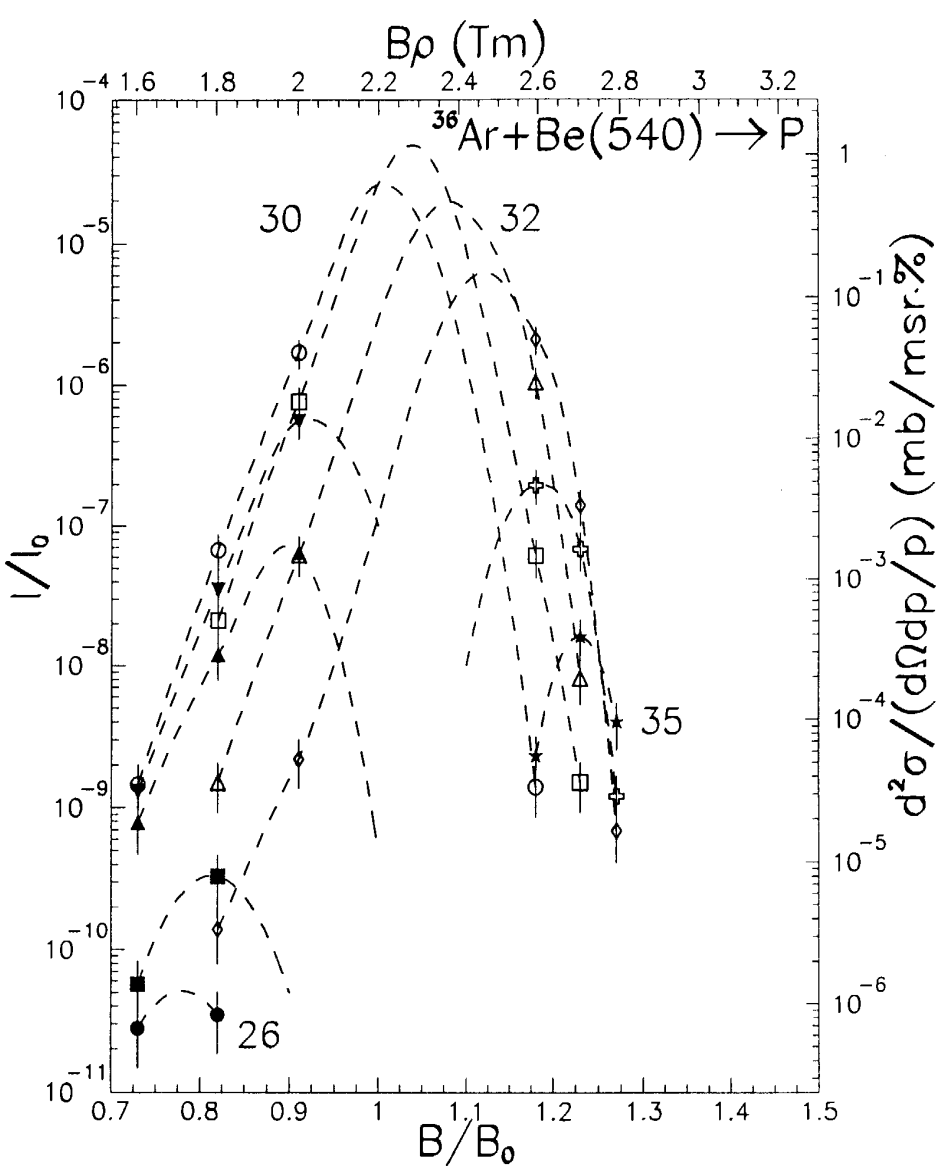
Bρ (Tm)
^{36}Ar+Be(540) → P
30
32
35
26
I/I$_0$
d^{2}σ/(dΩdp/p) (mb/msr·%)
B/B$_0$

Fig. 8d

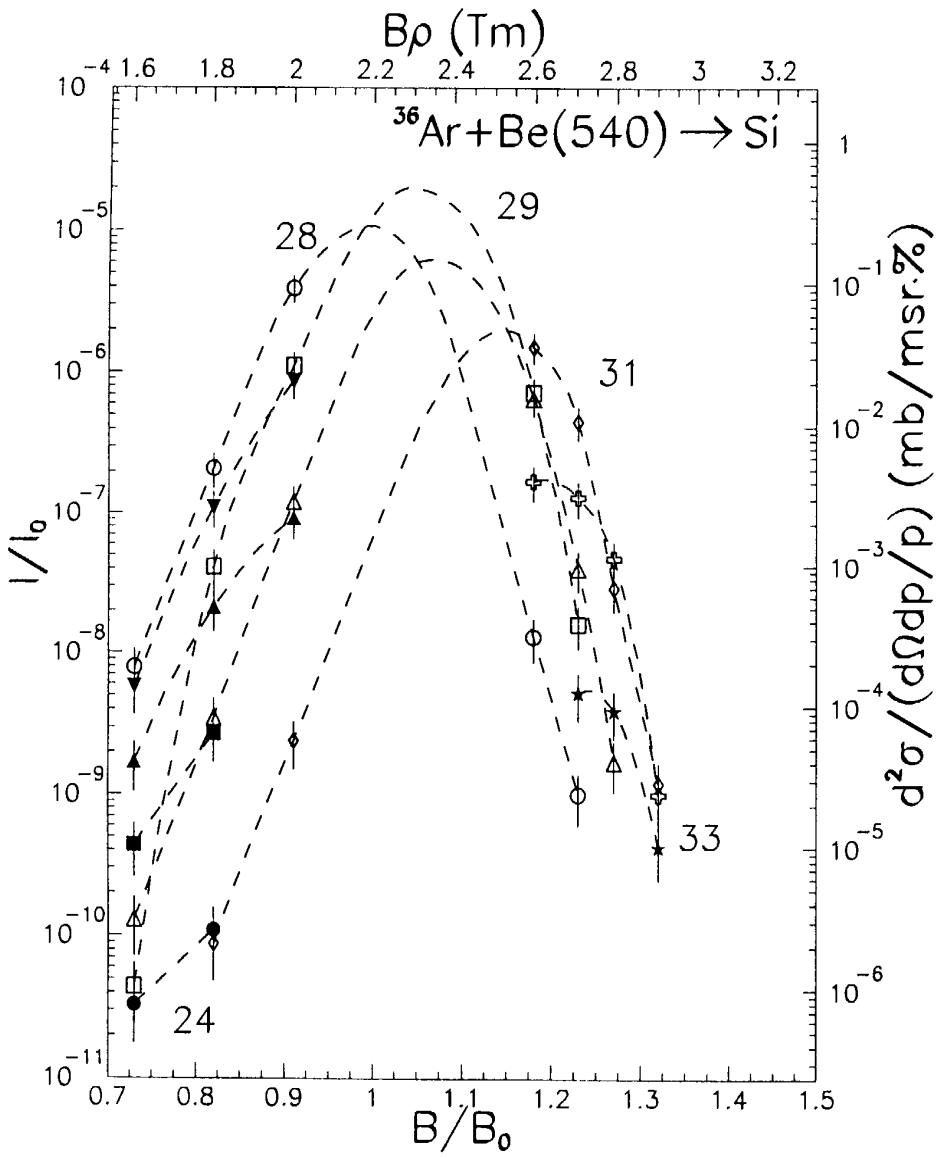
Bρ (Tm)
^{36}Ar+Be(540) → Si
28
29
31
33
24
I/I$_0$
B/B$_0$
d^{2}σ/(dΩdp/p) (mb/msr·%)

Fig. 8e

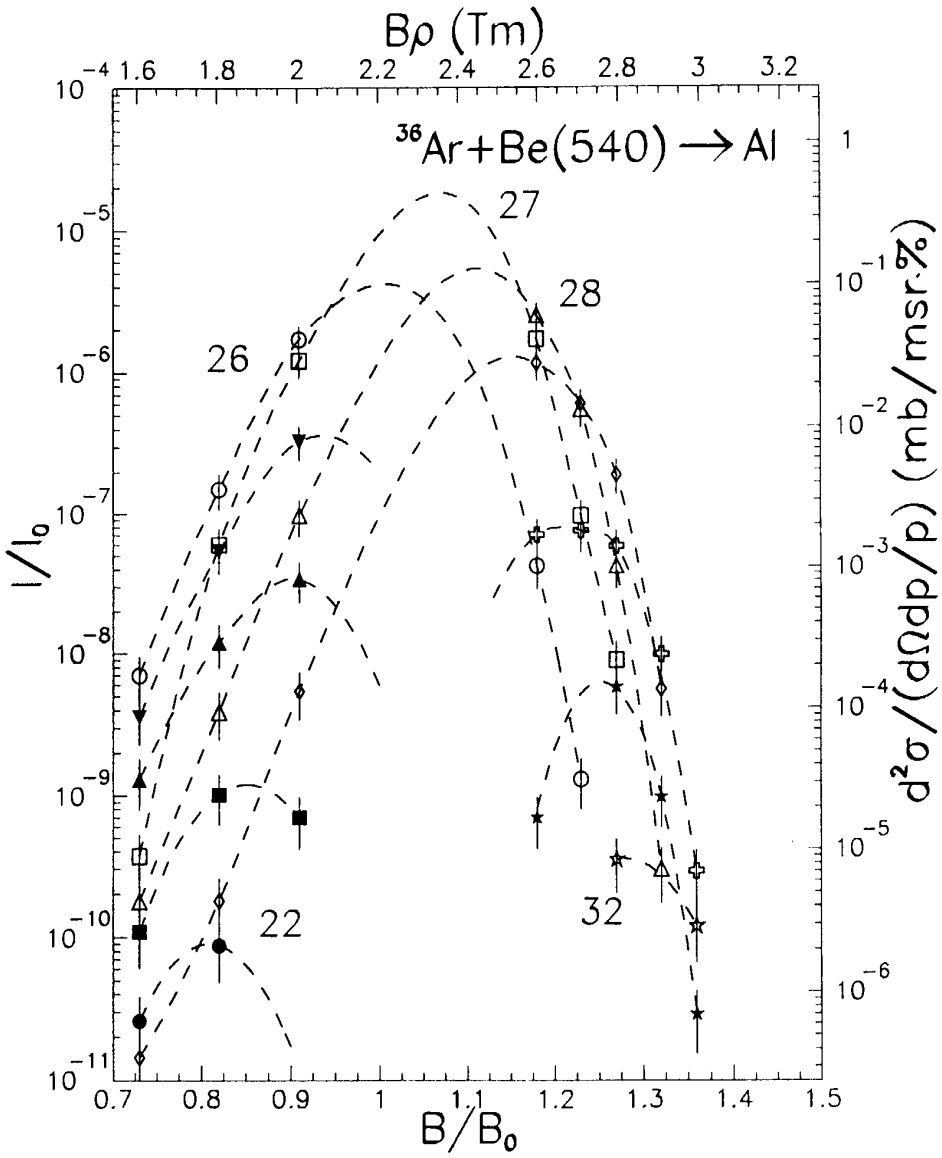
Bρ (Tm)
^{36}Ar+Be(540) → Al
26
27
28
32
22
I/I$_0$
B/B$_0$
d^{2}σ/(dΩdp/p) (mb/msr·%)

Fig. 8f

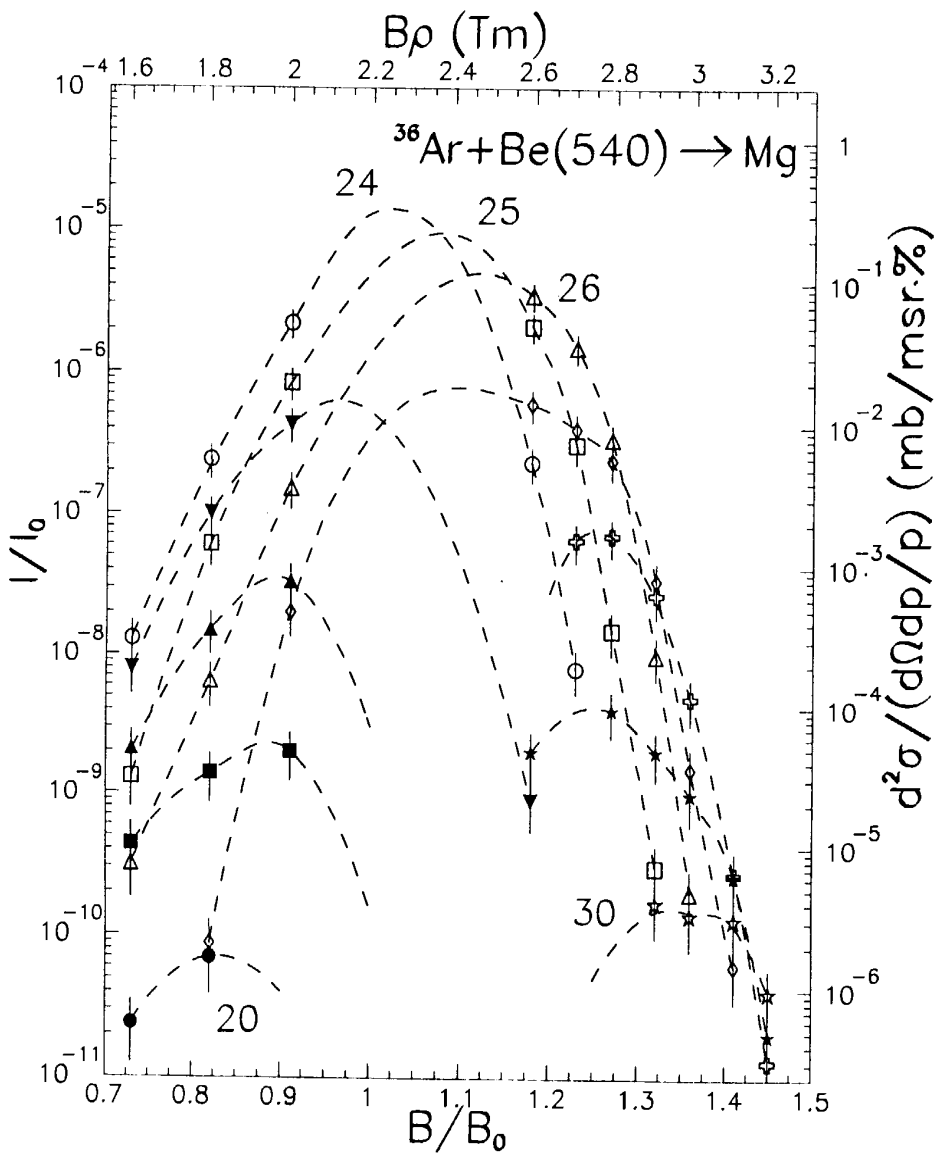
Bρ (Tm)
^{36}Ar+Be(540) → Mg
24
25
26
30
20
I/I$_0$
B/B$_0$
d^{2}σ/(dΩdp/p) (mb/msr·%)

Fig. 8g

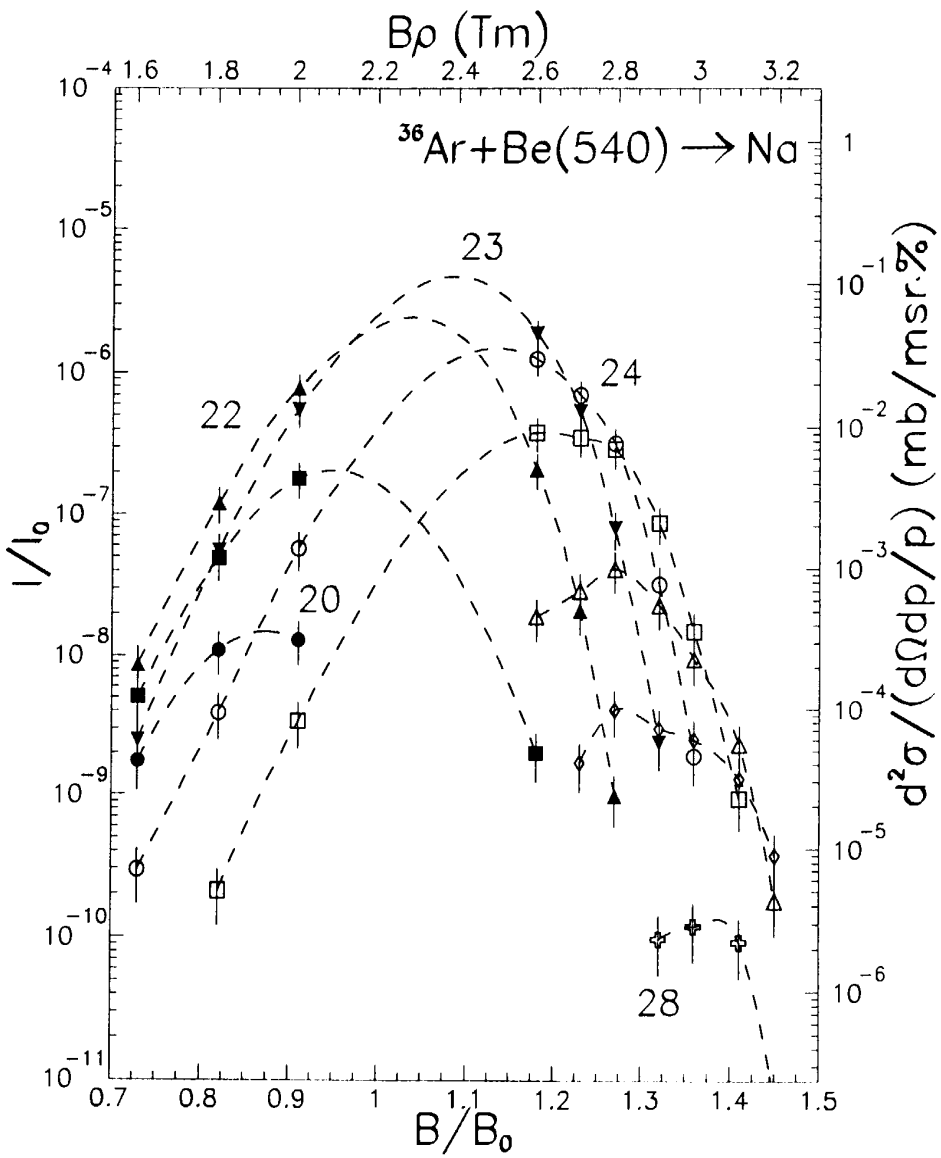
Bρ (Tm)
^{36}Ar+Be(540) → Na
23
22
24
20
28
I/I$_0$
B/B$_0$
d^{2}σ/(dΩdp/p) (mb/msr·%)

Fig. 8h

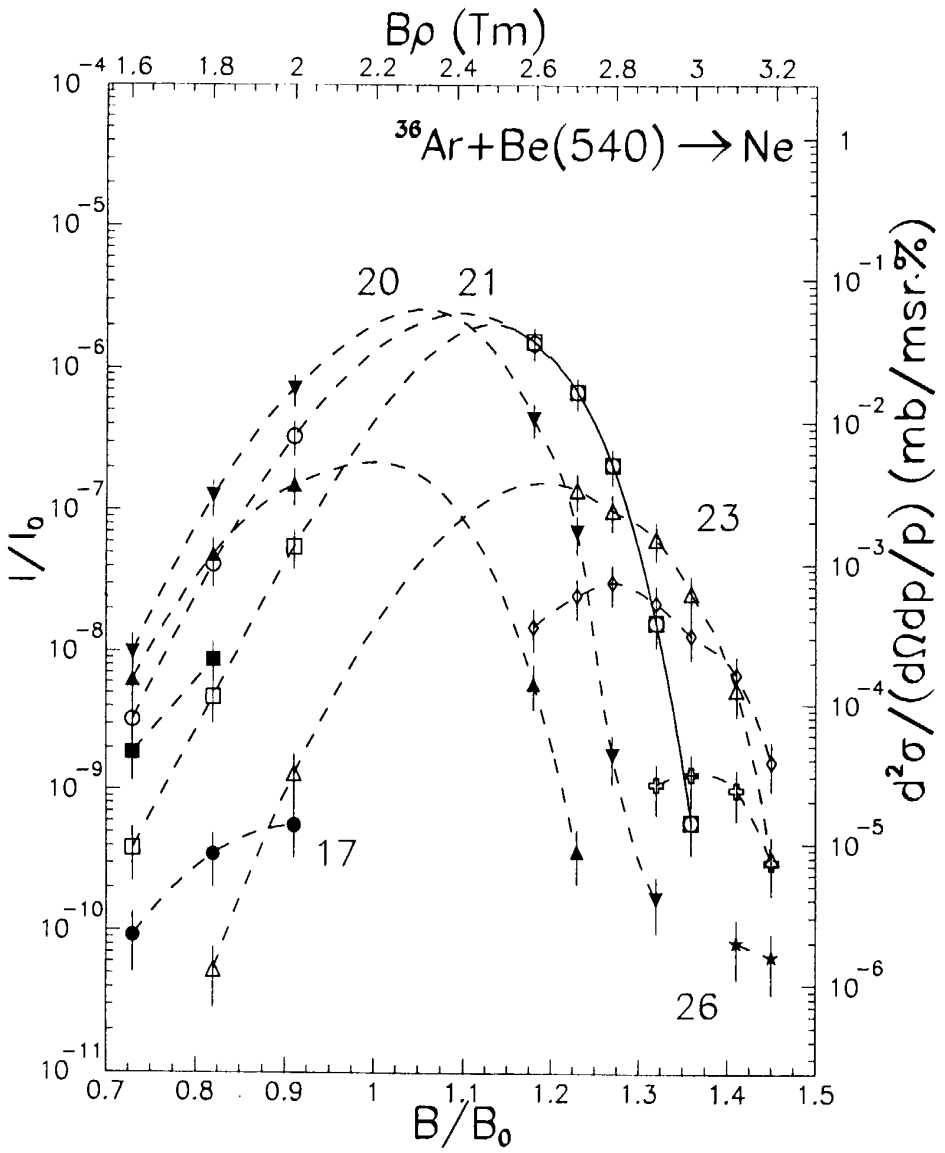
Bρ (Tm)
^{36}Ar+Be(540) → Ne
20
21
23
17
26
I/I$_0$
d^{2}σ/(dΩdp/p) (mb/msr.%)
B/B$_0$

Fig. 8i

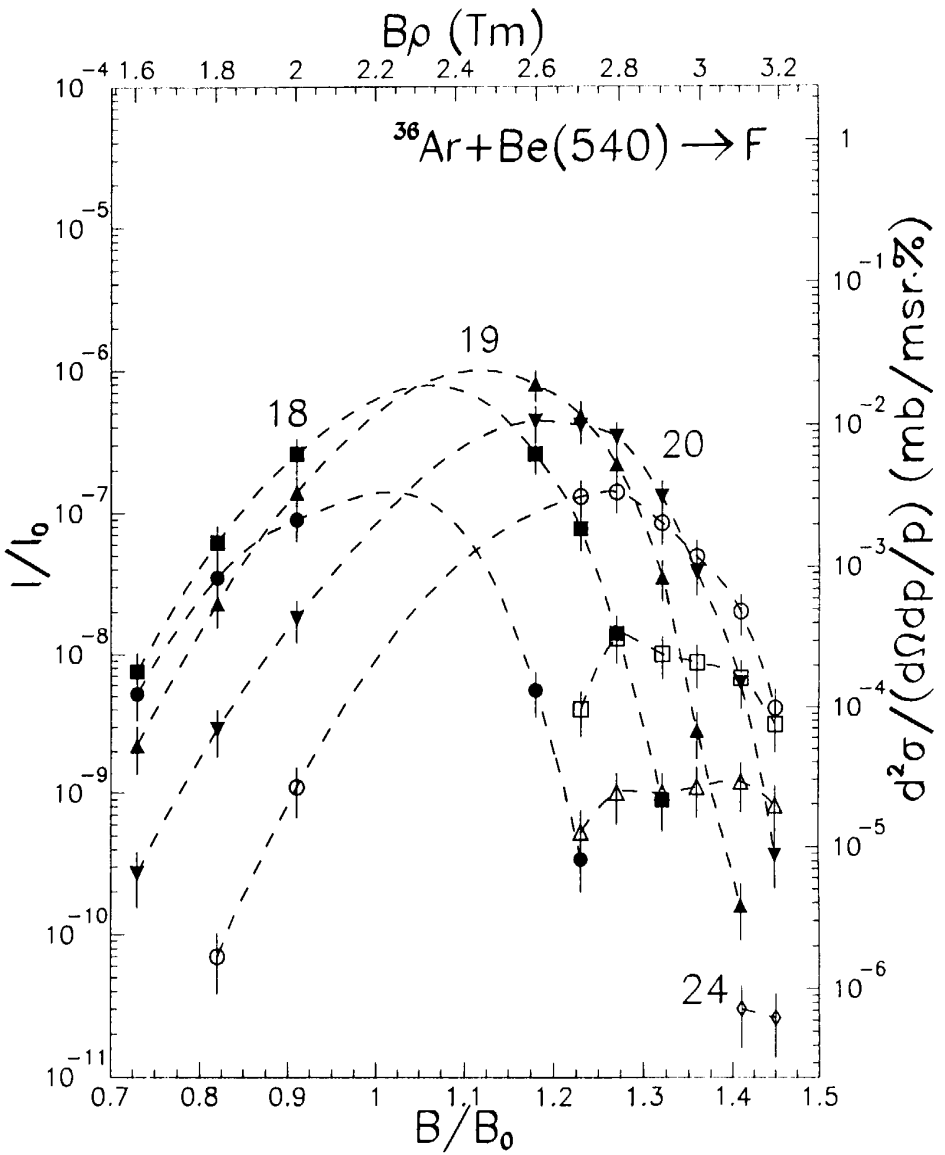
Bρ (Tm)
^{36}Ar+Be(540) → F
19
18
20
24
I/I$_0$
d^{2}σ/(dΩdp/p) (mb/msr.%)
B/B$_0$

Fig. 8j

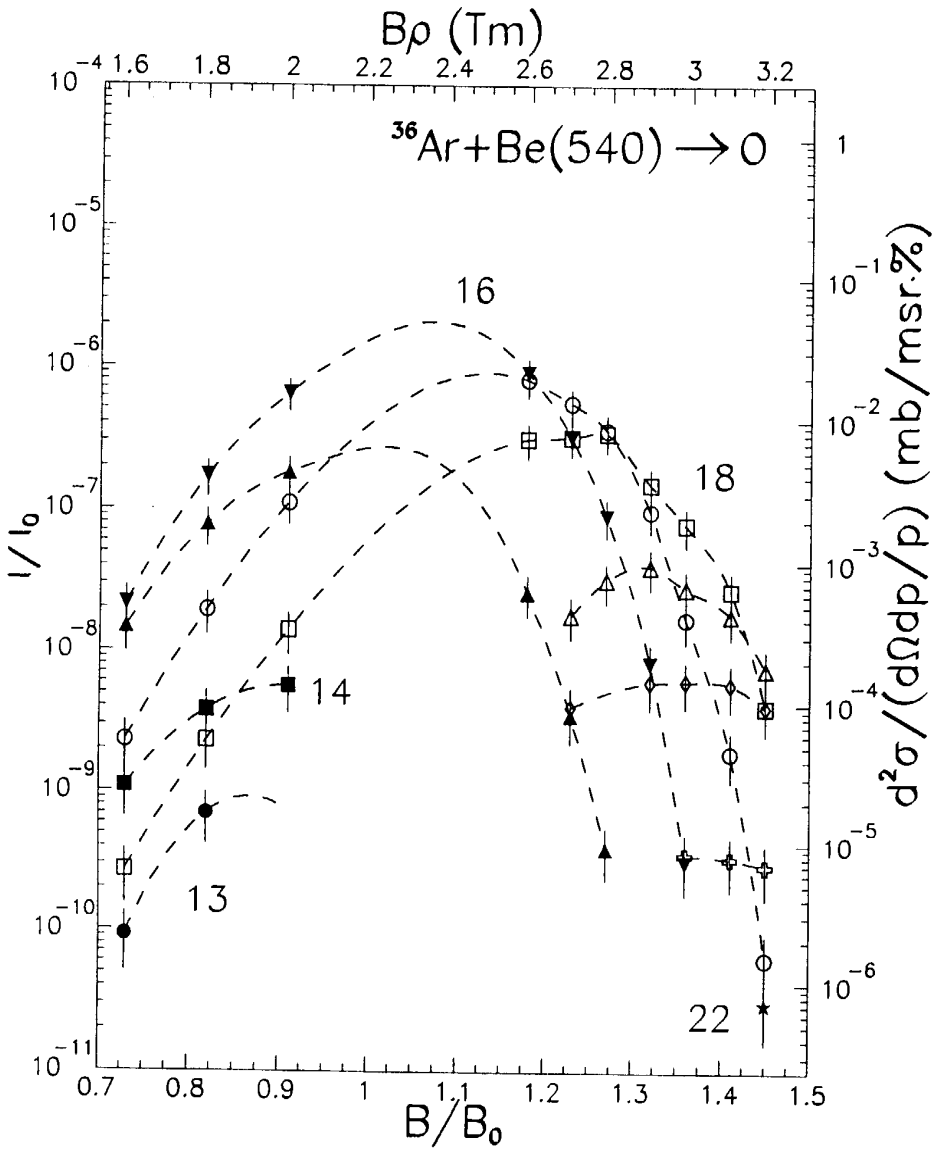
Bρ (Tm)
^{36}Ar+Be(540) → 0
16
18
14
13
22
I / I$_0$
d^{2}σ/(dΩdp/p) (mb/msr·%)
B/B$_0$

Fig. 8k

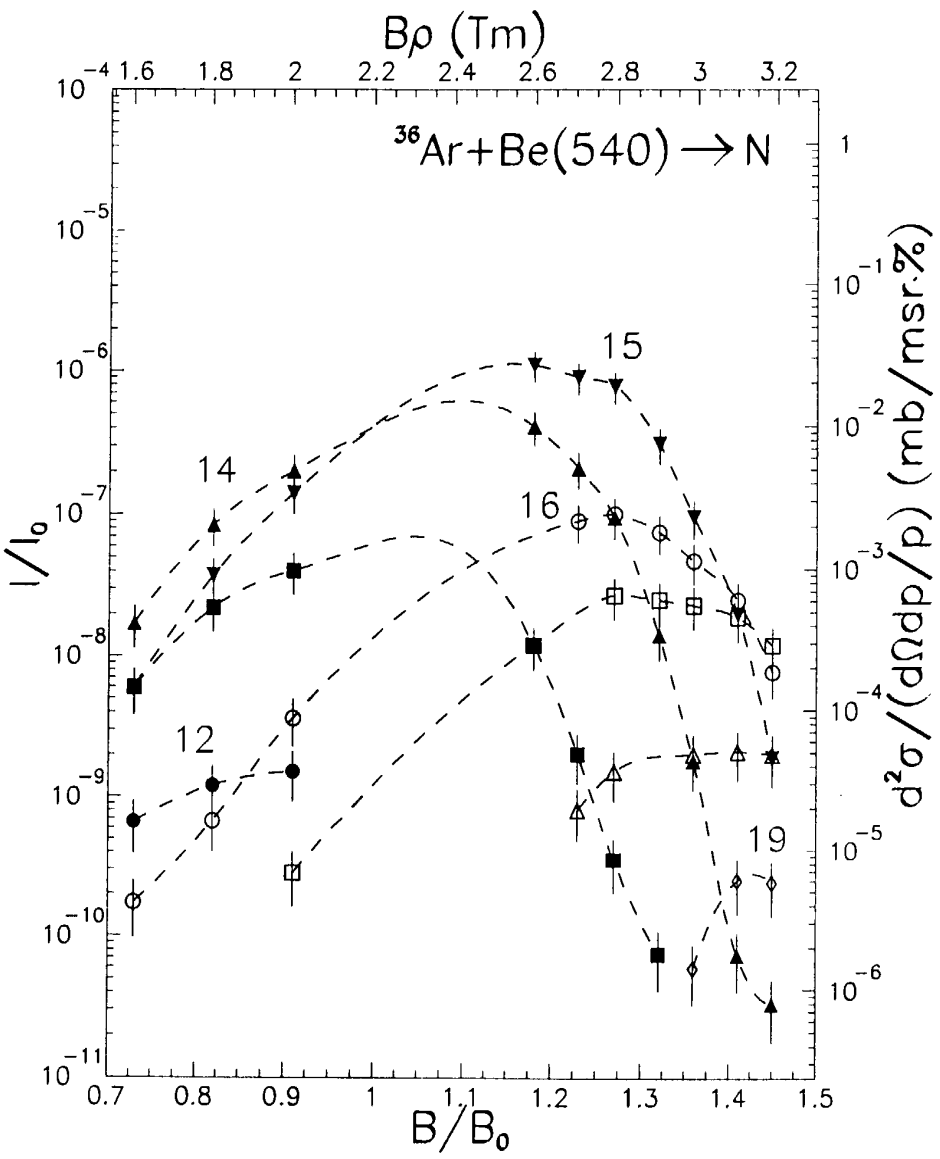
Bρ (Tm)
^{36}Ar+Be(540) → N
15
14
16
12
19
I / I$_0$
d^{2}σ/(dΩdp/p) (mb/msr·%)
B/B$_0$

Fig. 8l

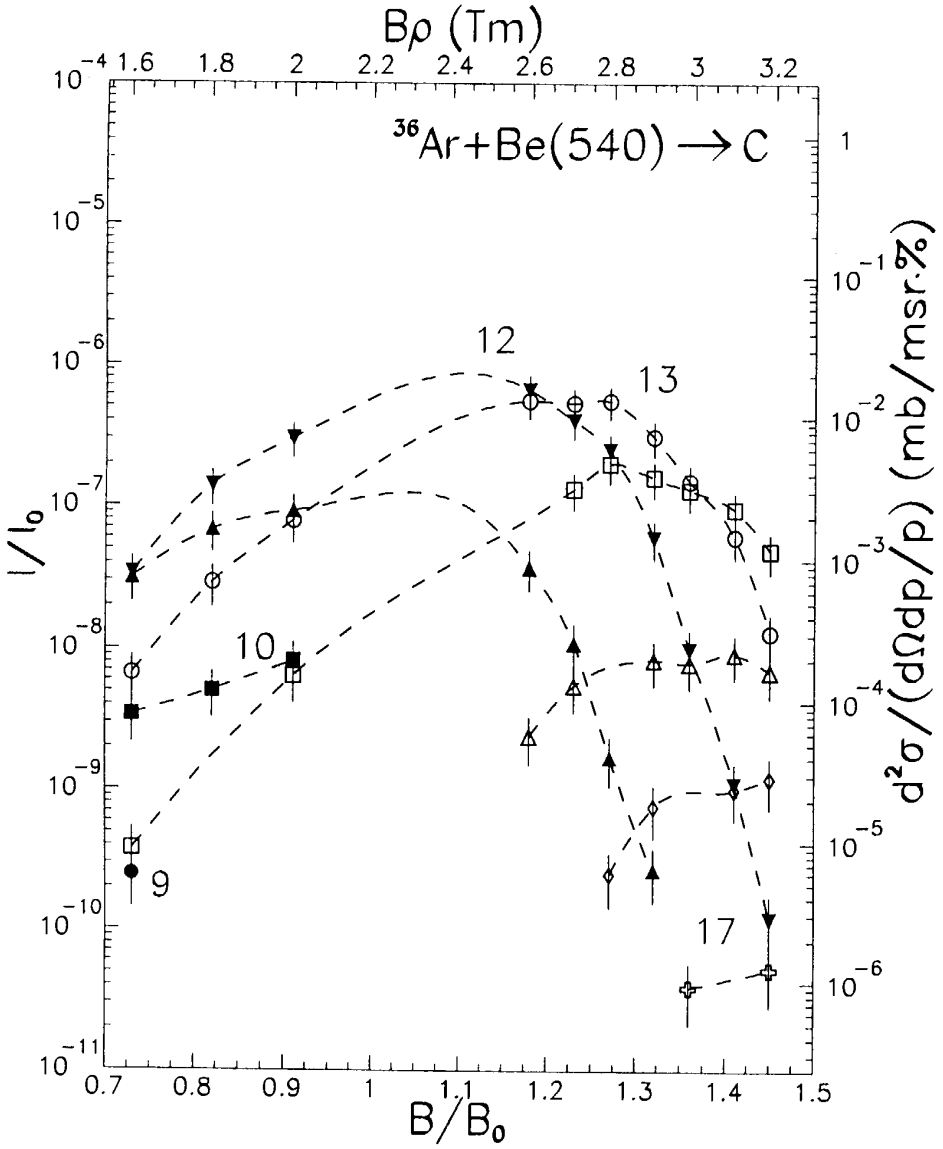
Bρ (Tm)
^{36}Ar+Be(540) → C
I/I$_0$
d^{2}σ/(dΩdp/p) (mb/msr·%)
B/B$_0$
9
10
12
13
17

Fig. 8m

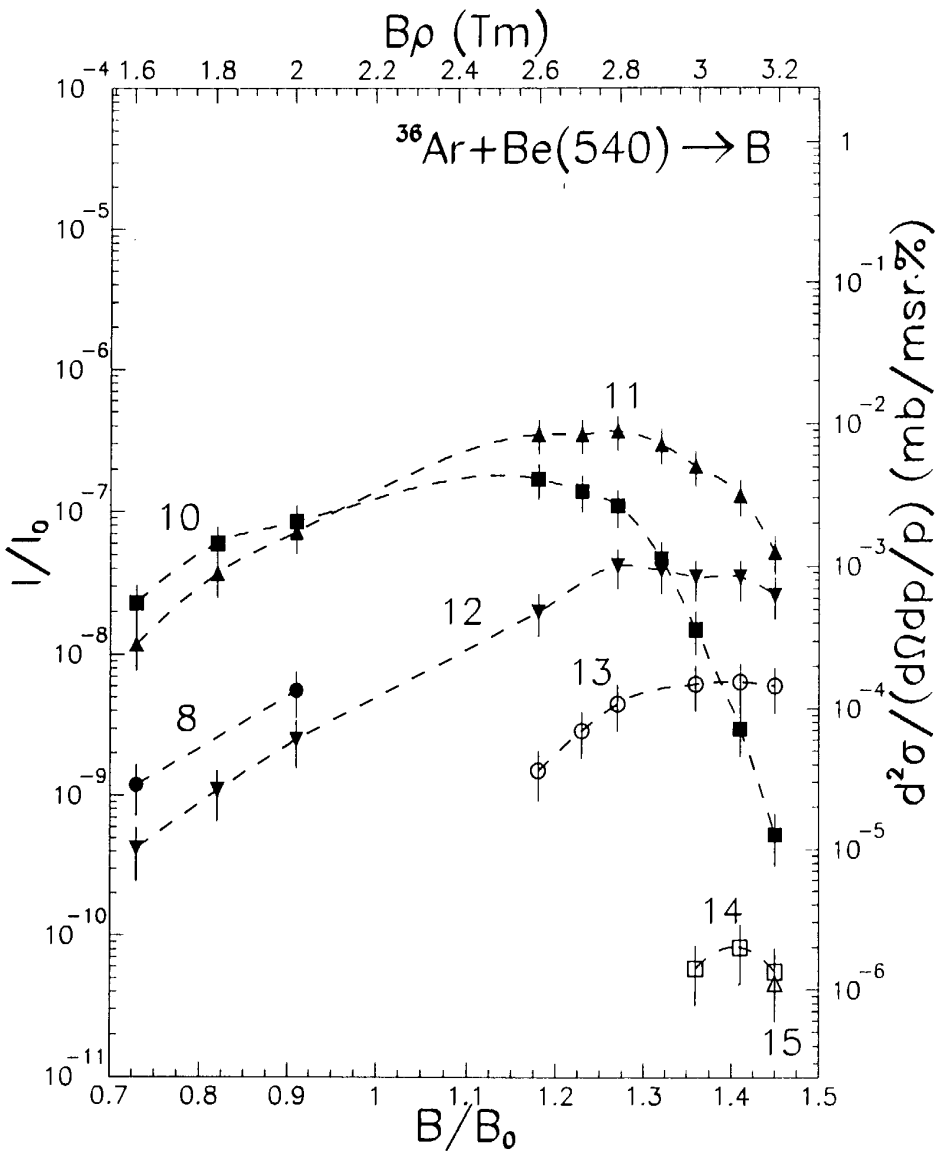
Bρ (Tm)
^{36}Ar+Be(540) → B
I/I$_0$
d^{2}σ/(dΩdp/p) (mb/msr·%)
B/B$_0$
8
10
11
12
13
14
15

Fig. 8n

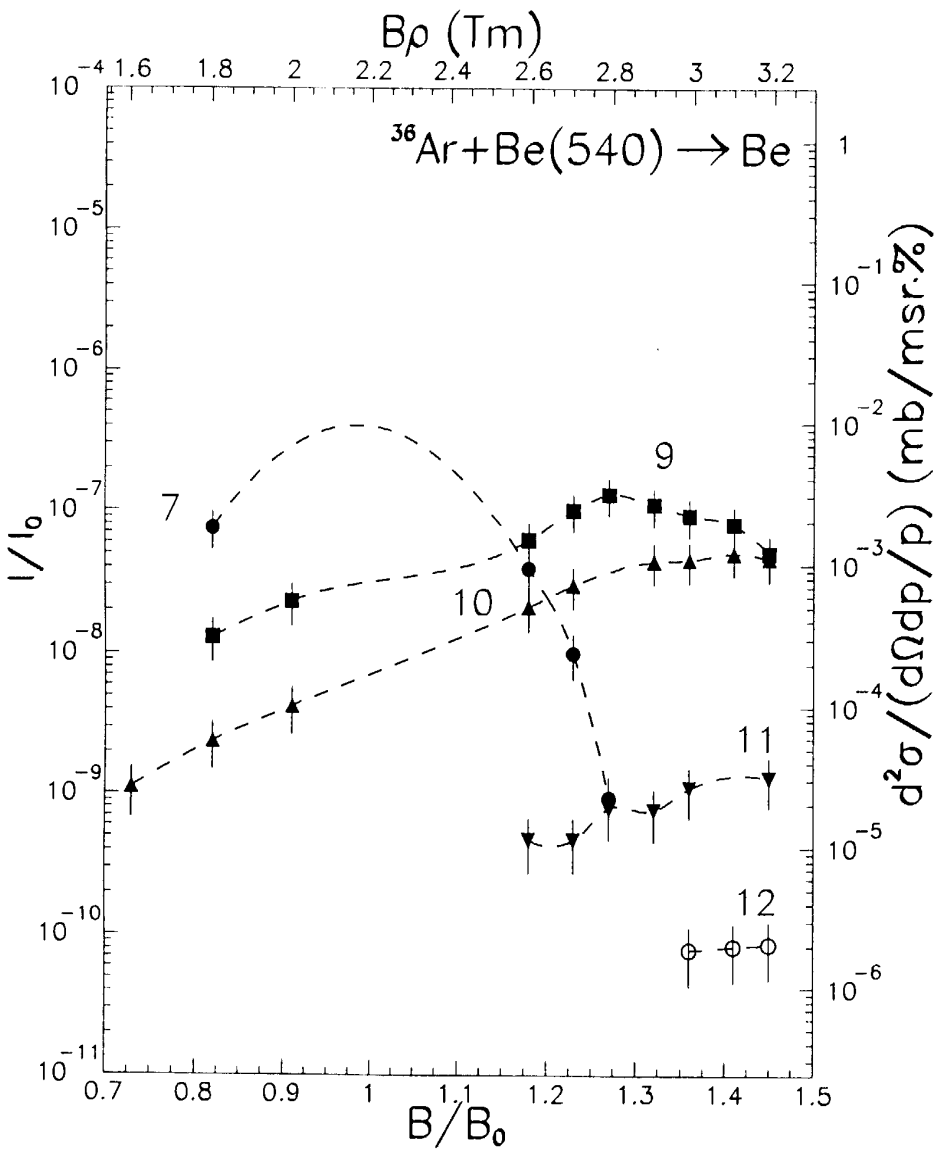
Bρ (Tm)
^{36}Ar+Be(540) → Be
I/I$_0$
d^{2}σ/(dΩdp/p) (mb/msr.%)
B/B$_0$
7
9
10
11
12

Fig. 8o

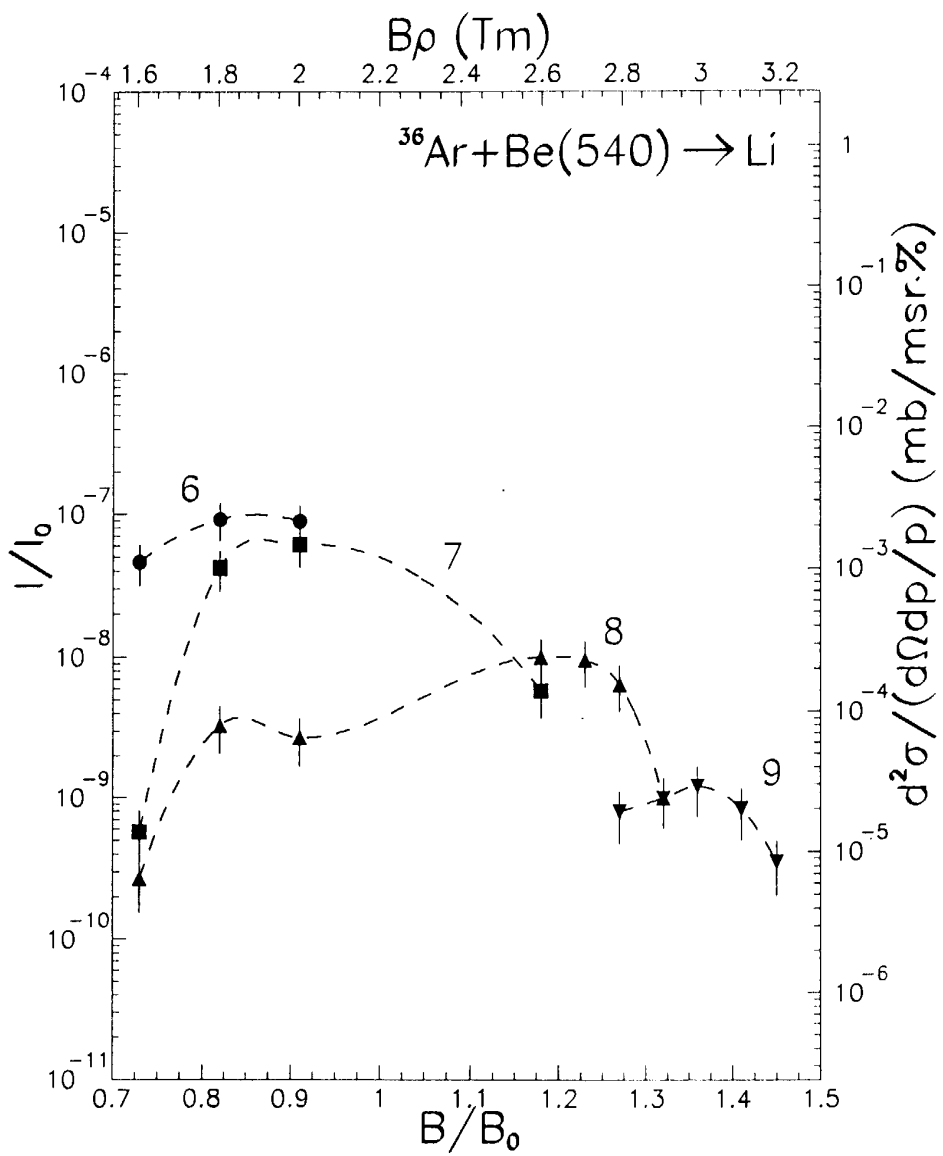
Bρ (Tm)
^{36}Ar+Be(540) → Li
I/I$_0$
d^{2}σ/(dΩdp/p) (mb/msr.%)
B/B$_0$
6
7
8
9

Fig. 8p

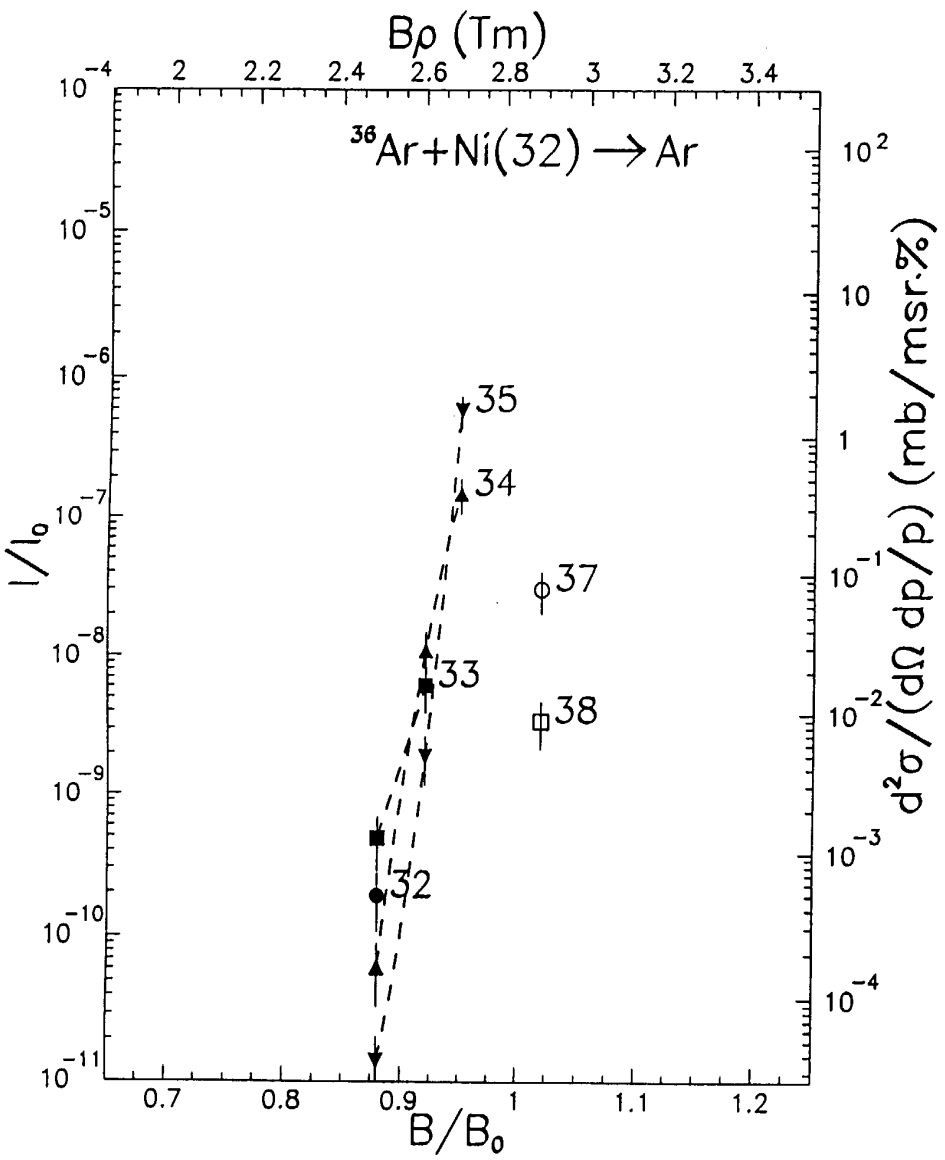
Bρ (Tm)
2
2.2
2.4
2.6
2.8
3
3.2
3.4
^{36}Ar+Ni(32) → Ar
35
34
37
33
38
32
I/I$_0$
d^{2}σ/(dΩ dp/p) (mb/msr·%)
B/B$_0$
0.7
0.8
0.9
1
1.1
1.2

Fig. 9a

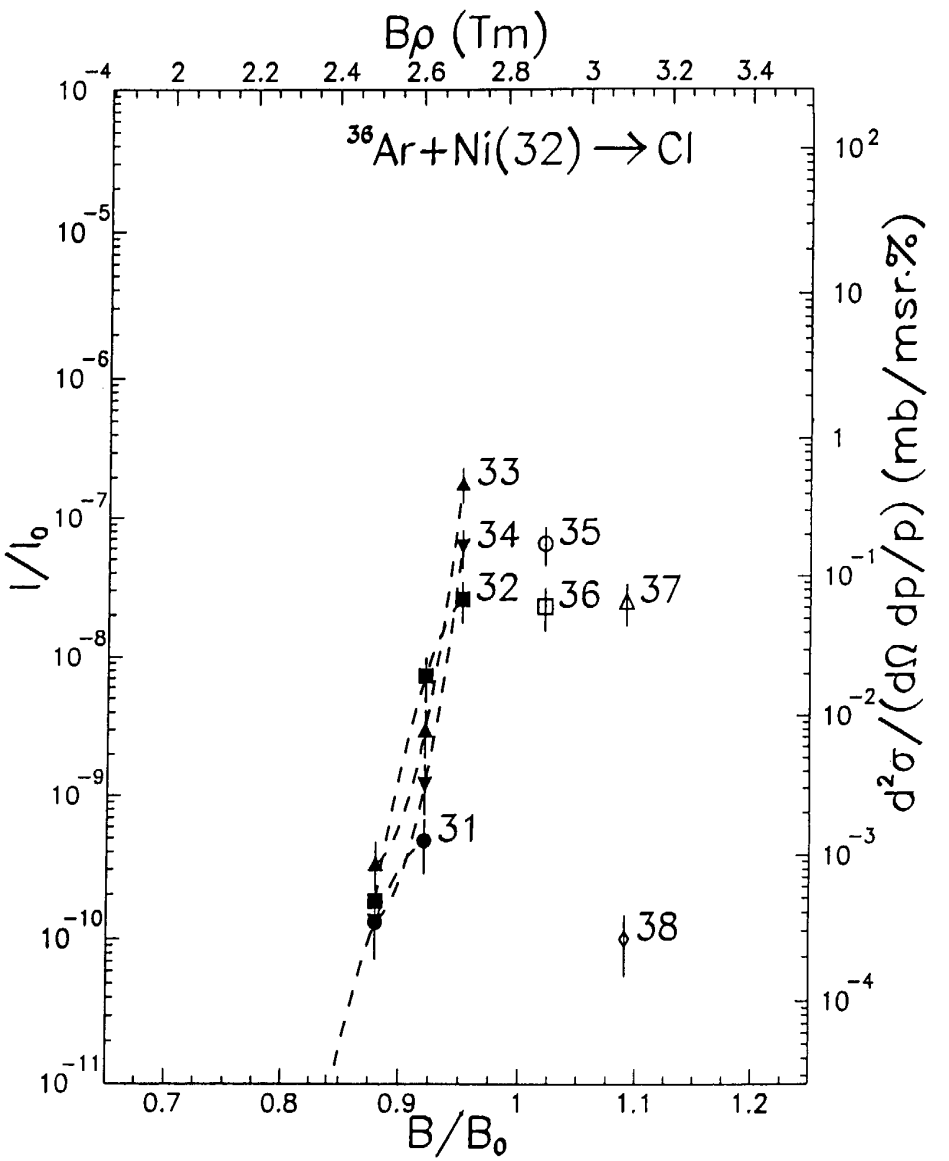
Bρ (Tm)
2
2.2
2.4
2.6
2.8
3
3.2
3.4
^{36}Ar+Ni(32) → Cl
33
34
35
32
36
37
31
38
I/I$_0$
d^{2}σ/(dΩ dp/p) (mb/msr·%)
B/B$_0$
0.7
0.8
0.9
1
1.1
1.2

Fig. 9b

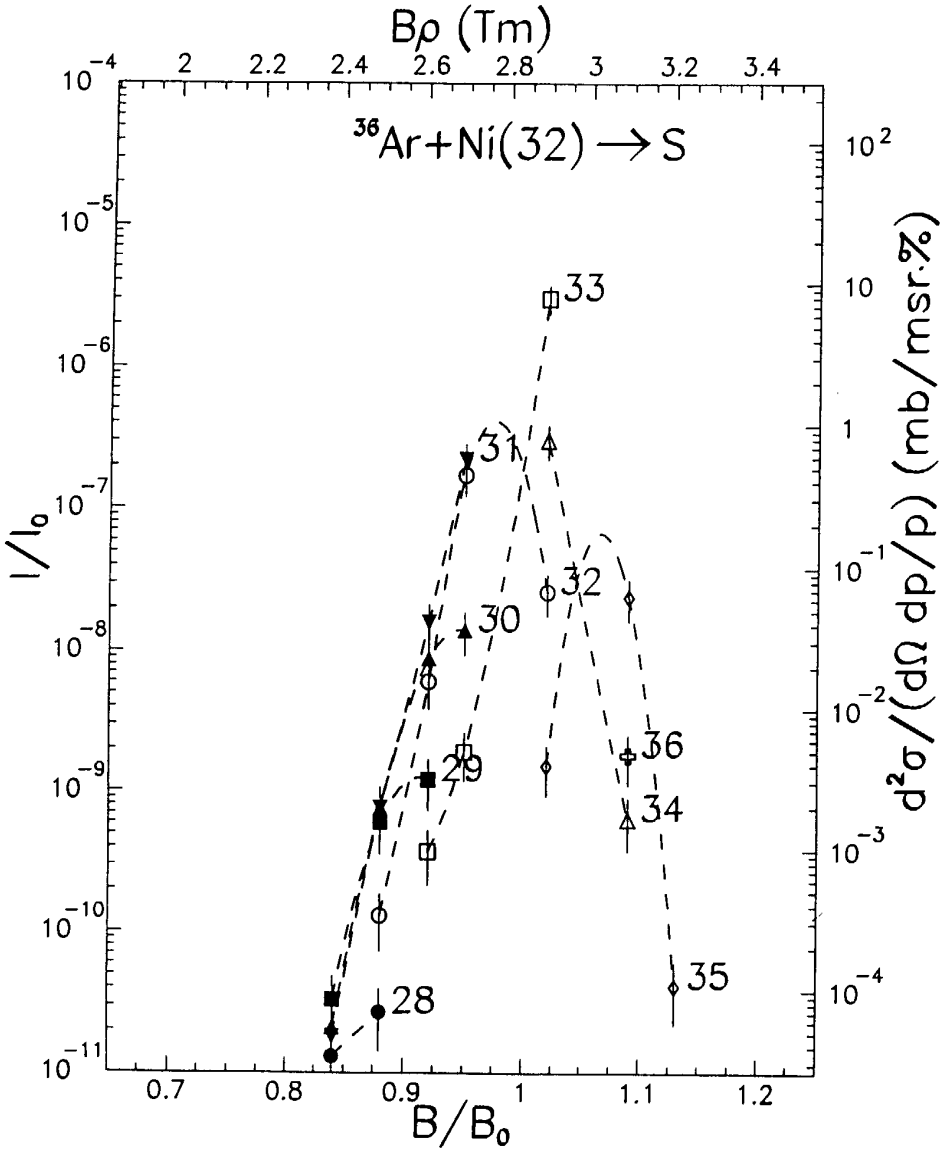
Bρ (Tm)
^{36}Ar+Ni(32) → S
I/I$_0$
d^{2}σ/(dΩ dp/p) (mb/msr.%)
B/B$_0$
28
29
30
31
32
33
34
35
36

Fig. 9c

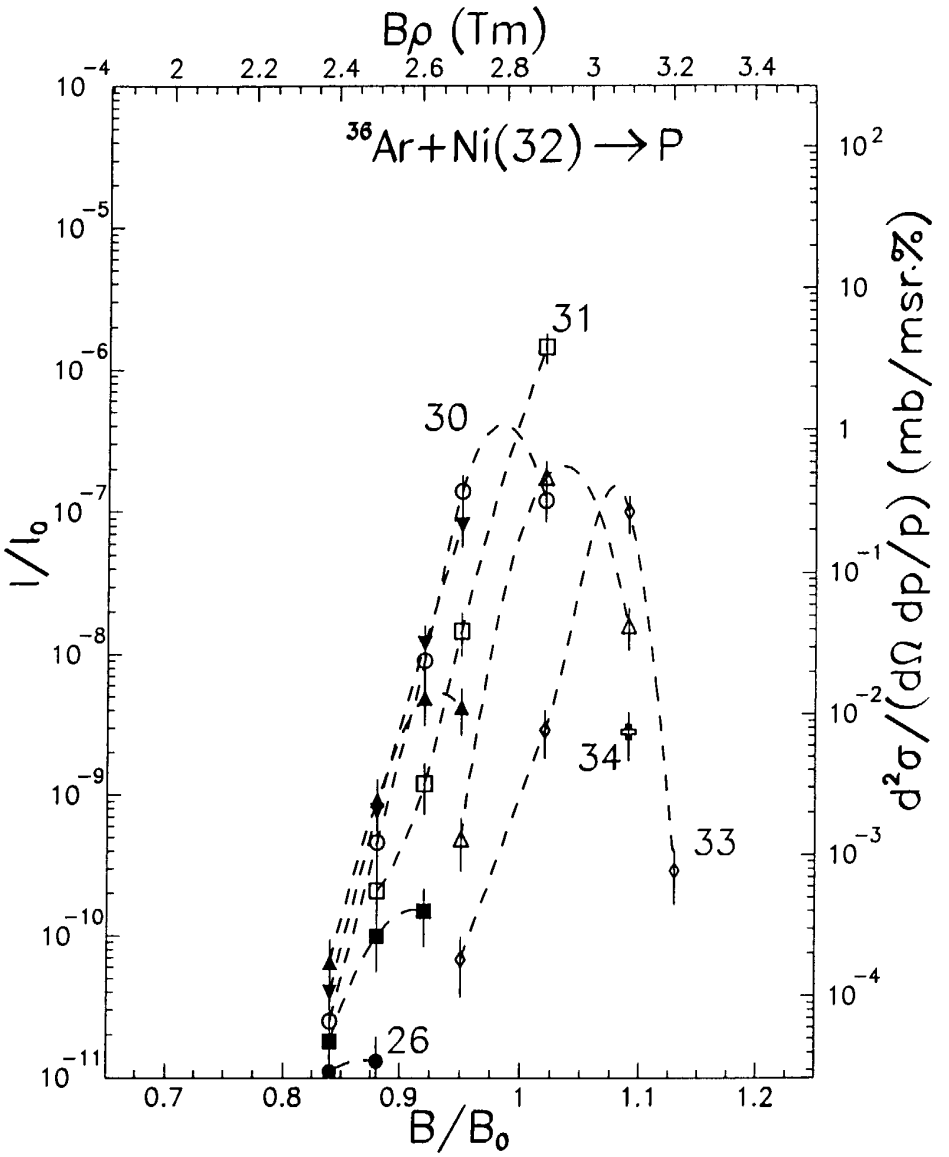
Bρ (Tm)
^{36}Ar+Ni(32) → P
I/I$_0$
d^{2}σ/(dΩ dp/p) (mb/msr.%)
B/B$_0$
26
30
31
33
34

Fig. 9d

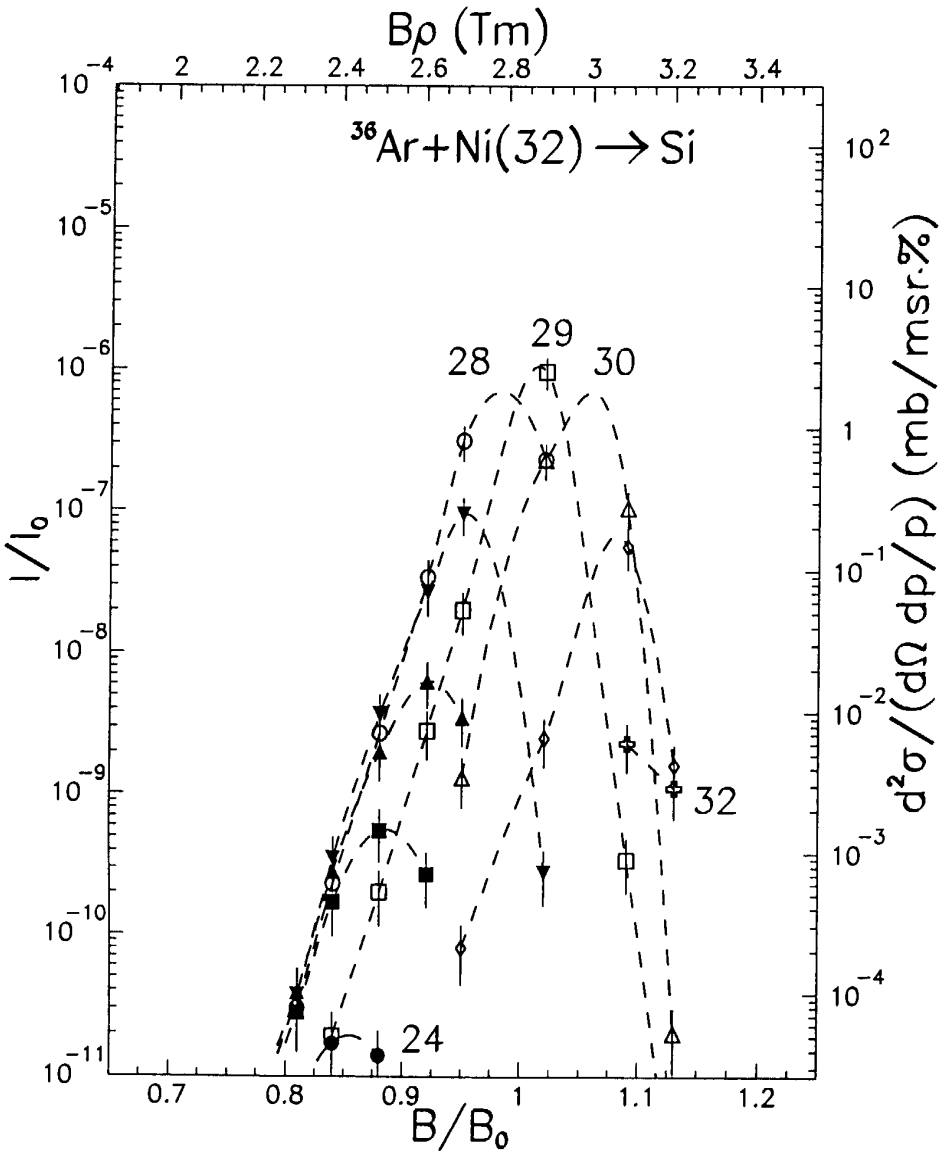
Bρ (Tm)
^{36}Ar+Ni(32) → Si
I/I$_0$
d^{2}σ/(dΩ dp/p) (mb/msr·%)
B/B$_0$
28
29
30
32
24

Fig. 9e

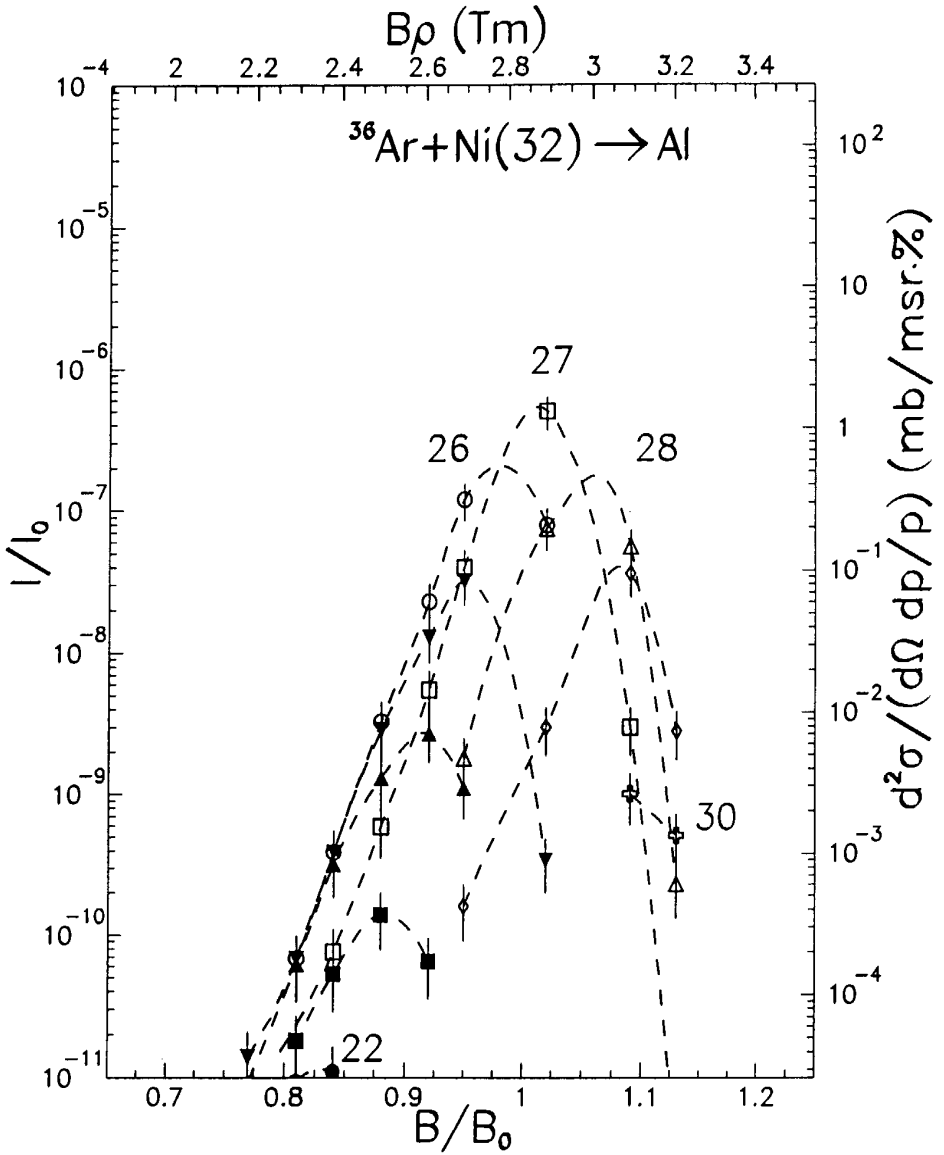
Bρ (Tm)
^{36}Ar+Ni(32) → Al
I/I$_0$
d^{2}σ/(dΩ dp/p) (mb/msr·%)
B/B$_0$
26
27
28
30
22

Fig. 9f

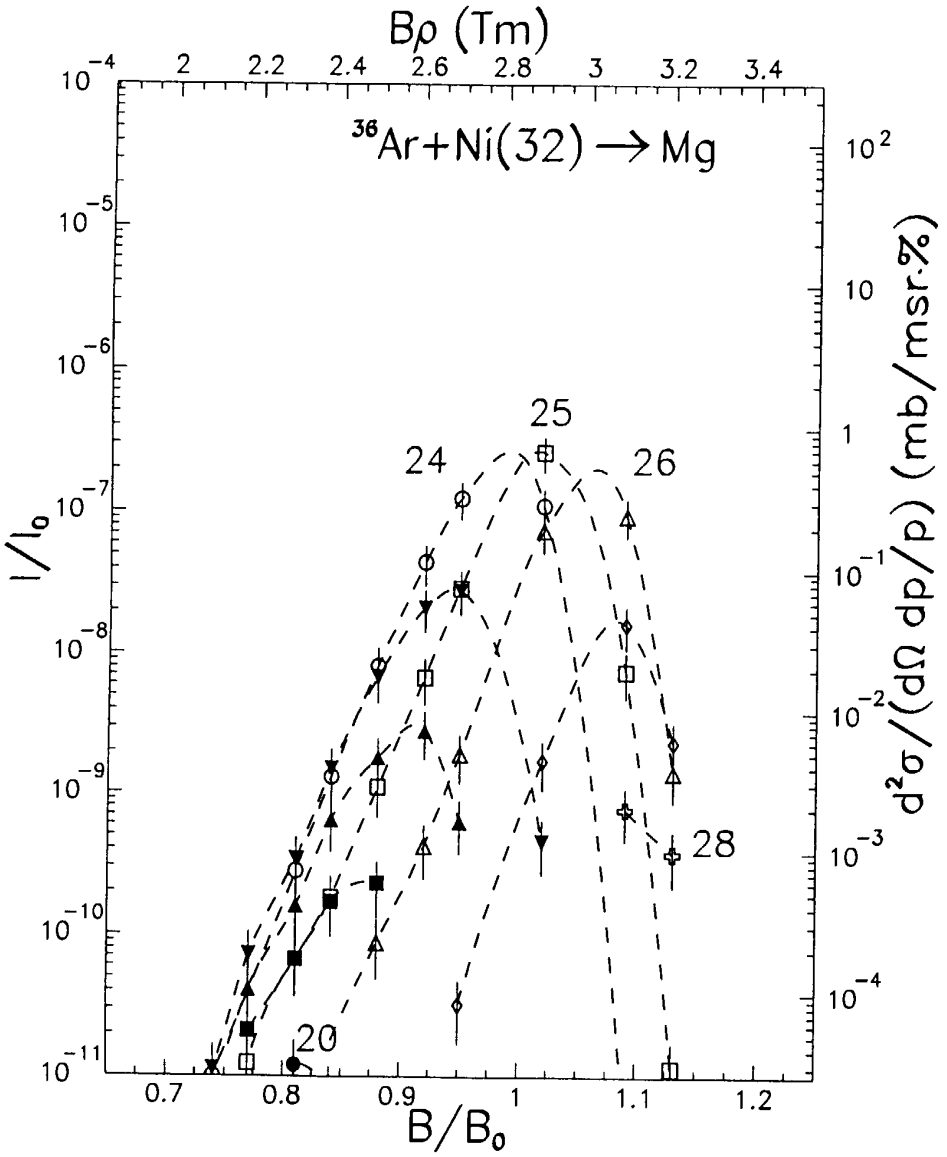
Bρ (Tm)
^{36}Ar+Ni(32) → Mg
I/I$_0$
d^{2}σ/(dΩ dp/p) (mb/msr·%)
B/B$_0$
20
24
25
26
28

Fig. 9g

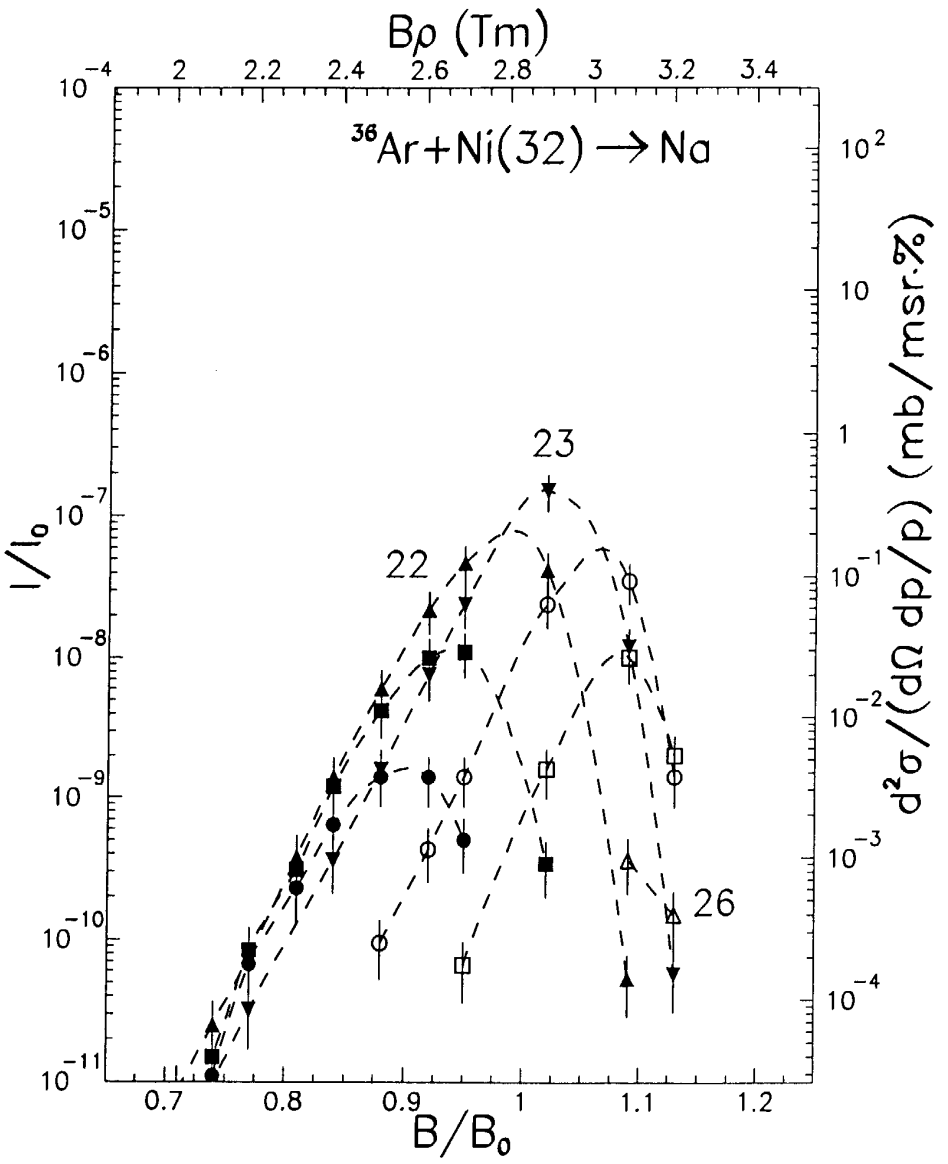
Bρ (Tm)
^{36}Ar+Ni(32) → Na
I/I$_0$
d^{2}σ/(dΩ dp/p) (mb/msr·%)
B/B$_0$
22
23
26

Fig. 9h

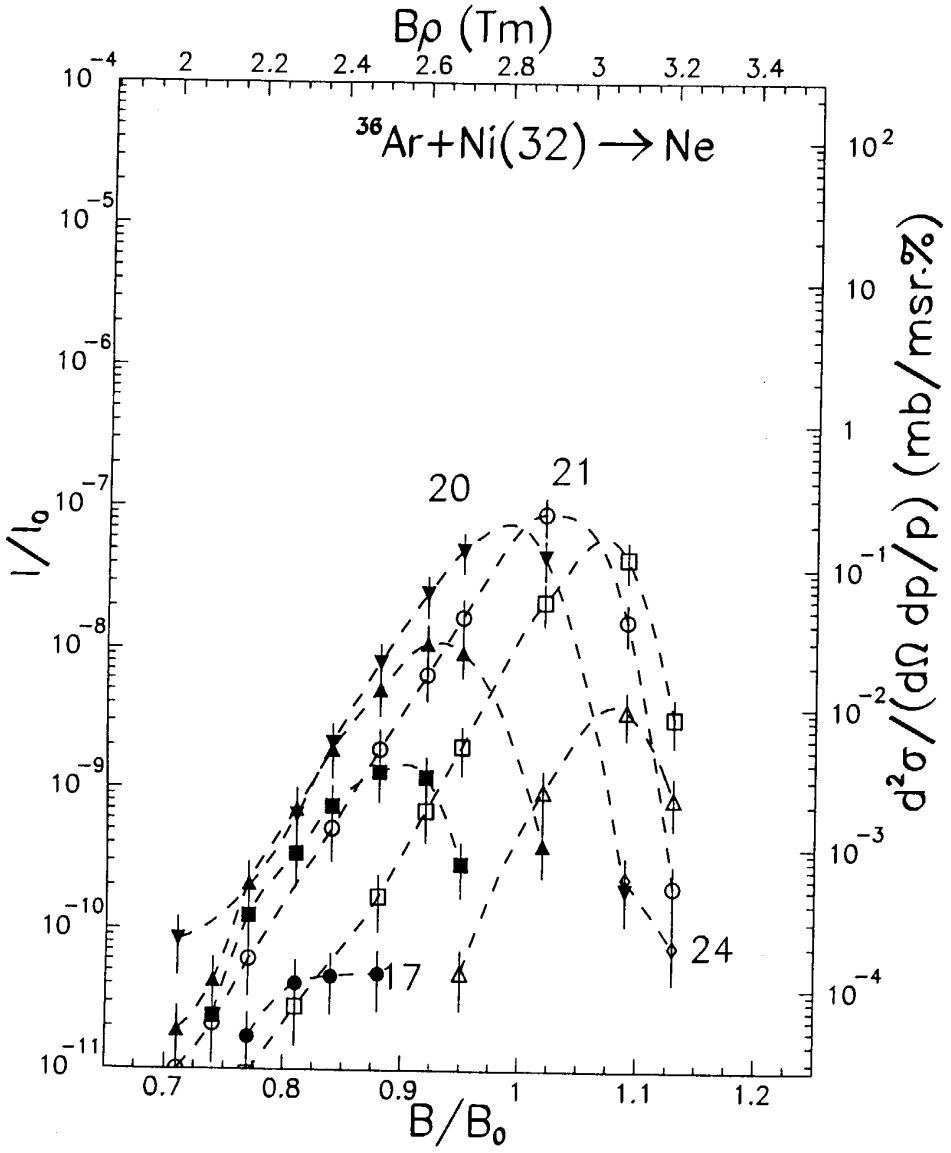
Bρ (Tm)
^{36}Ar+Ni(32) → Ne
I/I$_0$
d^{2}σ/(dΩ dp/p) (mb/msr·%)
B/B$_0$
20
21
17
24

Fig. 9i

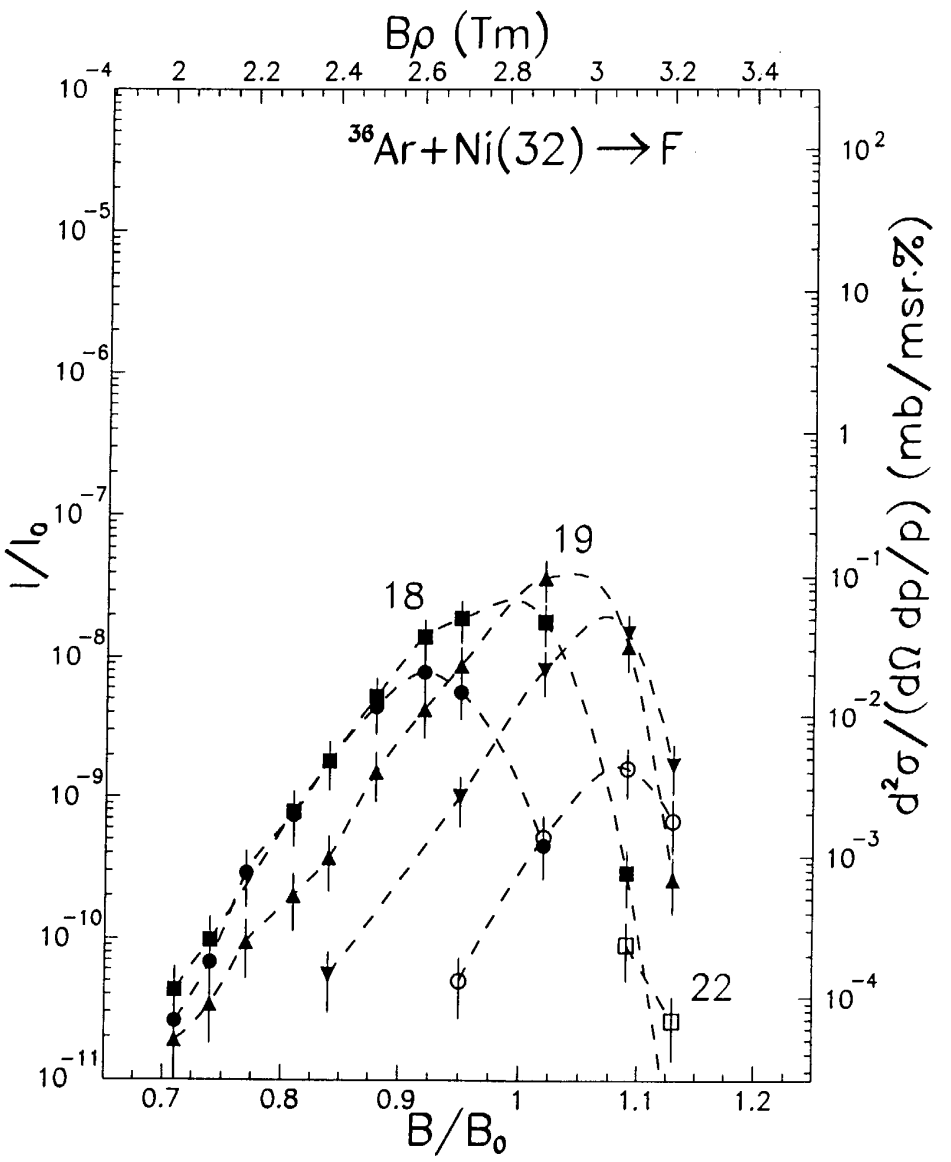
Bρ (Tm)
^{36}Ar+Ni(32) → F
I/I$_0$
d^{2}σ/(dΩ dp/p) (mb/msr·%)
B/B$_0$
18
19
22

Fig. 9j

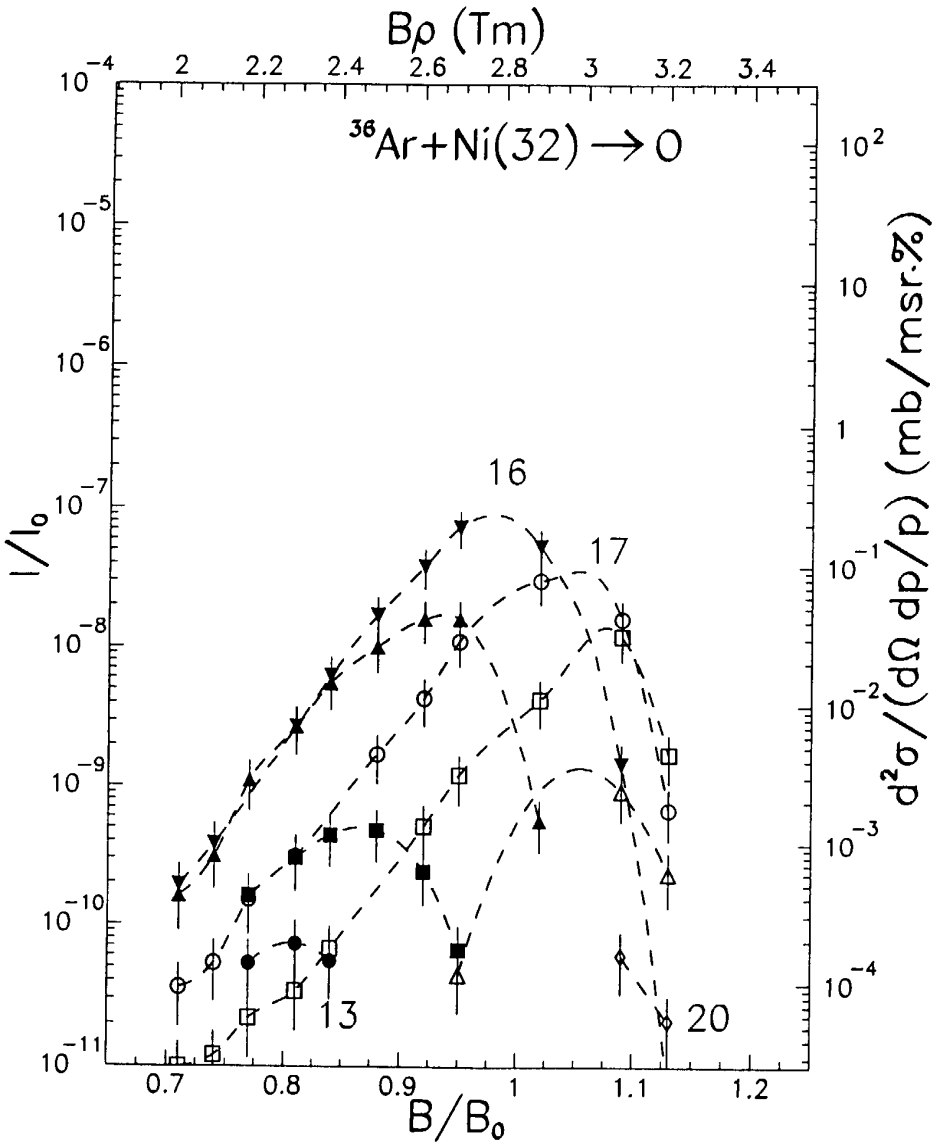
Bρ (Tm)
^{36}Ar+Ni(32) → O
I/I$_0$
d^{2}σ/(dΩ dp/p) (mb/msr·%)
B/B$_0$
16
17
13
20

Fig. 9k

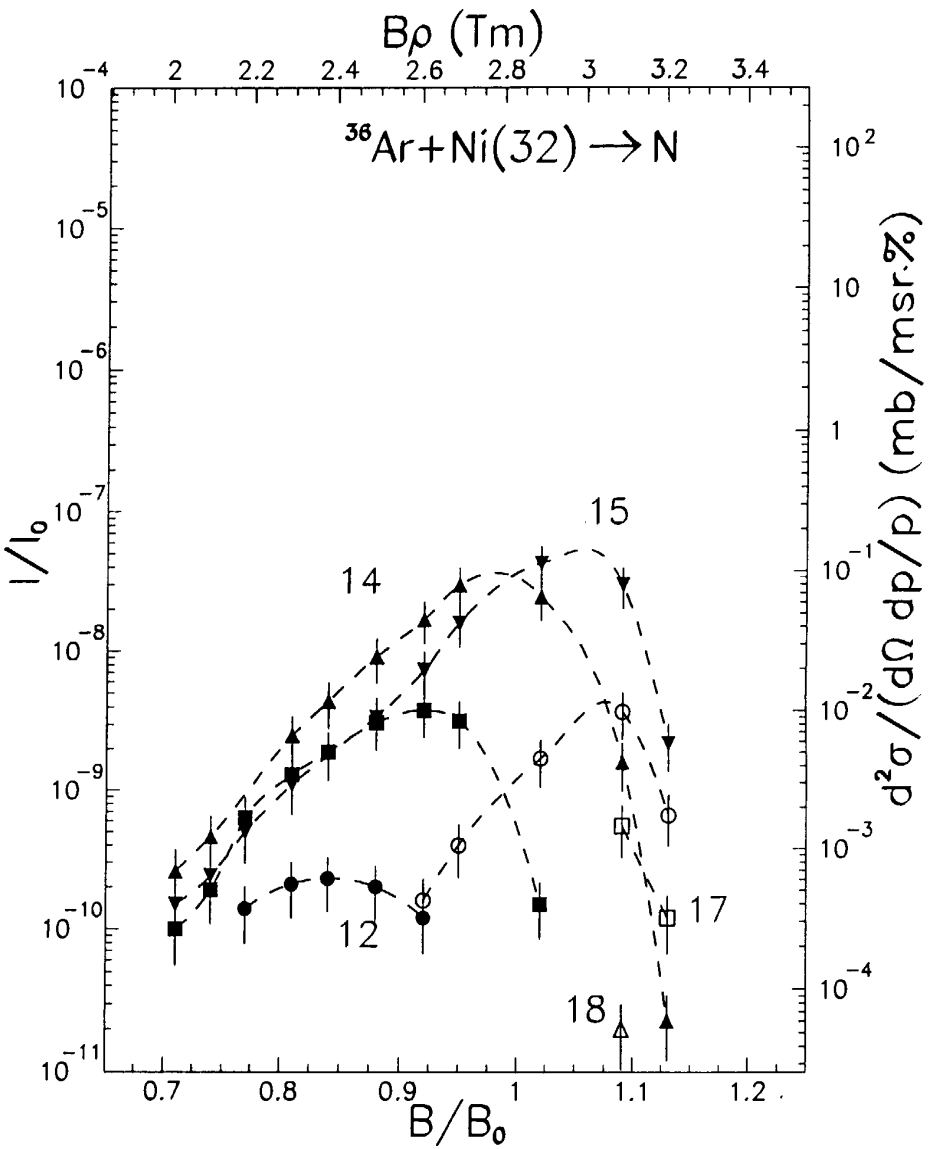
Bρ (Tm)
^{36}Ar+Ni(32) → N
I/I$_0$
d^{2}σ/(dΩ dp/p) (mb/msr·%)
B/B$_0$
15
14
12
17
18

Fig. 9l

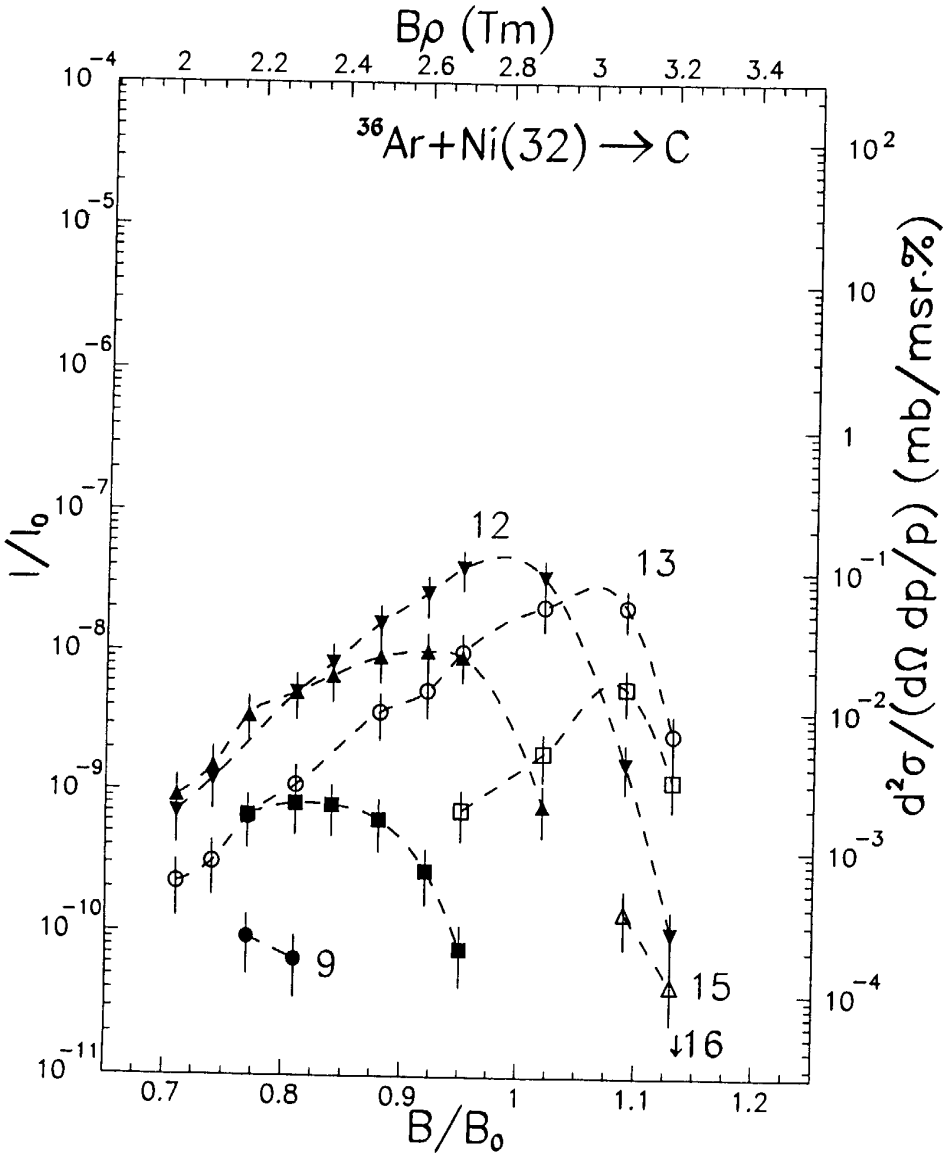
Bρ (Tm)
^{36}Ar+Ni(32) → C
I/I$_o$
B/B$_o$
d^{2}σ/(dΩ dp/p) (mb/msr·%)
9
12
13
15
↓16

Fig. 9m

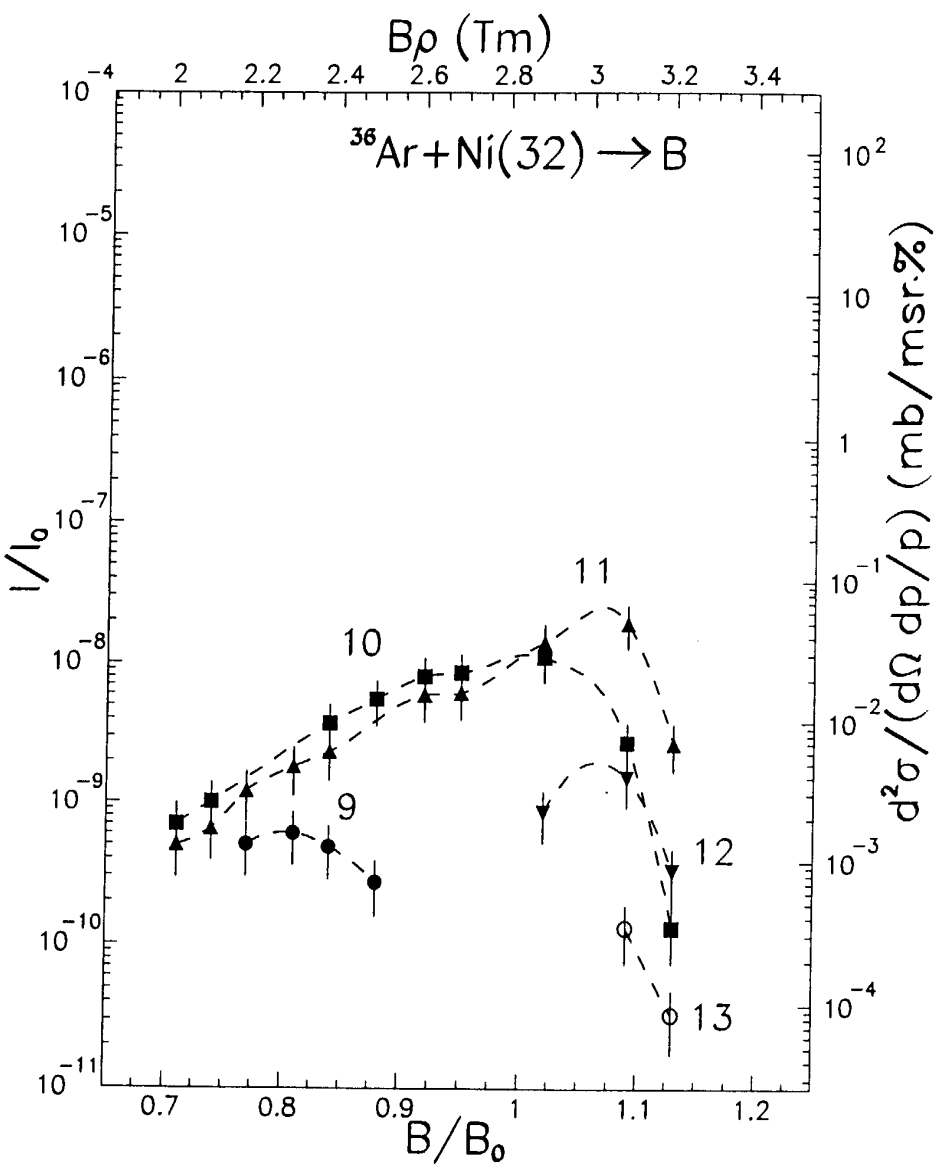
Bρ (Tm)
^{36}Ar+Ni(32) → B
I/I$_o$
B/B$_o$
d^{2}σ/(dΩ dp/p) (mb/msr·%)
9
10
11
12
13

Fig. 9n

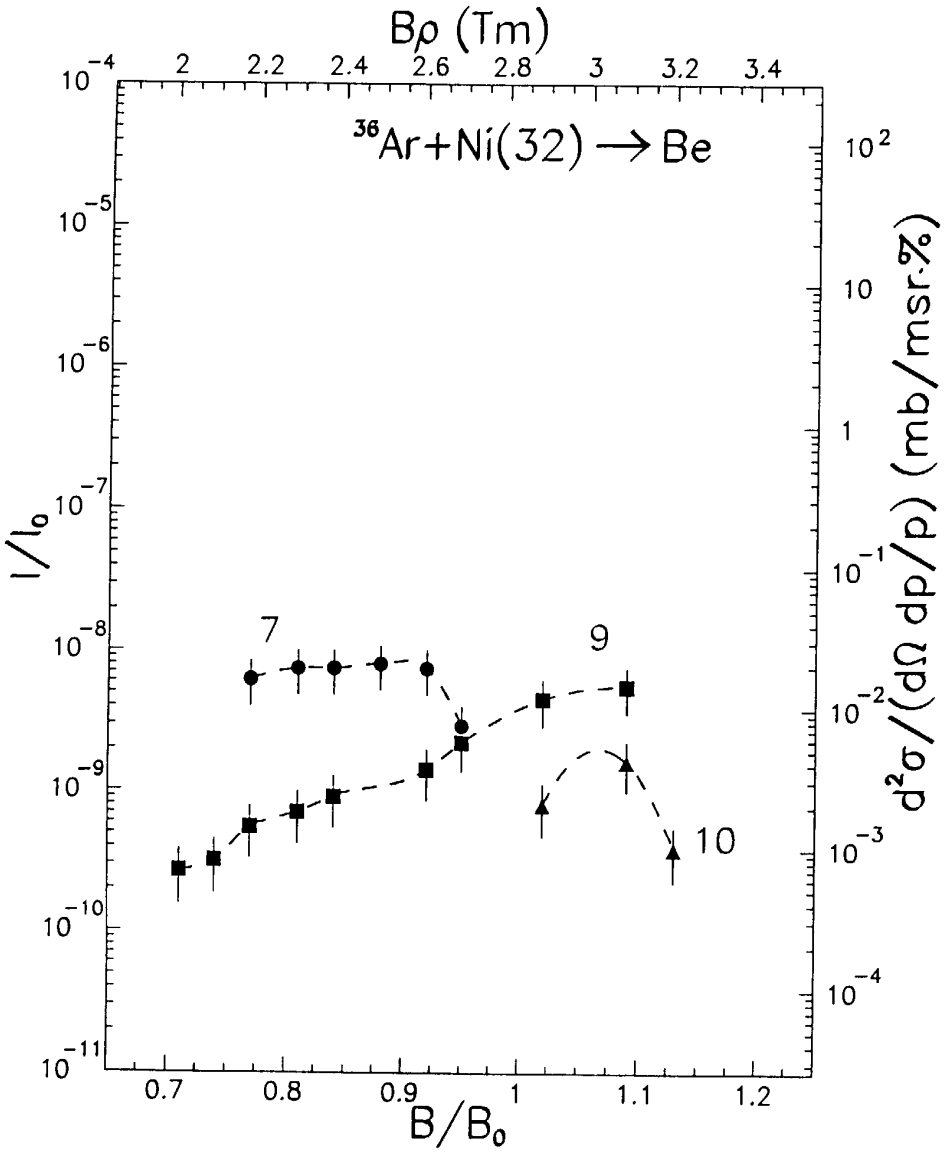
Bρ (Tm)
^{36}Ar+Ni(32) → Be
I/I$_0$
d^{2}σ/(dΩ dp/p) (mb/msr·%)
B/B$_0$
7
9
10

Fig. 9o

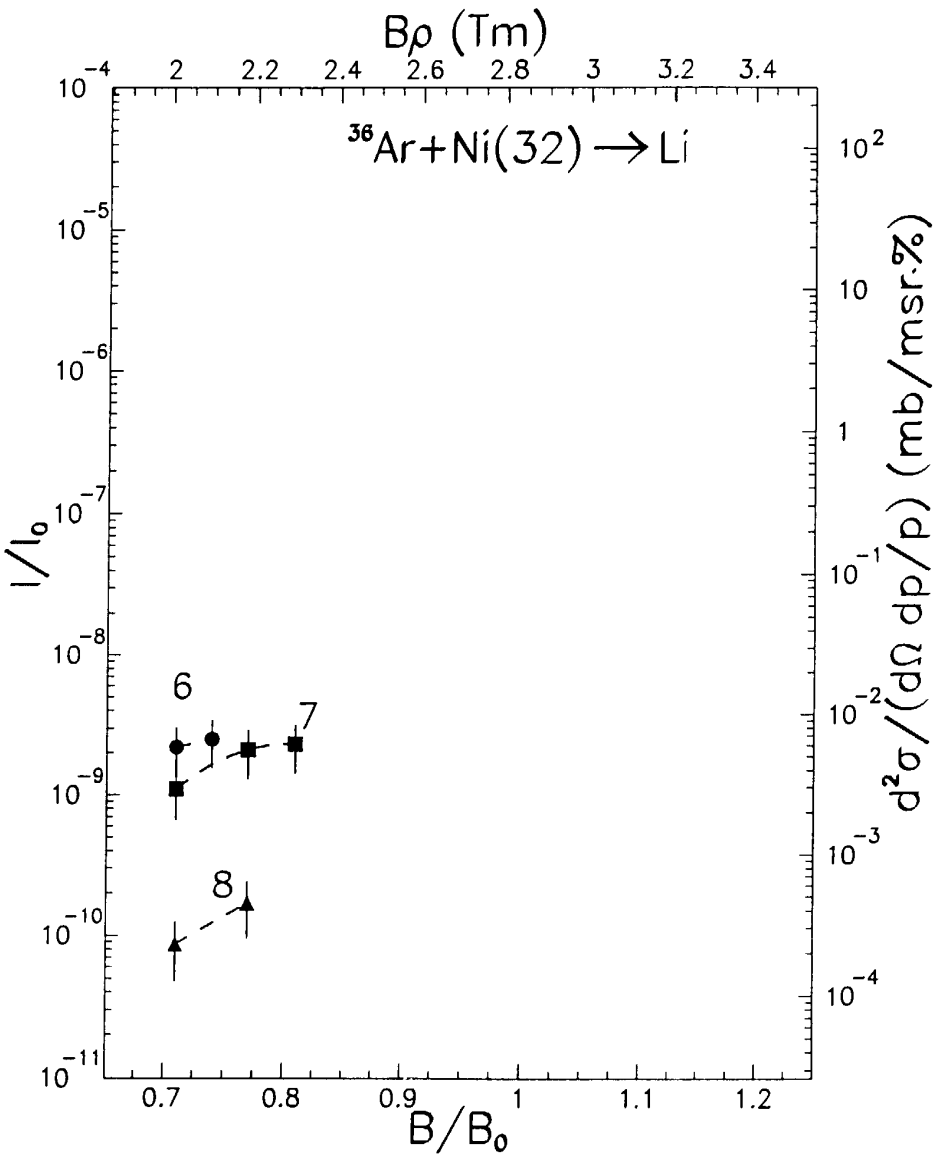
Bρ (Tm)
^{36}Ar+Ni(32) → Li
I/I$_0$
d^{2}σ/(dΩ dp/p) (mb/msr·%)
B/B$_0$
6
7
8

Fig. 9p

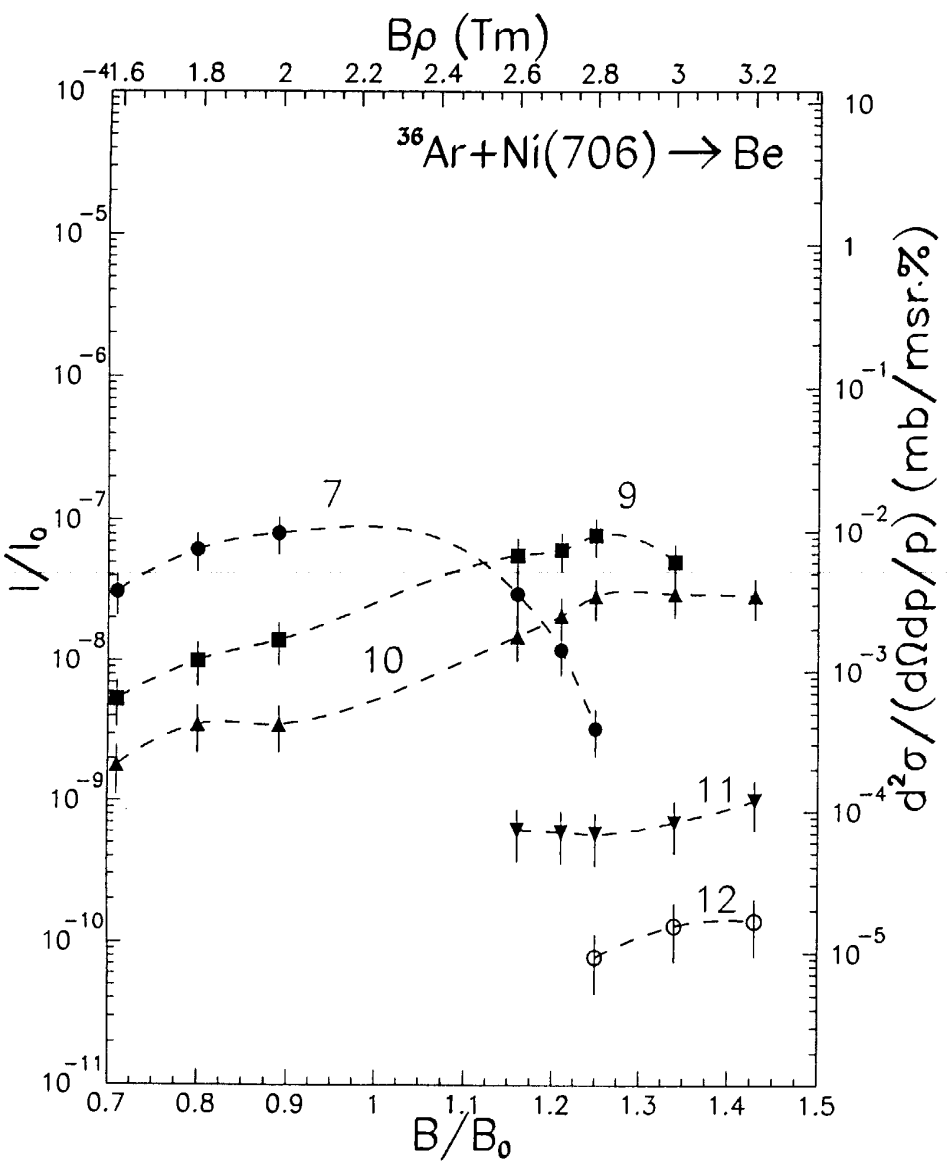

Fig. 11o

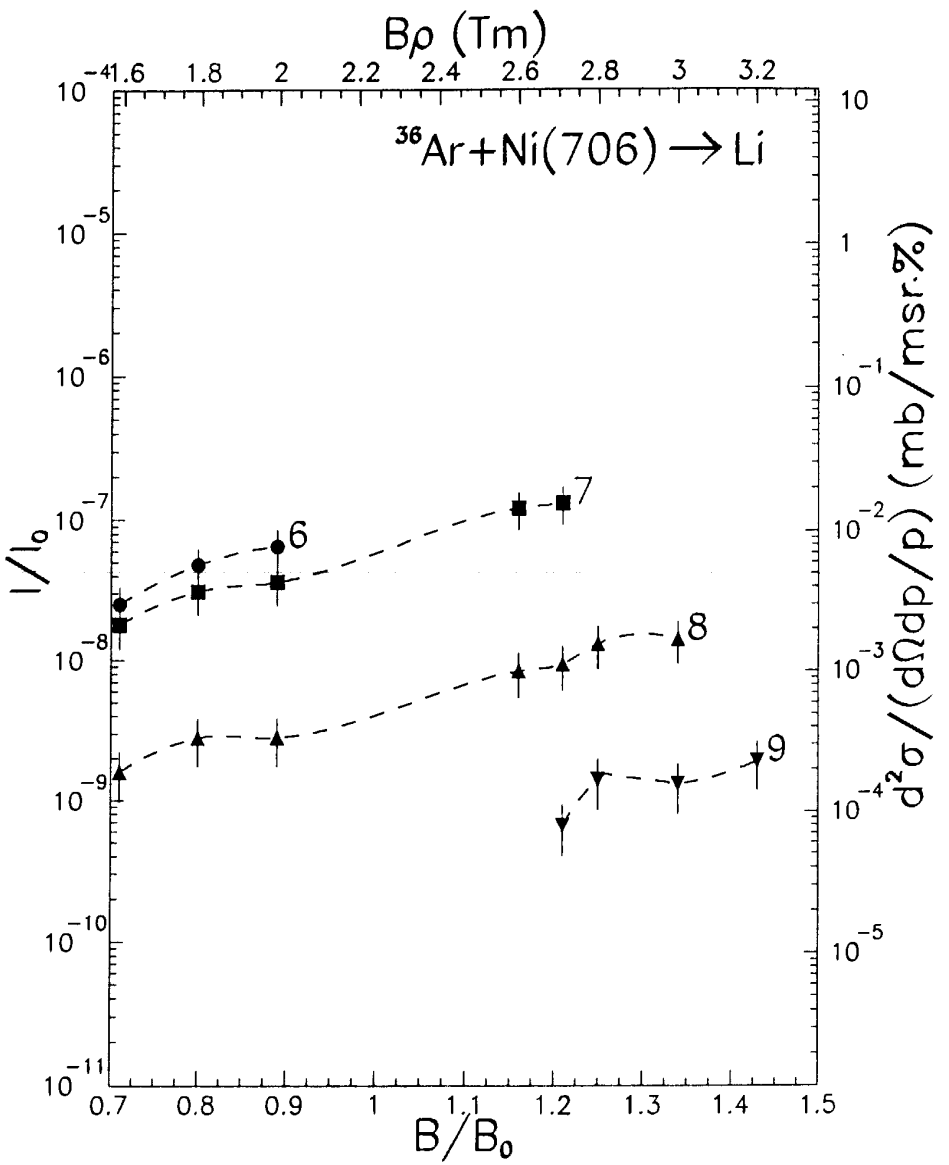

Fig. 11p

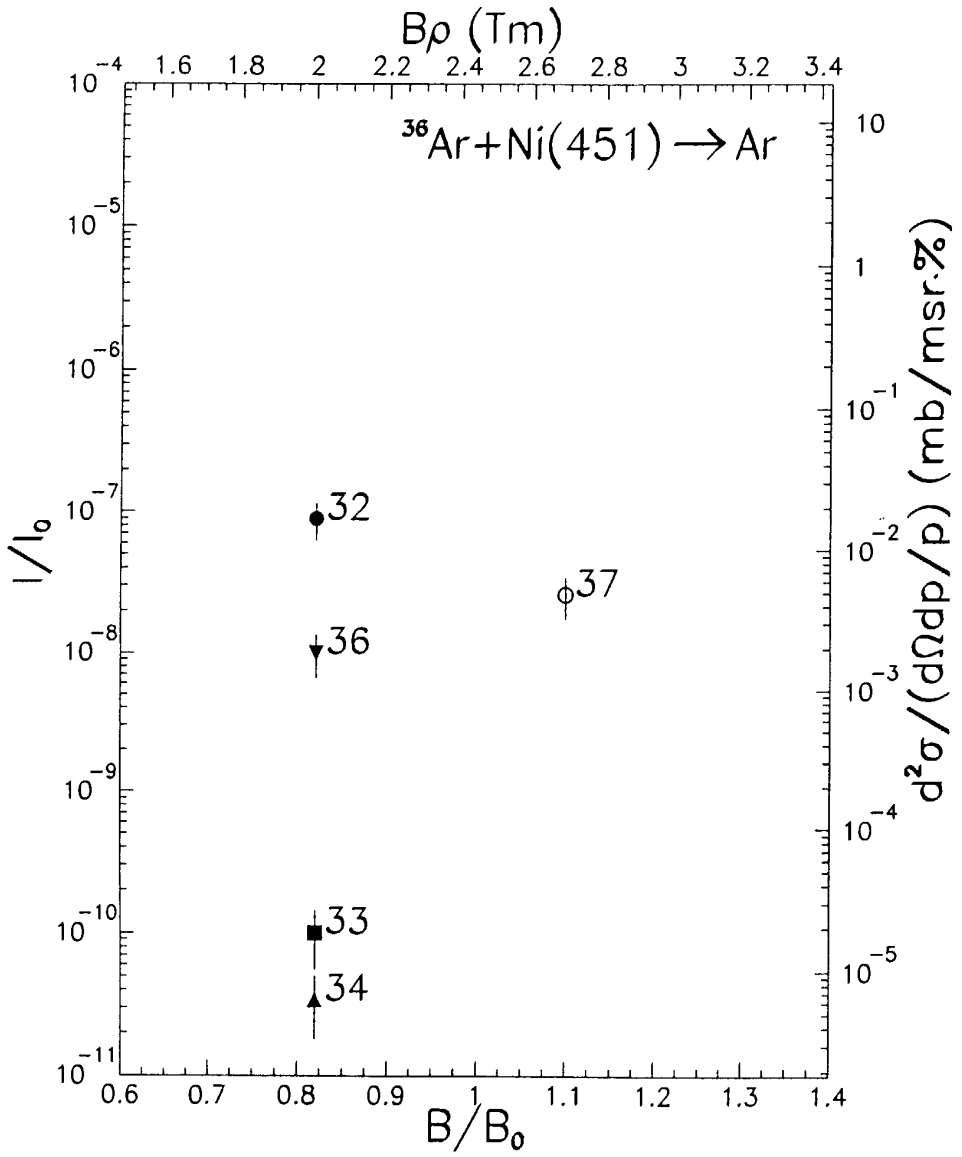

Fig. 10a

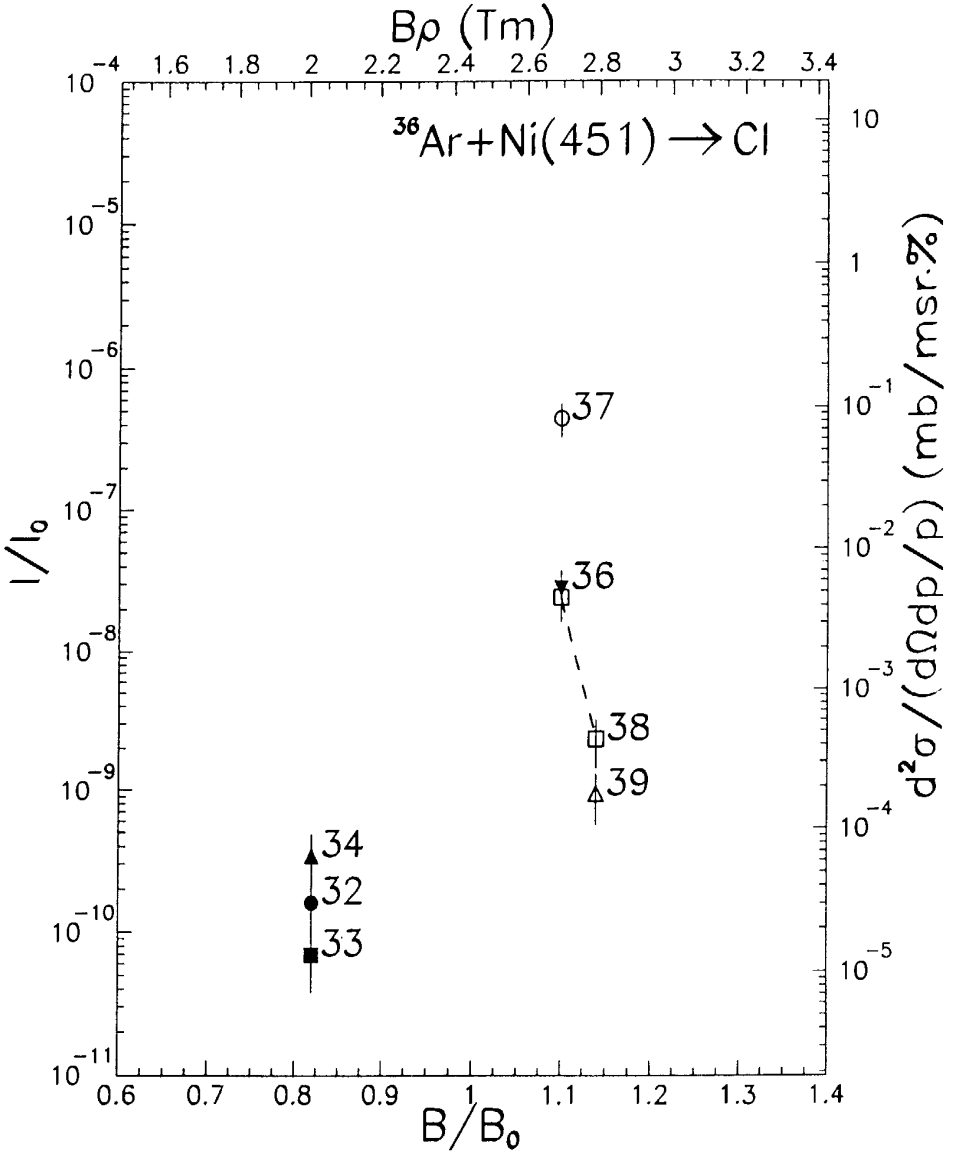

Fig. 10b

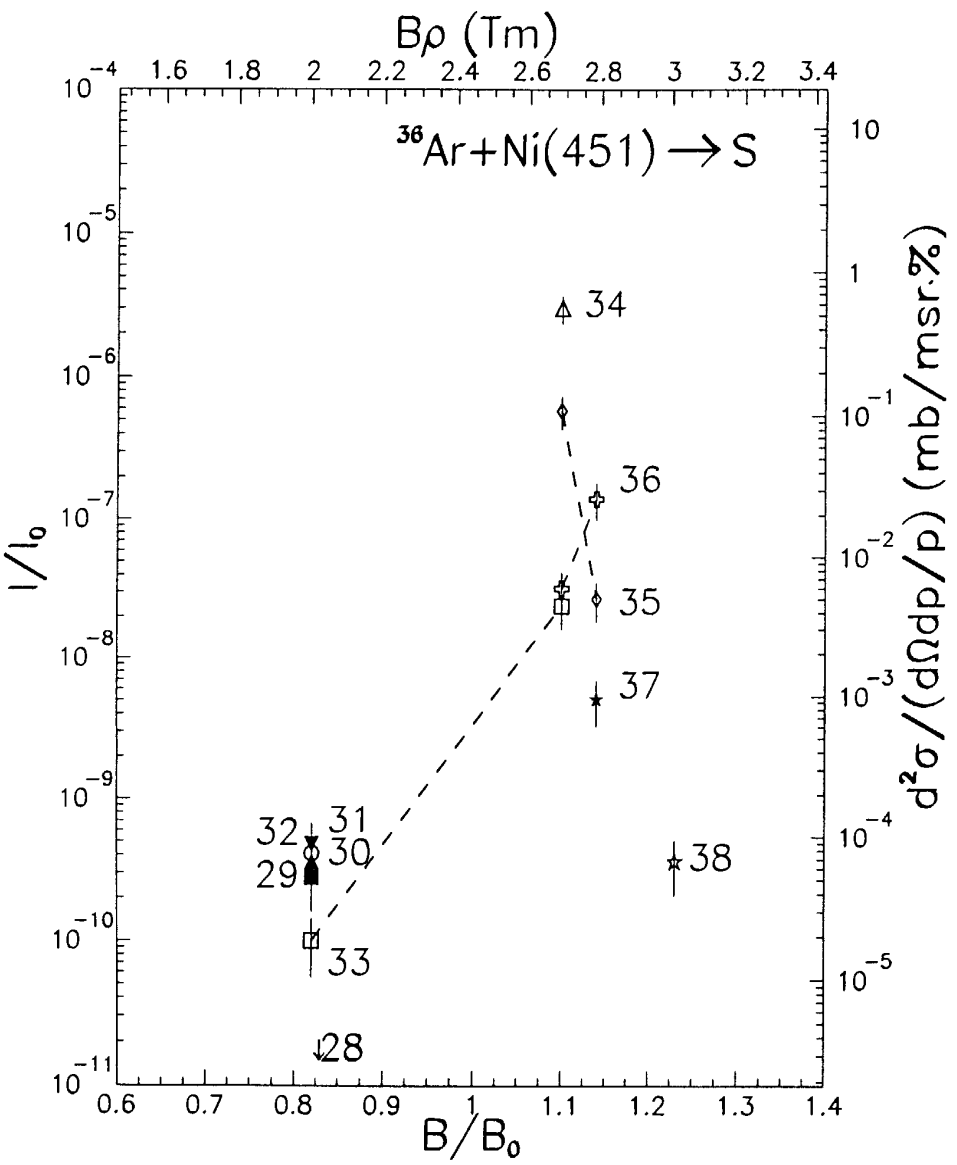

Fig. 10c

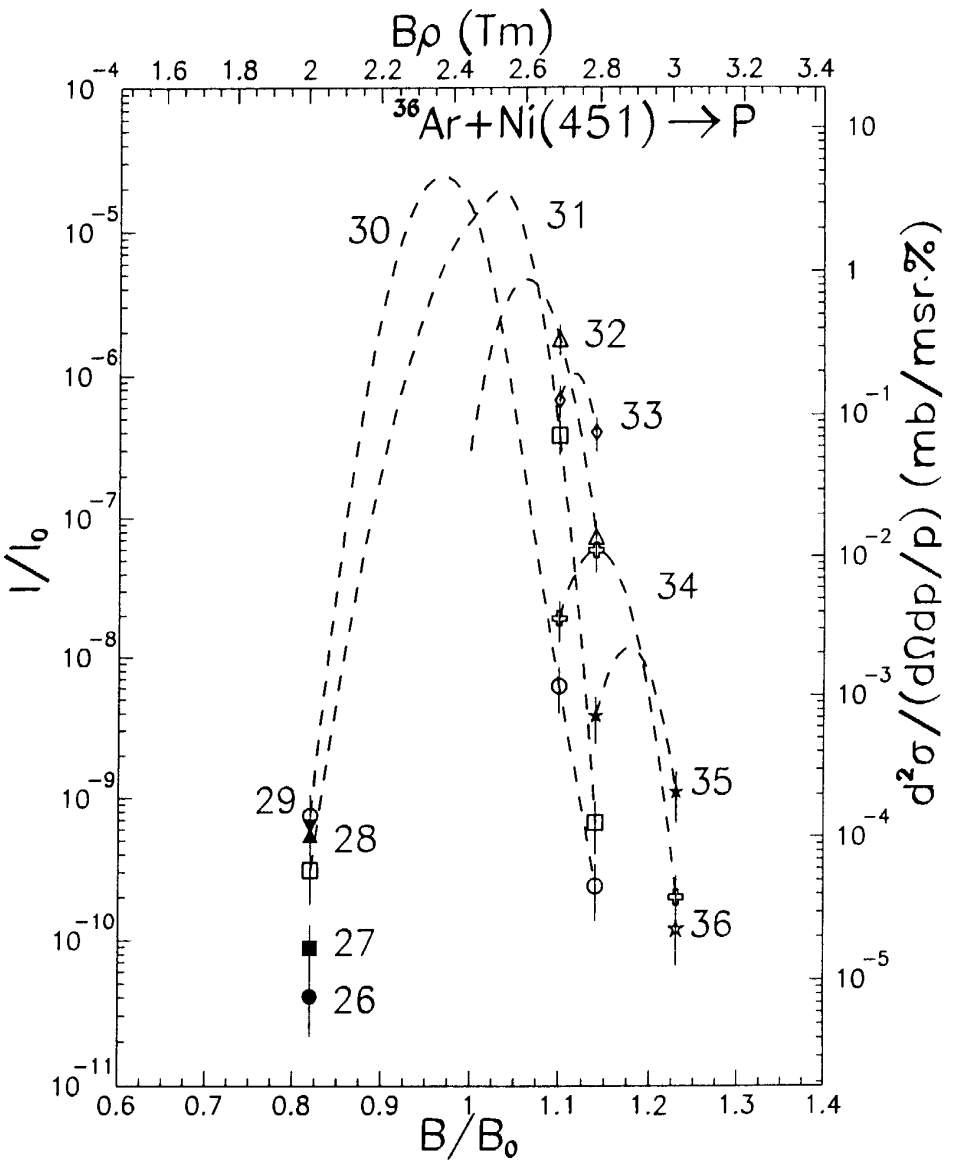

Fig. 10d

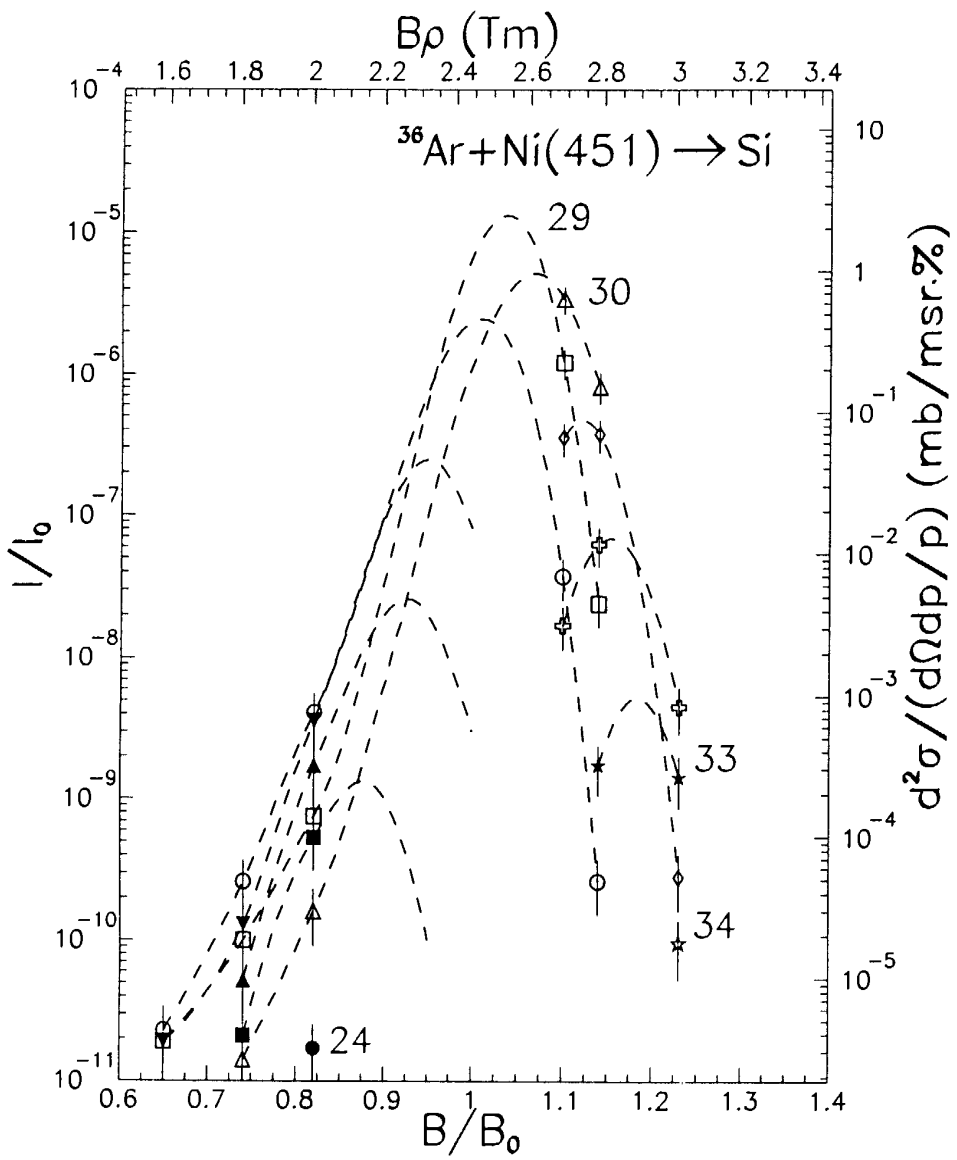

Fig. 10e

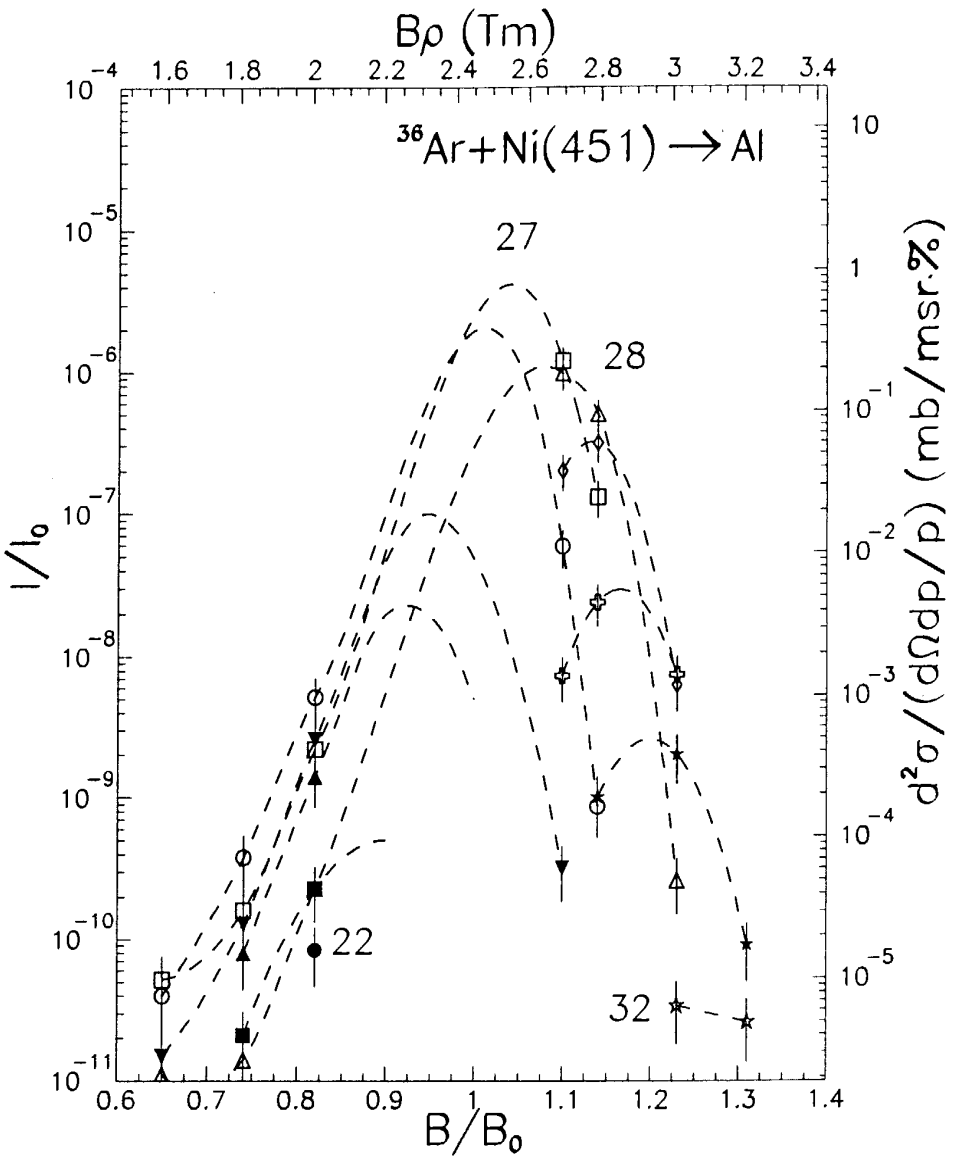

Fig. 10f

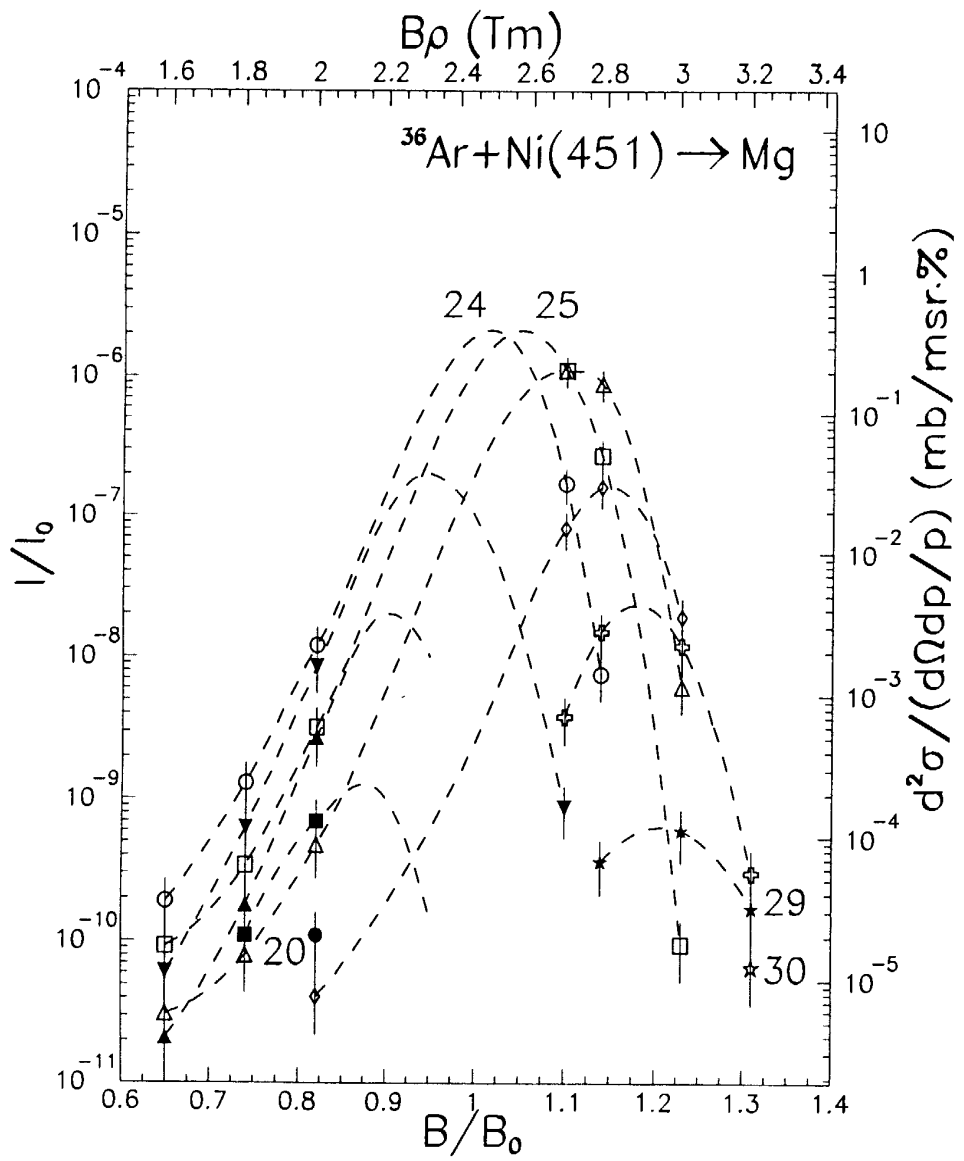

Fig. 10g

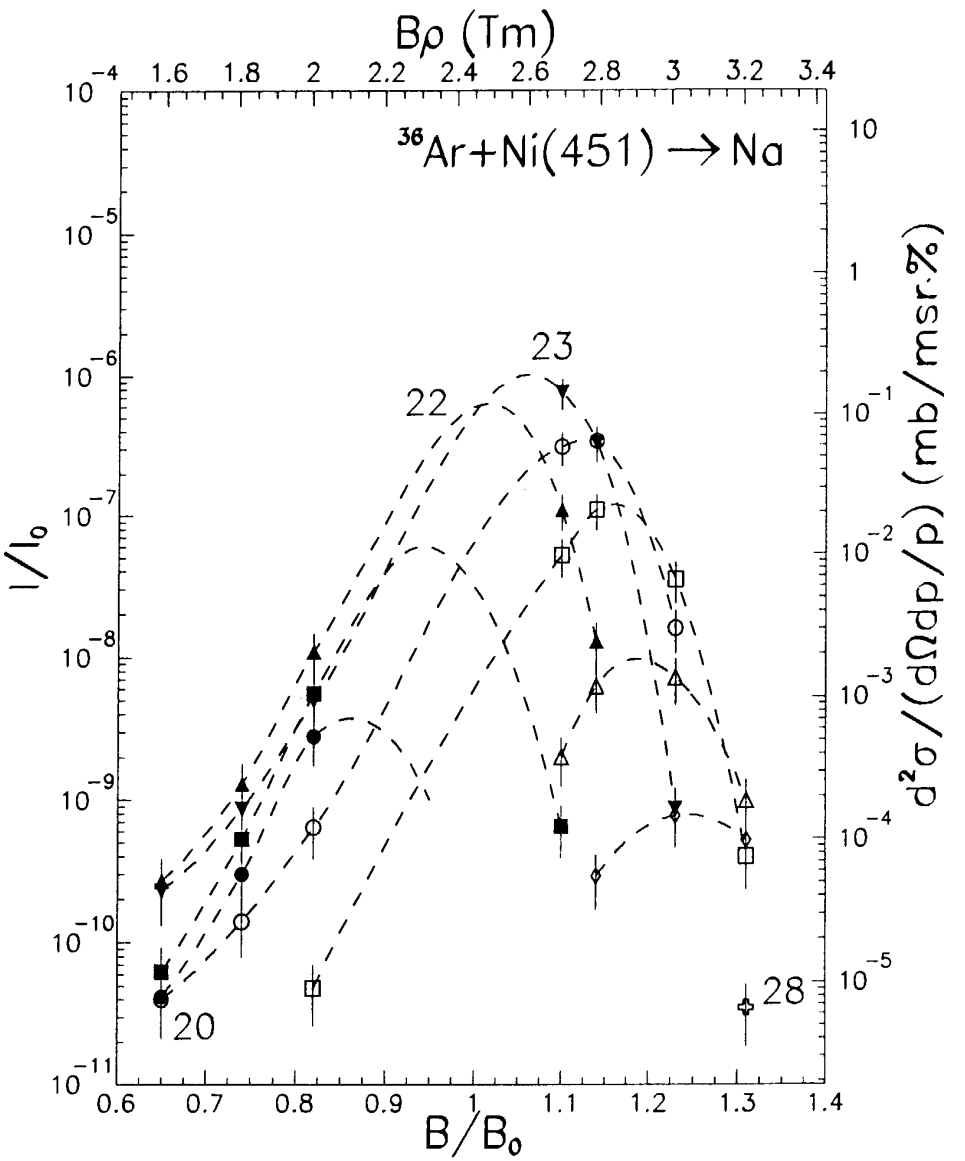

Fig. 10h

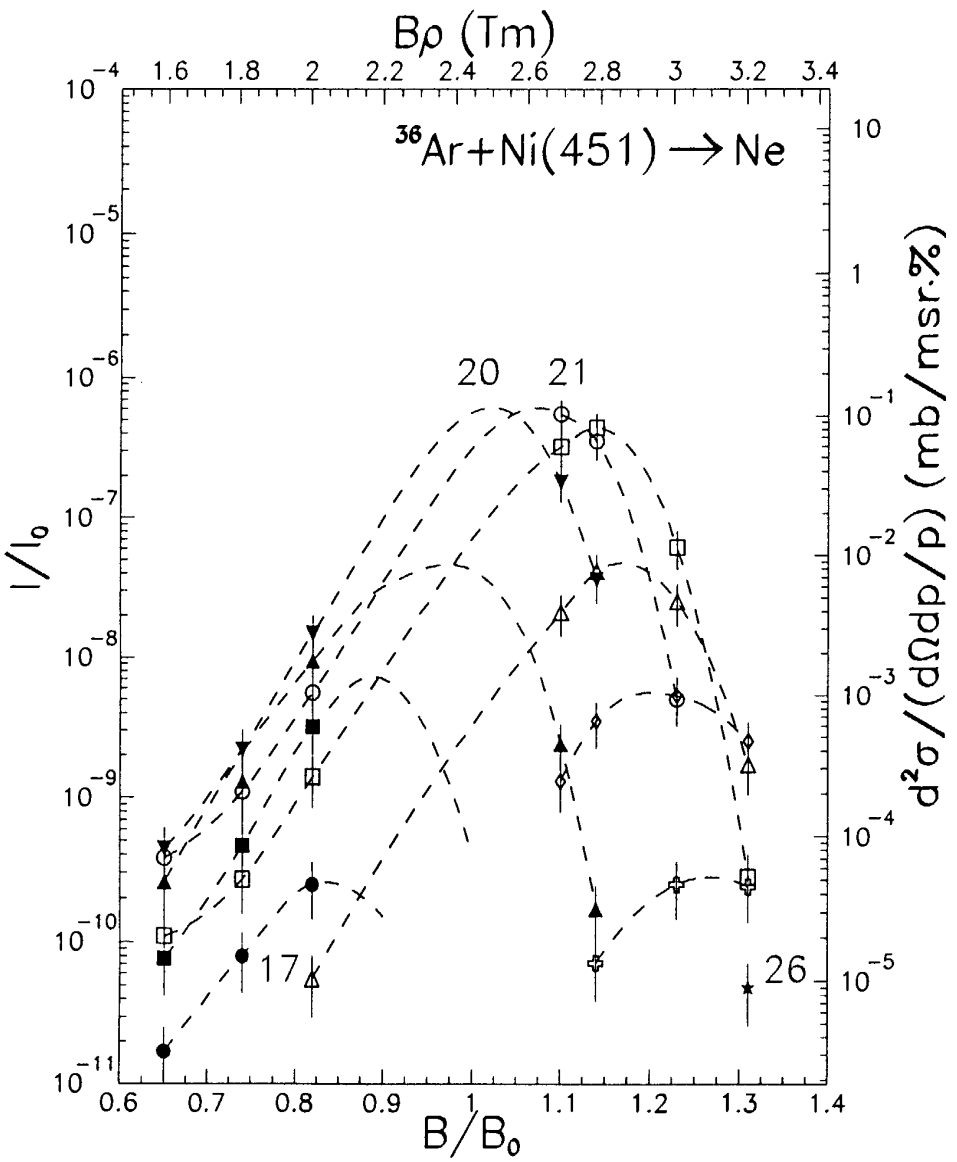

Fig. 10i

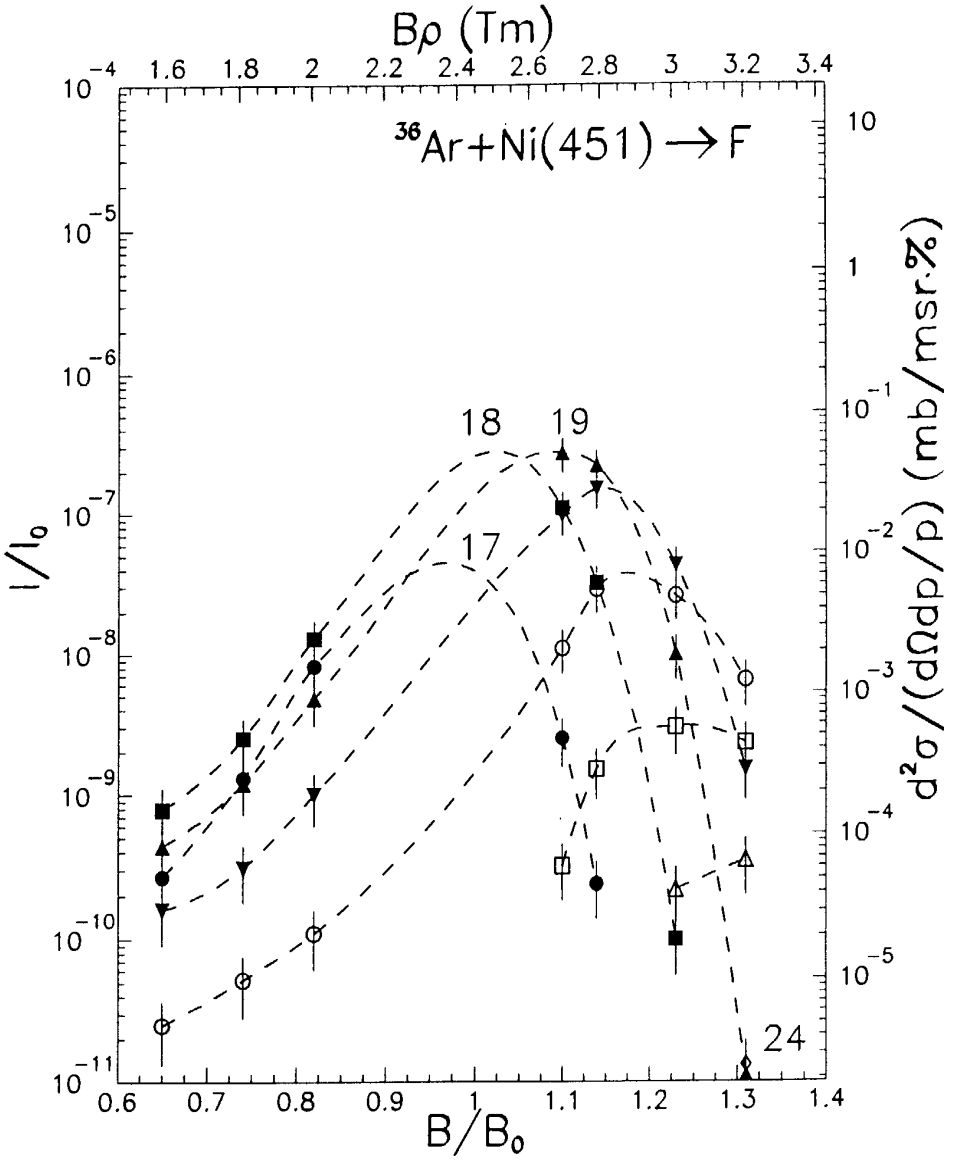

Fig. 10j

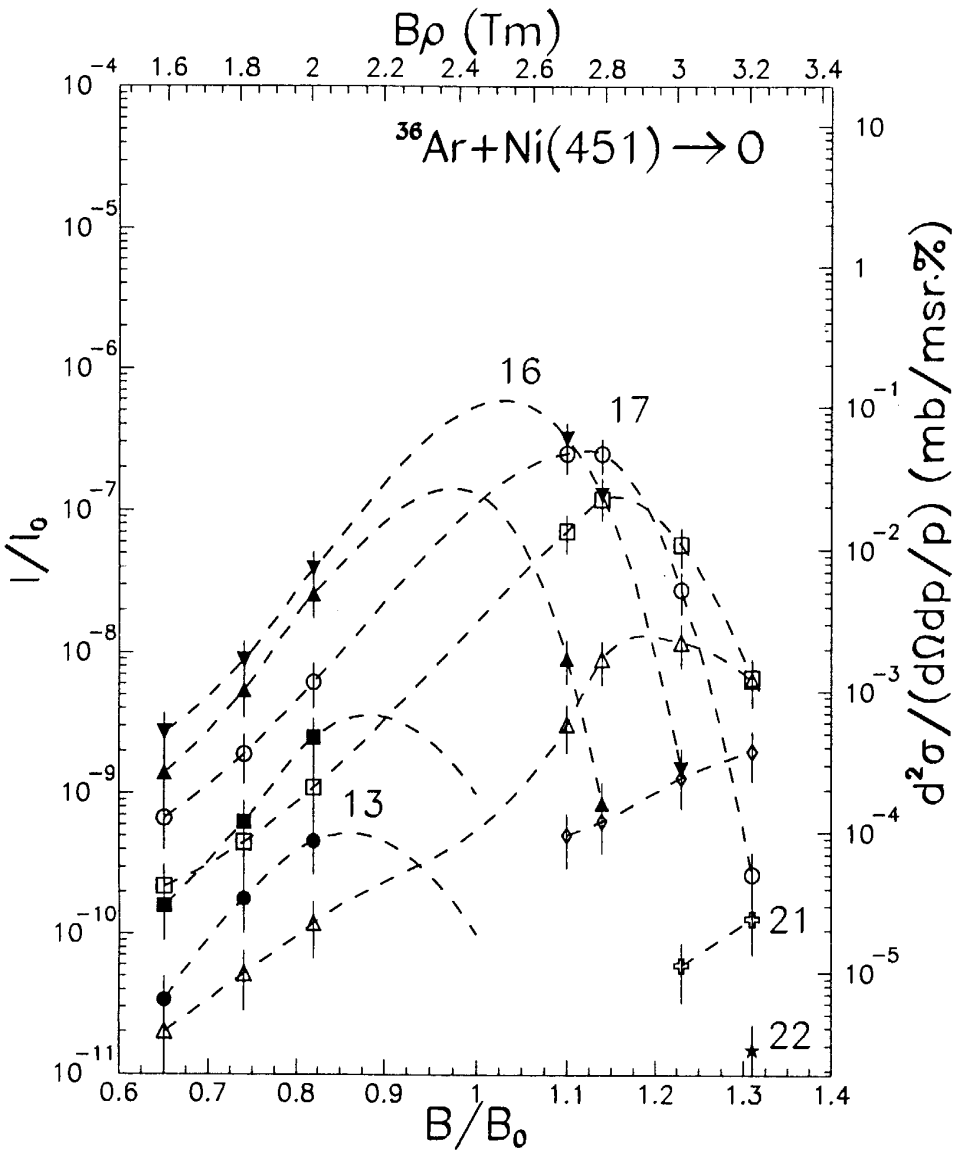

Fig. 10k

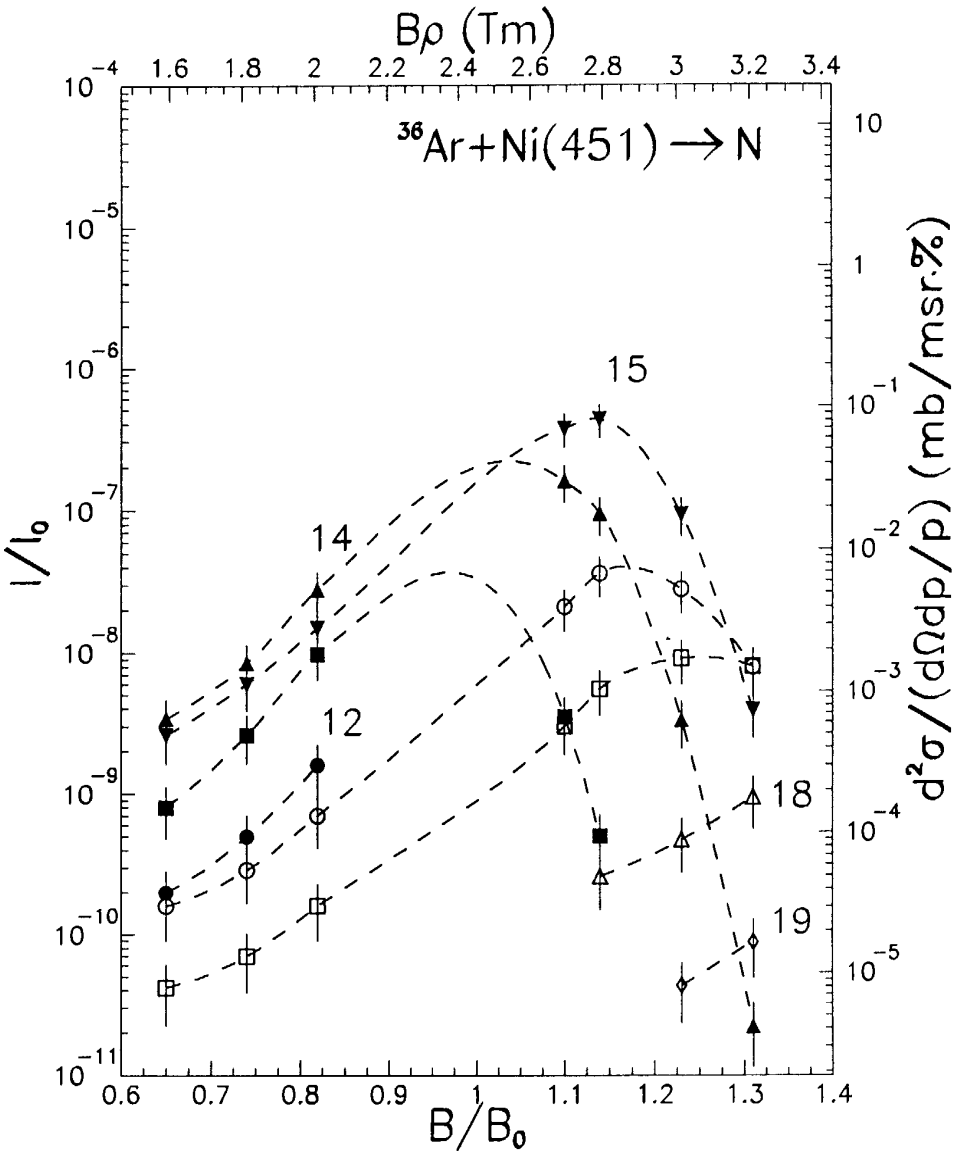

Fig. 10l

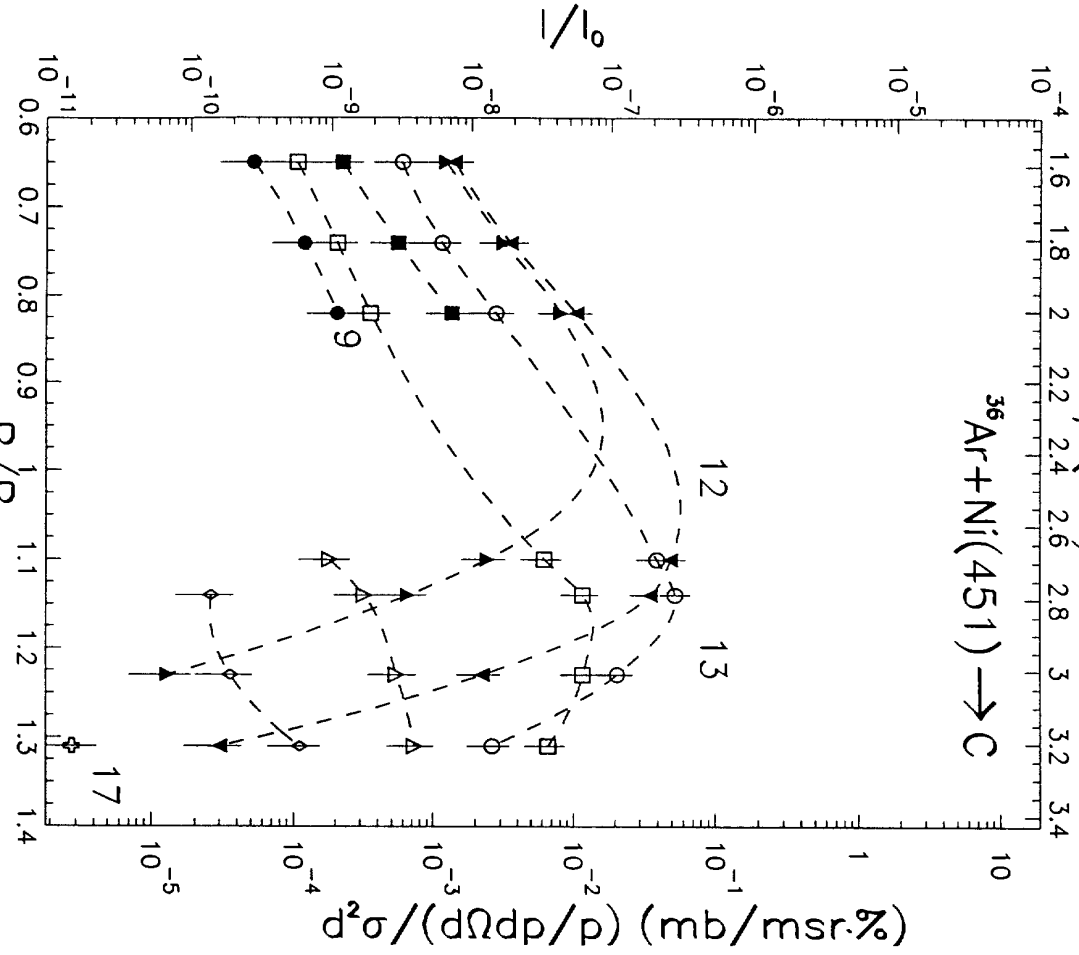

Fig. 10m

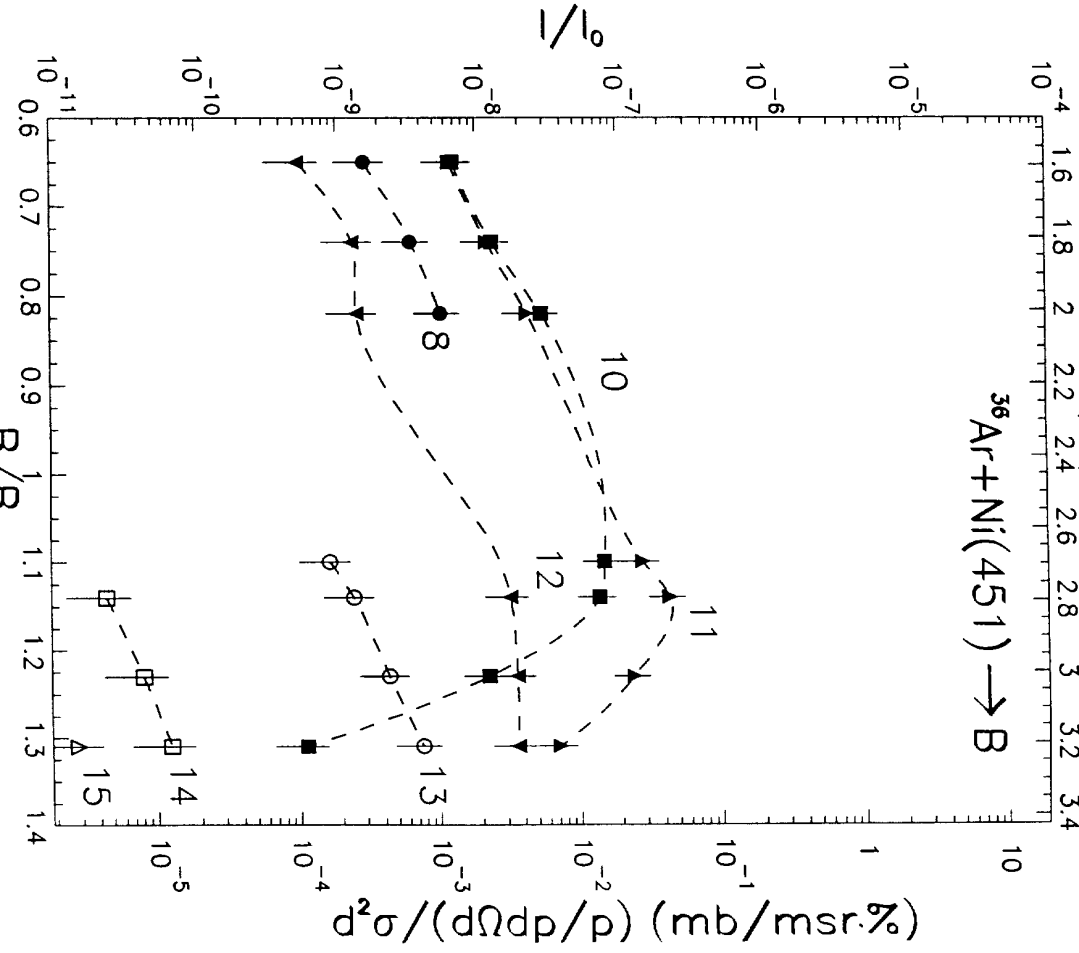

Fig. 10n

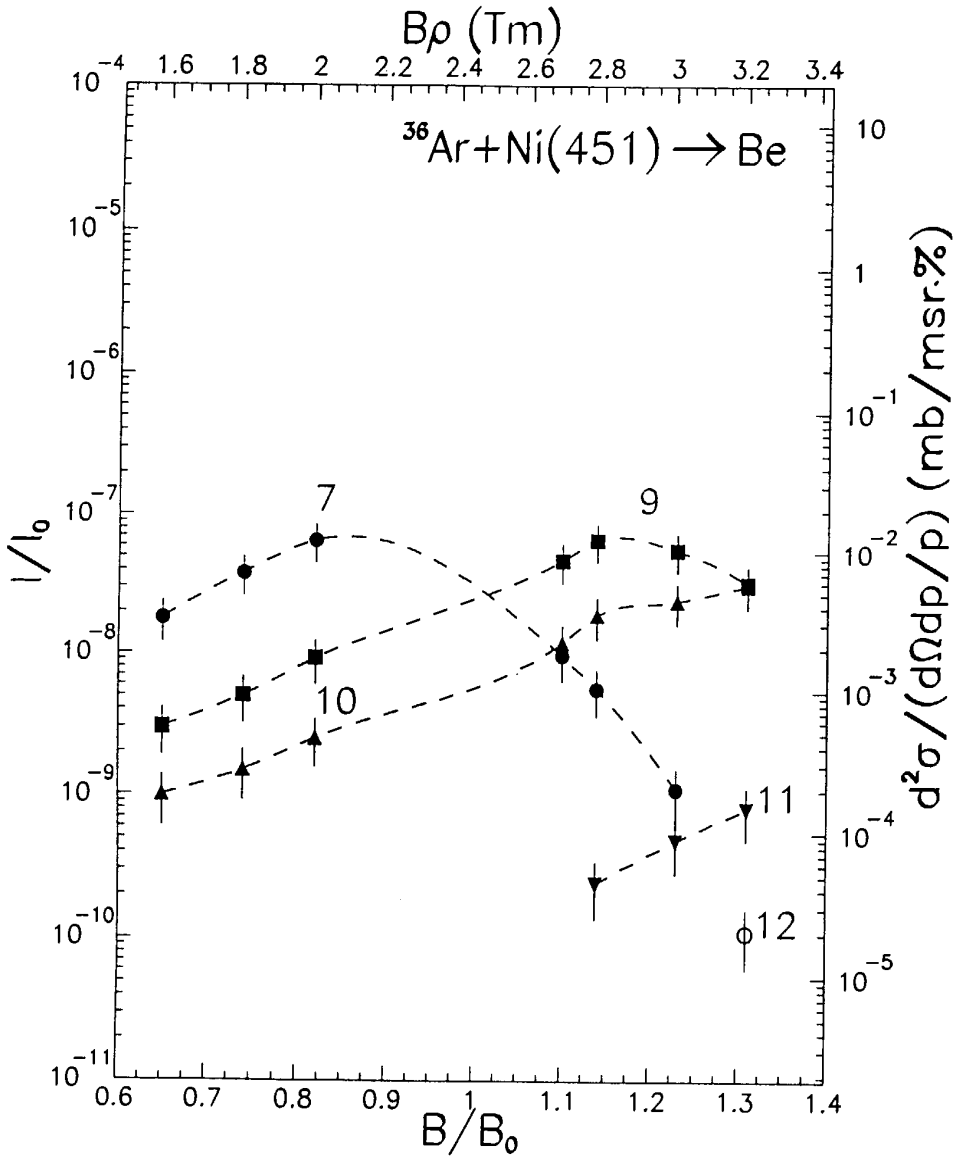

Fig. 10o

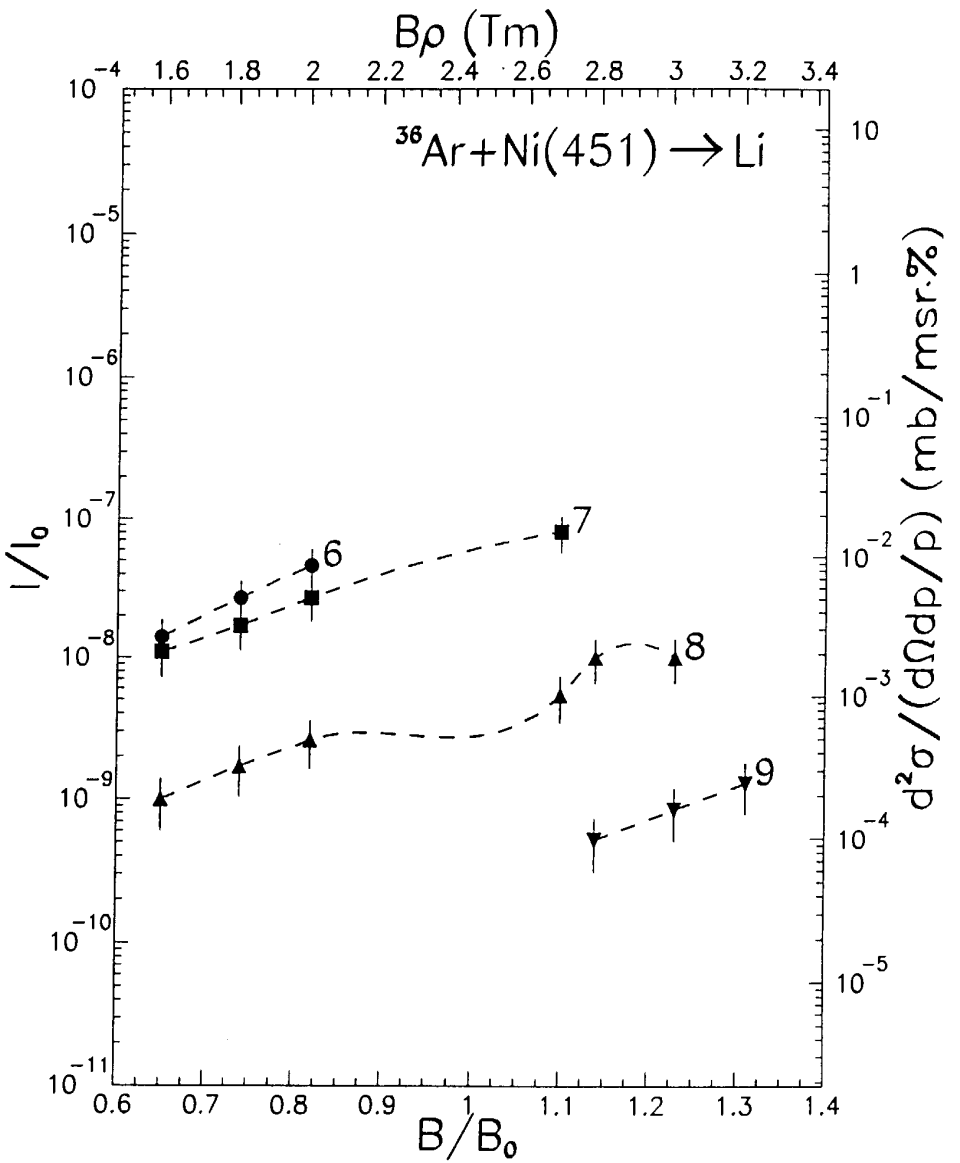

Fig. 10p

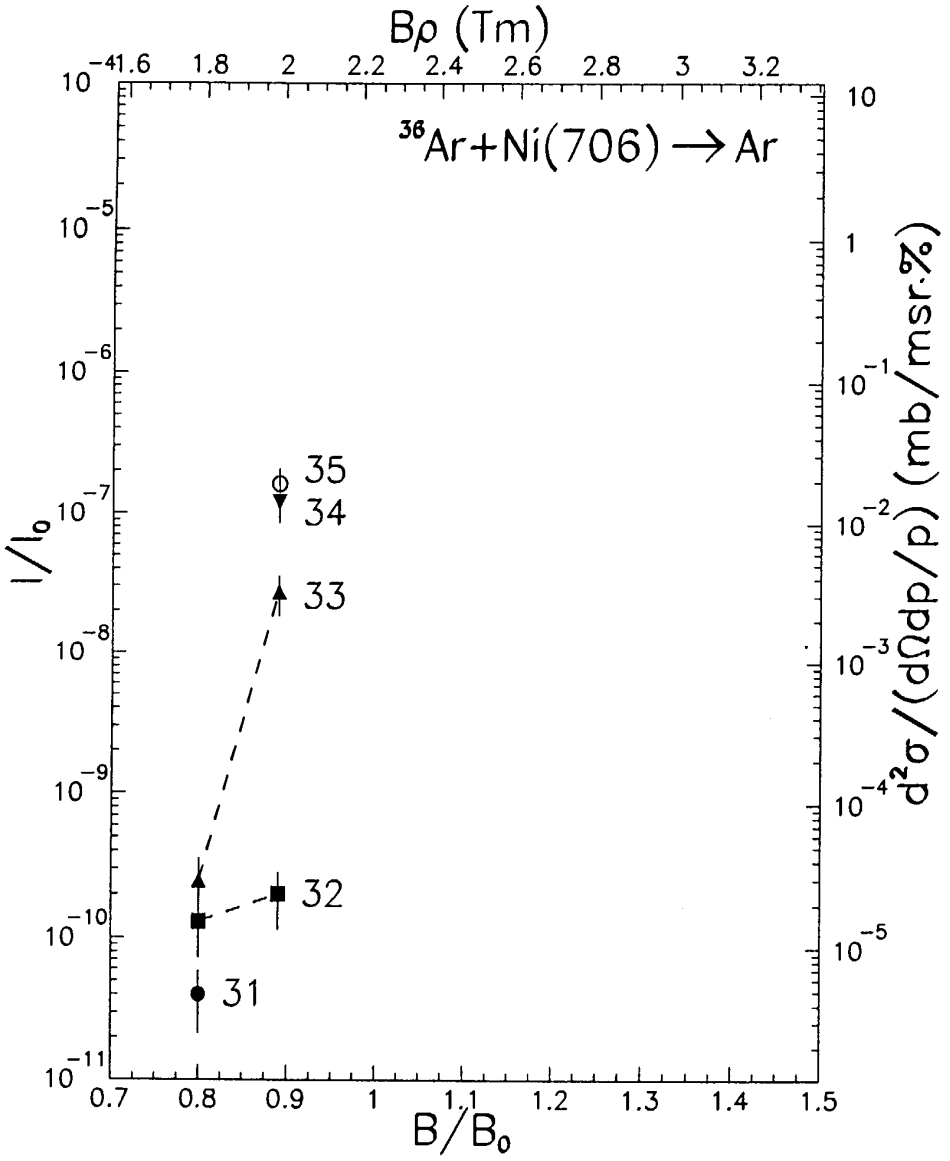

Fig. 11a

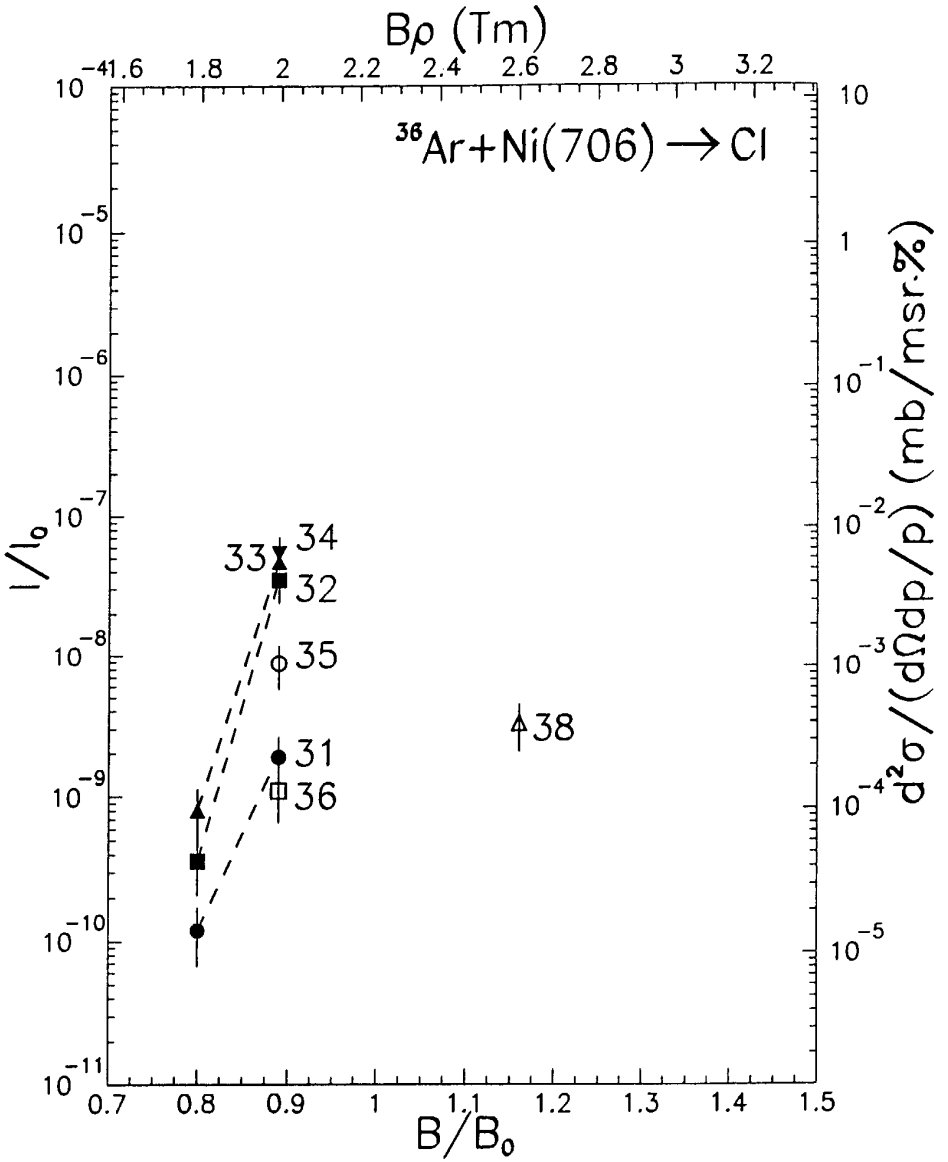

Fig. 11b

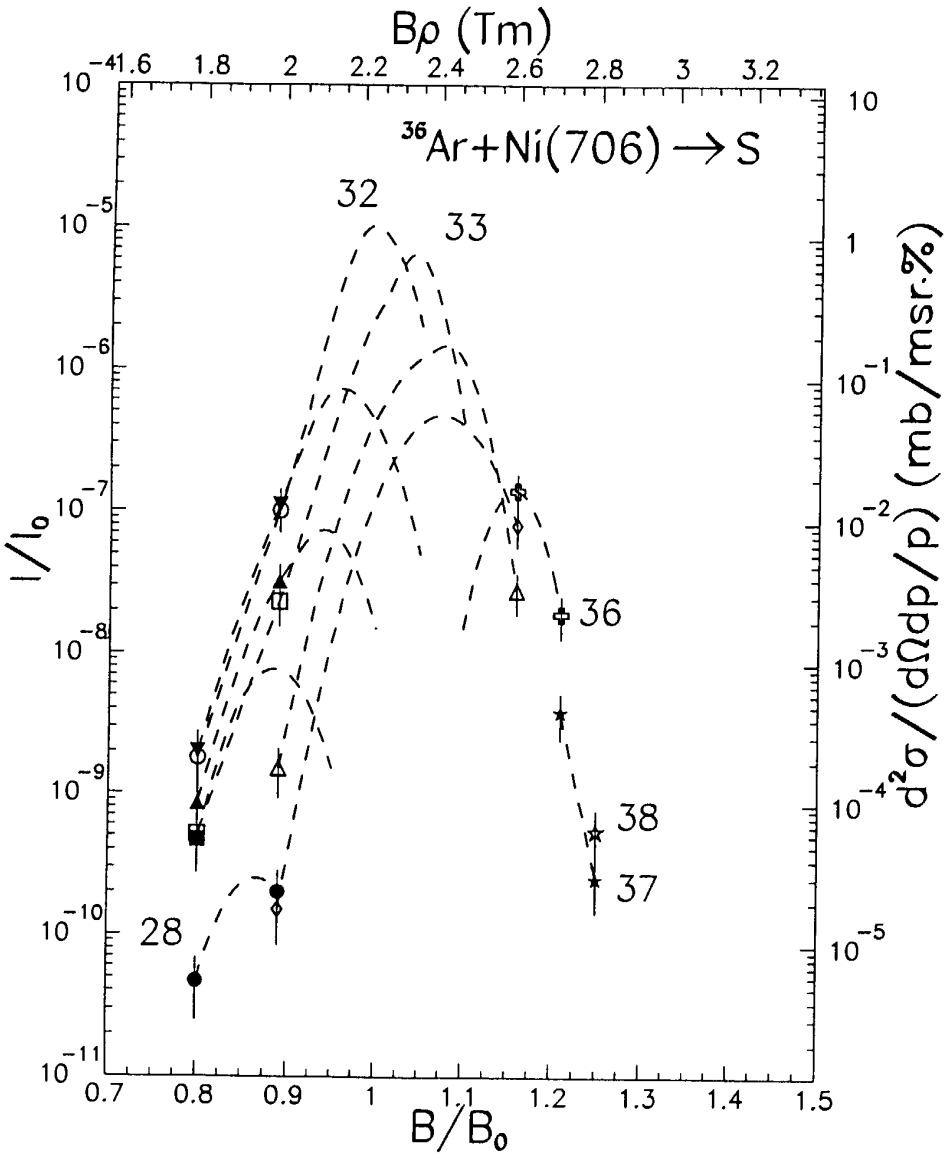

Fig. 11c

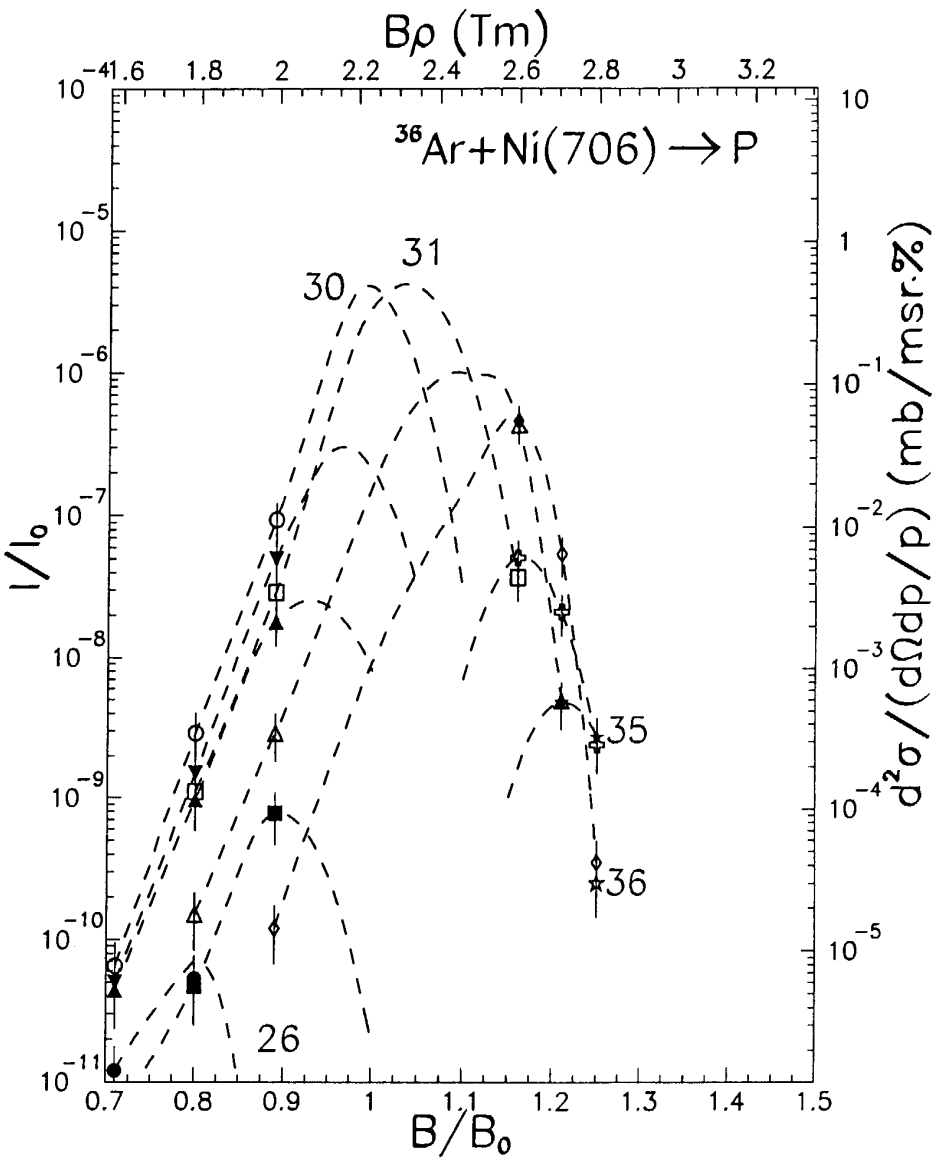

Fig. 11d

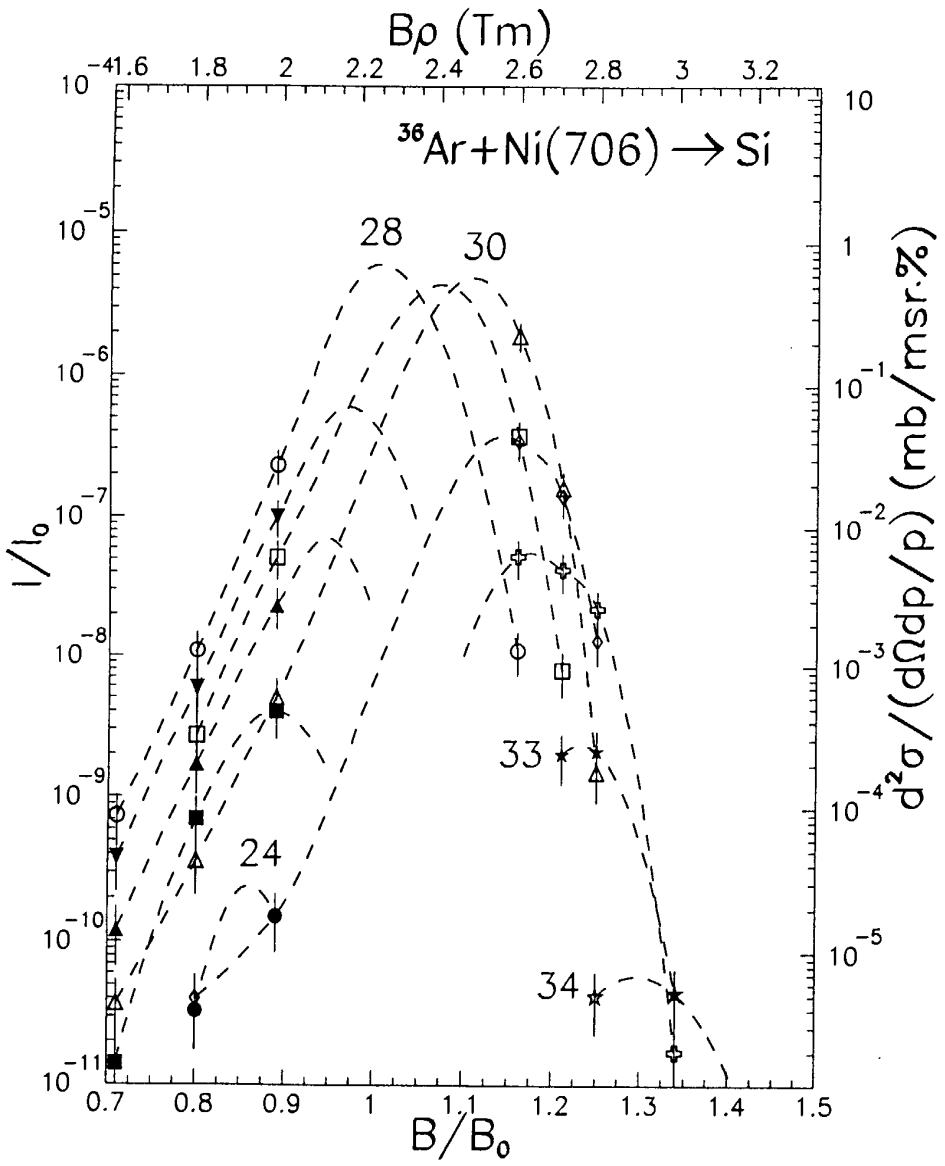

Fig. 11e

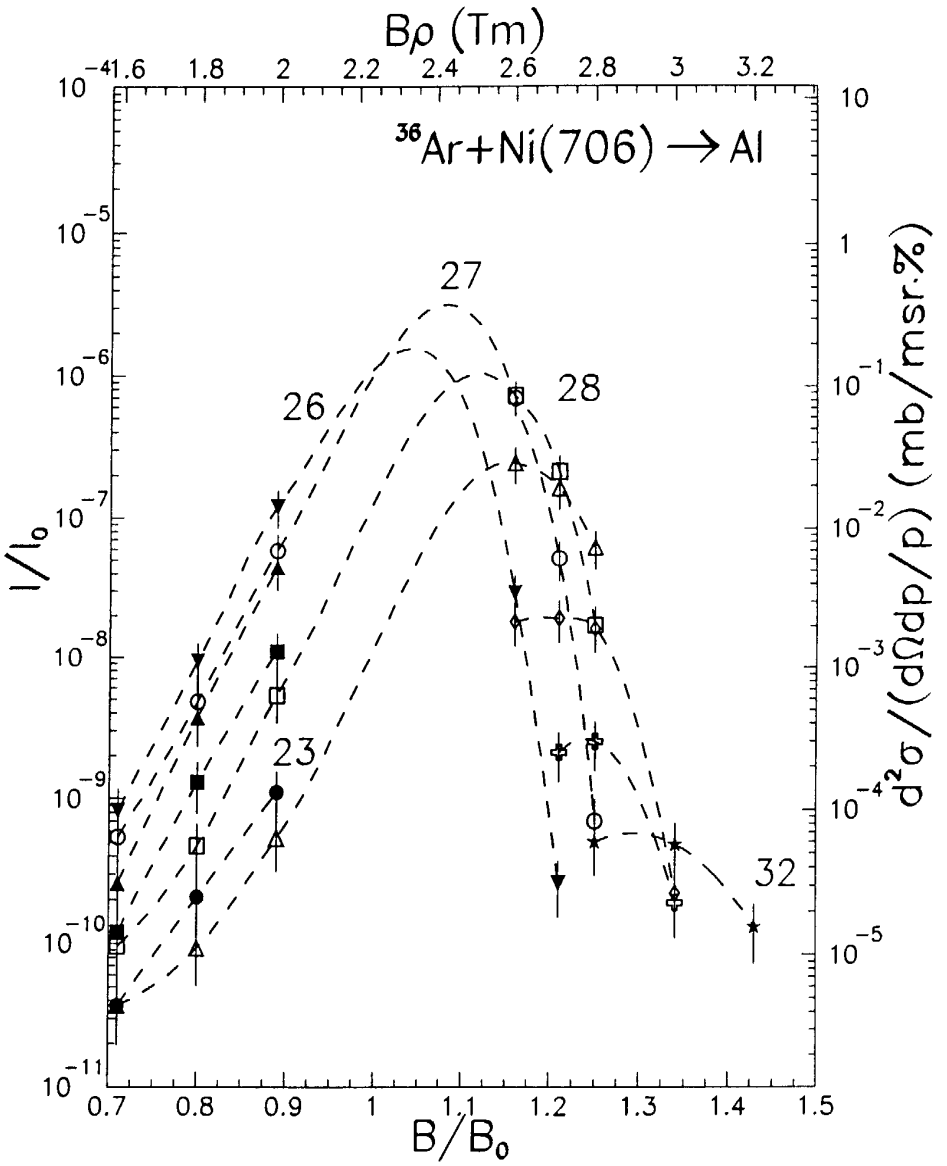

Fig. 11f

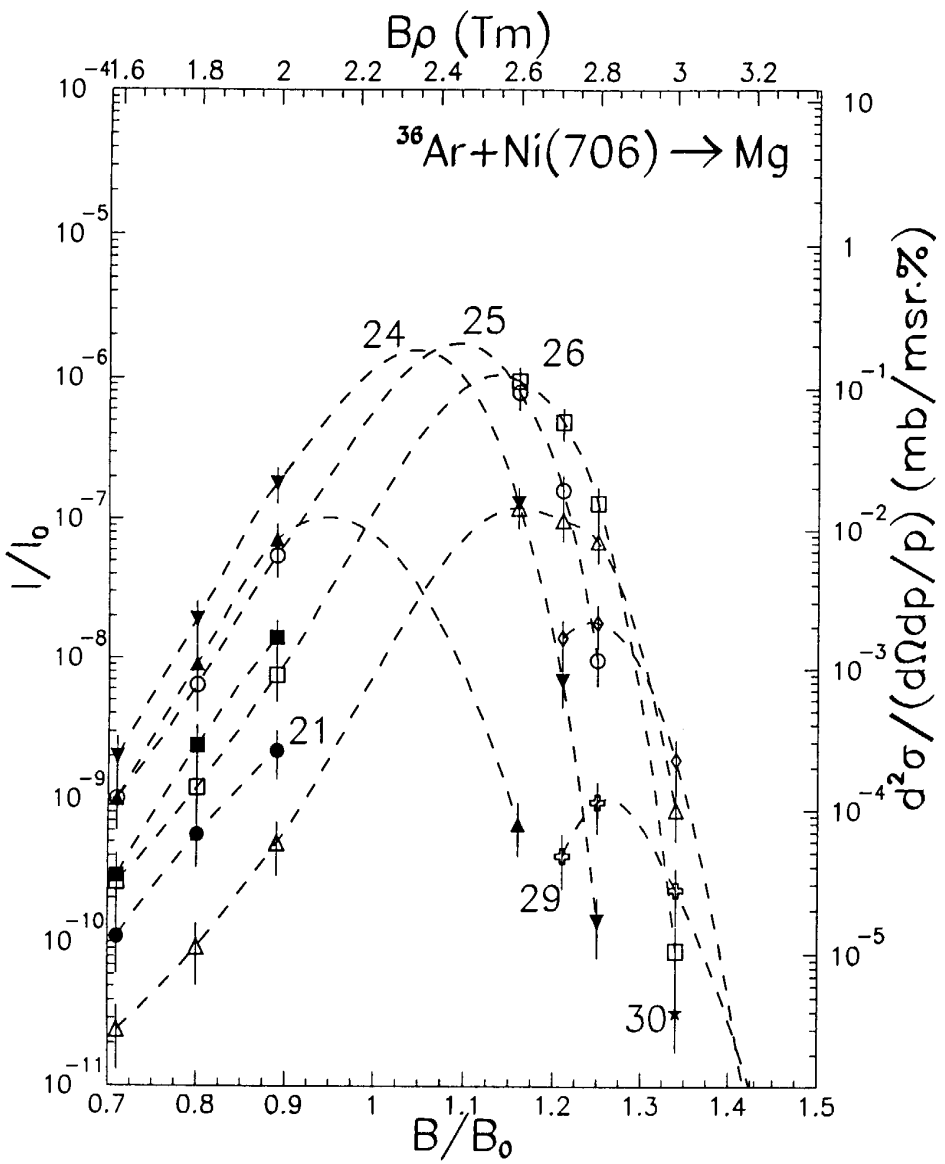

Fig. 11g

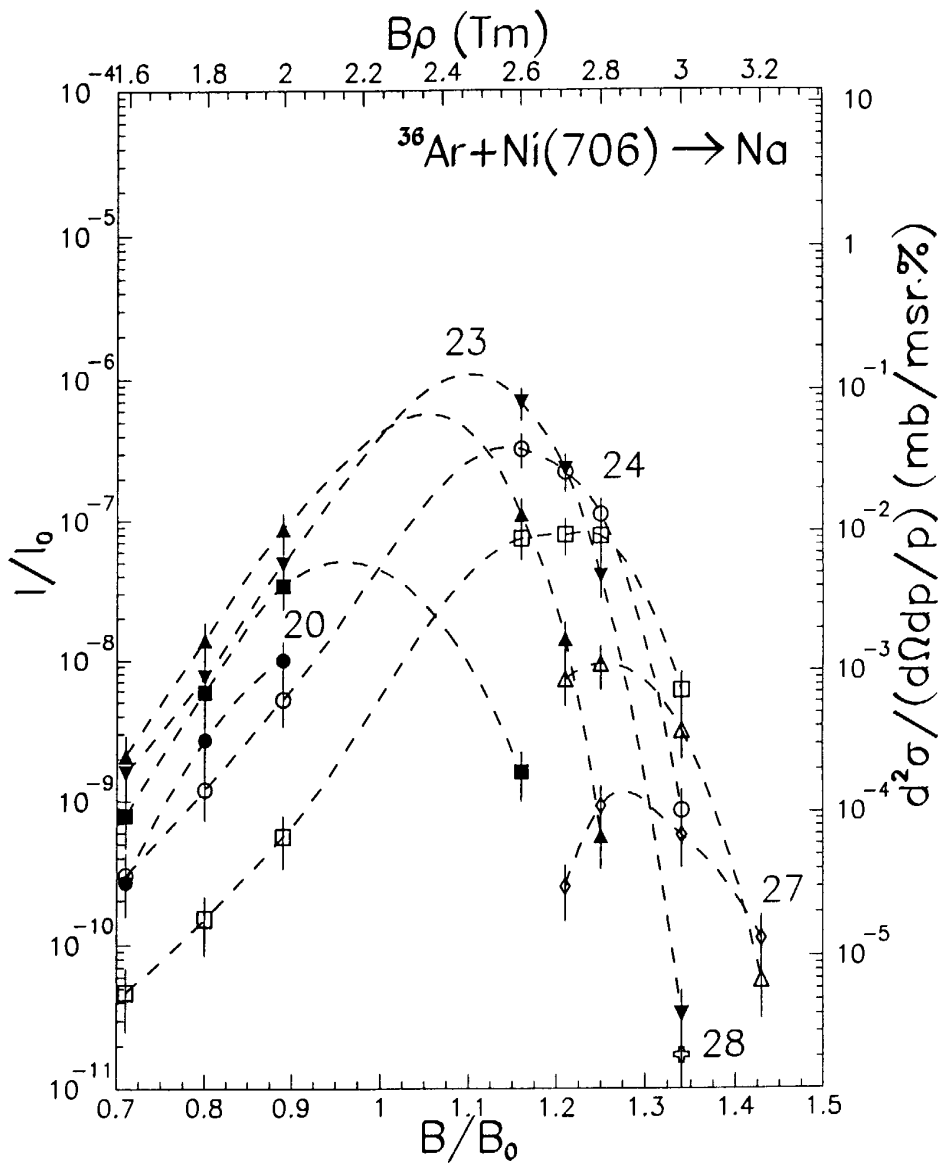

Fig. 11h

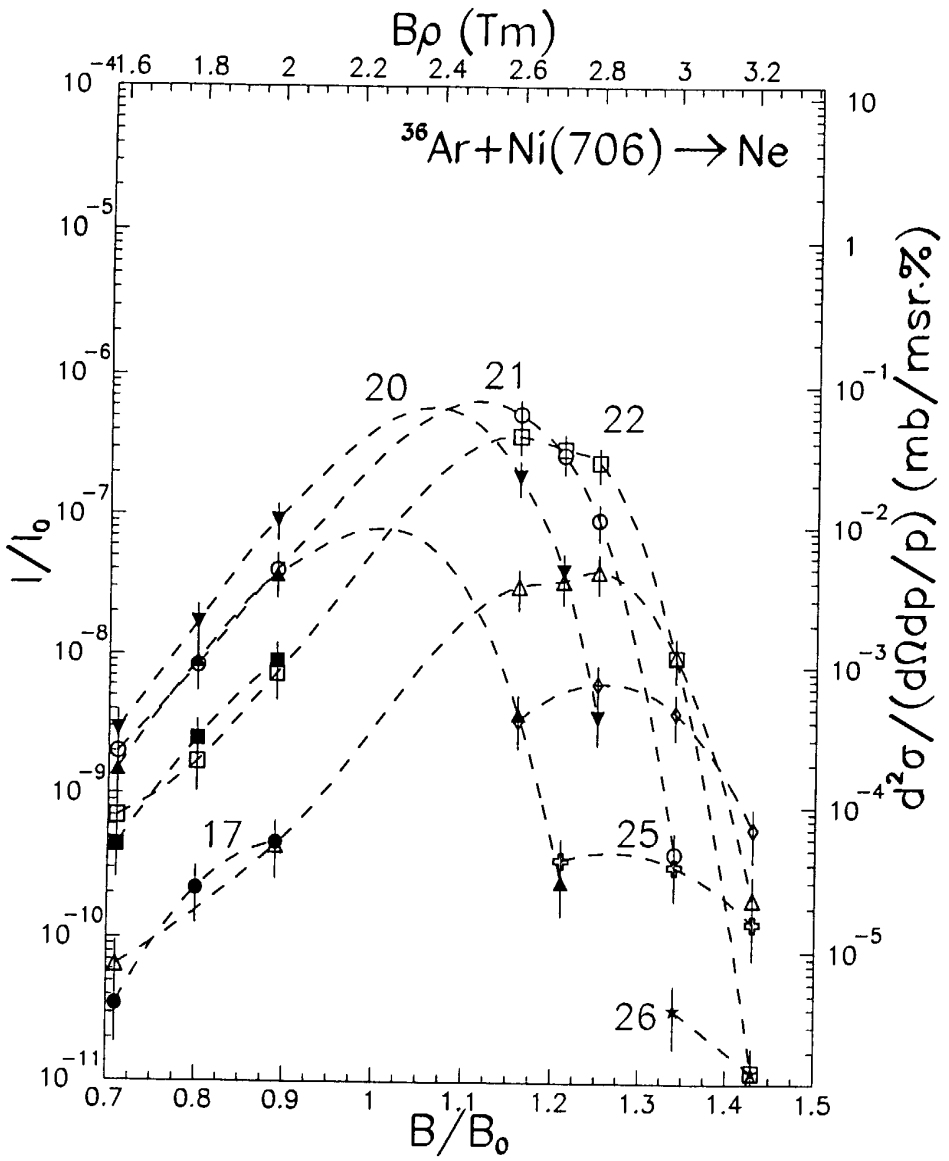

Fig. 11i

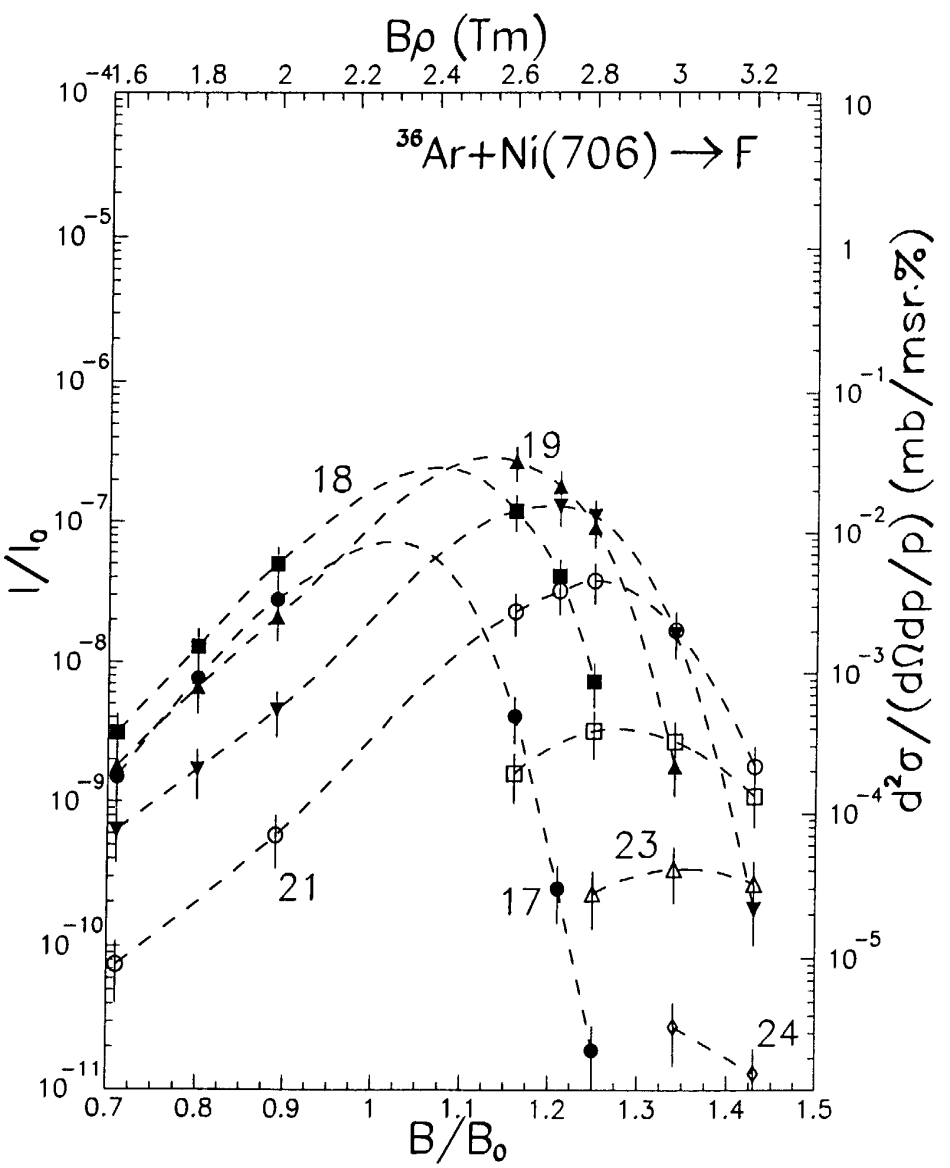

Fig. 11j

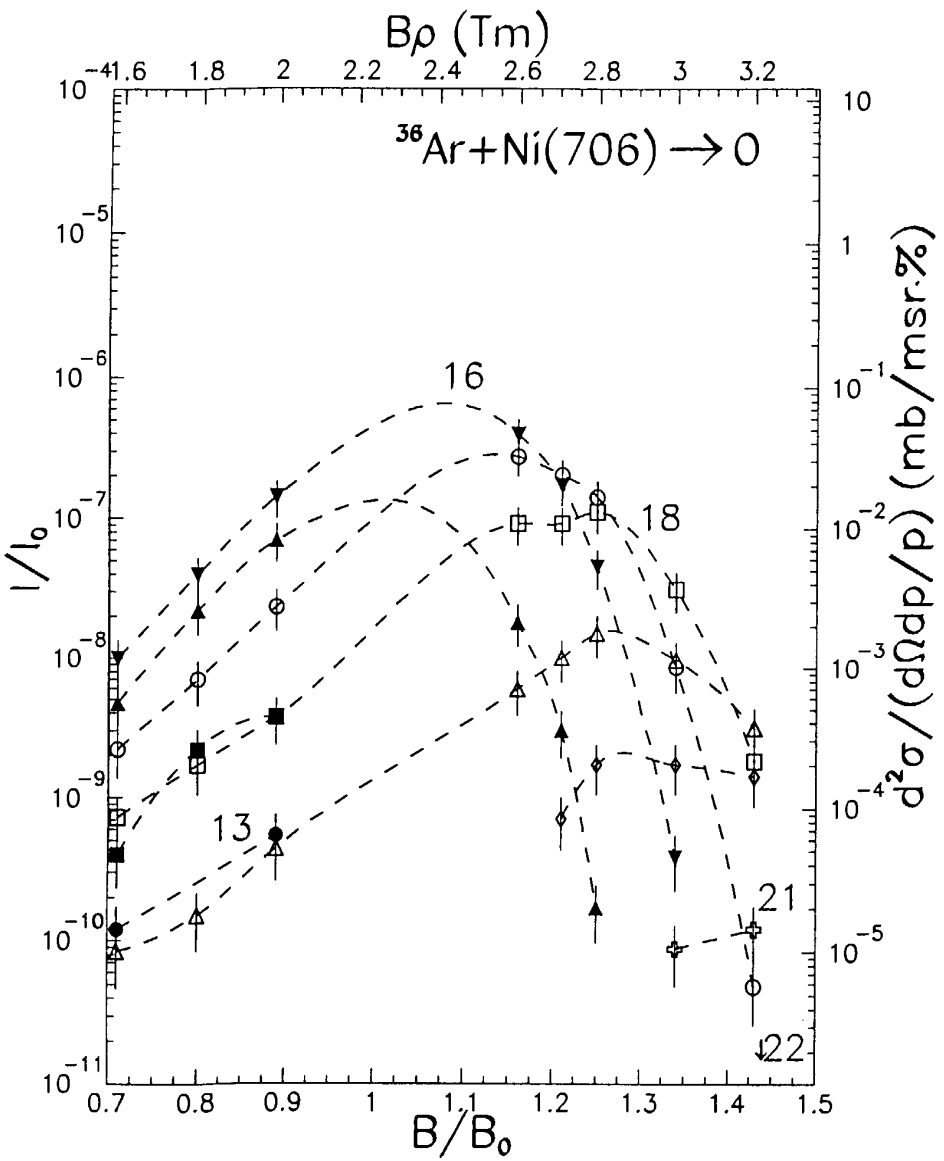

Fig. 11k

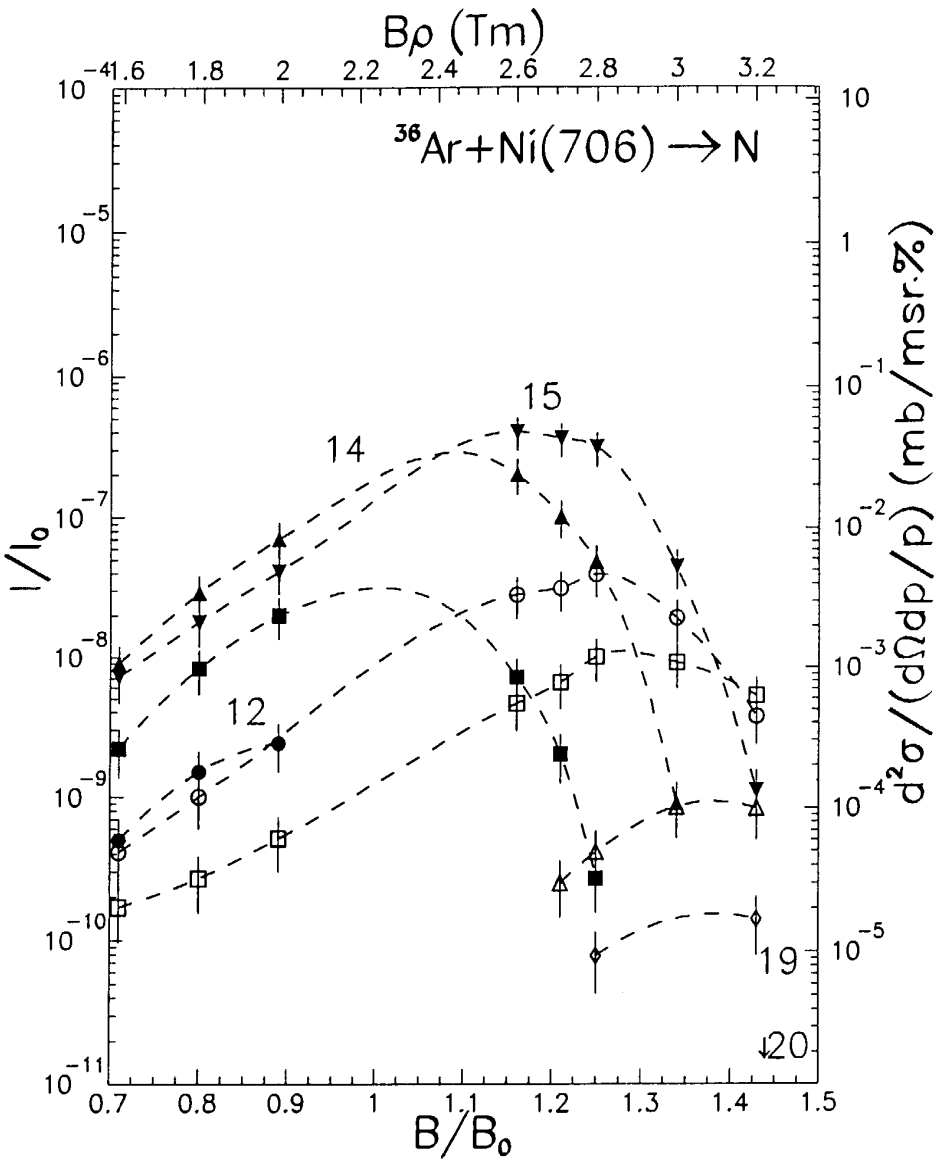

Fig. 11l

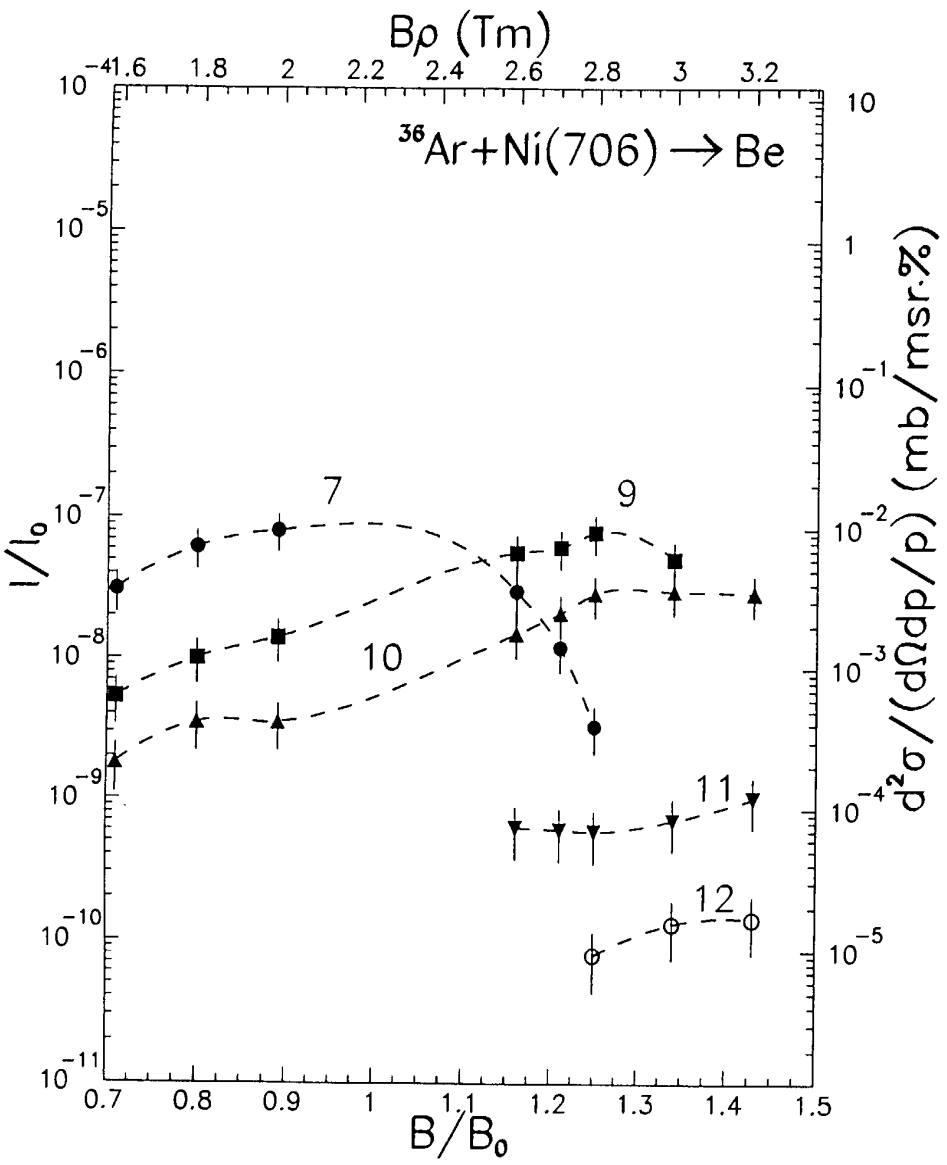

Fig. 11o

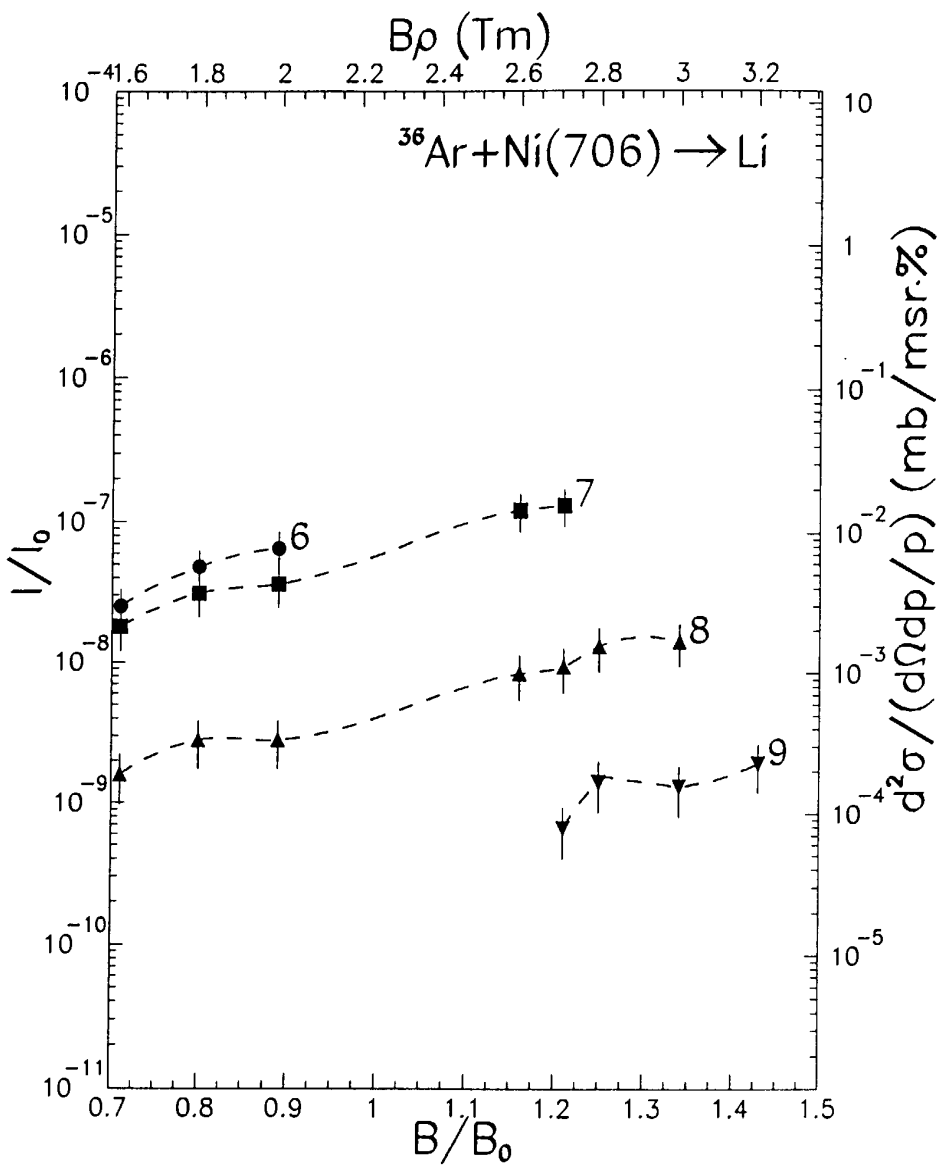

Fig. 11p

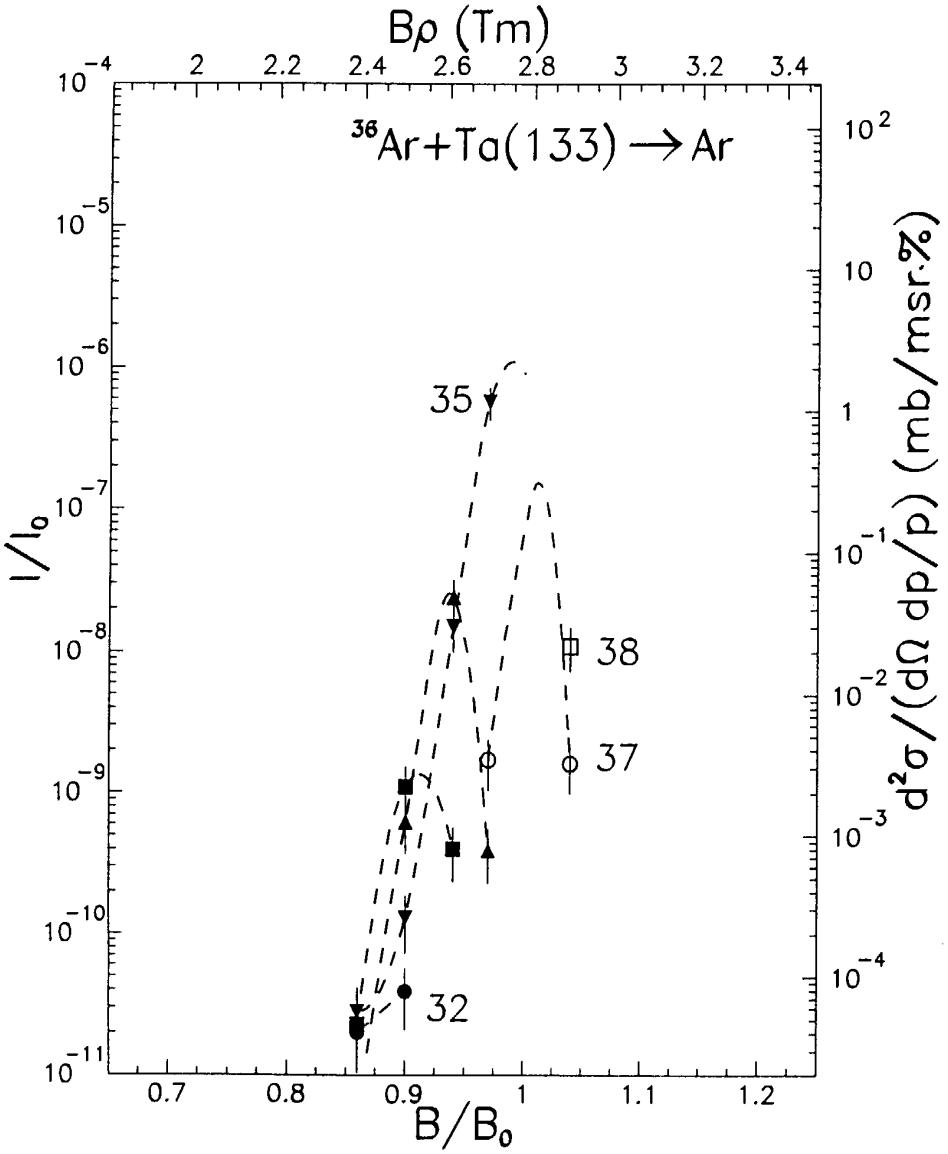

Fig. 12a

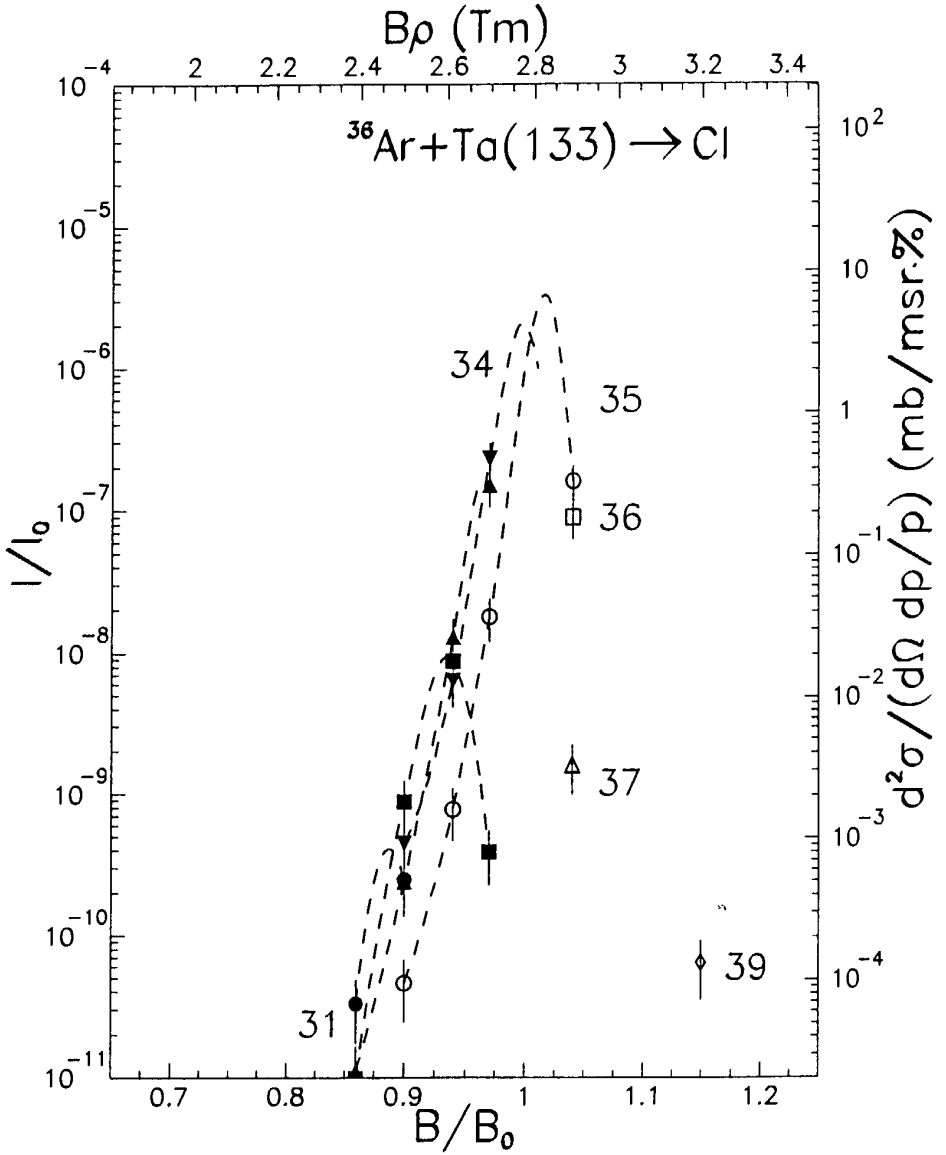

Fig. 12b

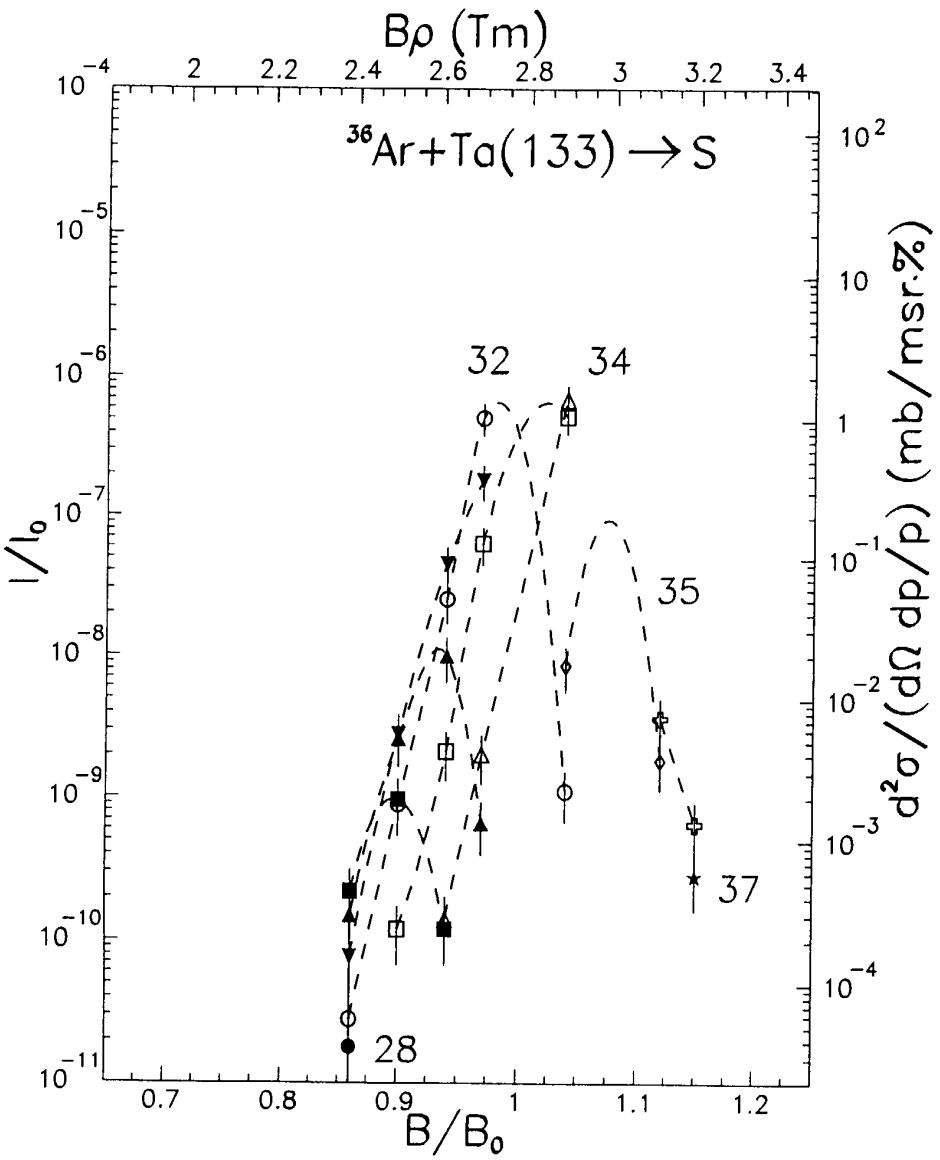

Fig. 12c

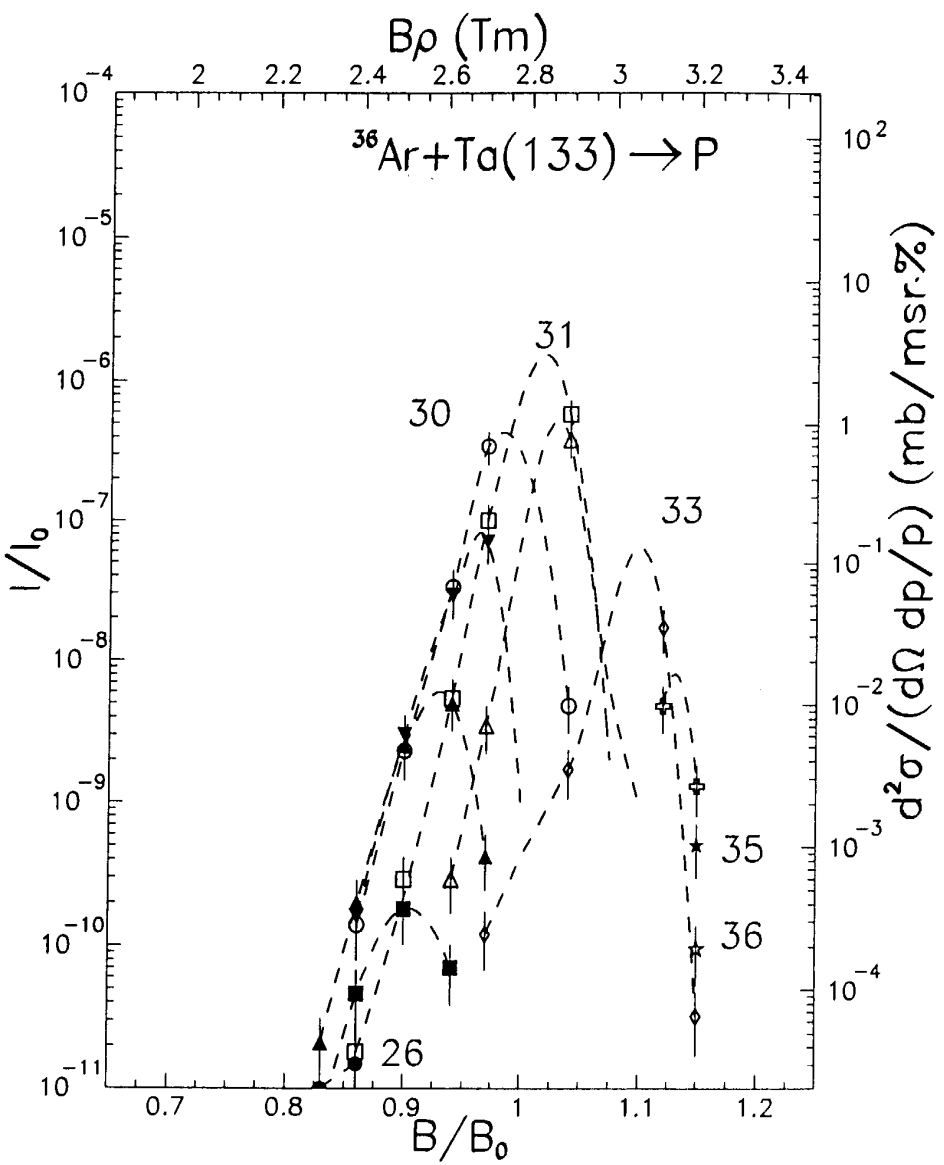

Fig. 12d

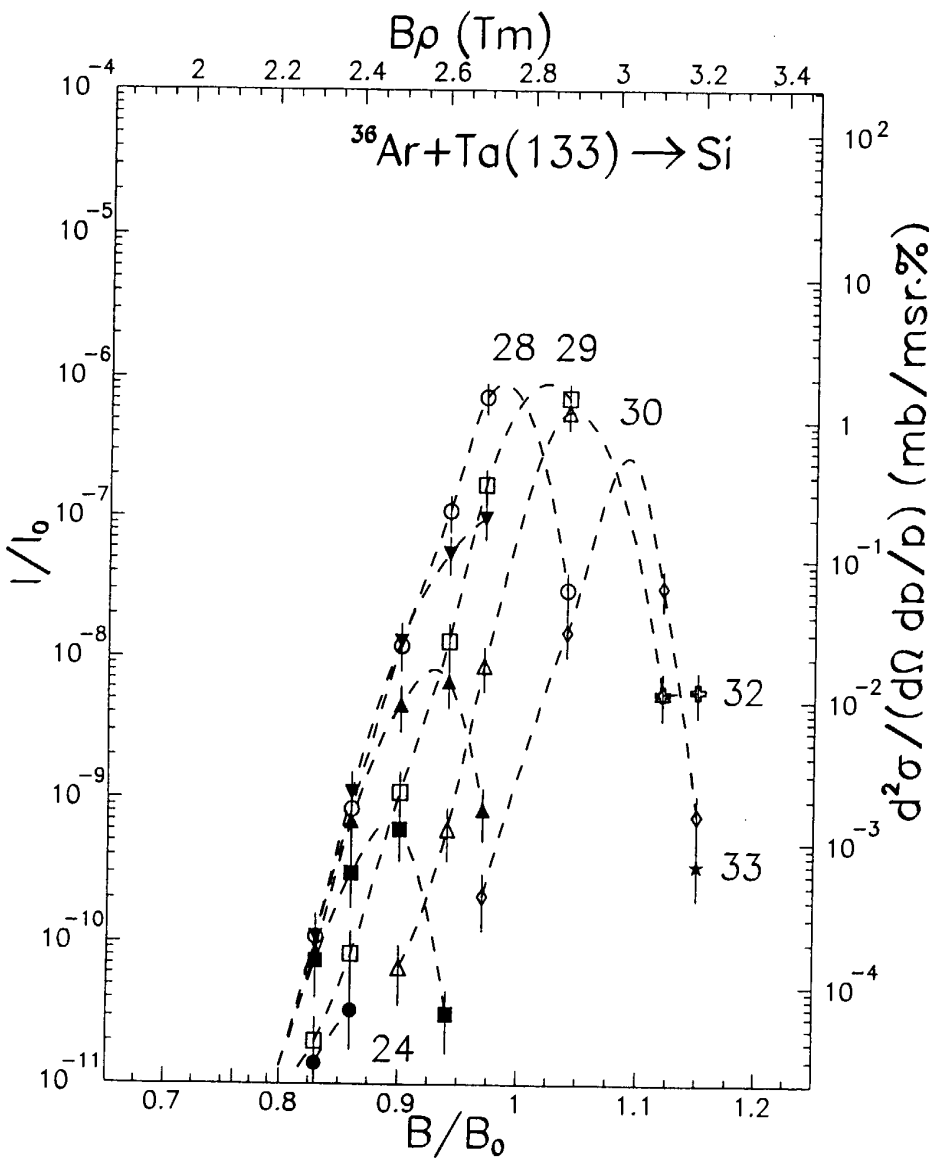

Fig. 12e

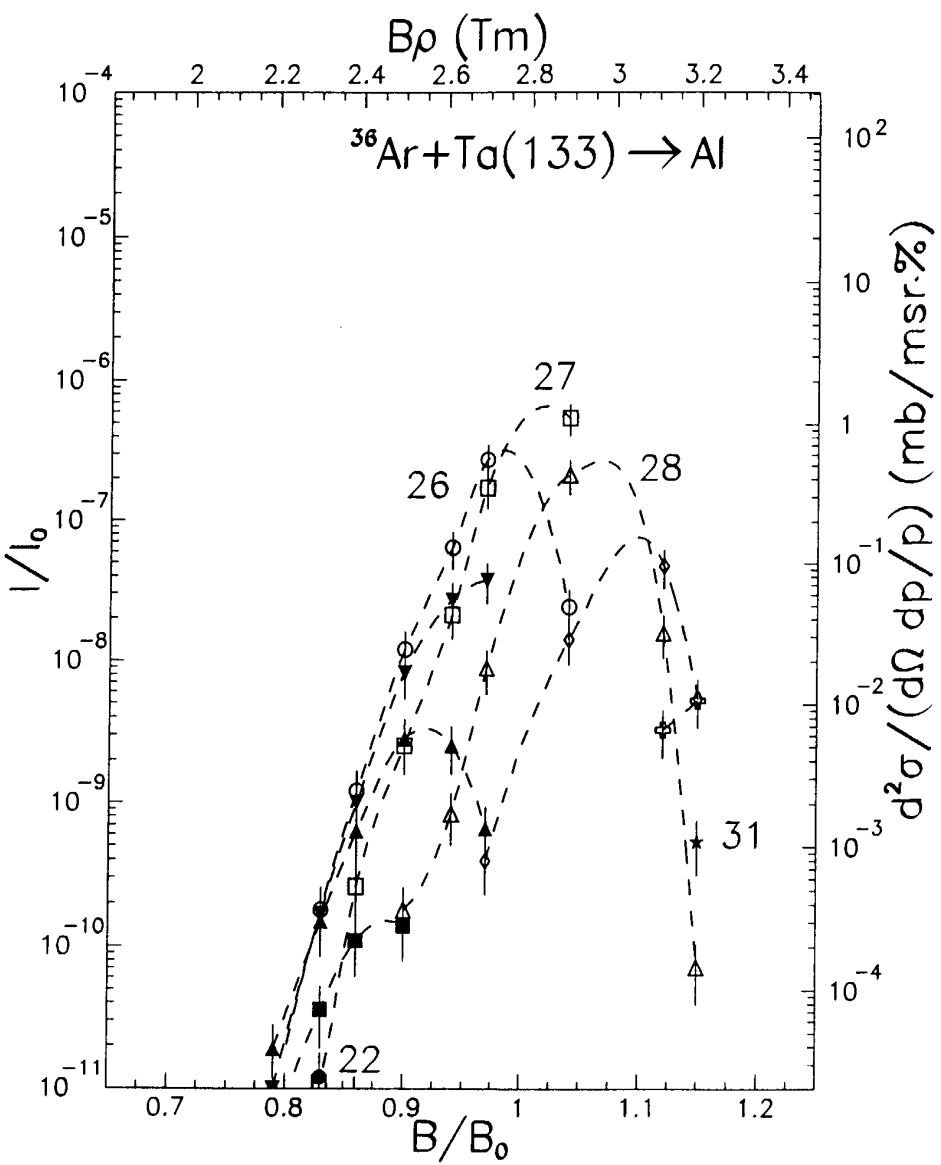

Fig. 12f

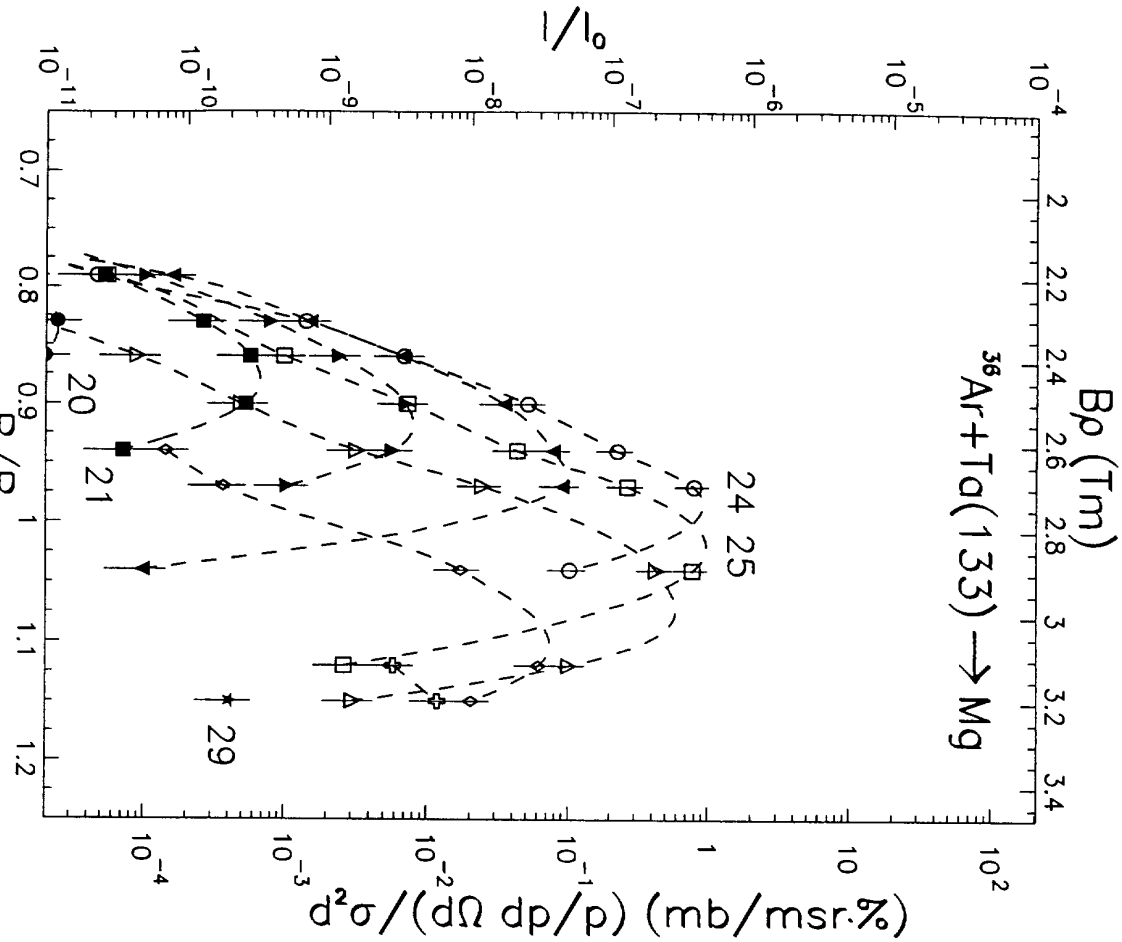

Fig. 12g

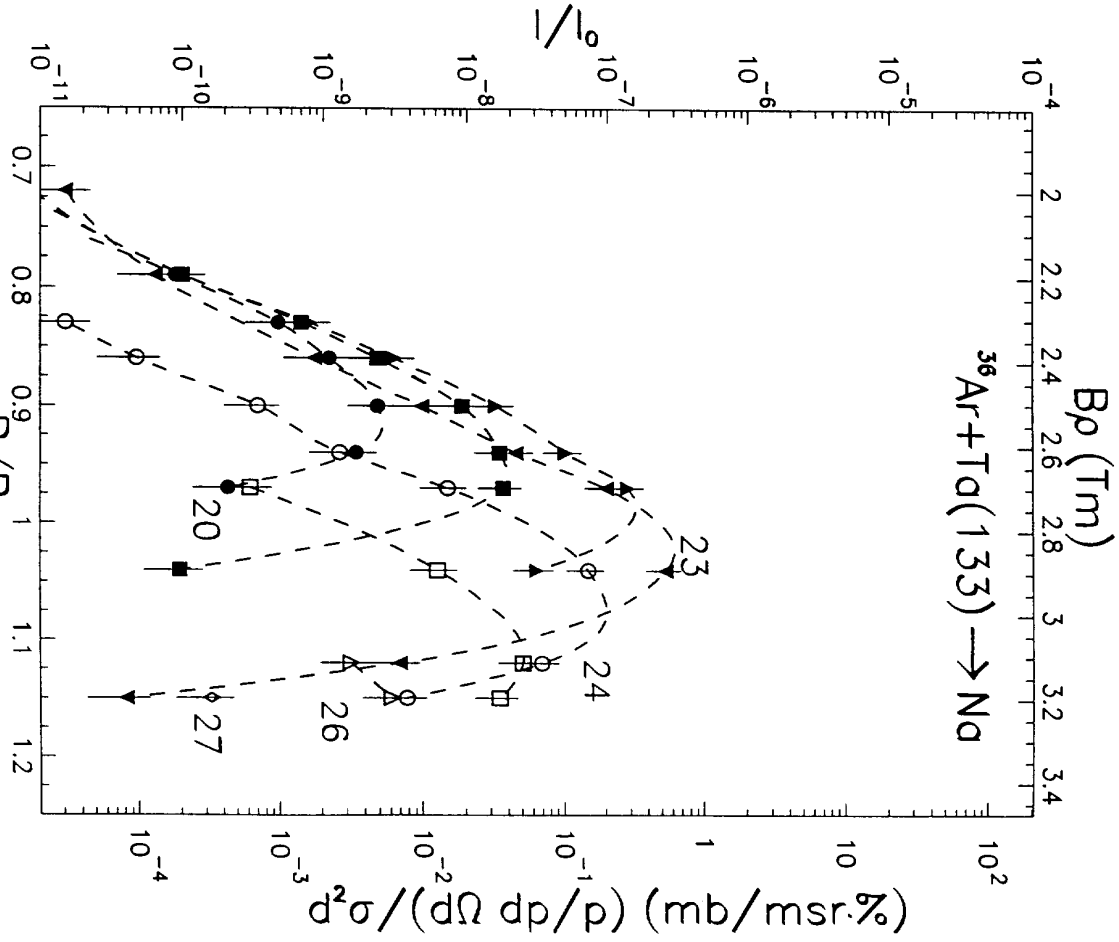

Fig. 12h

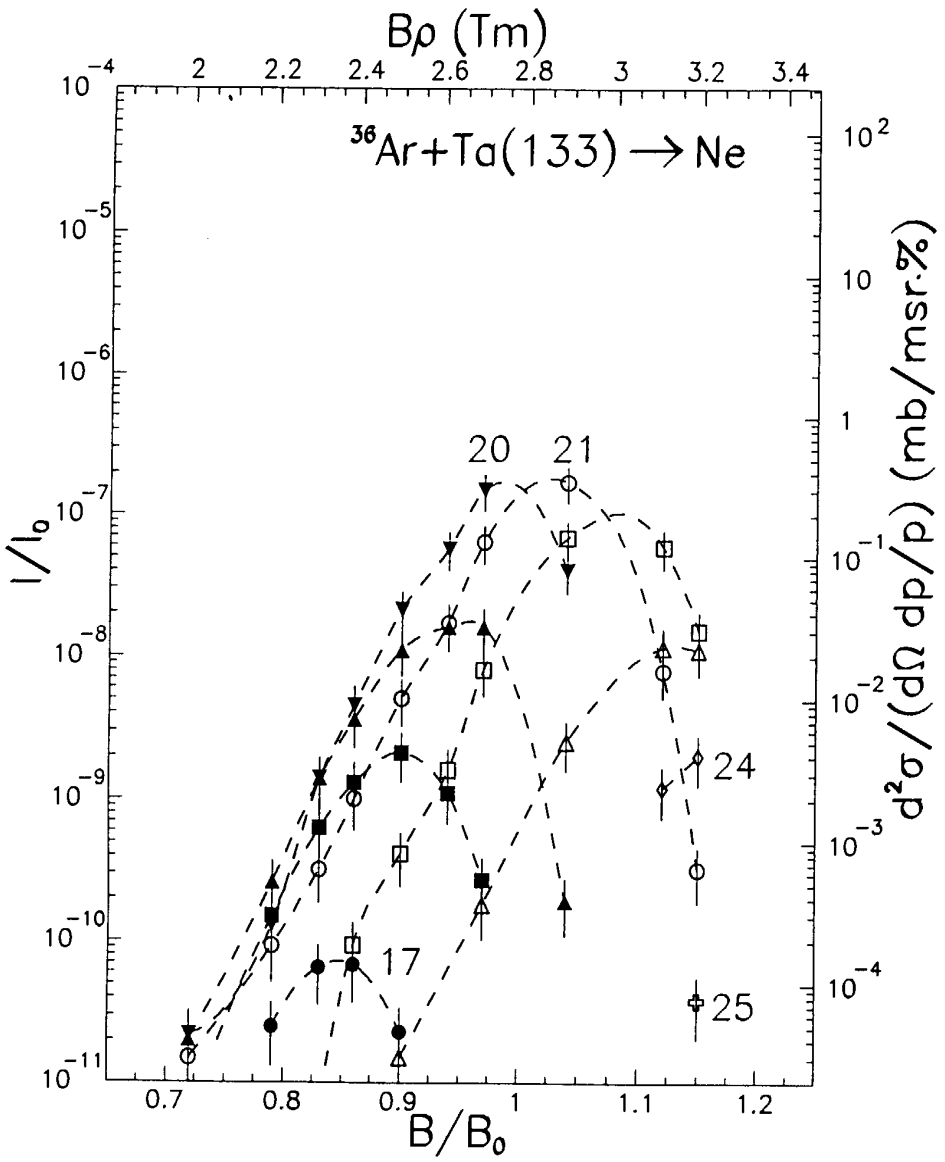

Fig. 12i

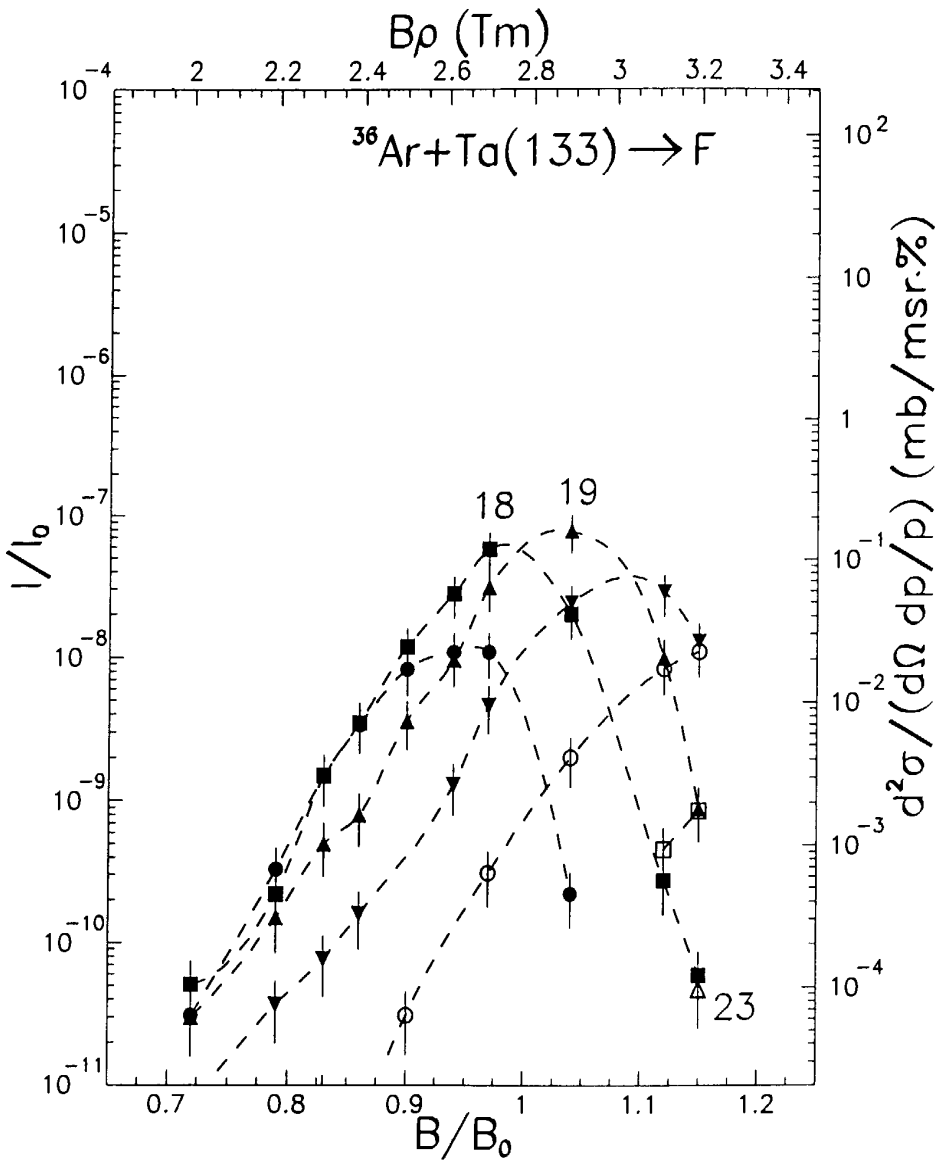

Fig. 12j

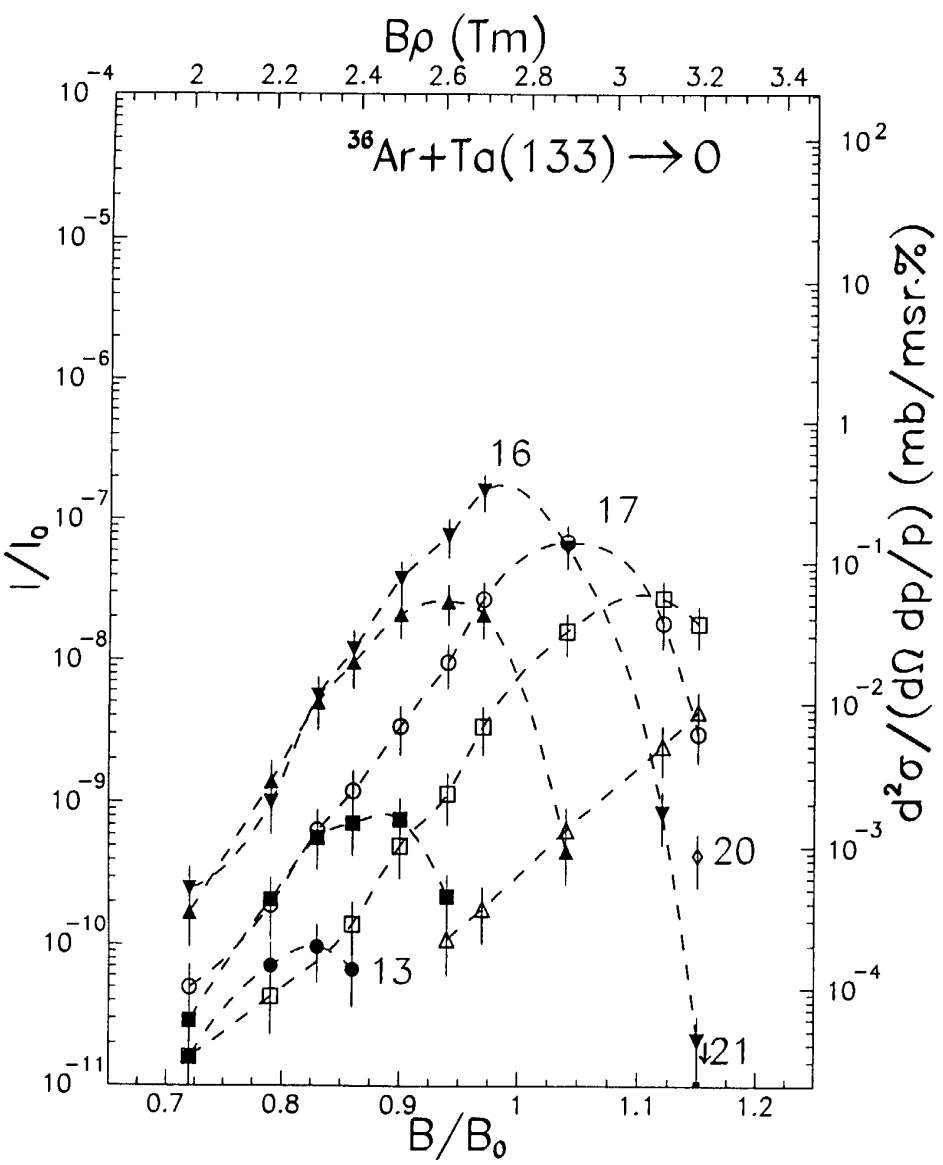

Fig. 12k

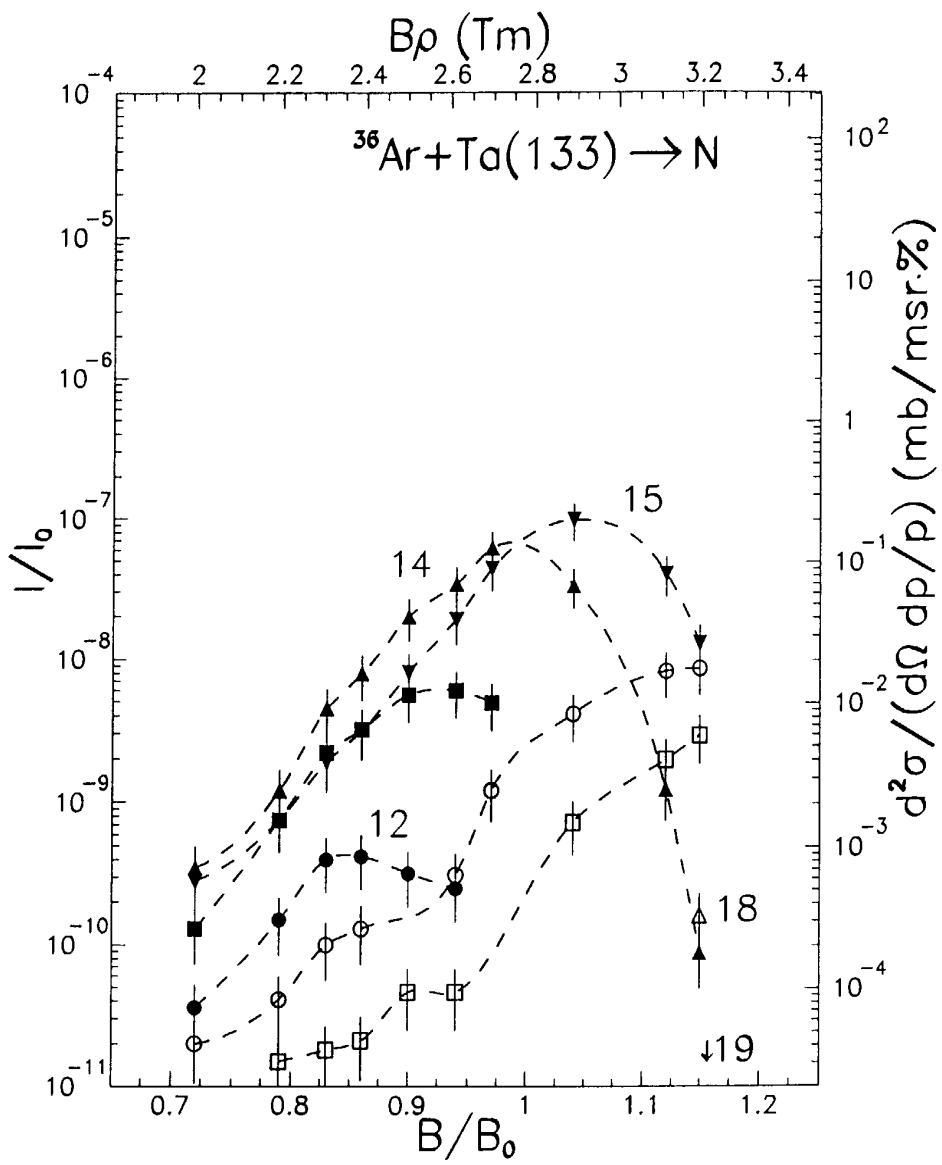

Fig. 12l

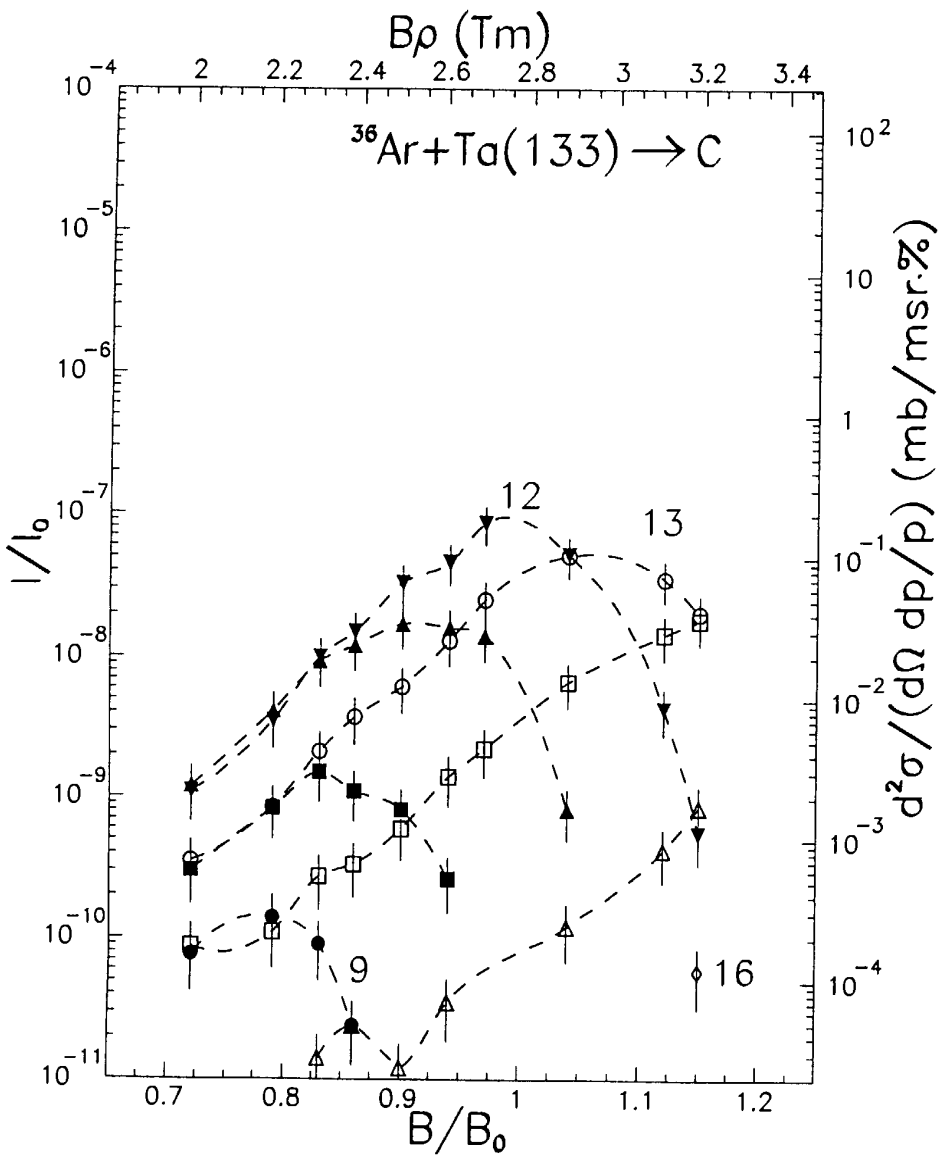

Fig. 12m

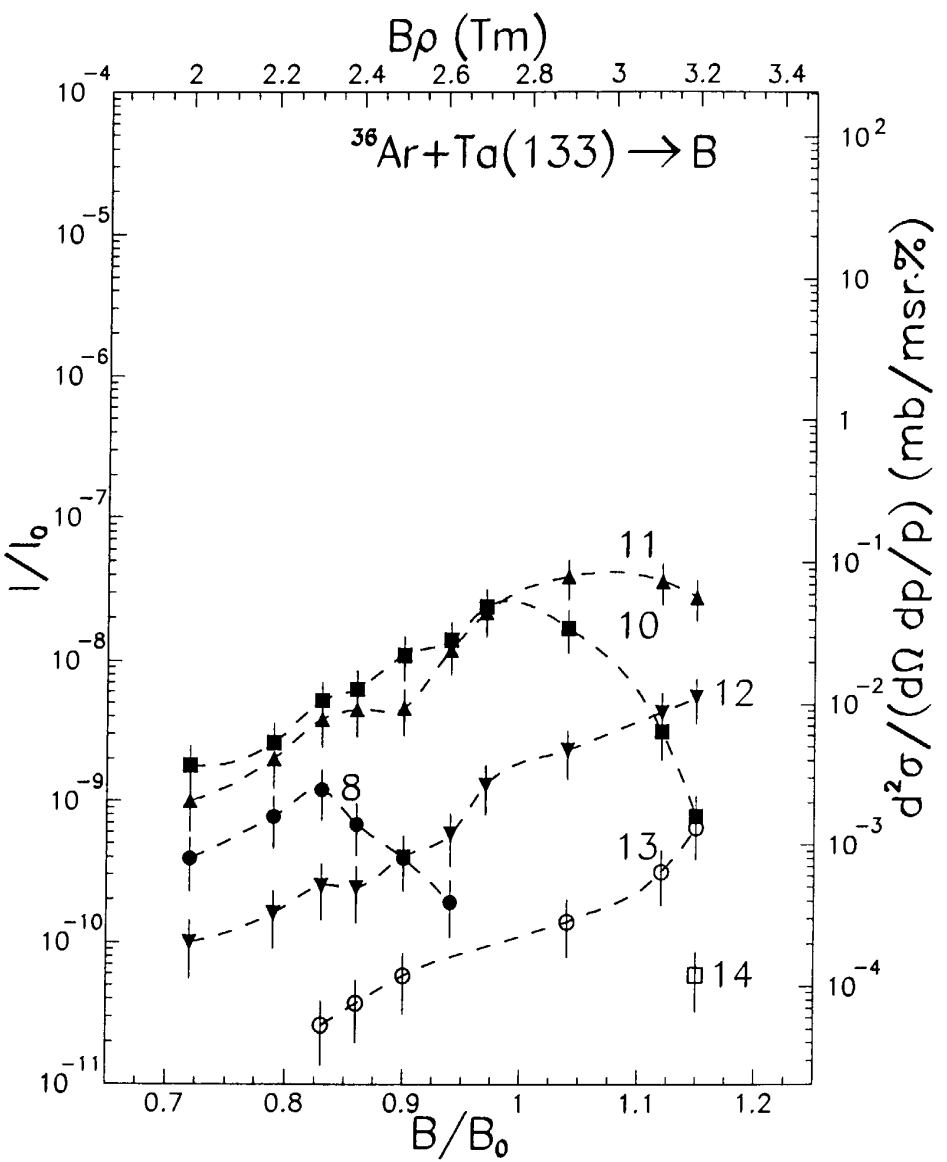

Fig. 12n

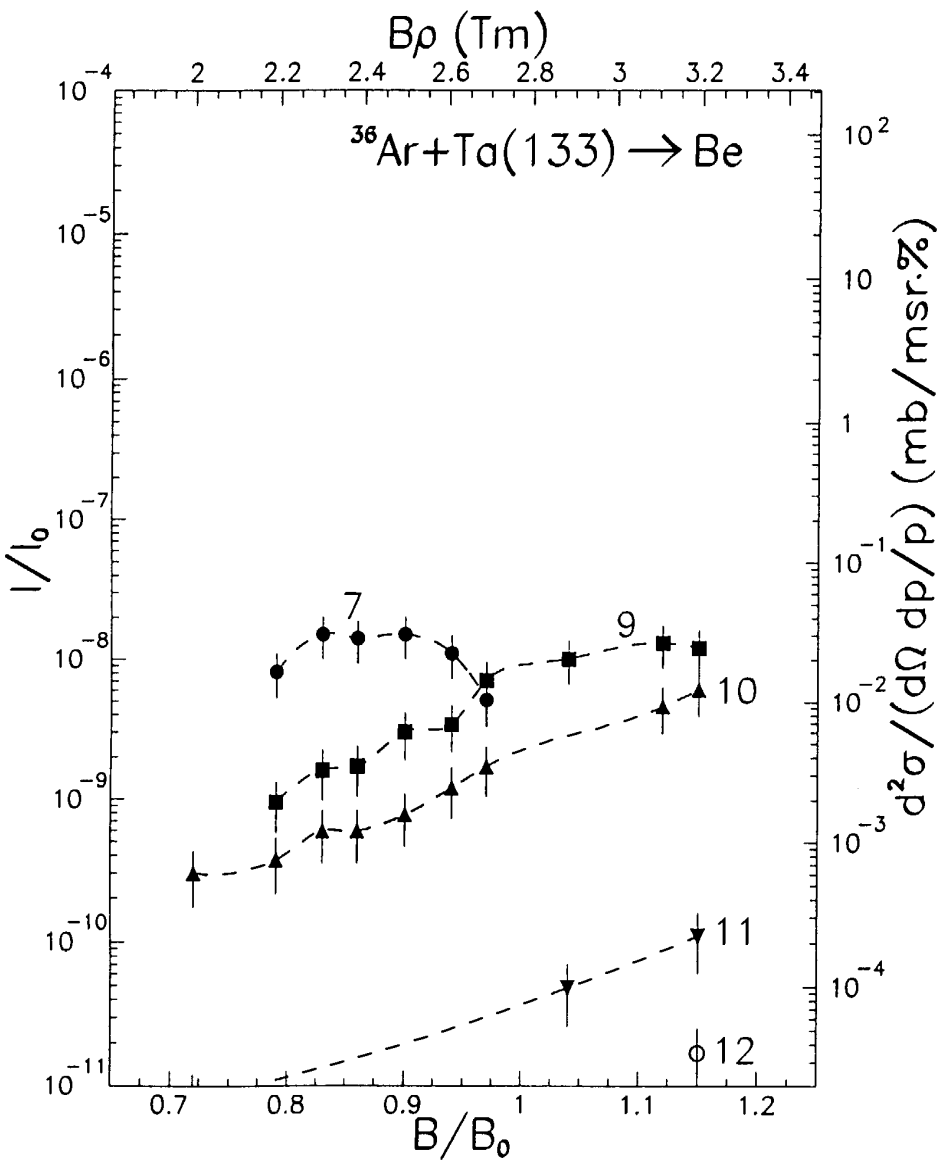

Fig. 12o

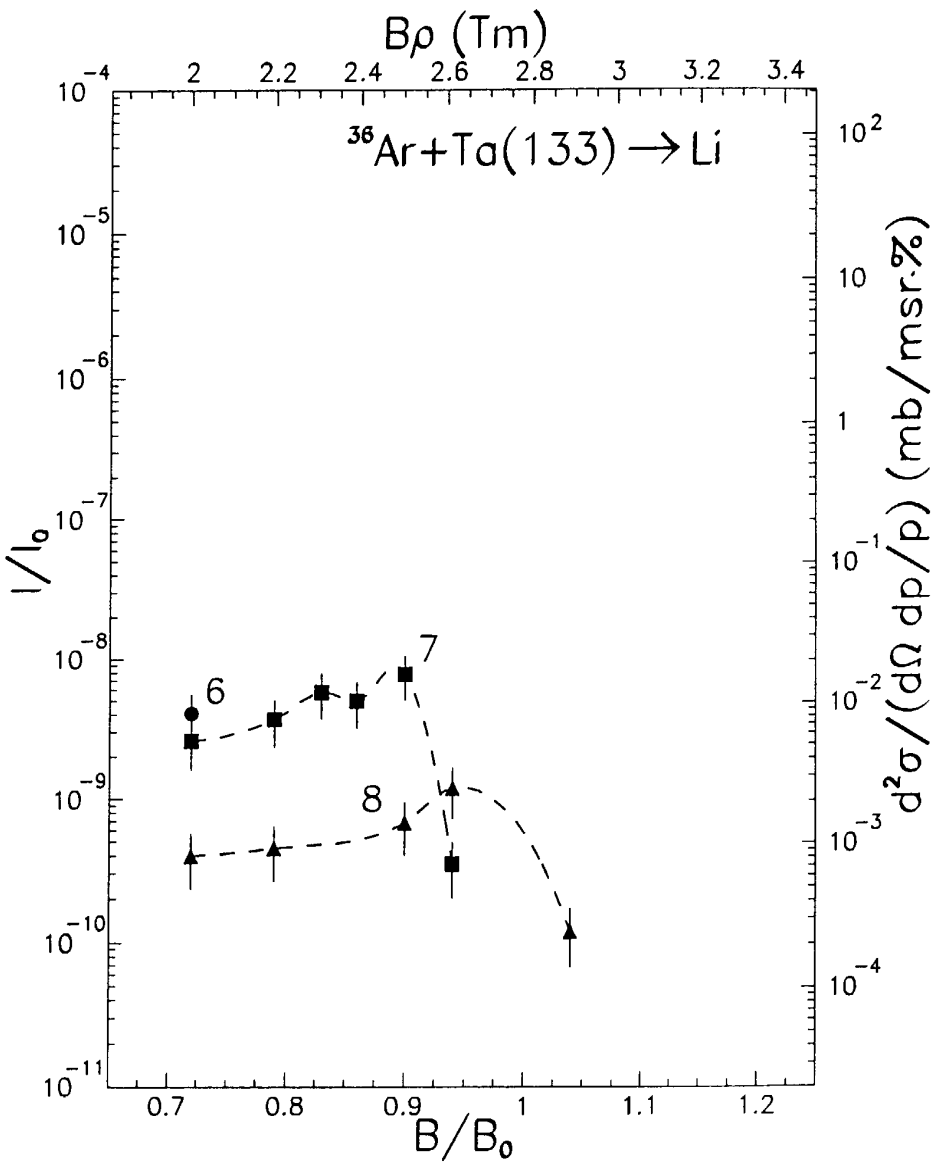

Fig. 12p

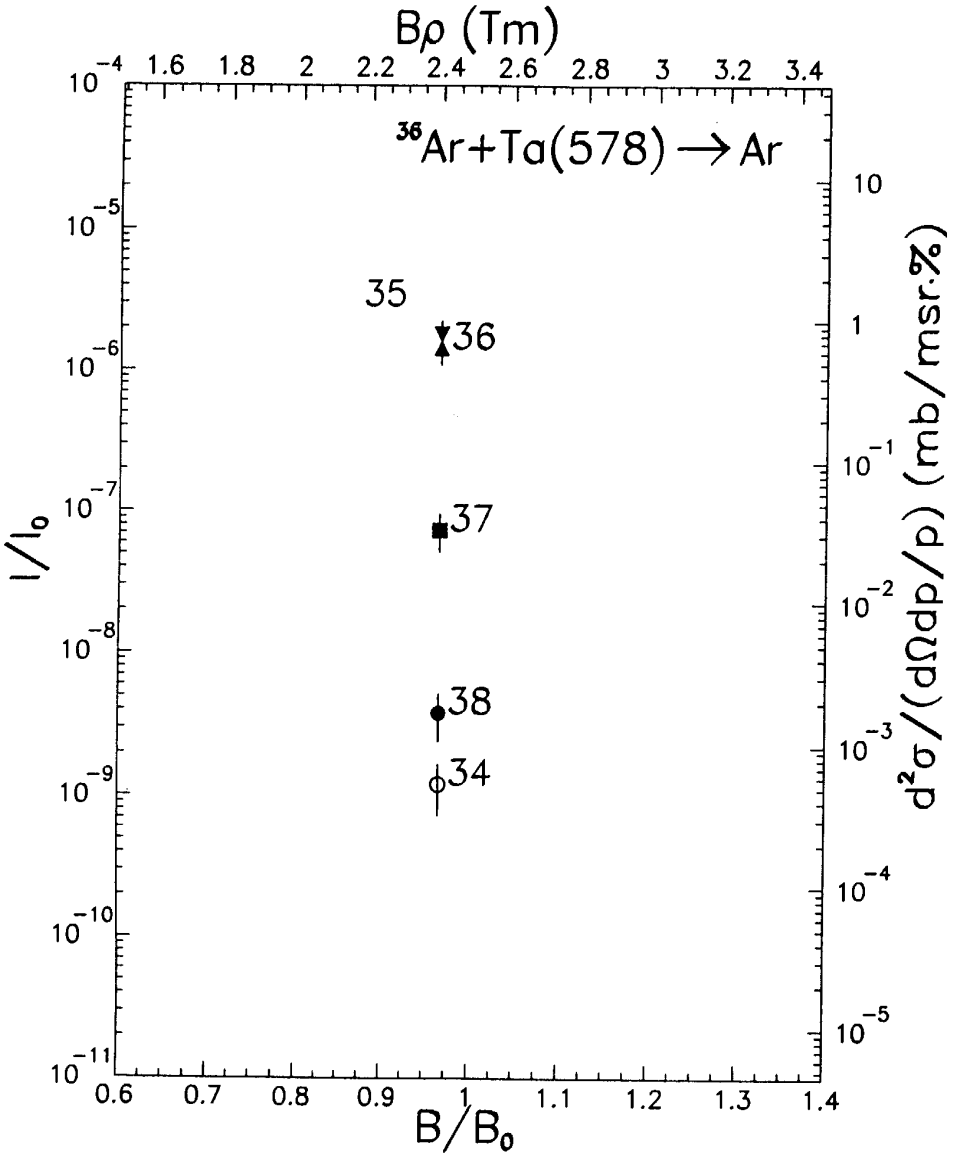

Fig. 13a

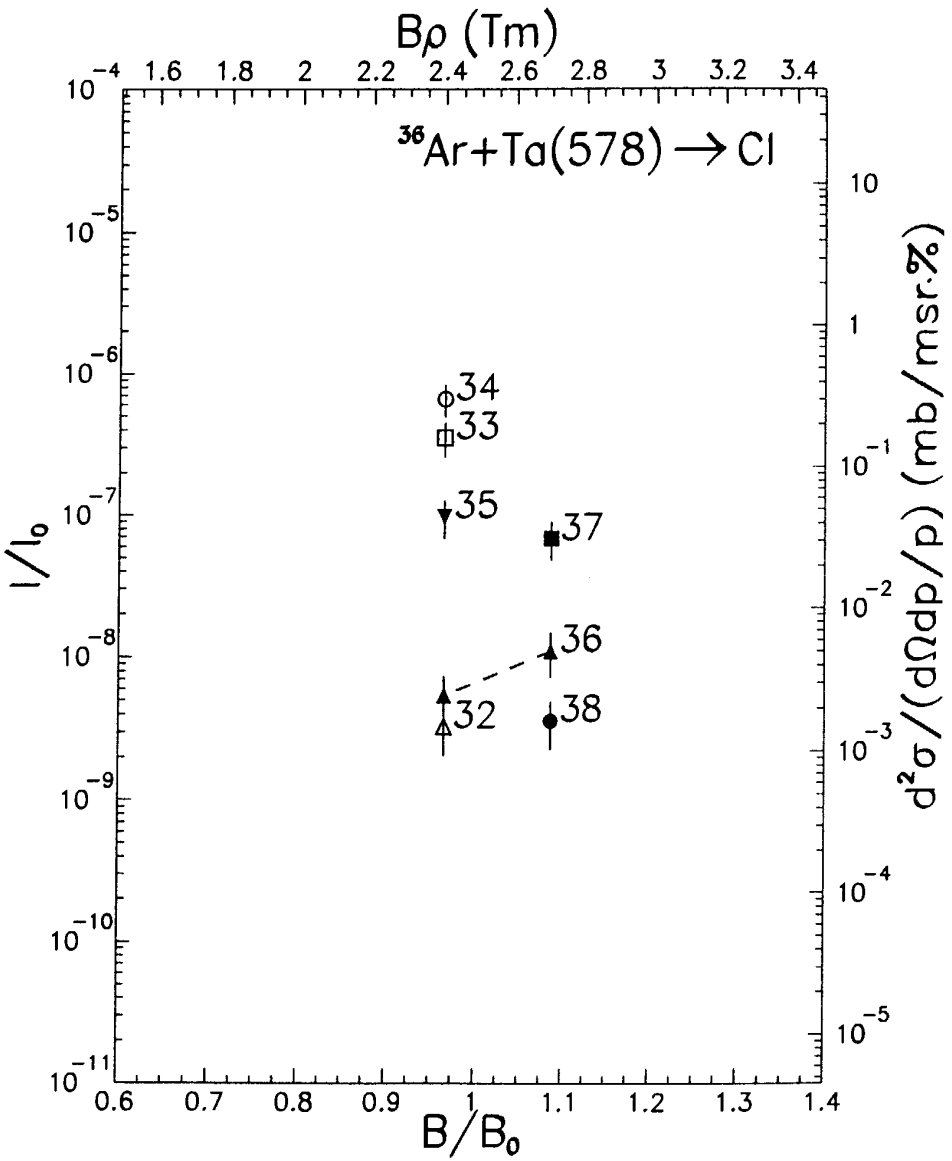

Fig. 13b

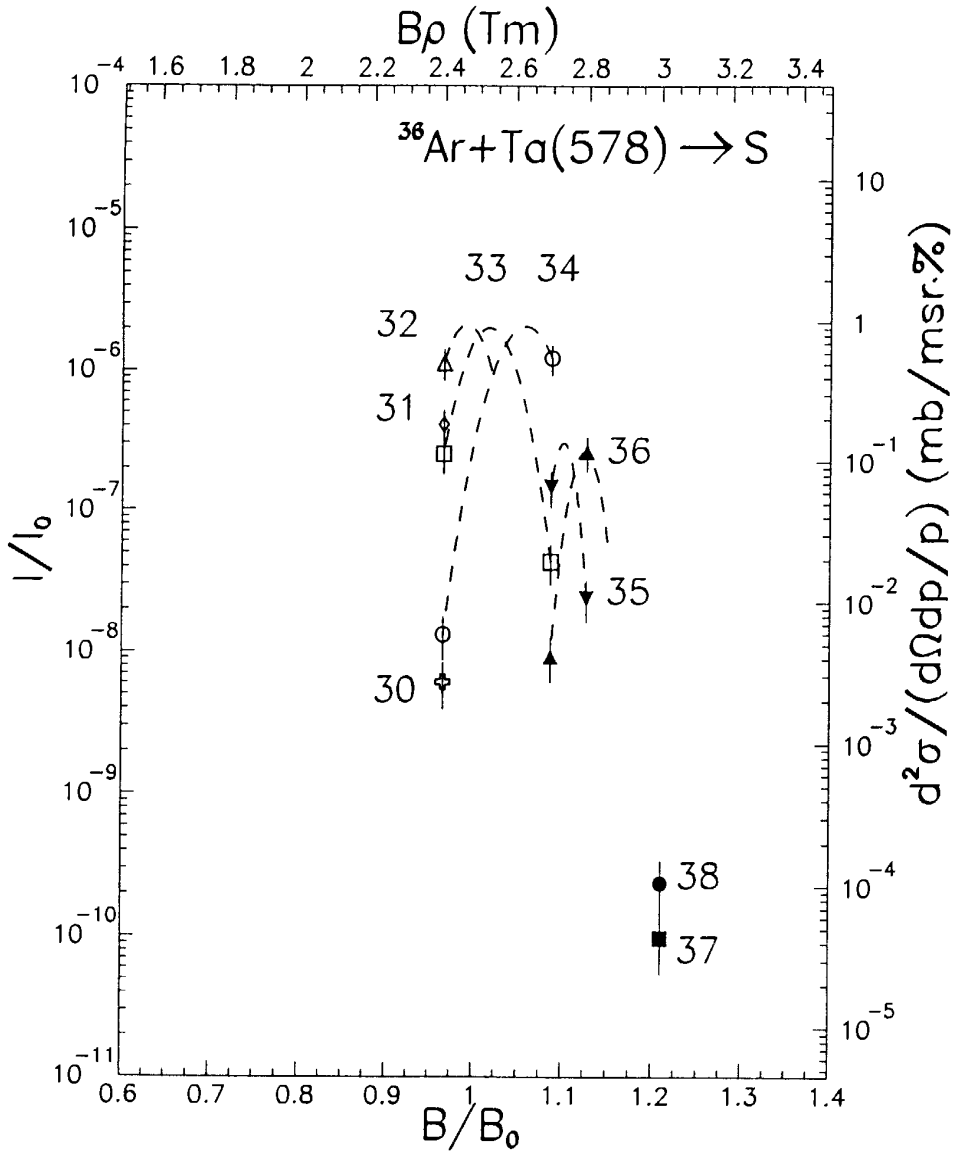

Fig. 13c

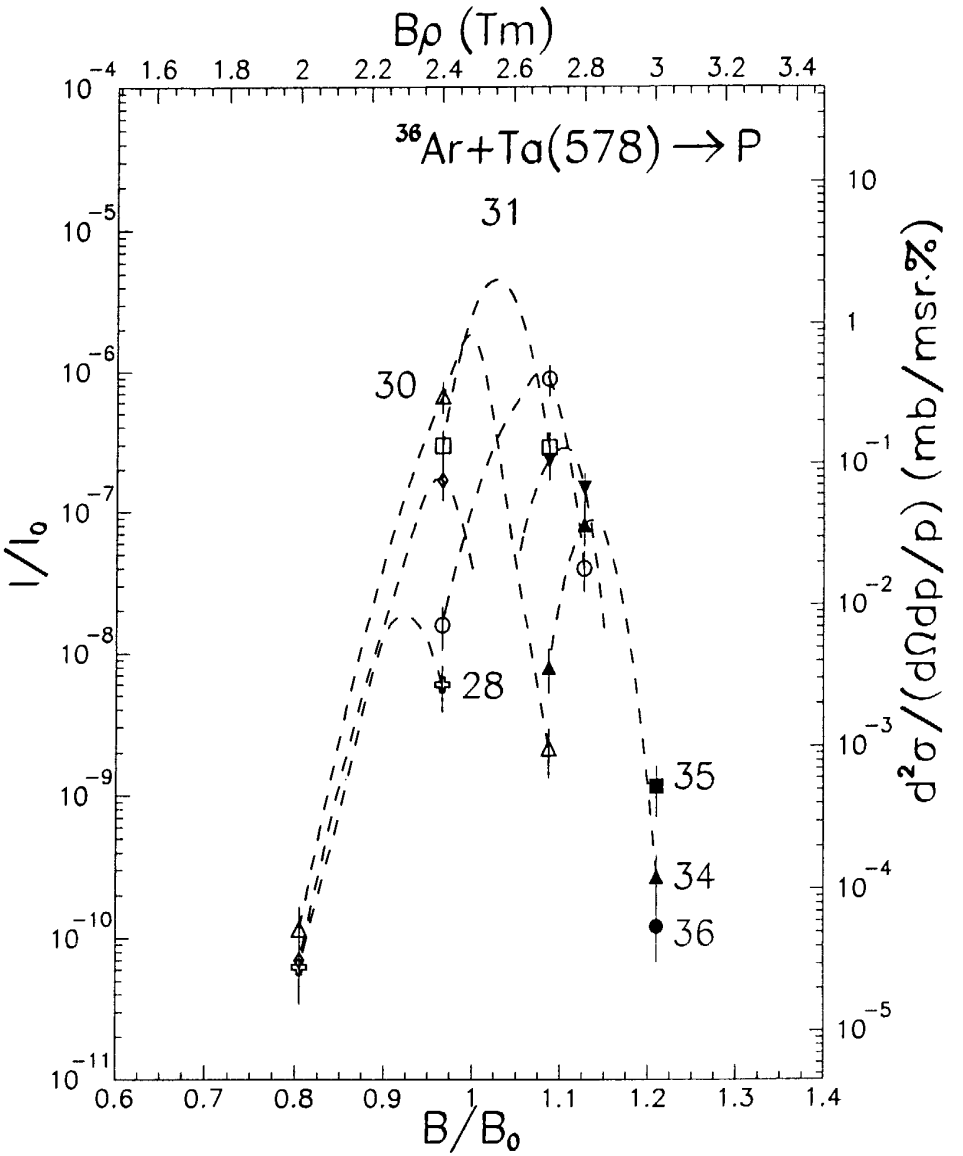

Fig. 13d

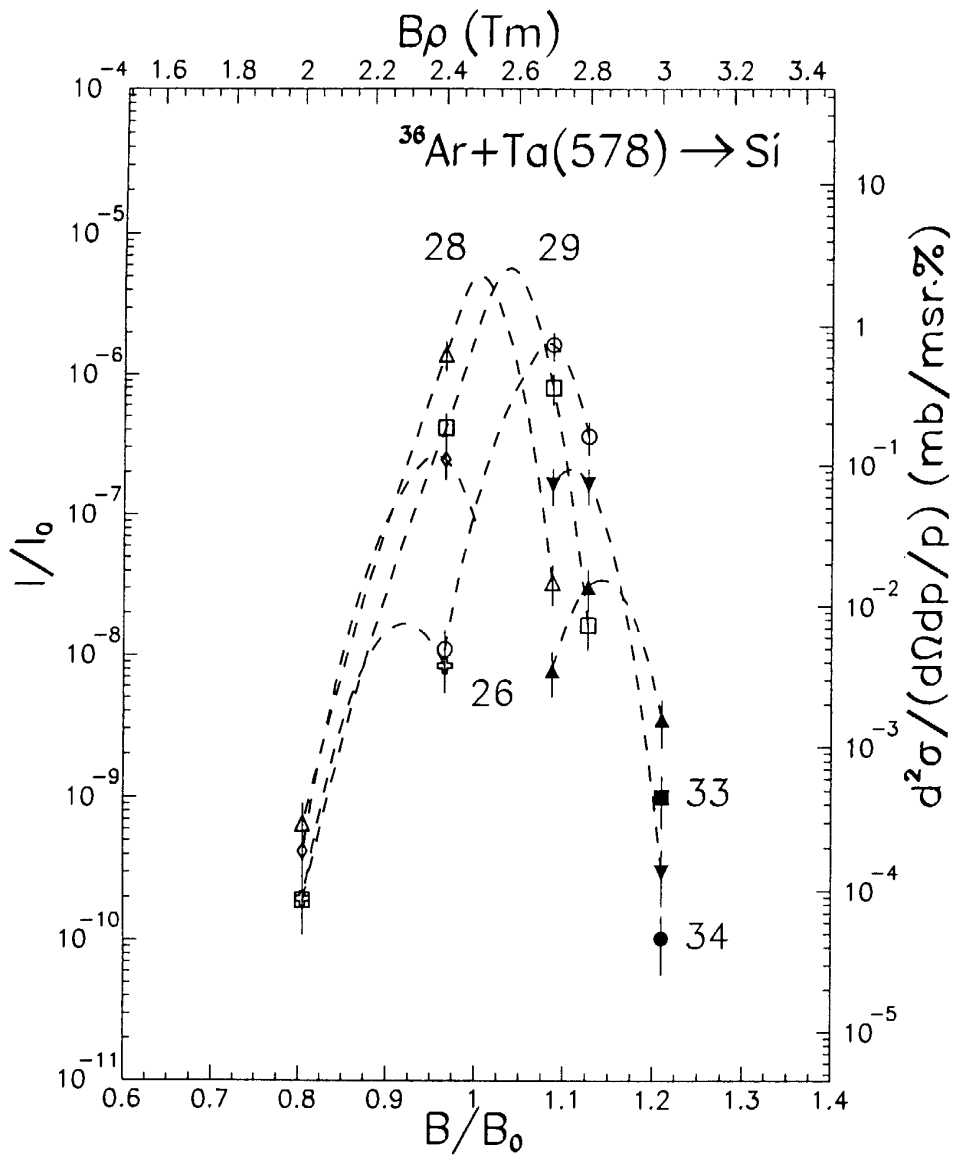

Fig.13e

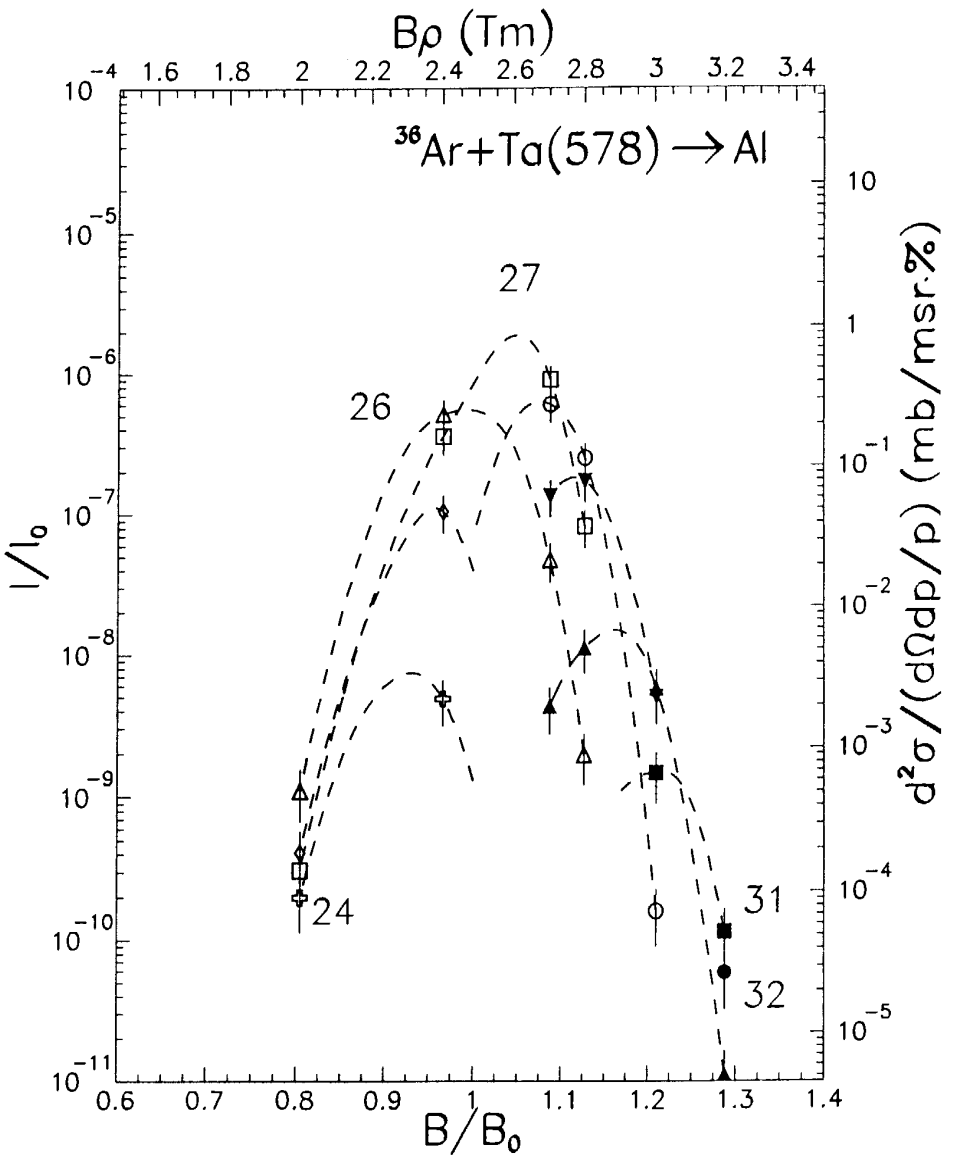

Fig.137f

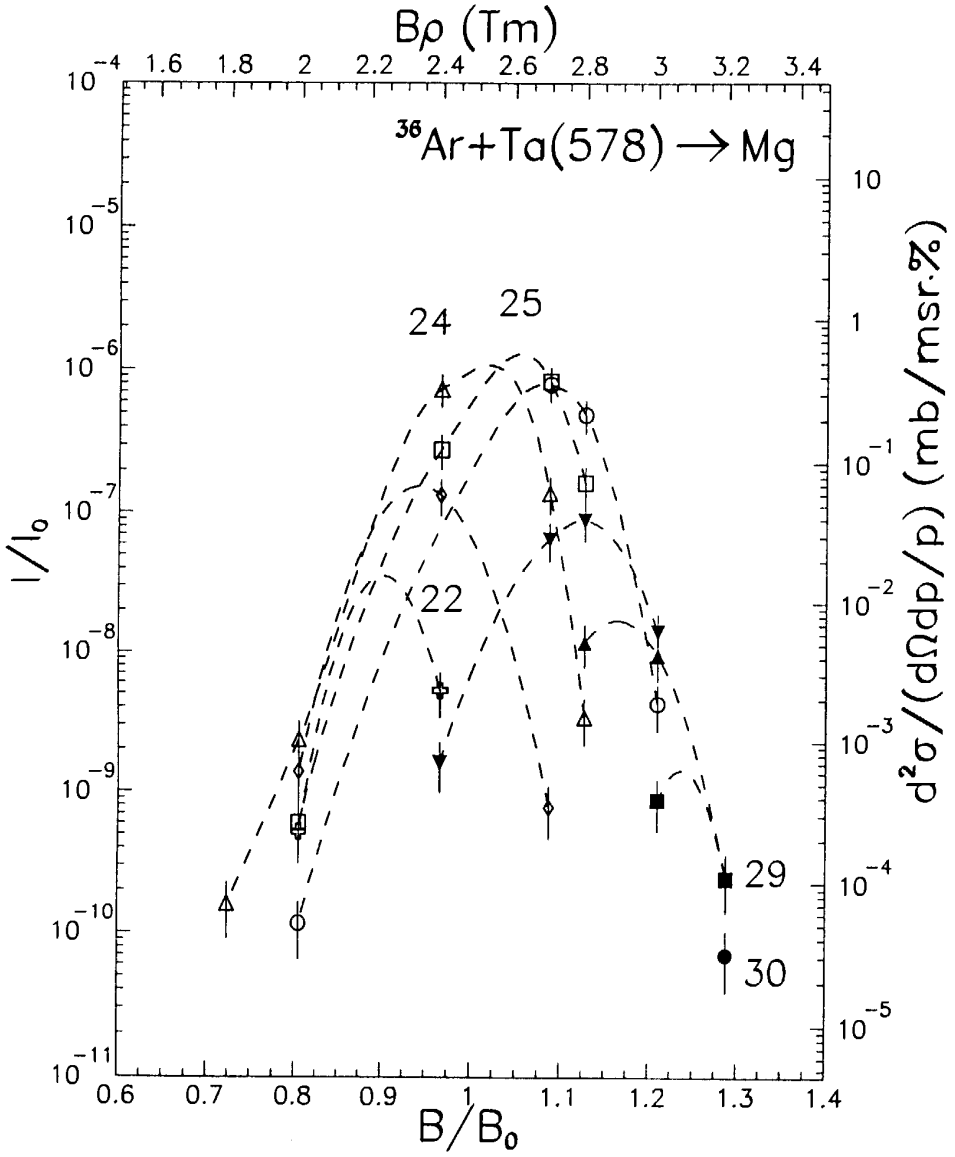

Fig.13g

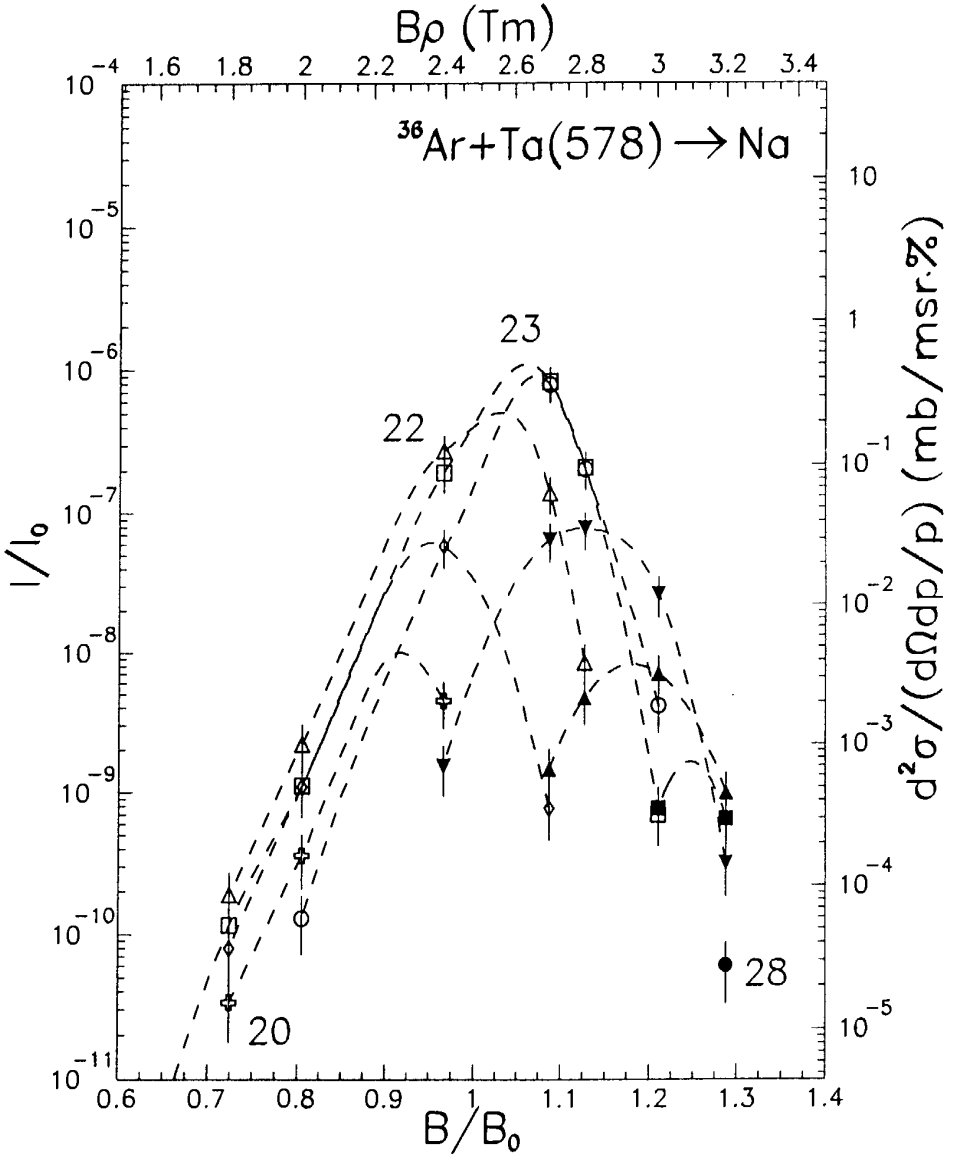

Fig. 13h

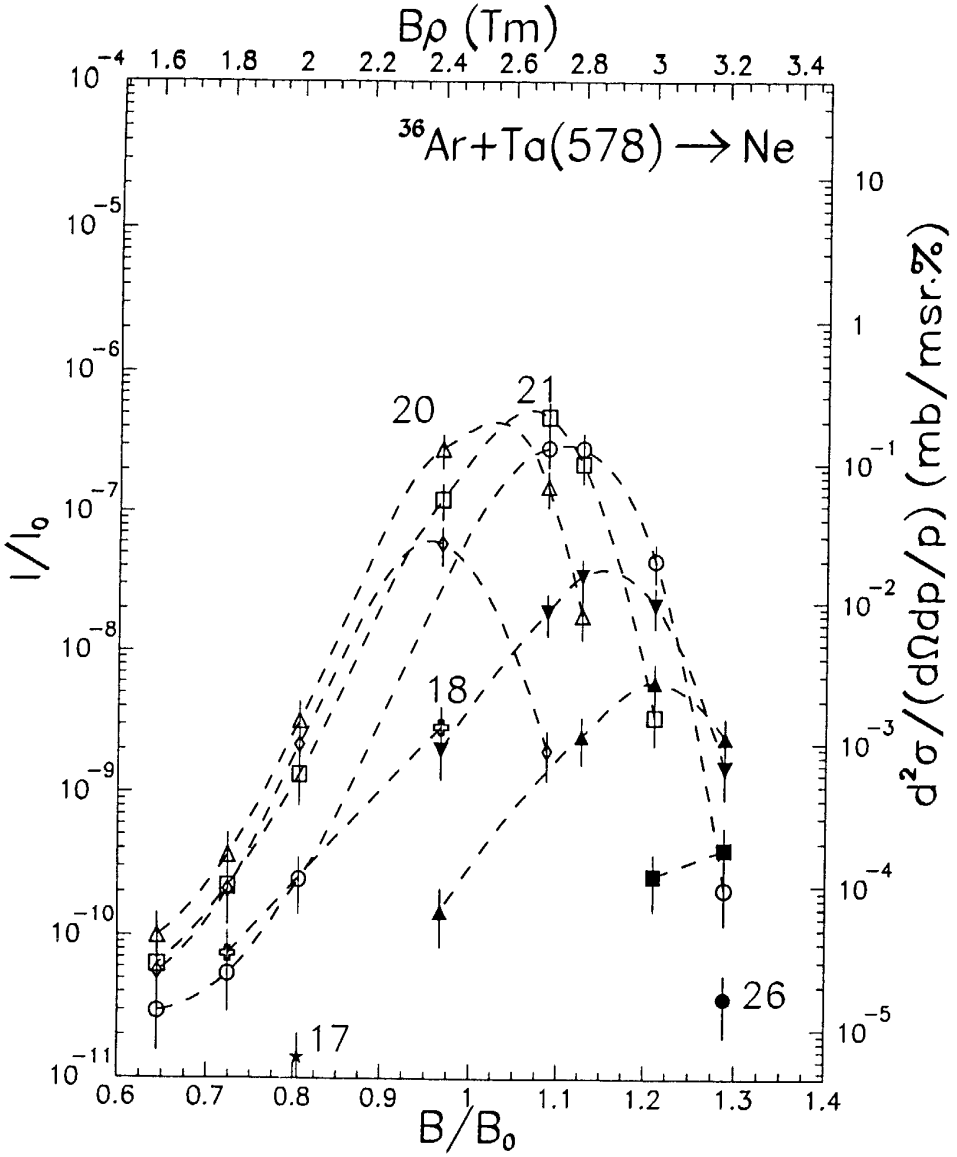

Fig. 13i

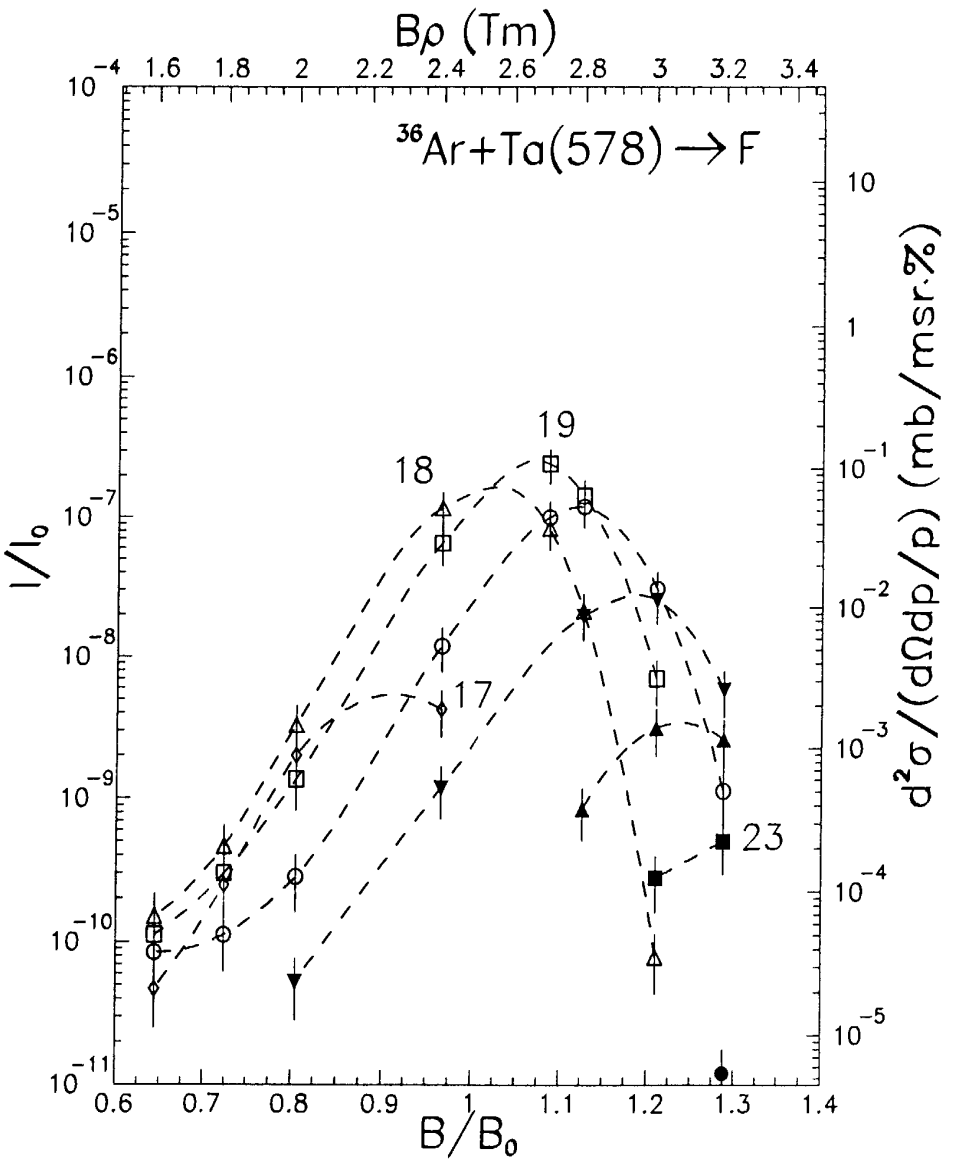

Fig. 13j

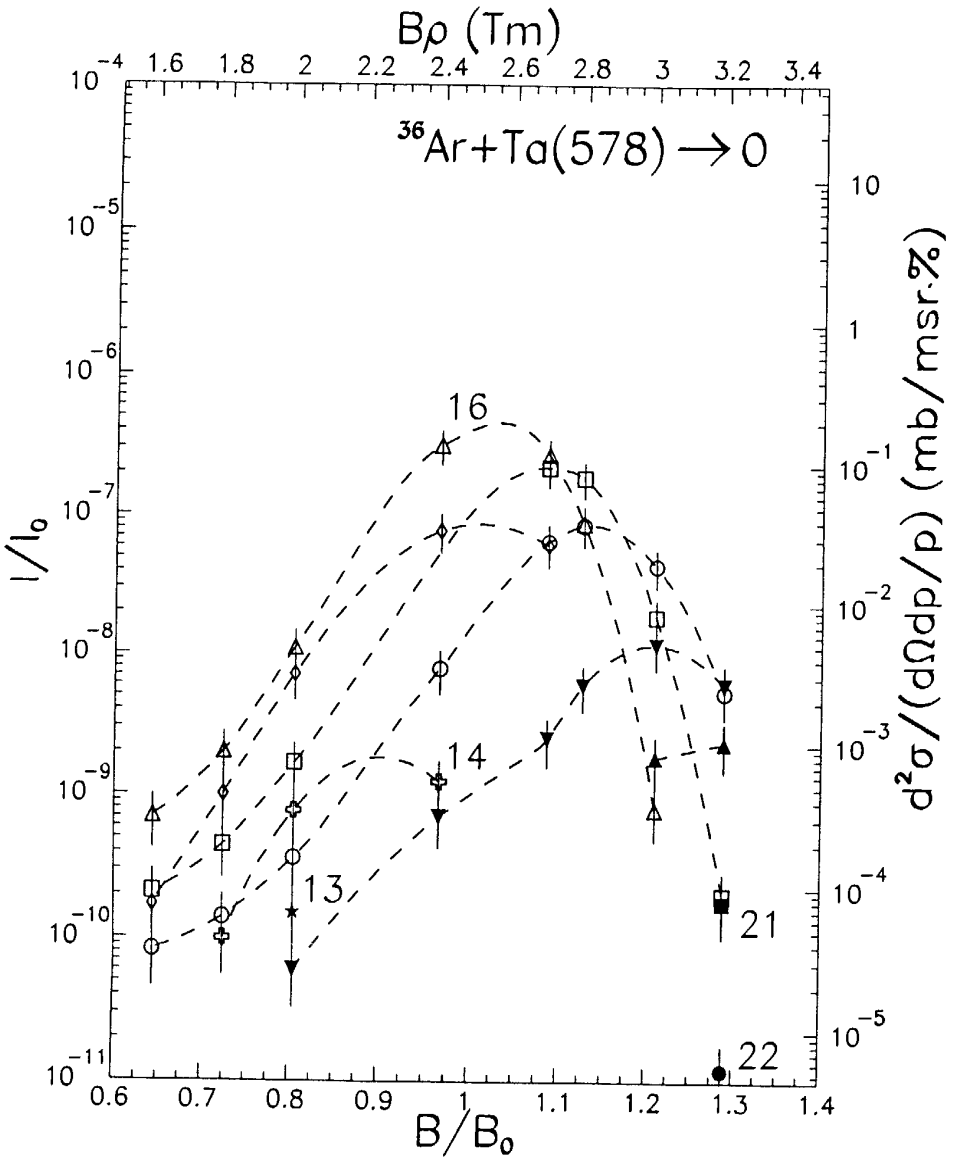

Fig. 13k

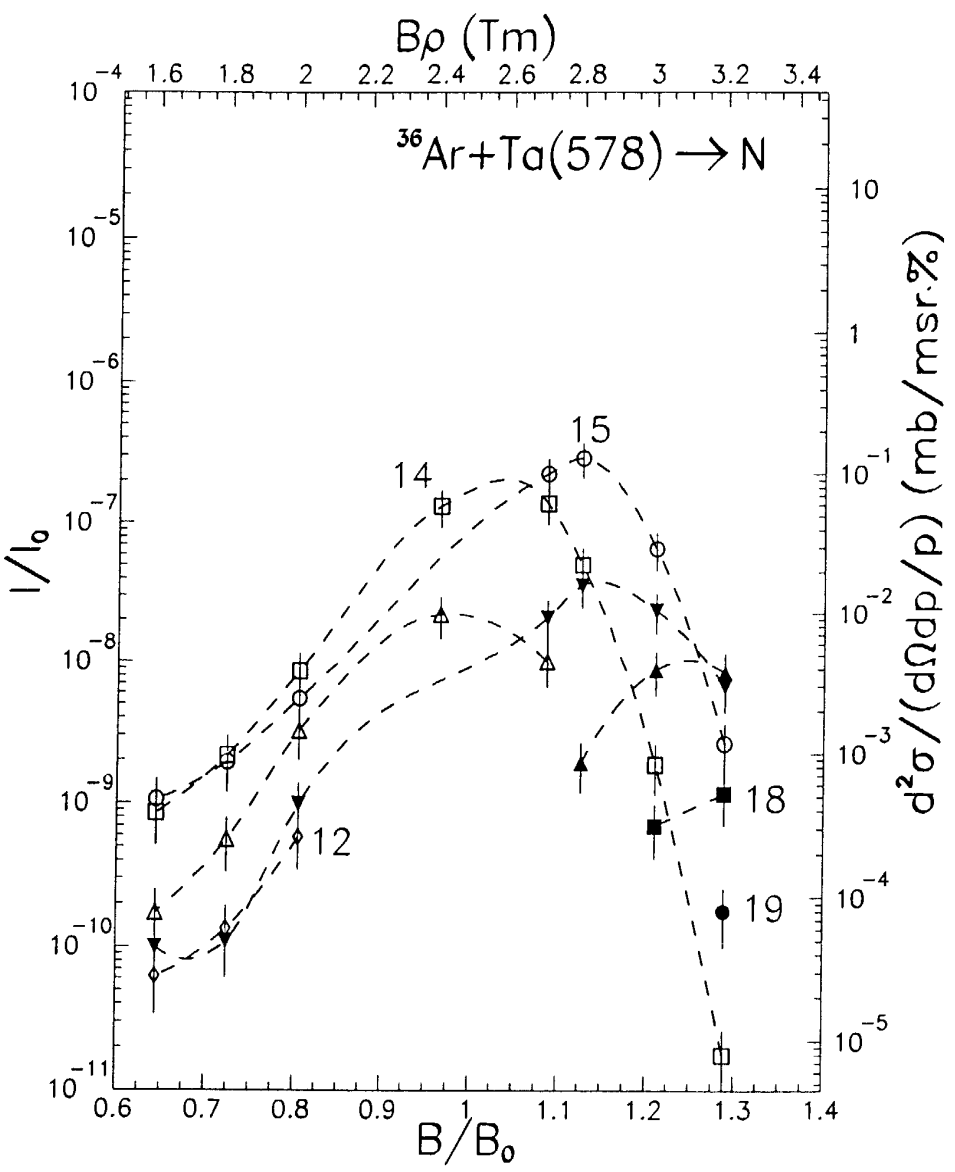

Fig. 13l

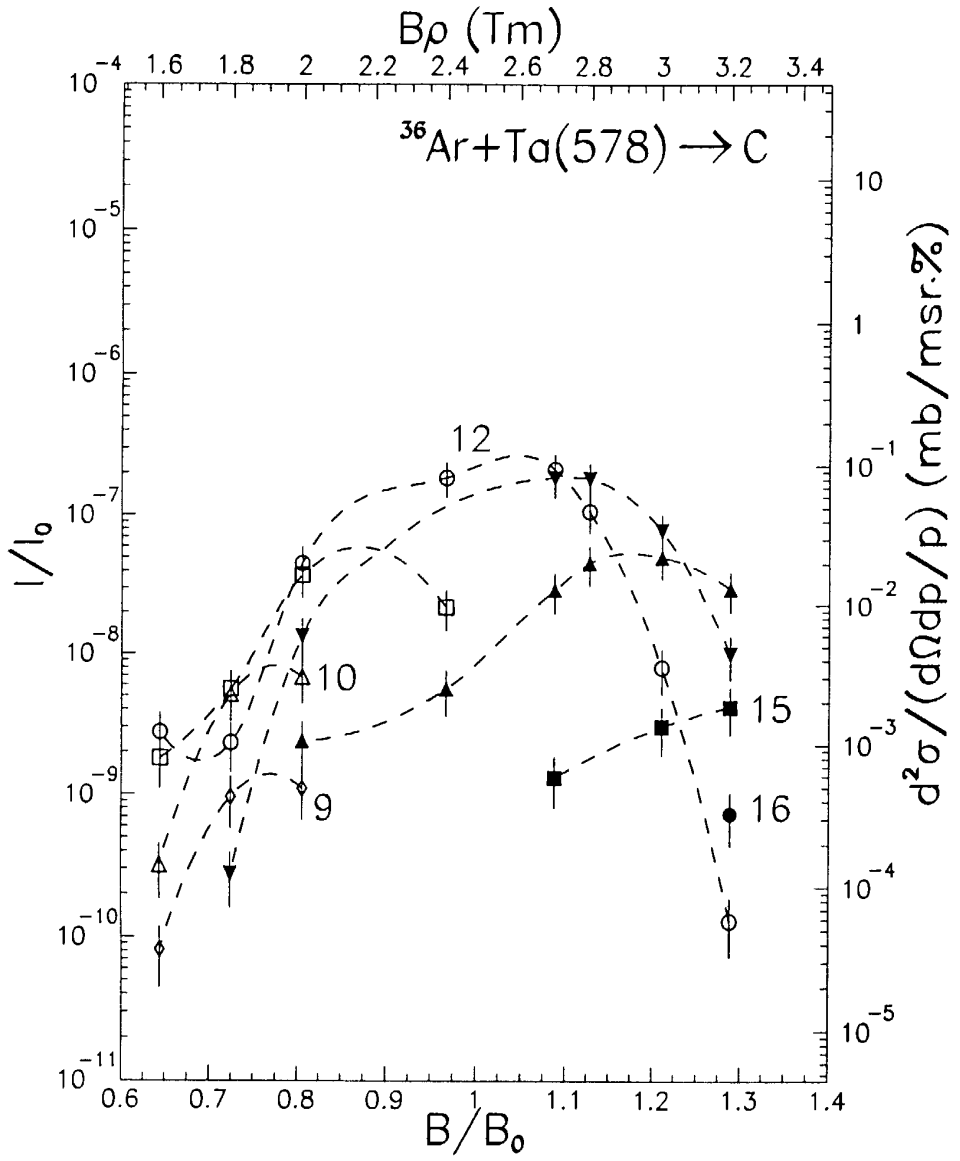

Fig. 13m

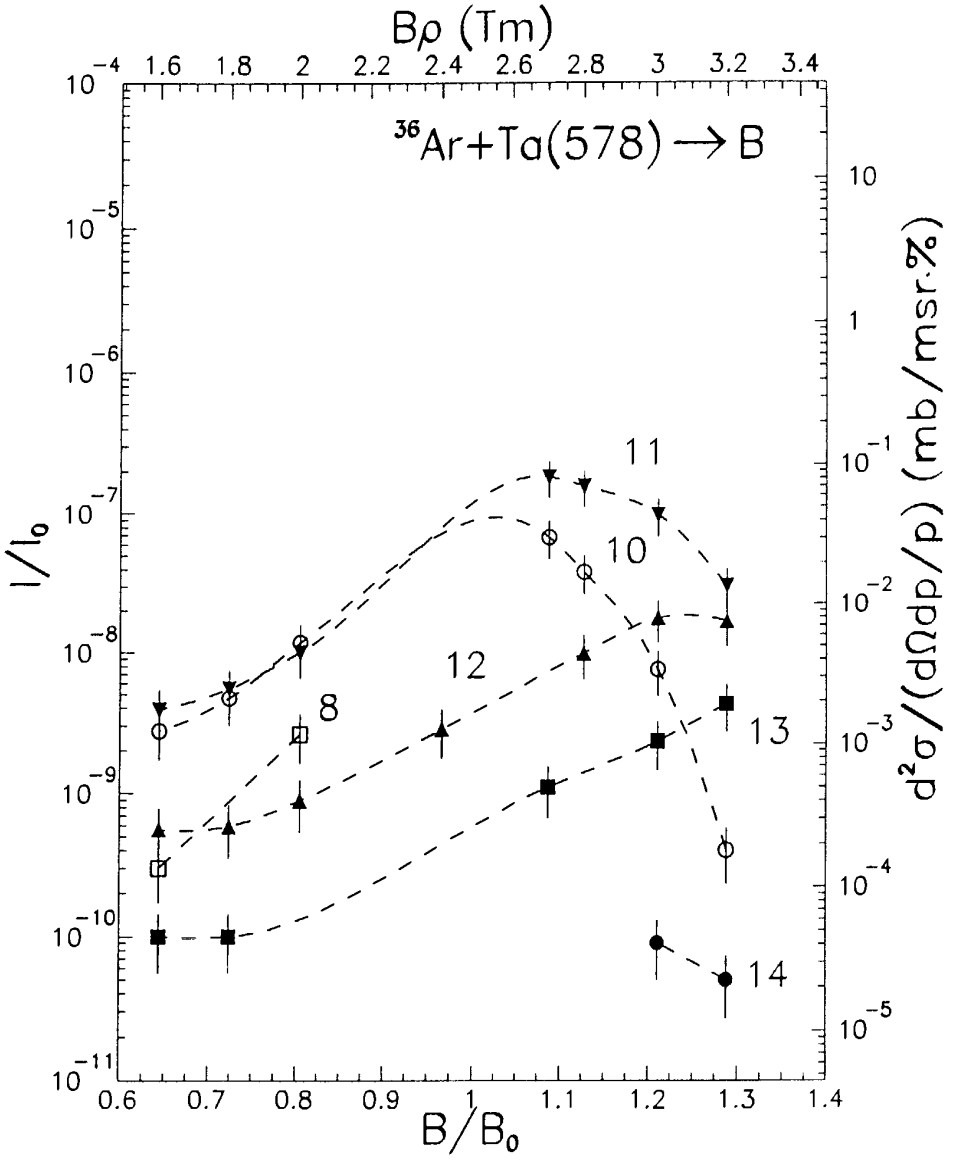

Fig. 13n

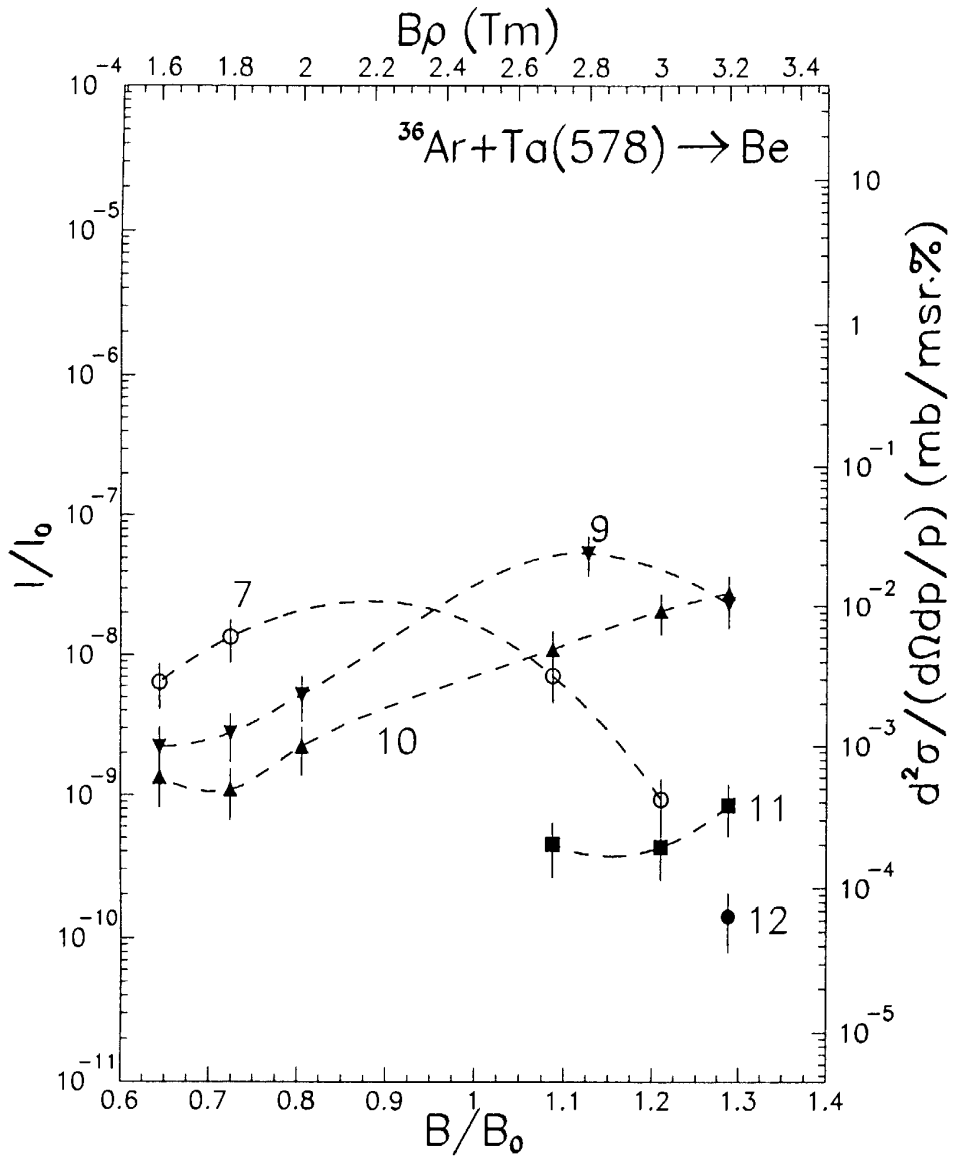

Fig. 13o

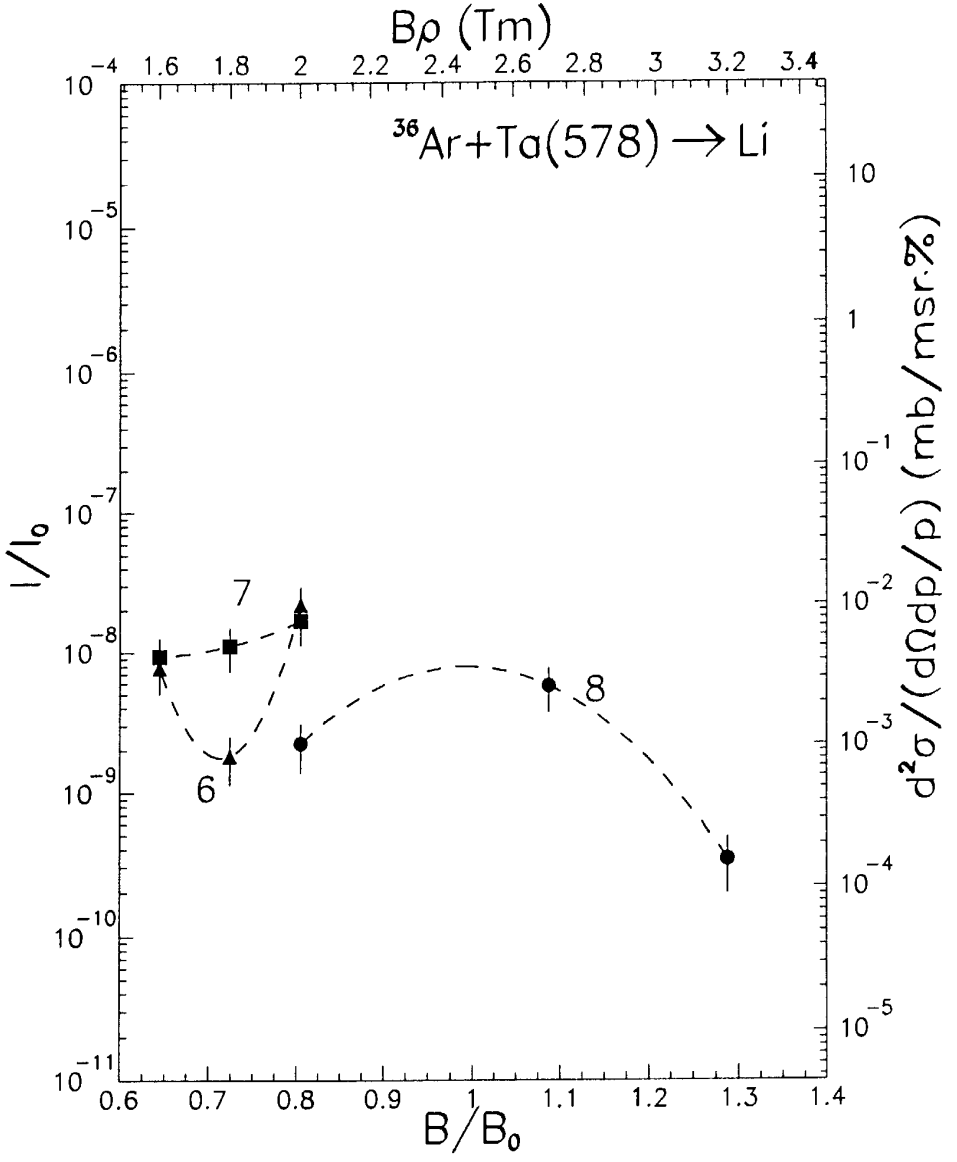

Fig. 13p

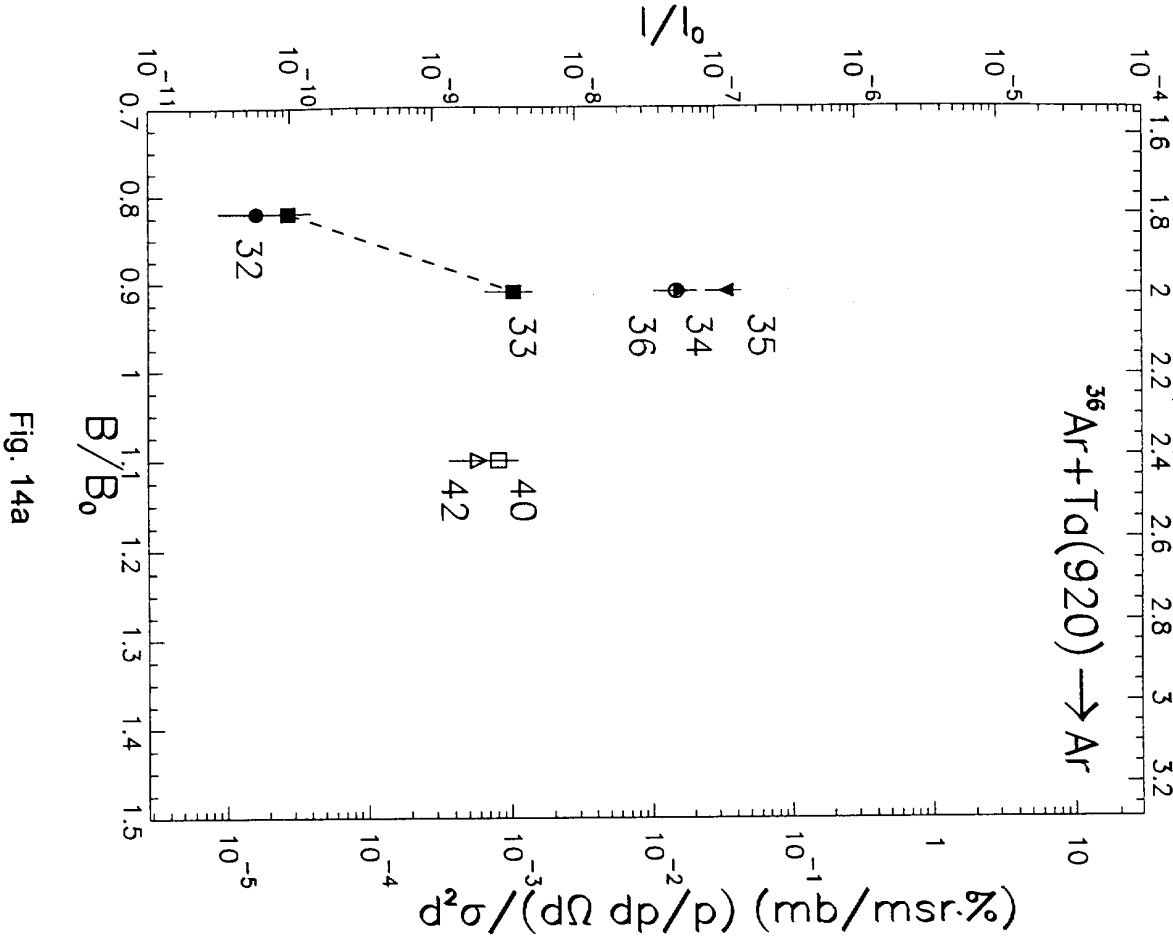

Fig. 14a

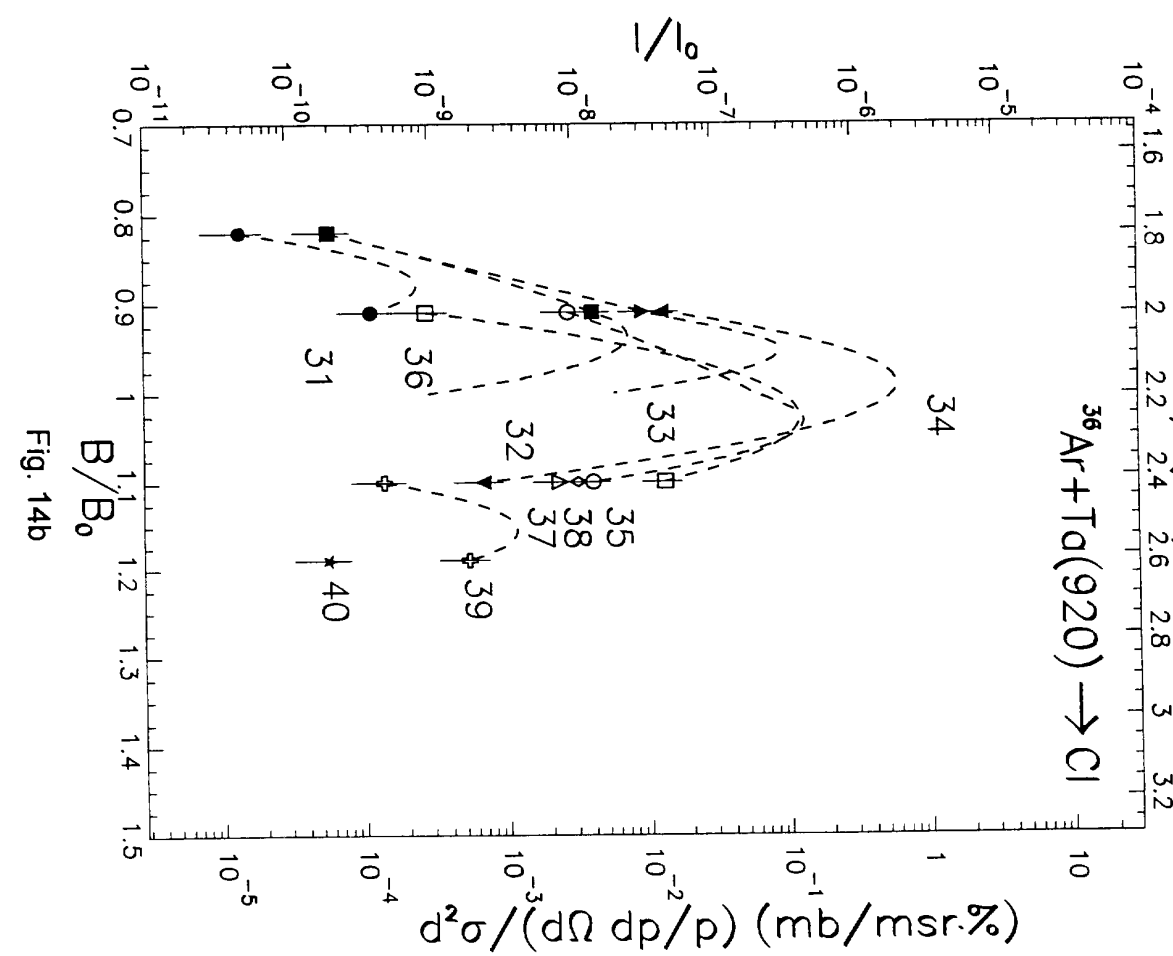

Fig. 14b

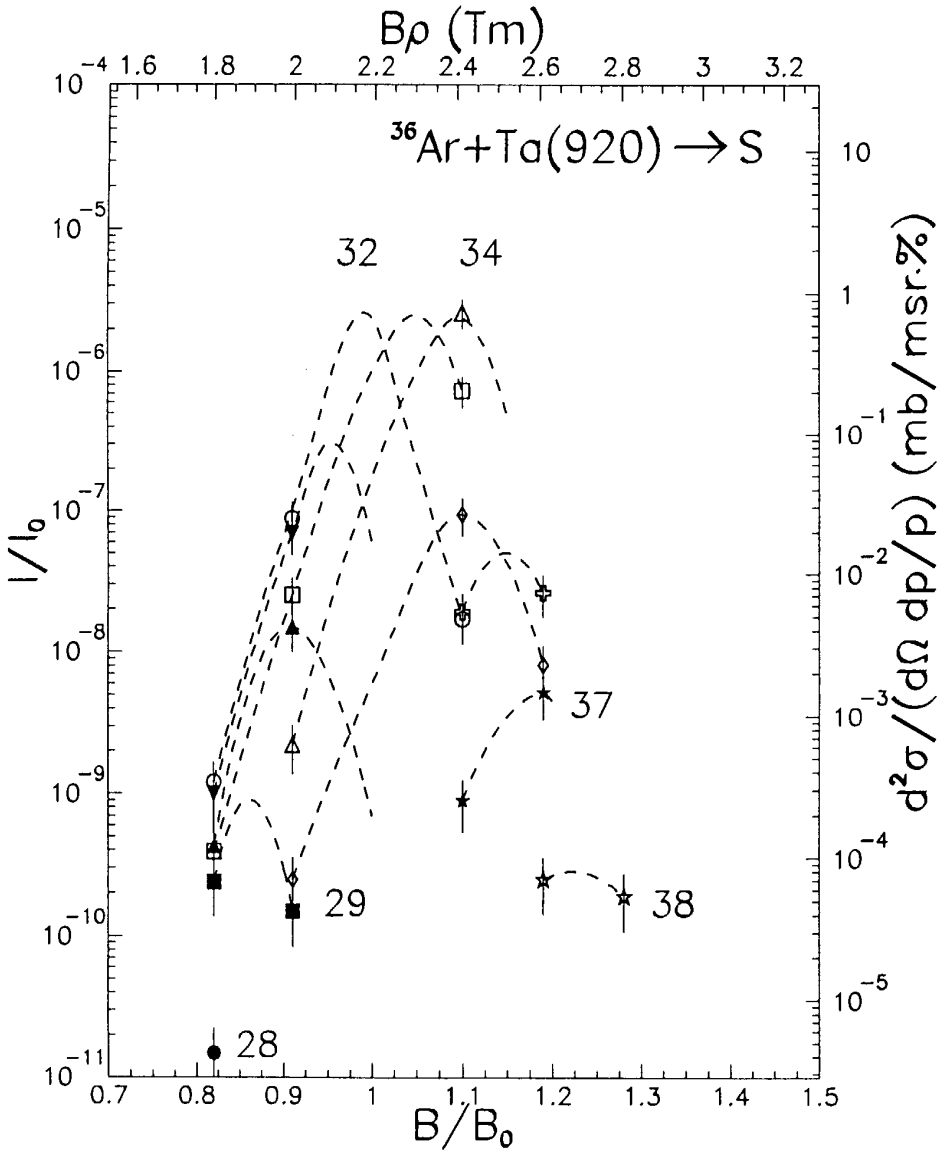

Fig. 14c

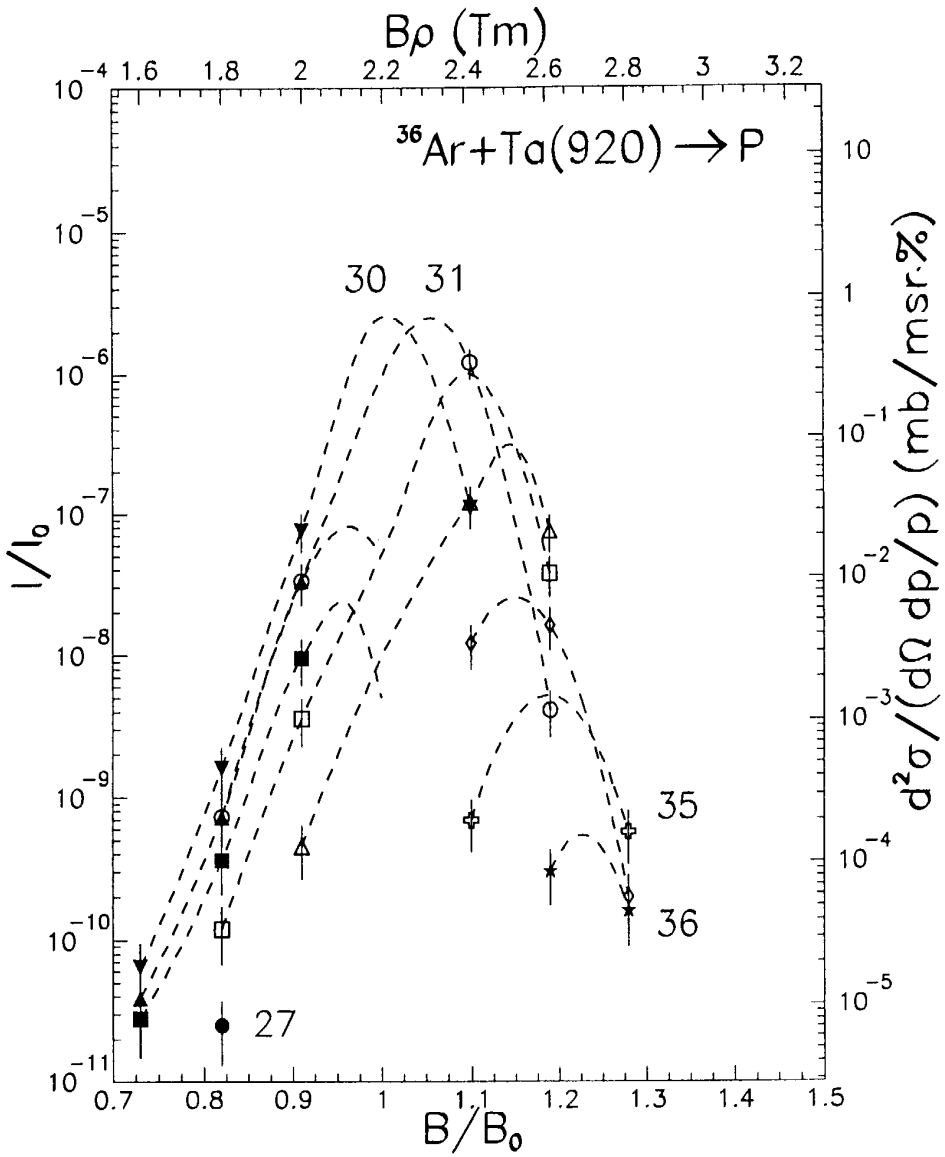

Fig. 14d

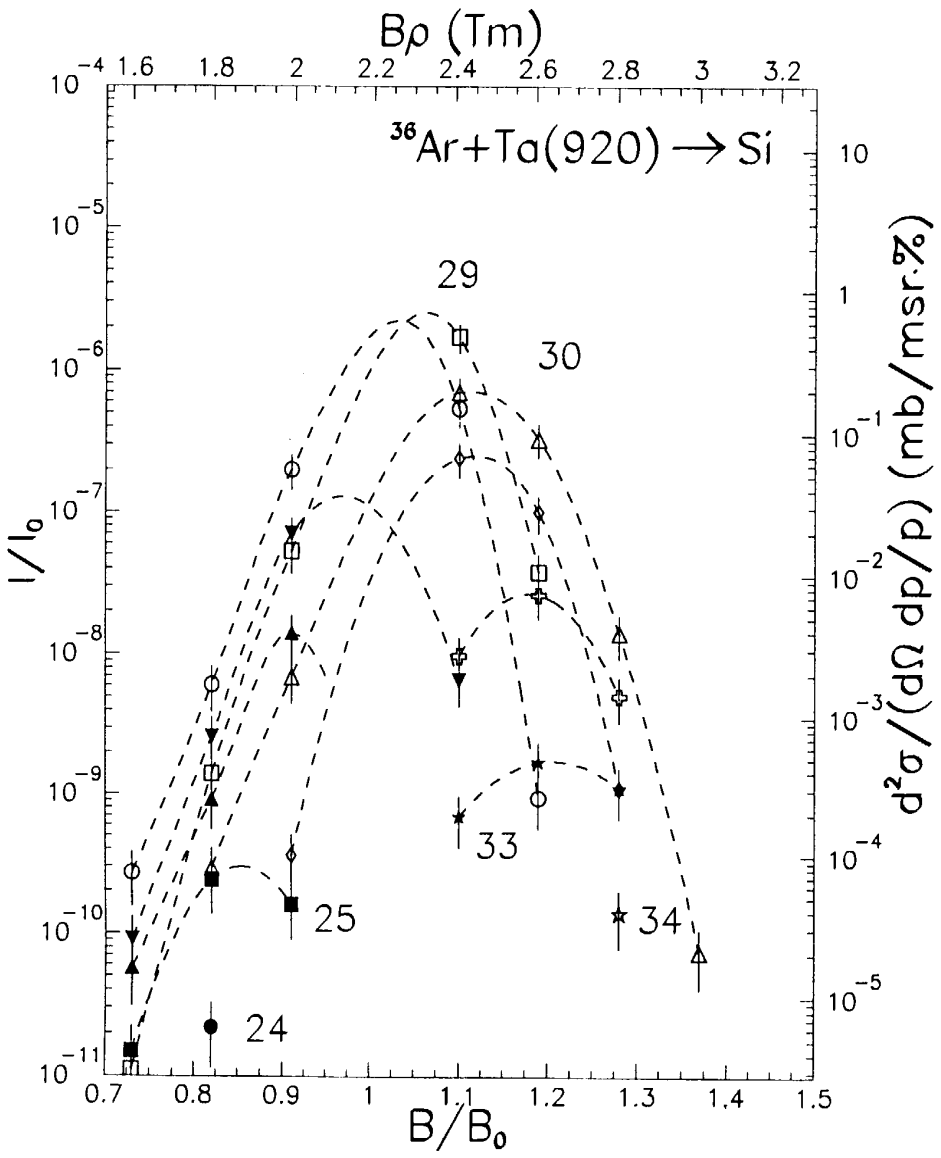

Fig. 14e

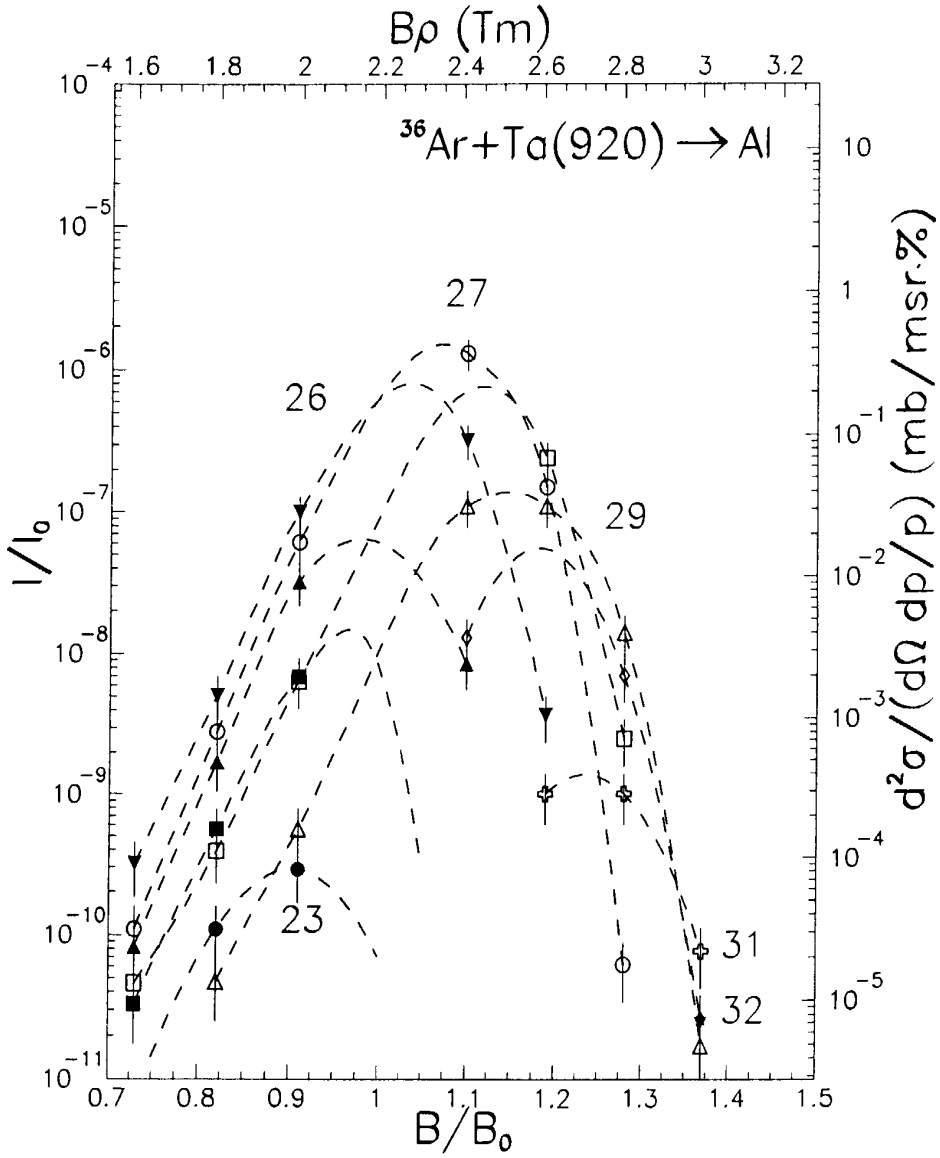

Fig. 14f

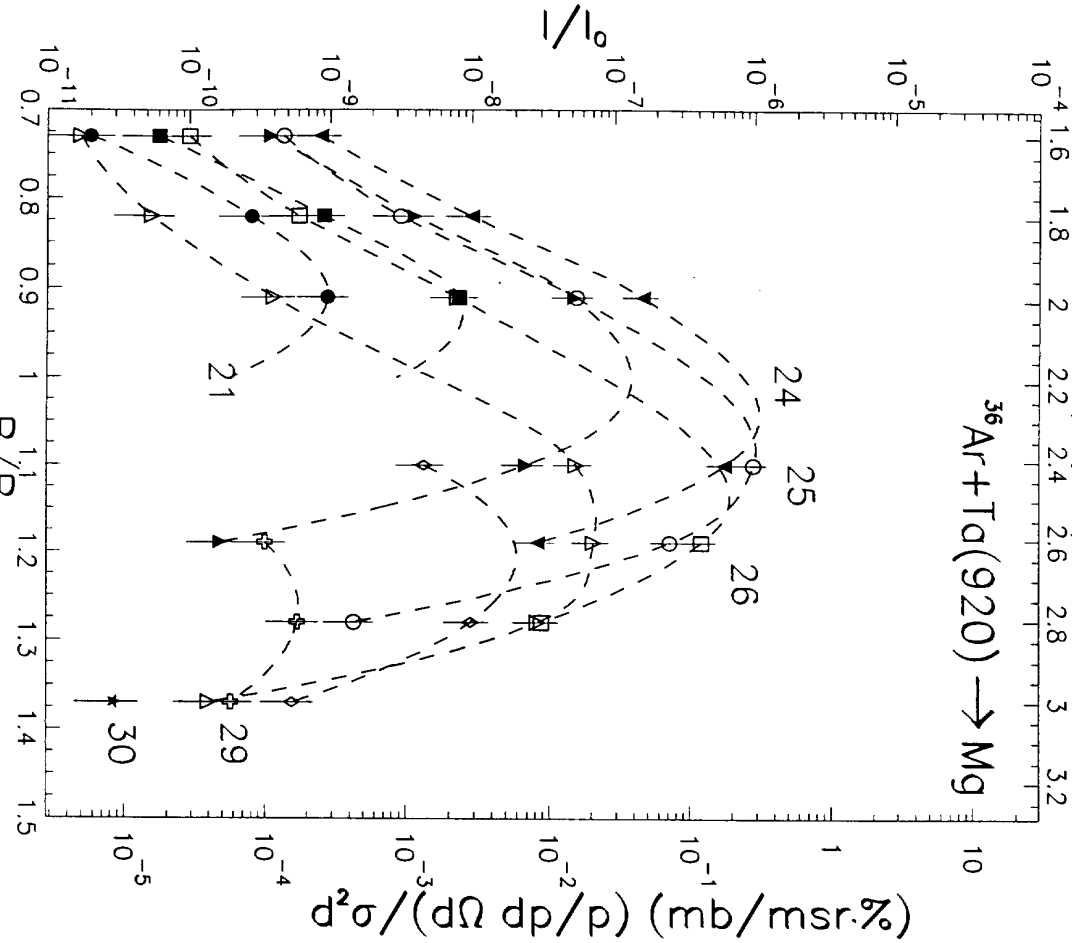

Fig. 14g

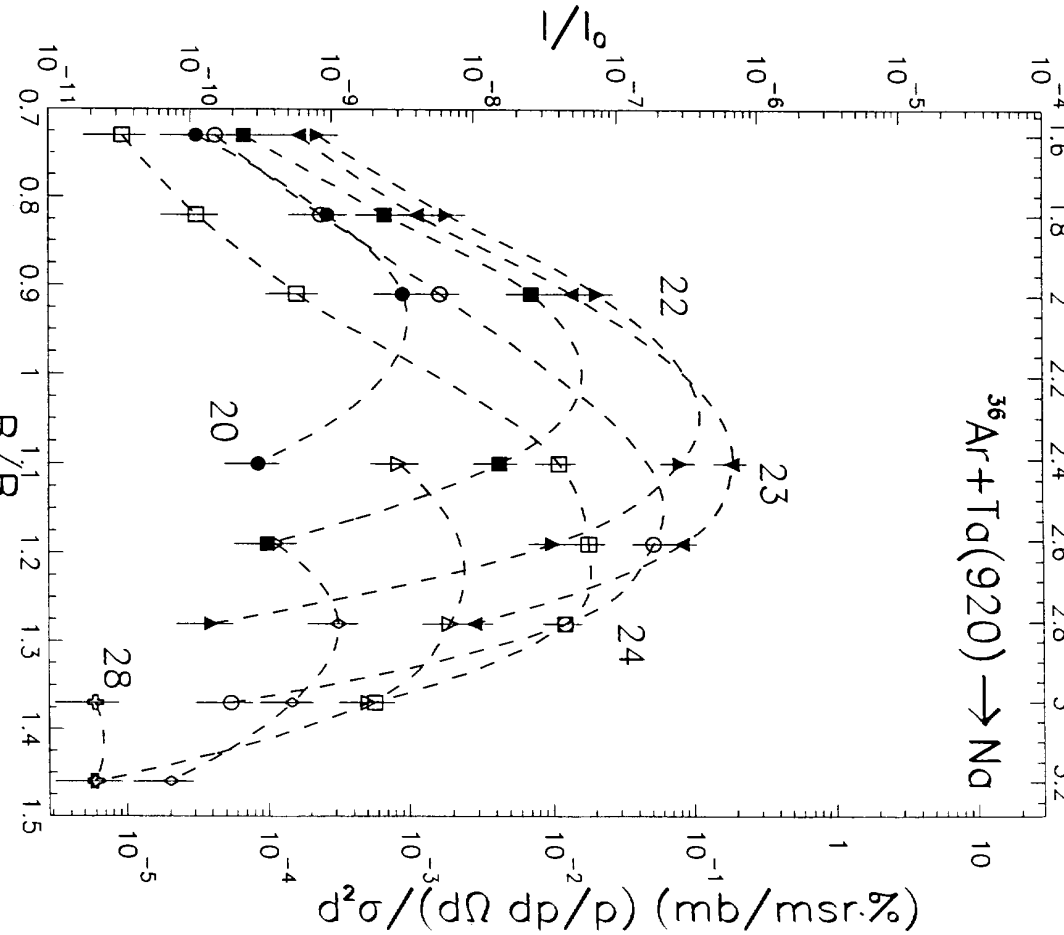

Fig. 14h

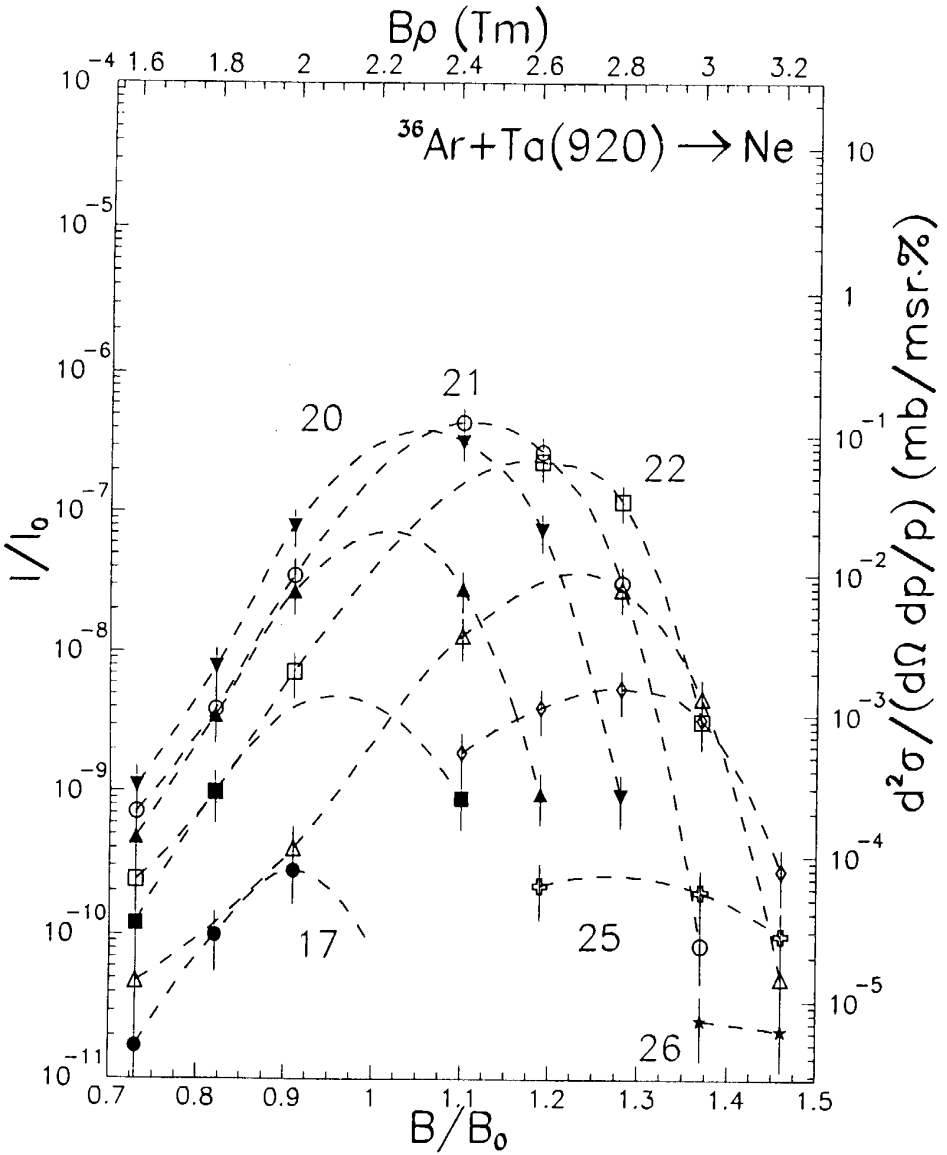

Fig. 14i

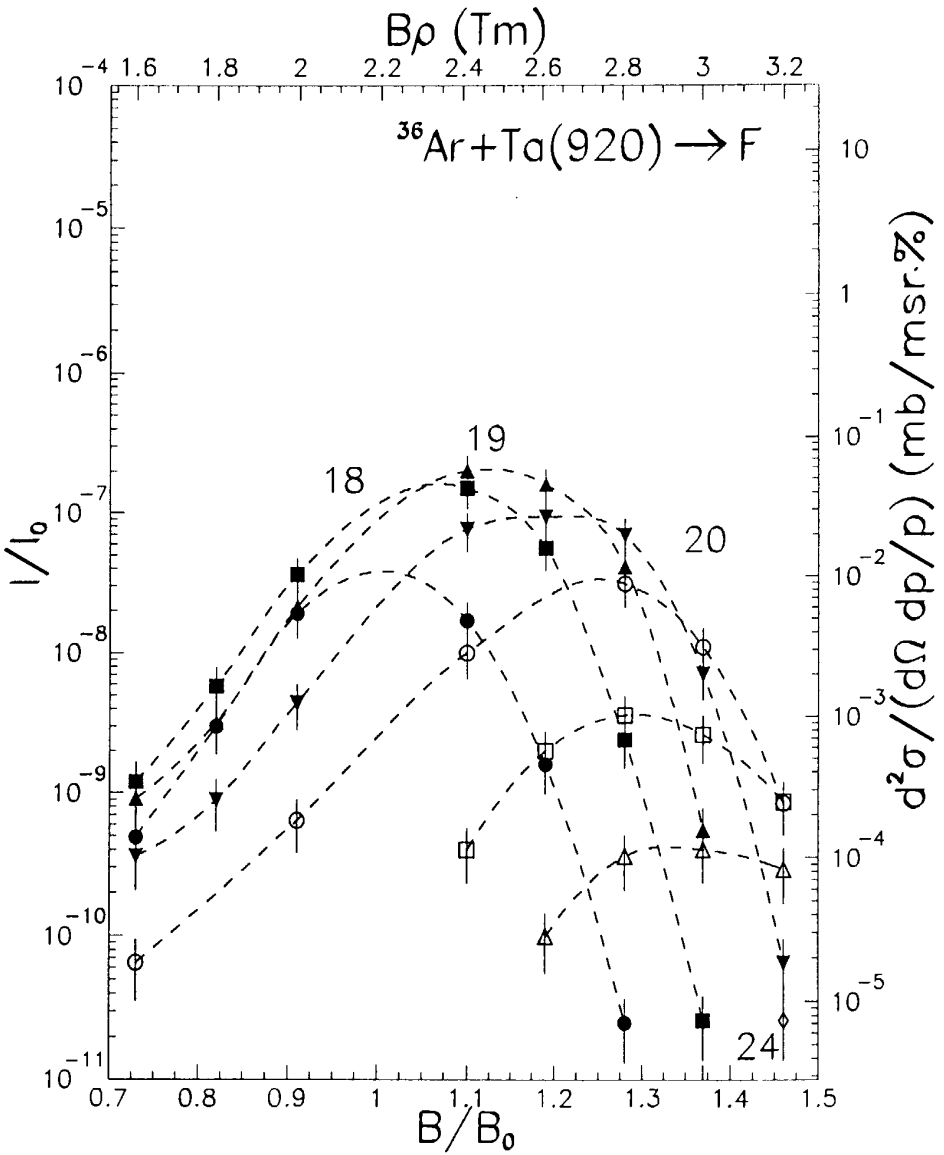

Fig. 14j

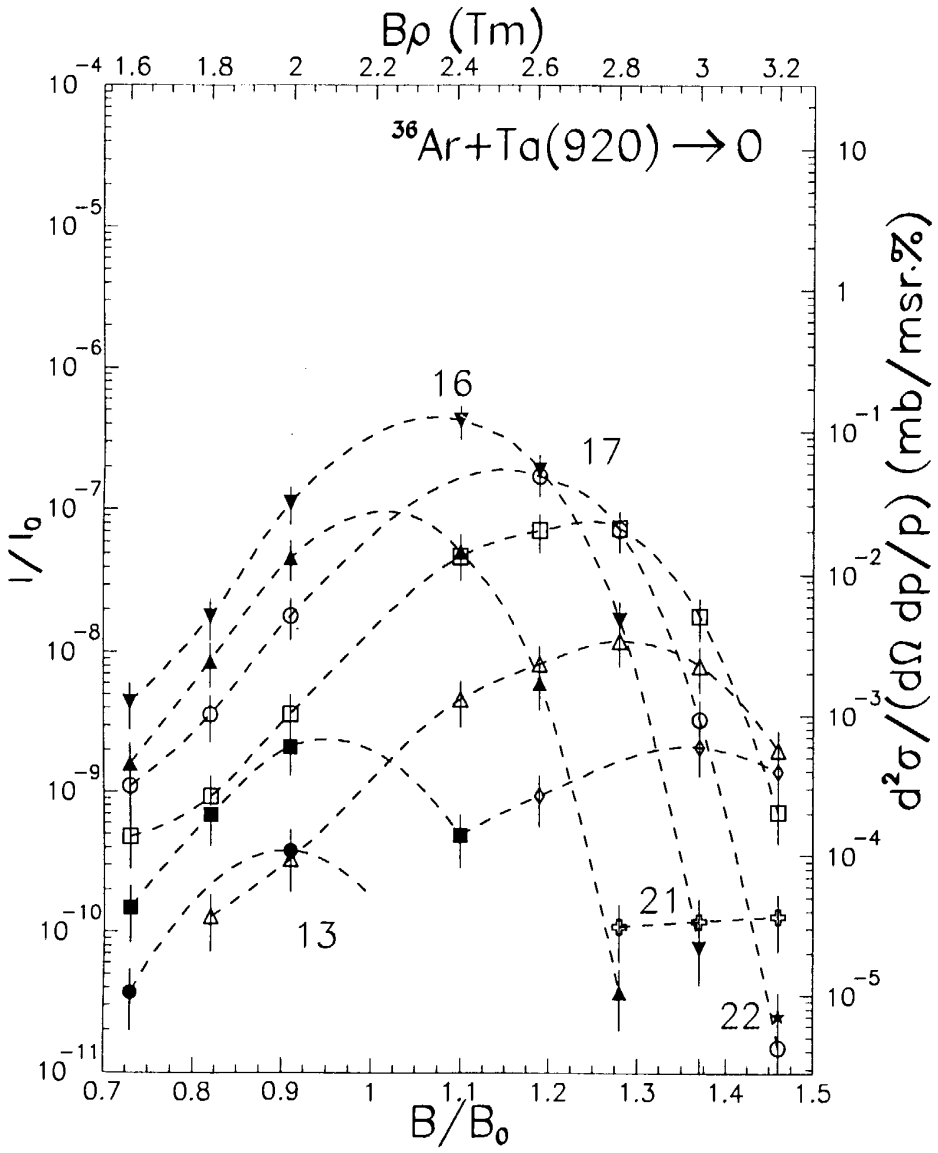

Fig. 14k

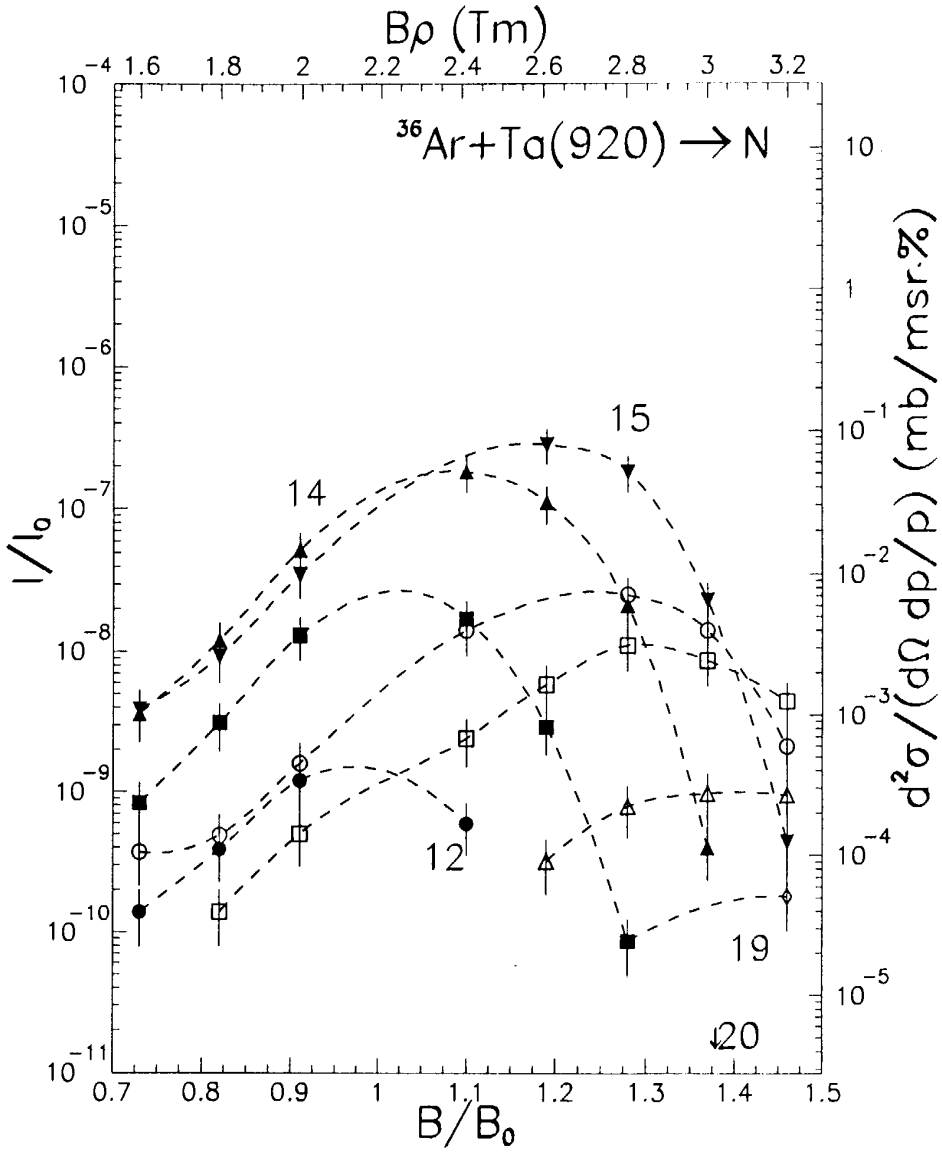

Fig. 14l

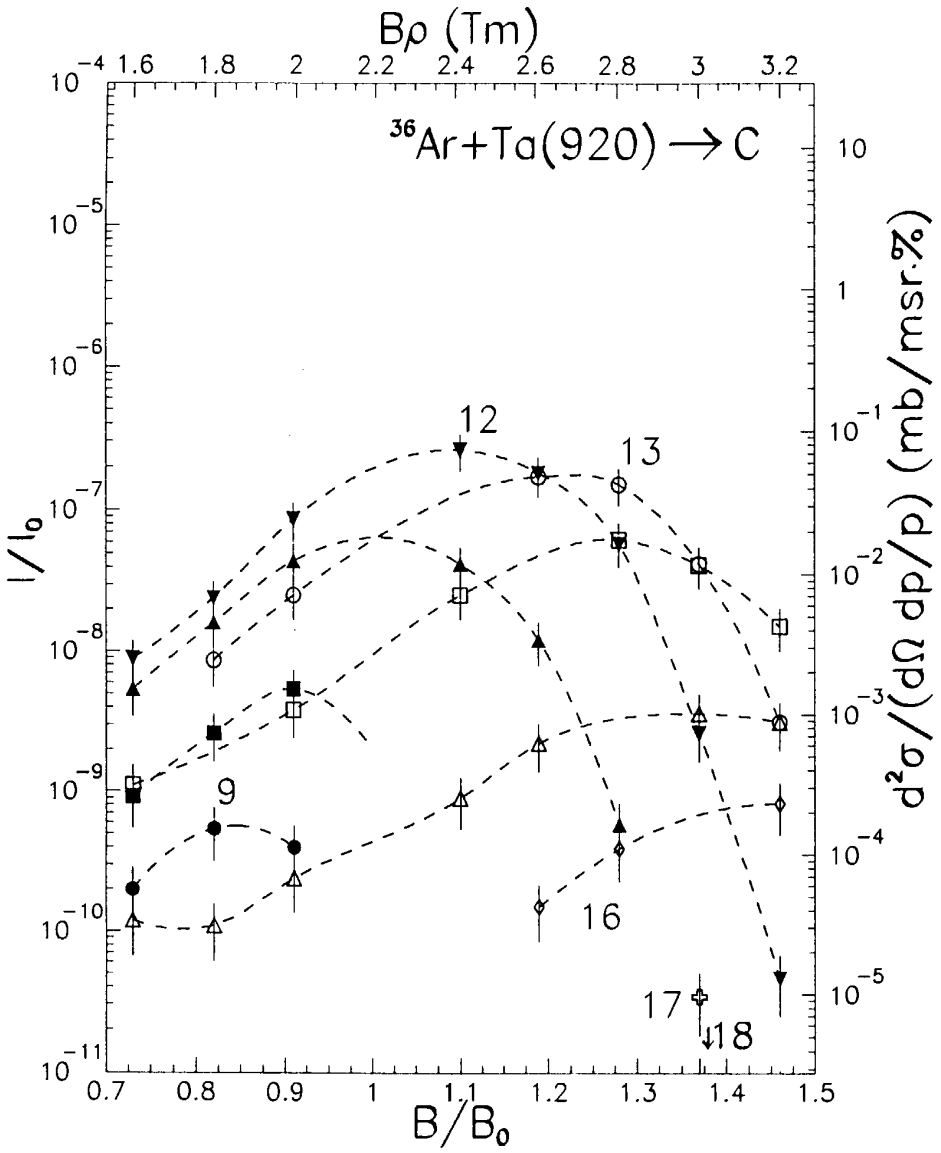

Fig. 14m

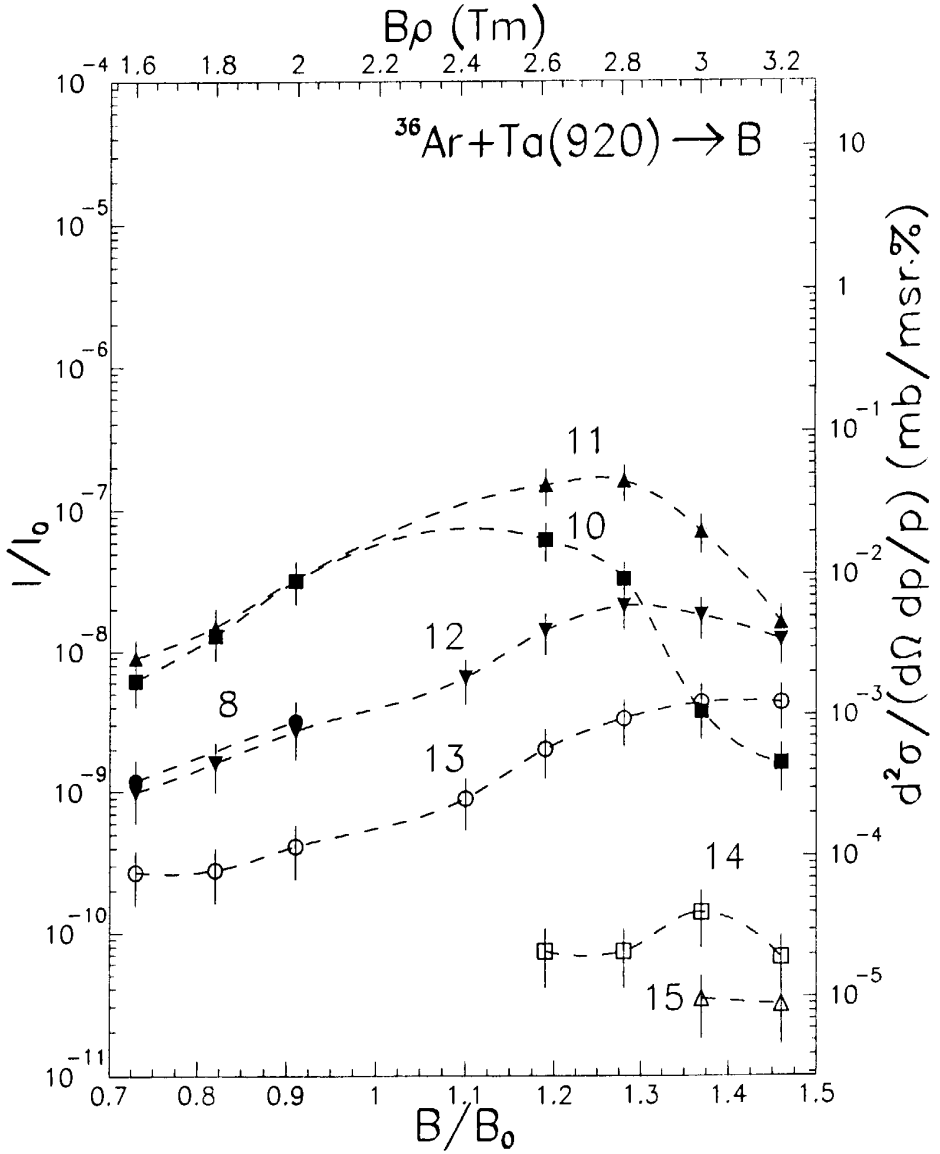

Fig. 14n

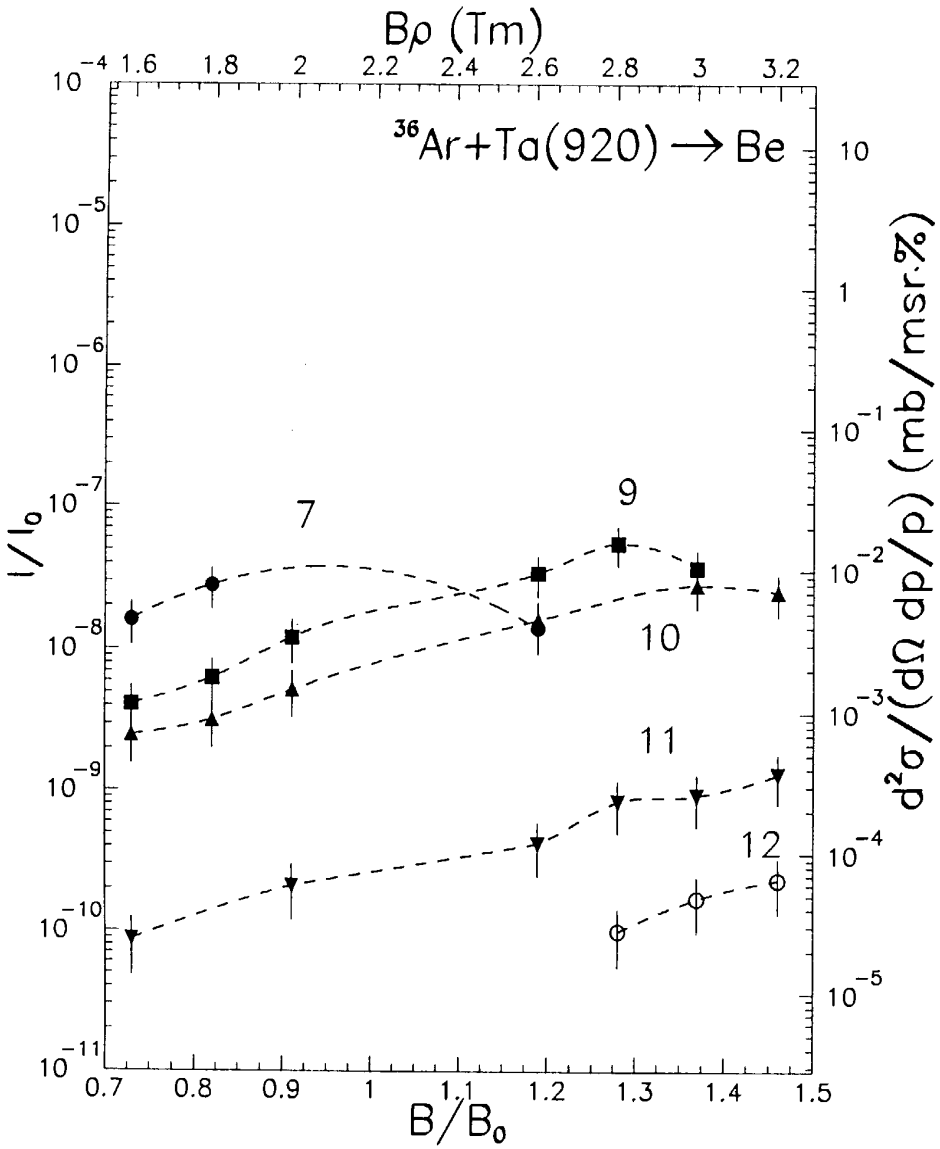

Fig. 14o

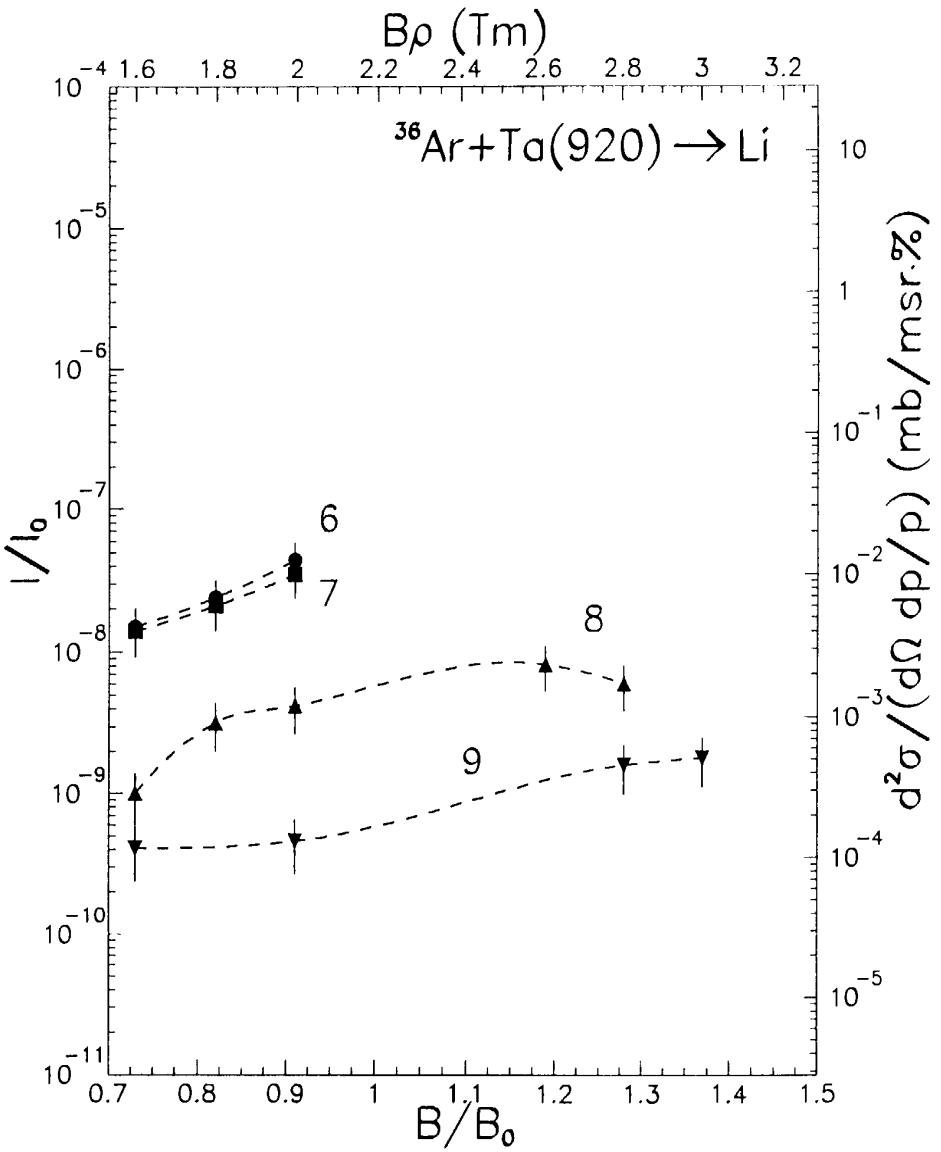

Fig. 14p

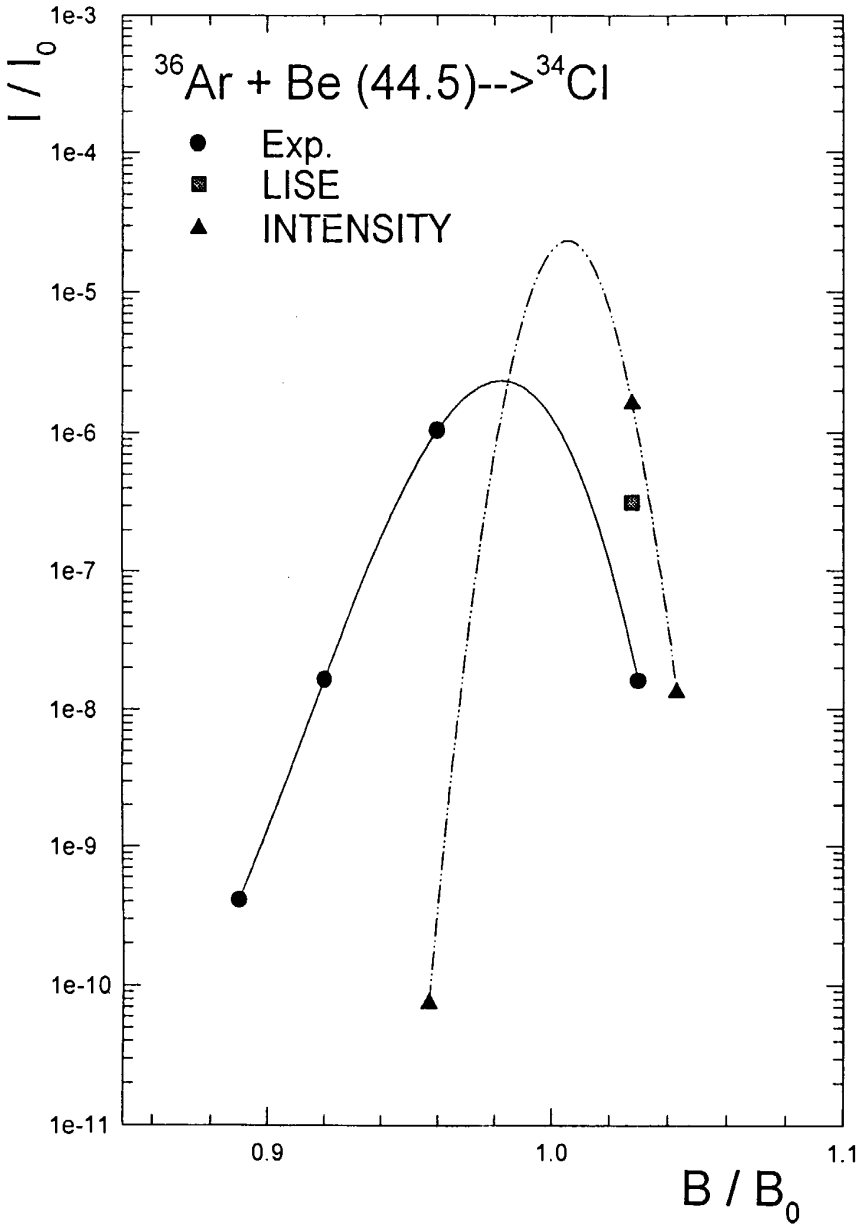

Fig. 15a

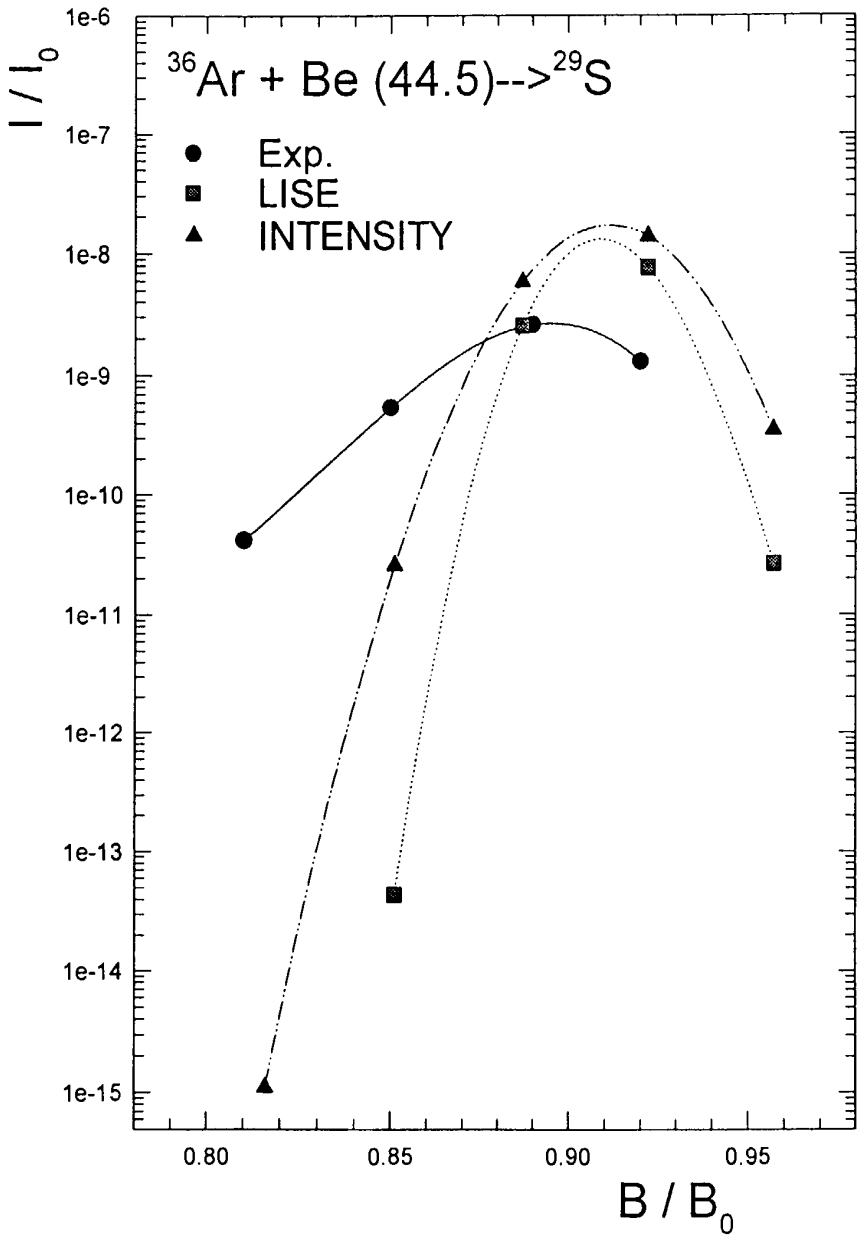

Fig. 15b

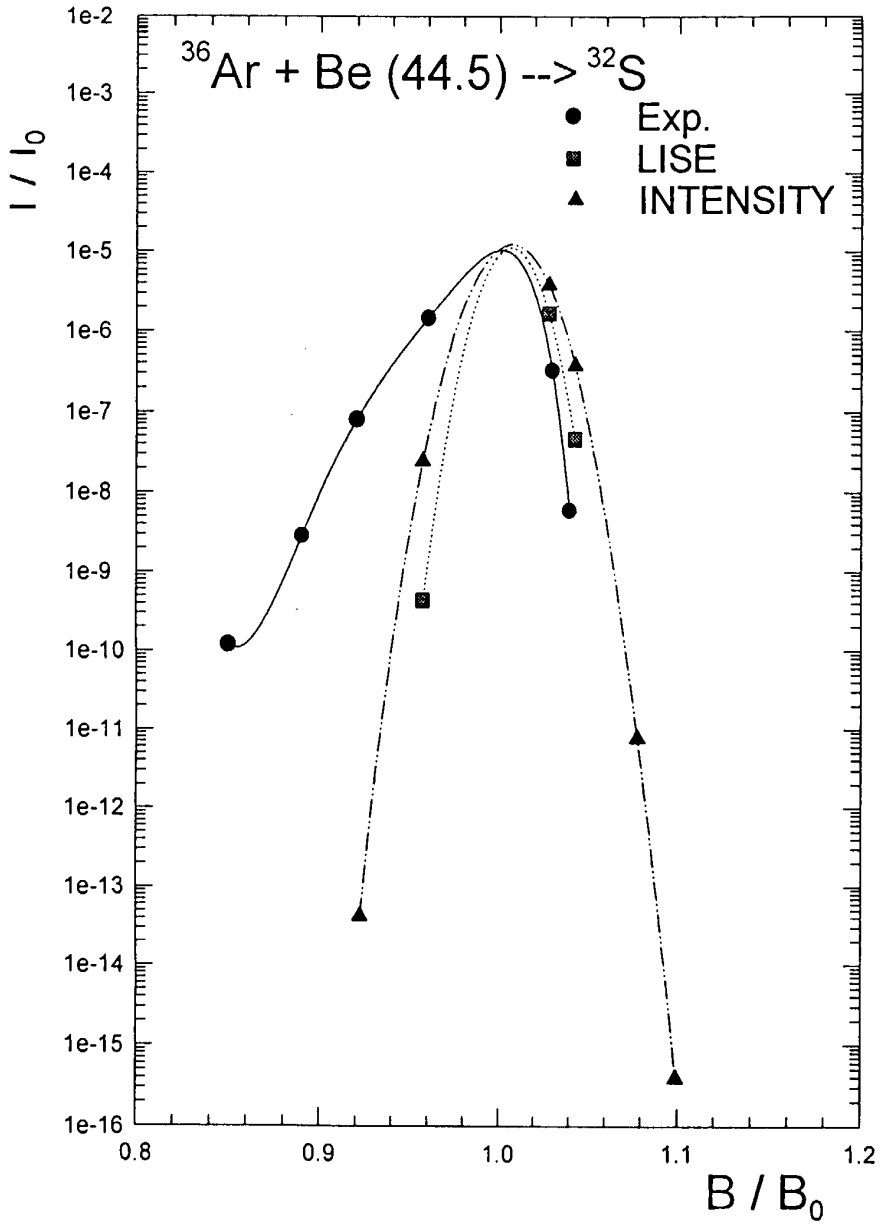

Fig. 15c

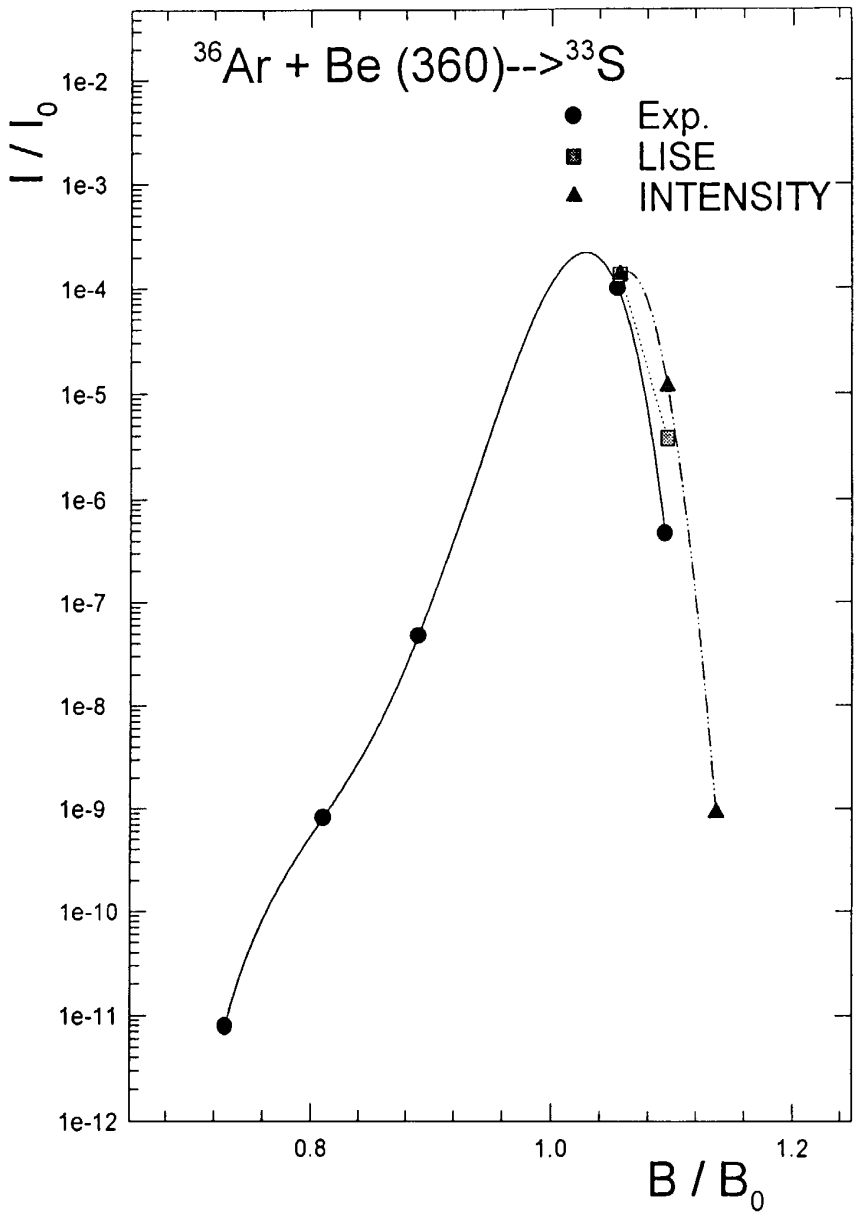

Fig. 15d

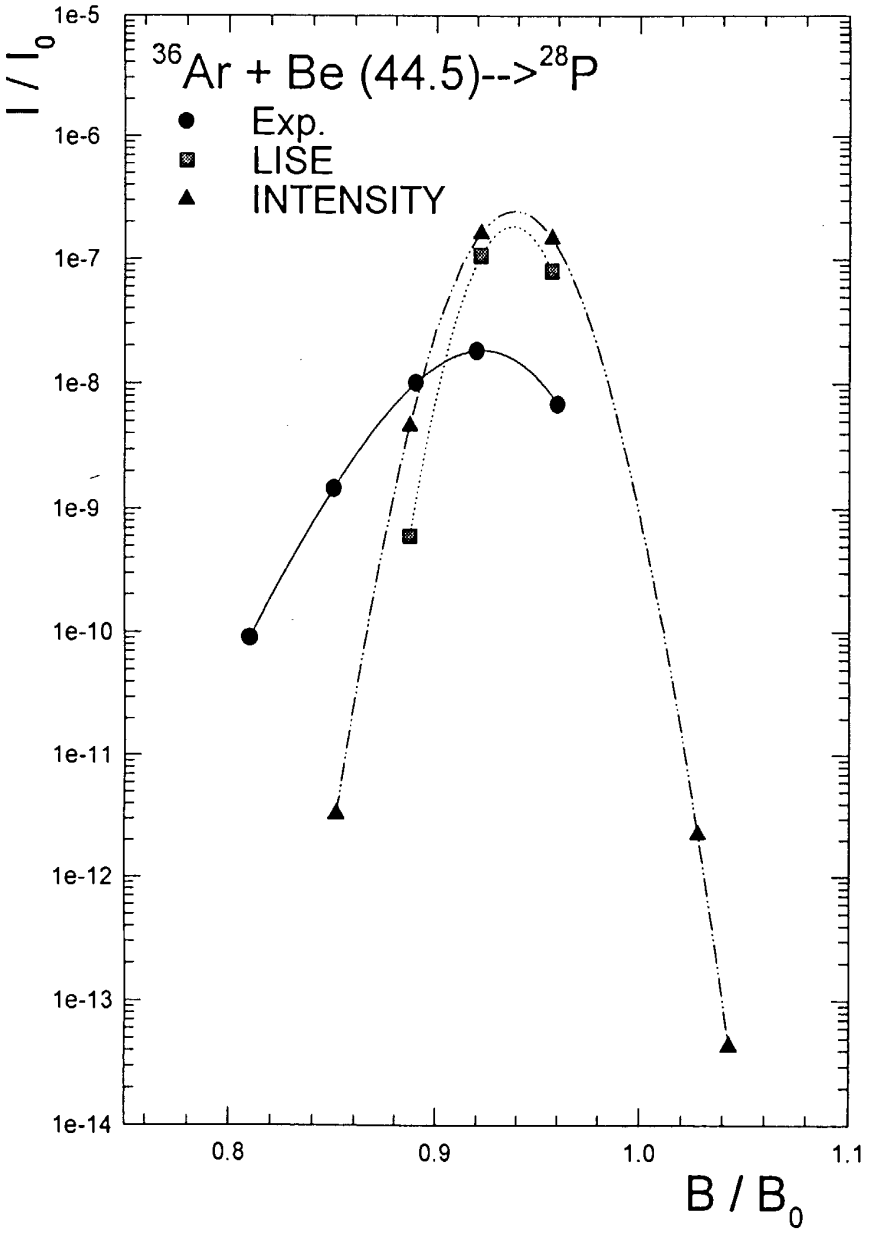

Fig. 15e

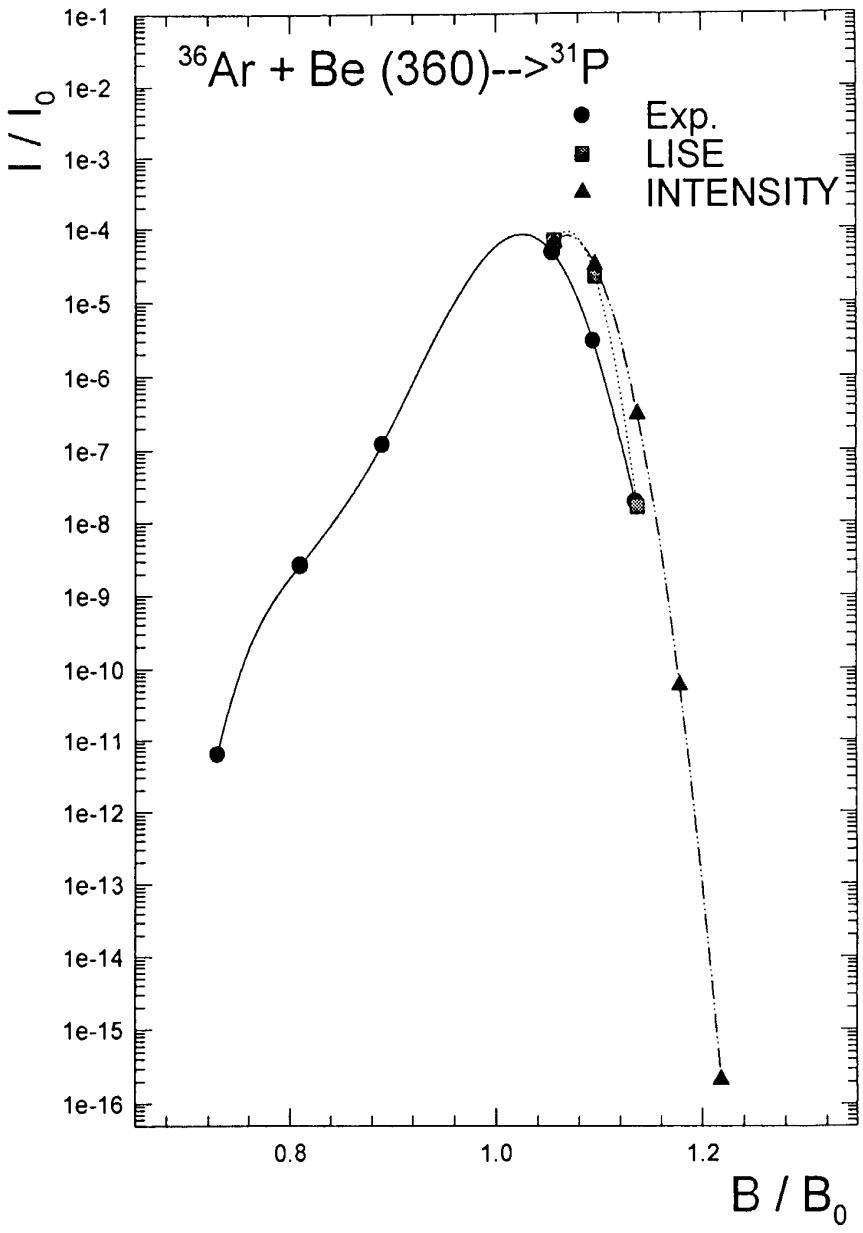

Fig. 15f

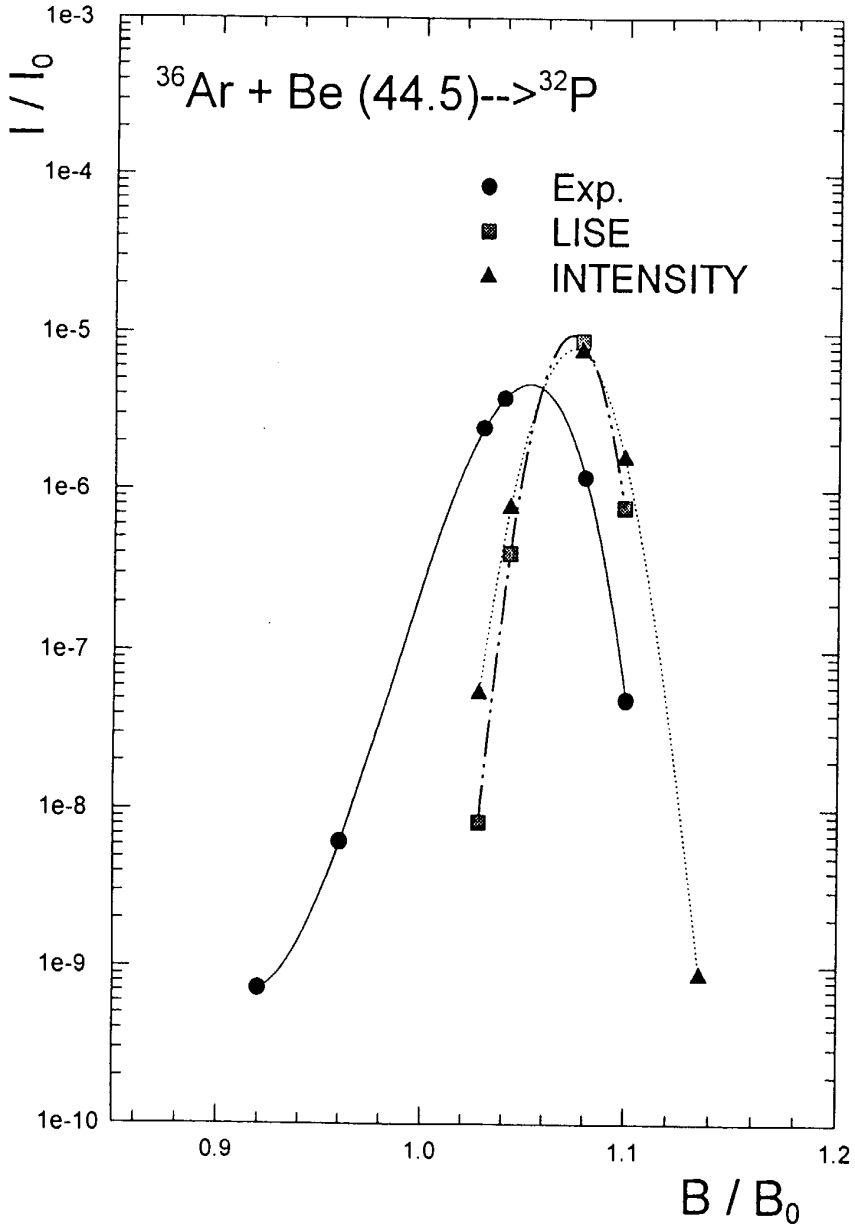

Fig. 15g

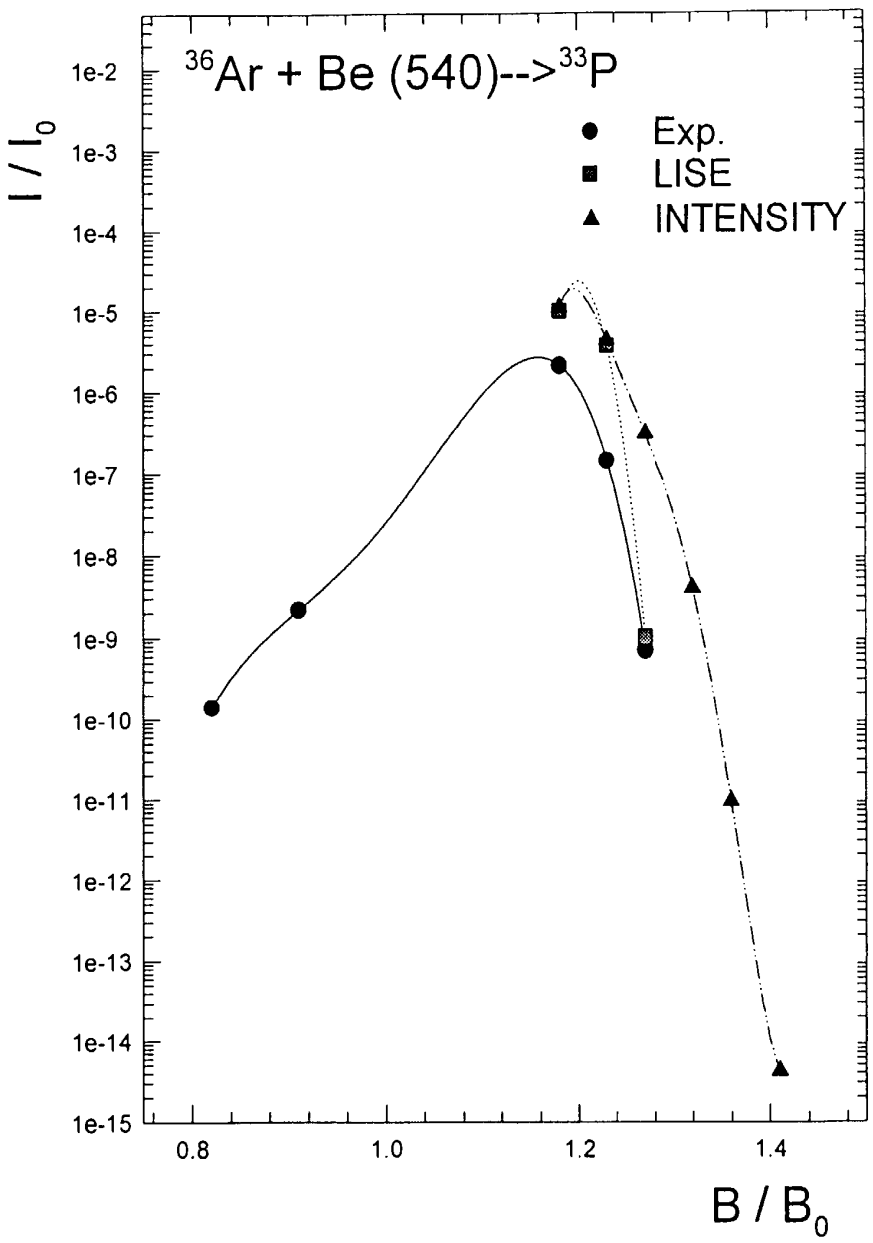

Fig. 15h

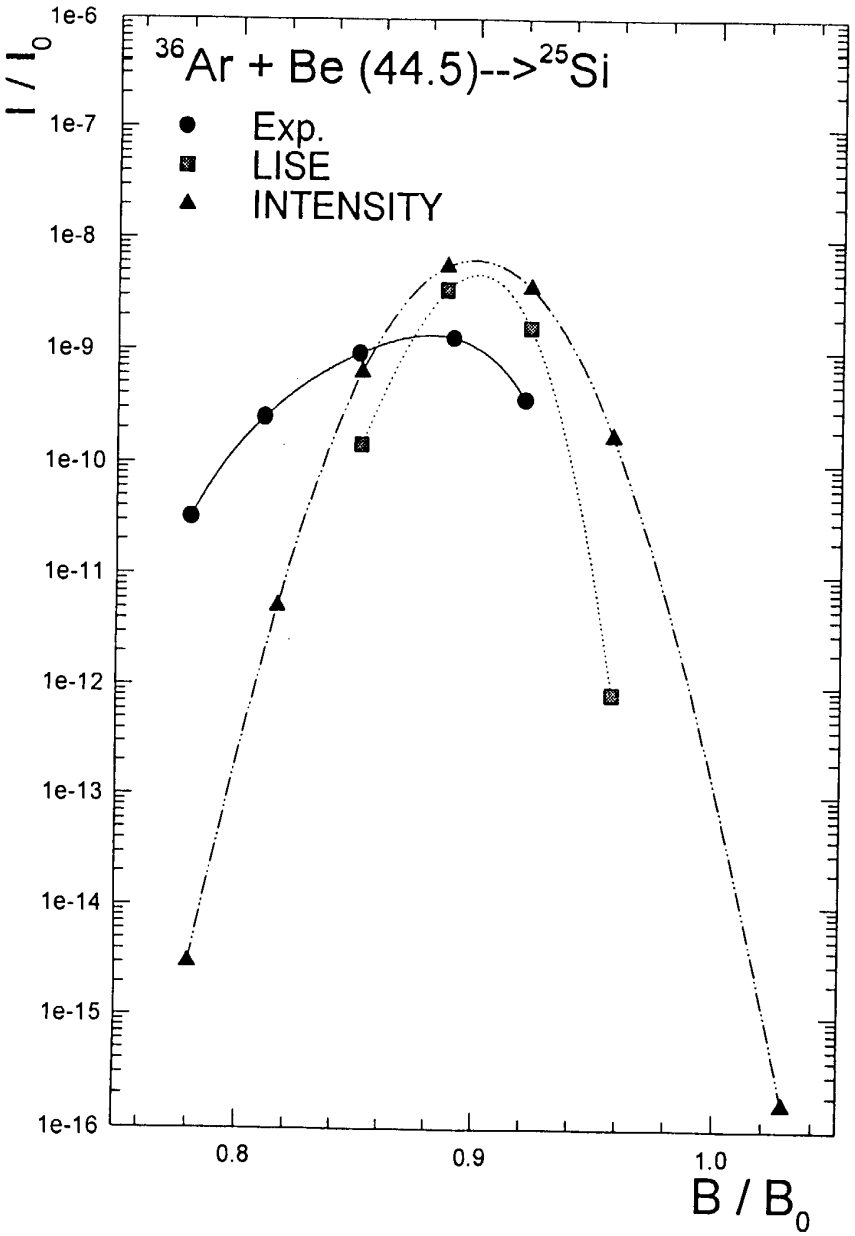

Fig. 15j

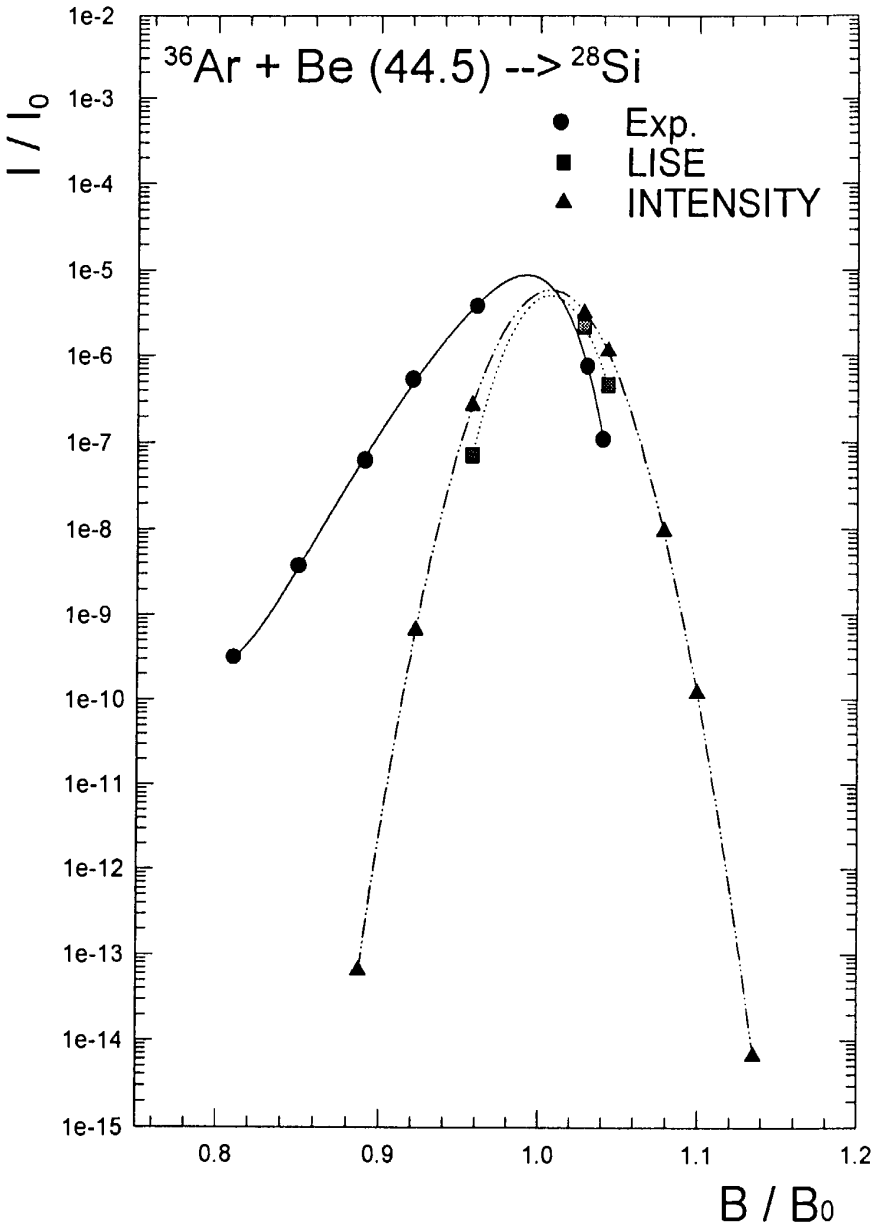

Fig. 15i

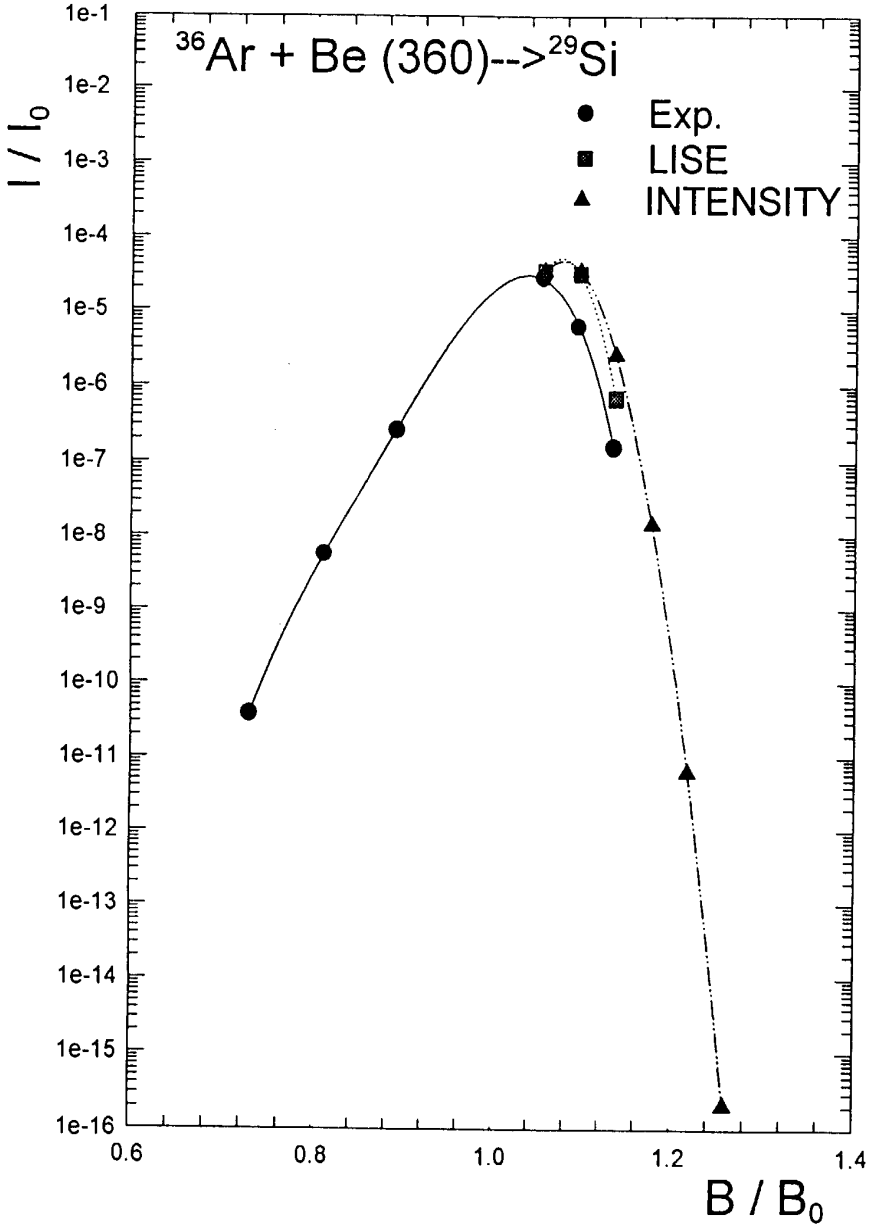

Fig. 15k

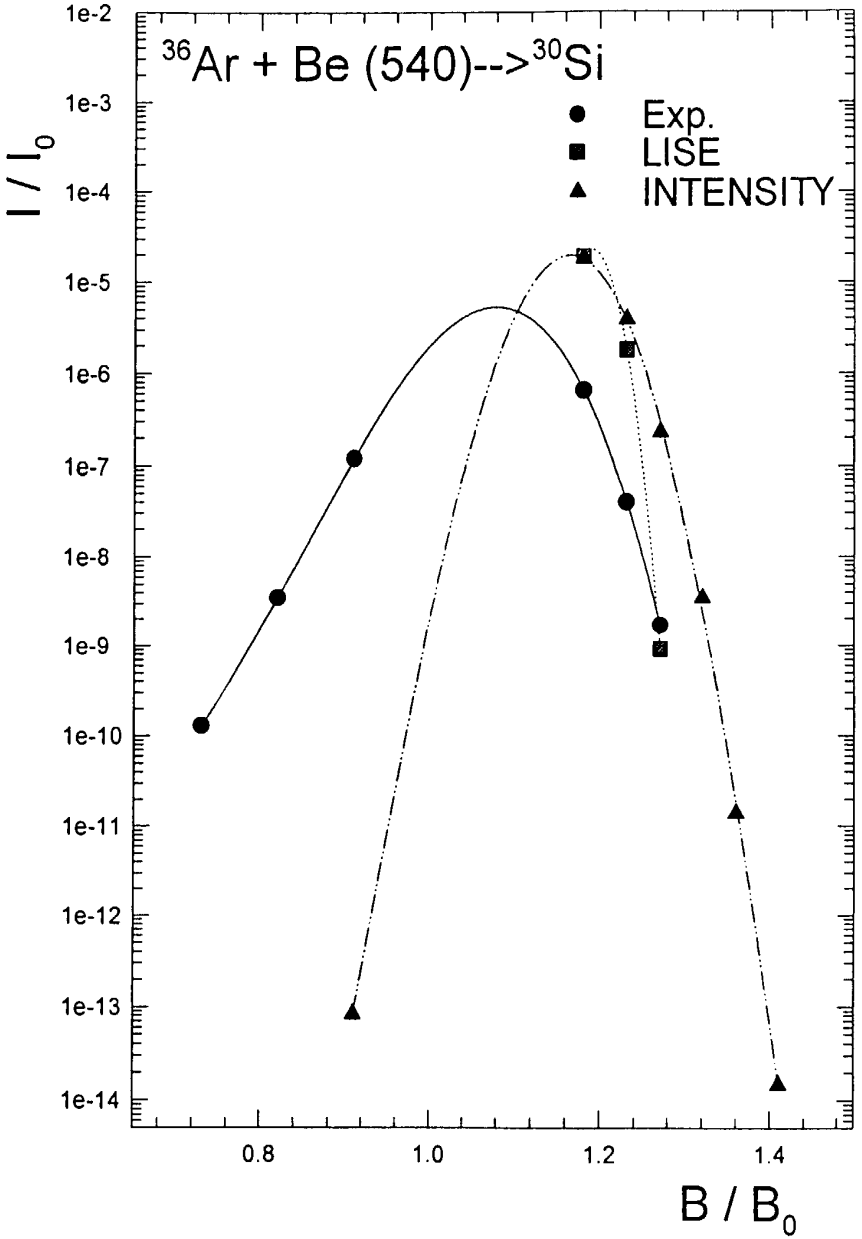

Fig. 15l

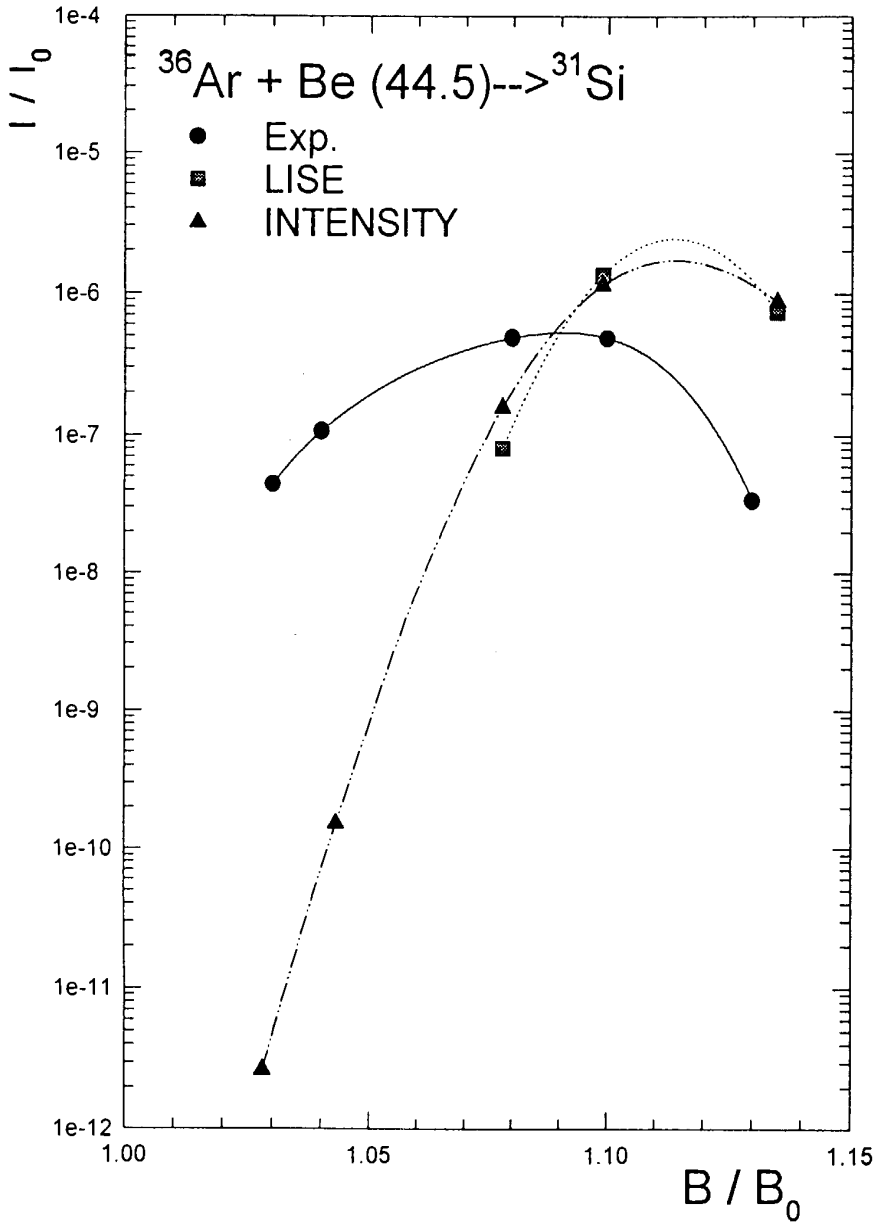

Fig. 15m

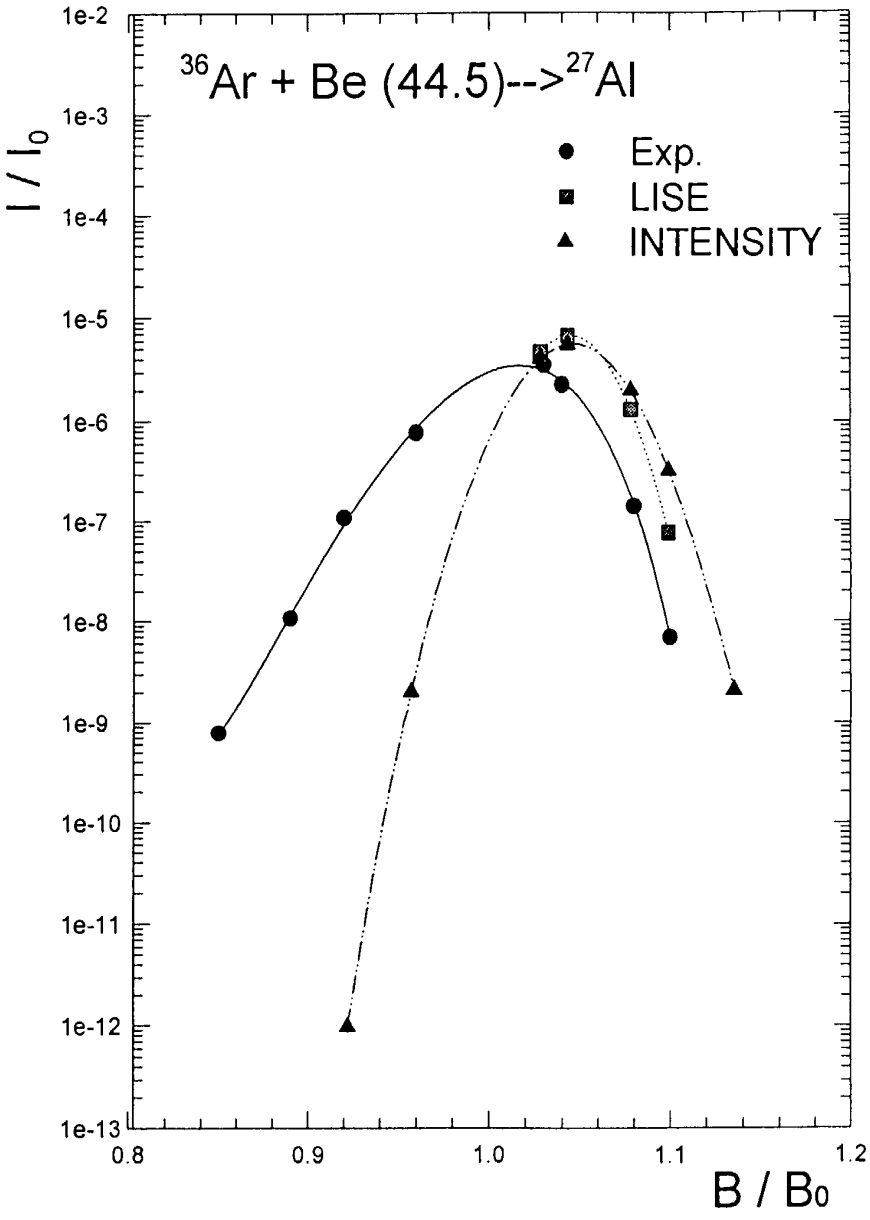

Fig. 15n

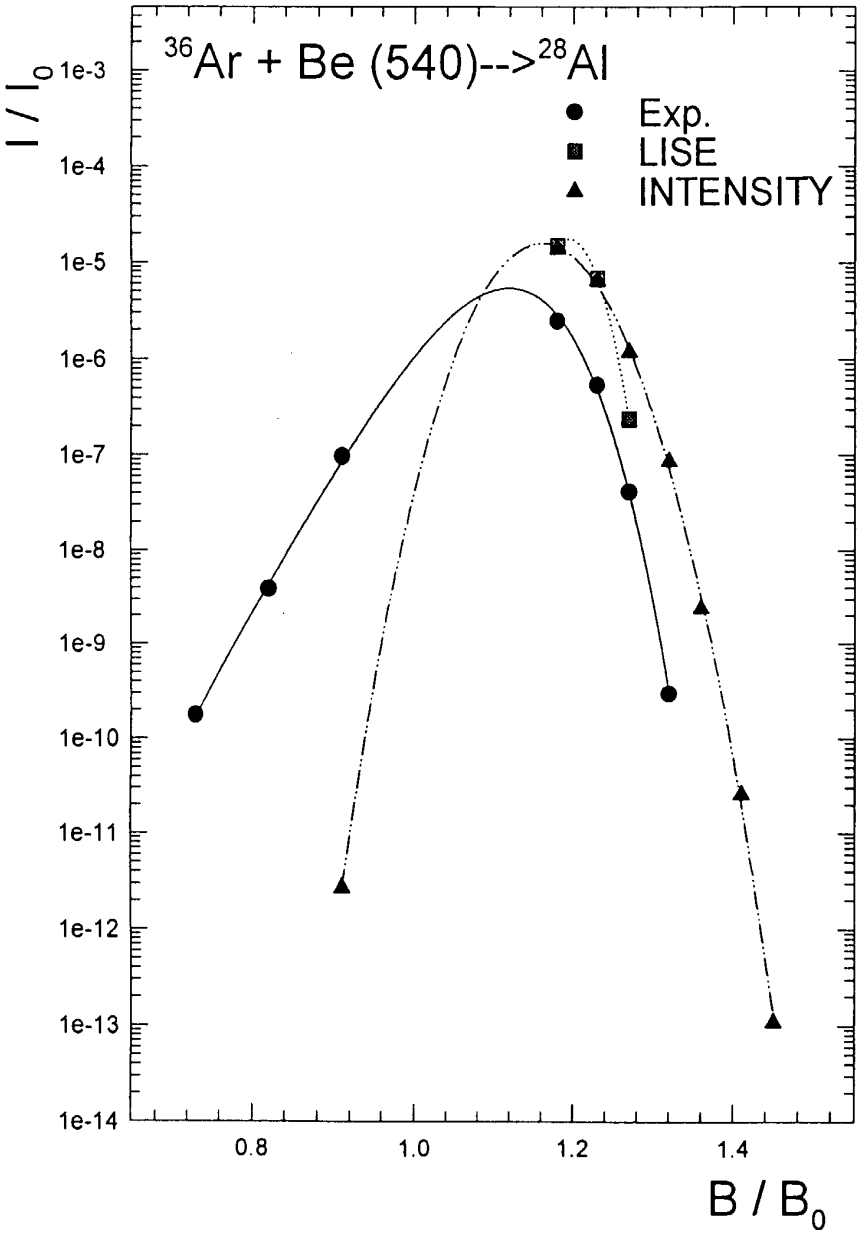

Fig. 15o

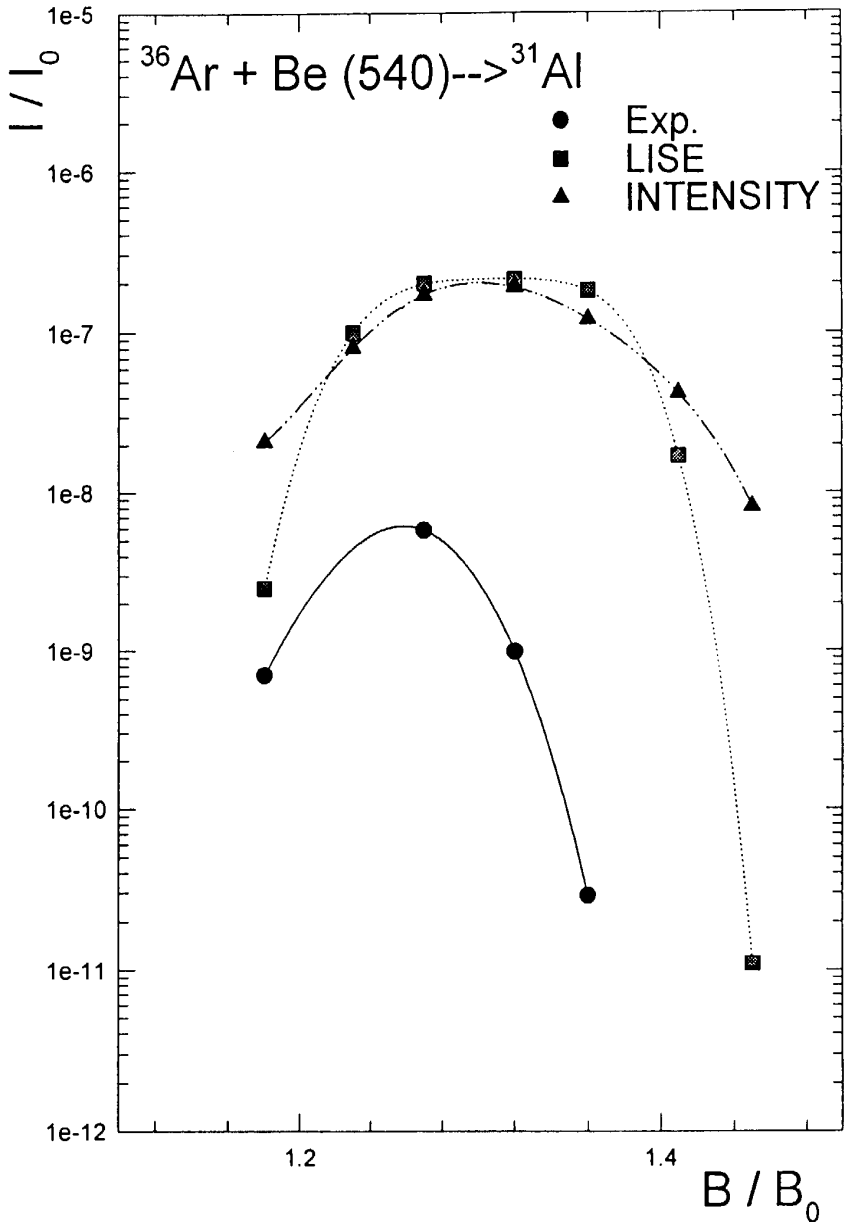

Fig. 15p

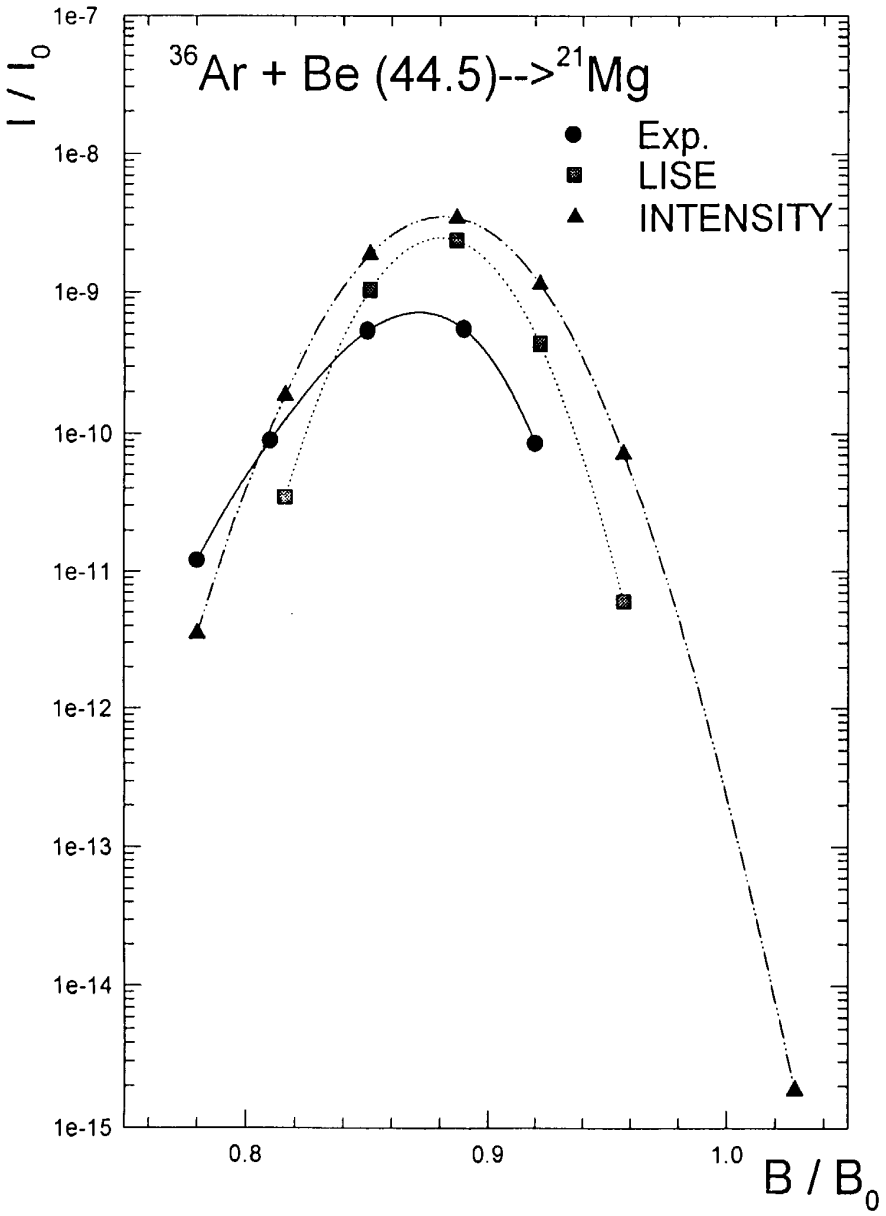

Fig. 15q

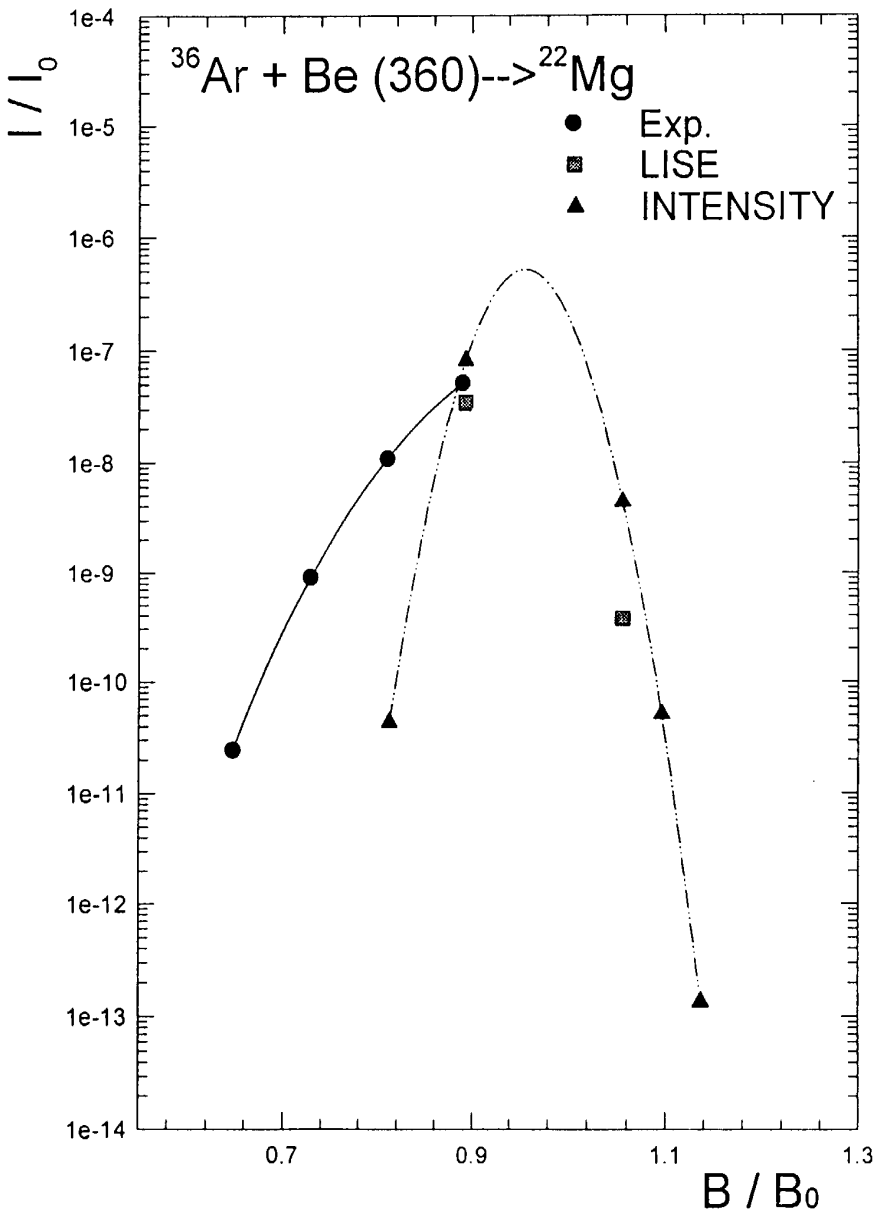

Fig. 15r

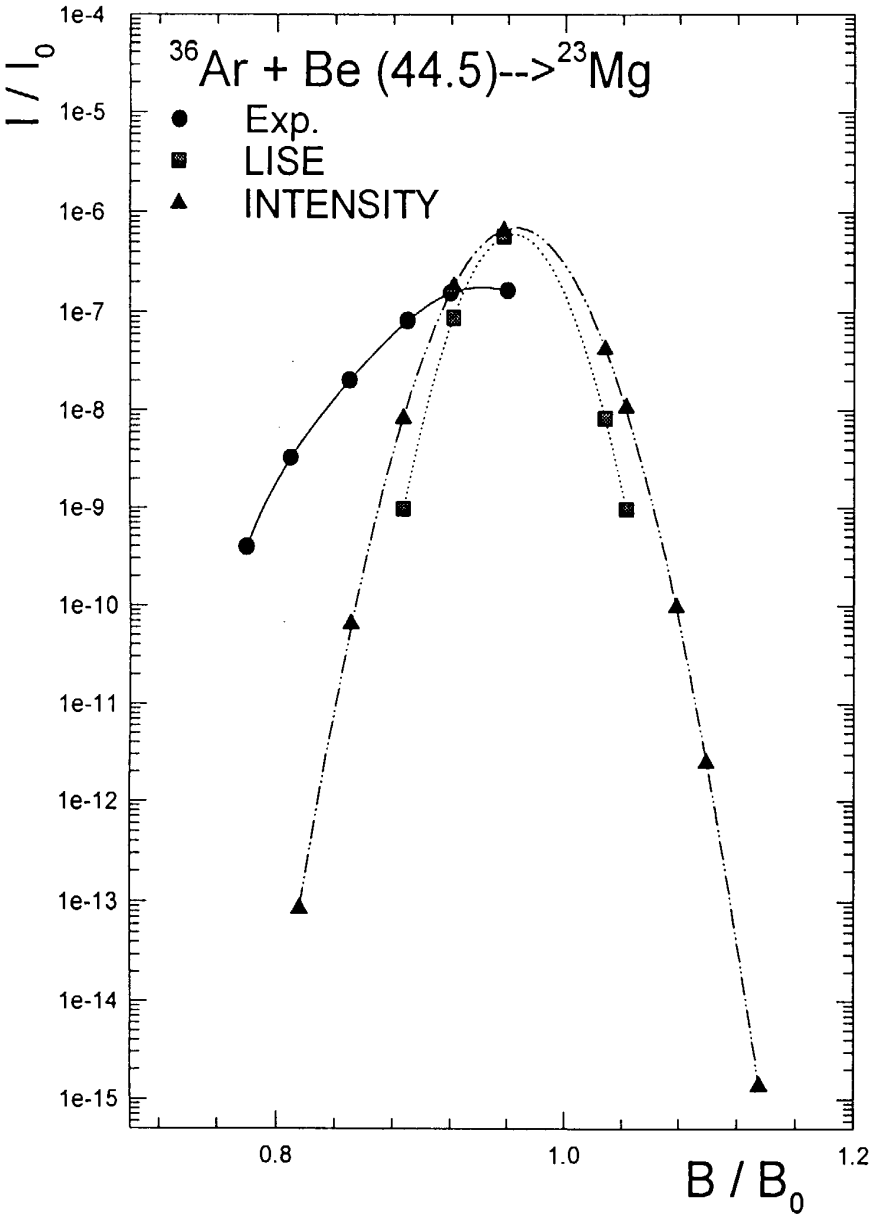

Fig. 15s

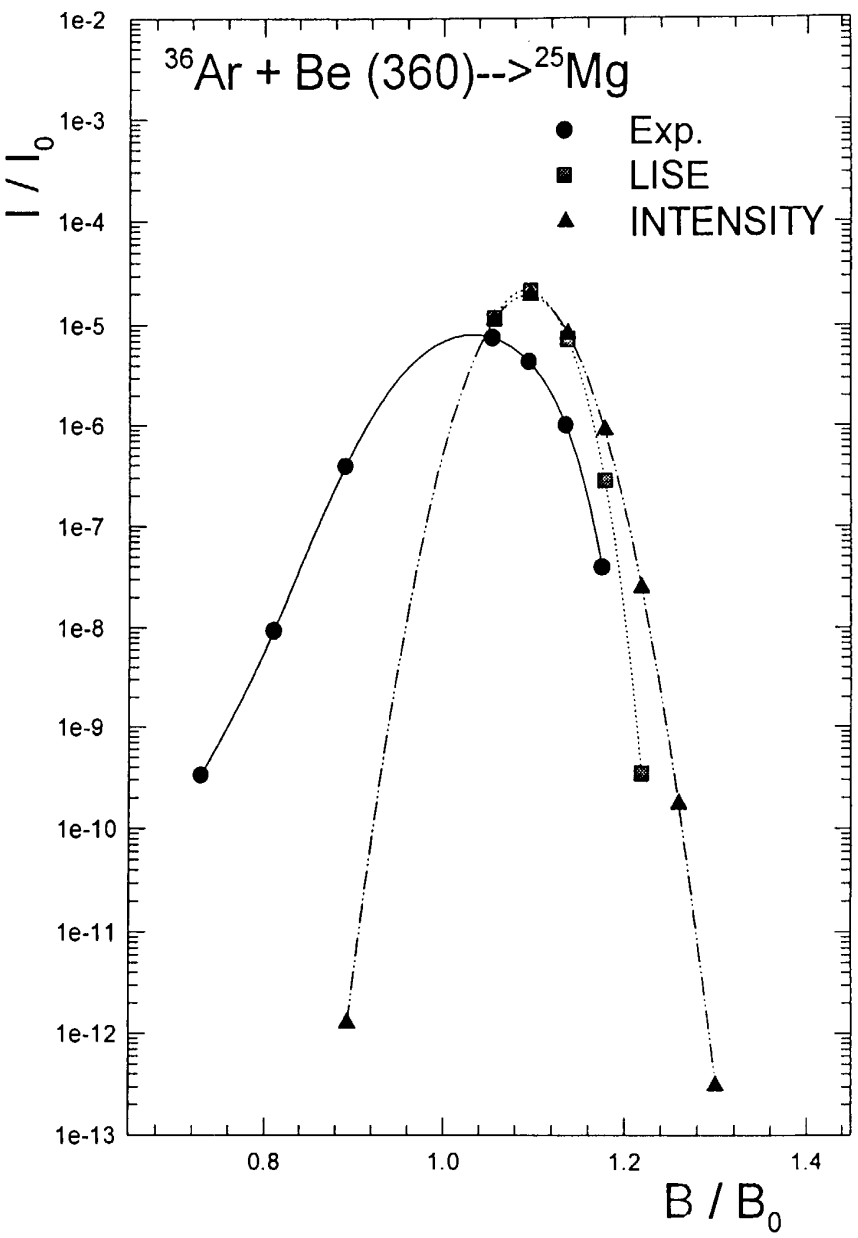

Fig. 15t

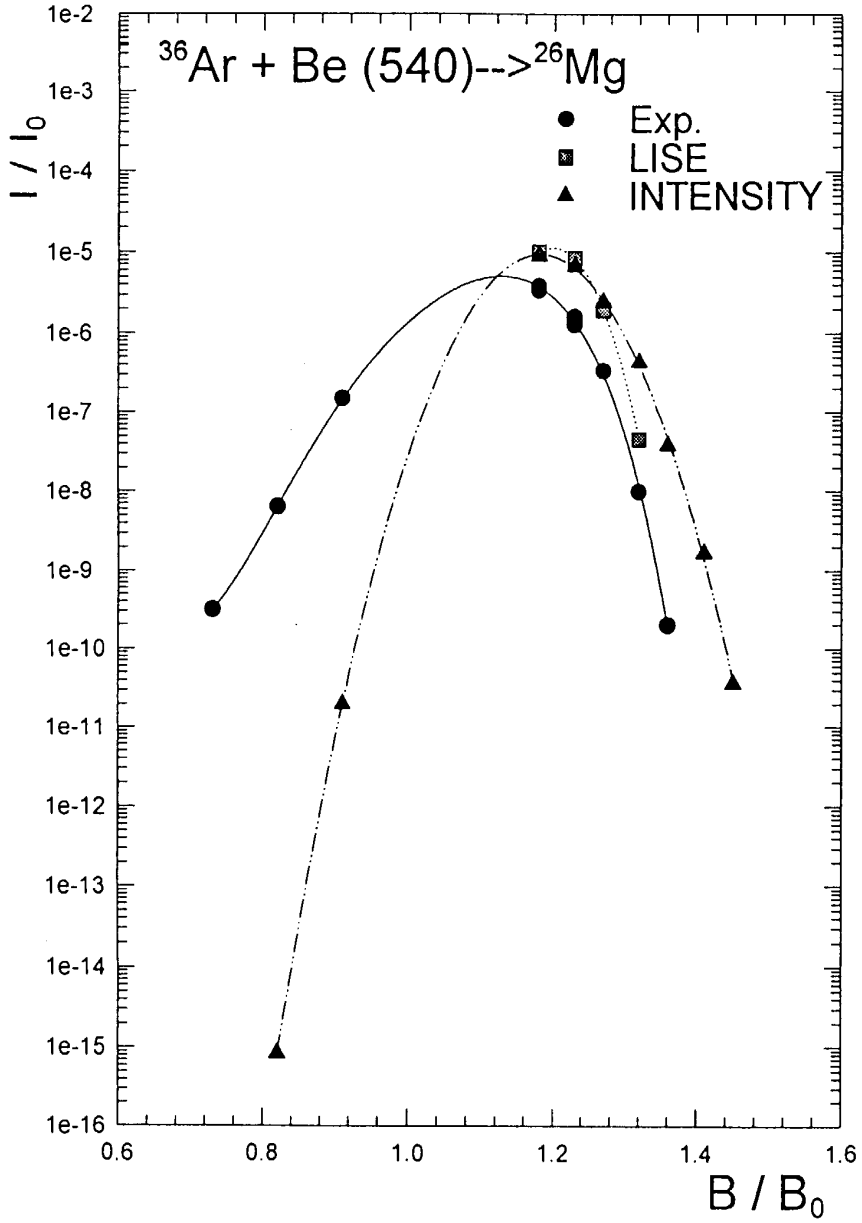

Fig. 15u

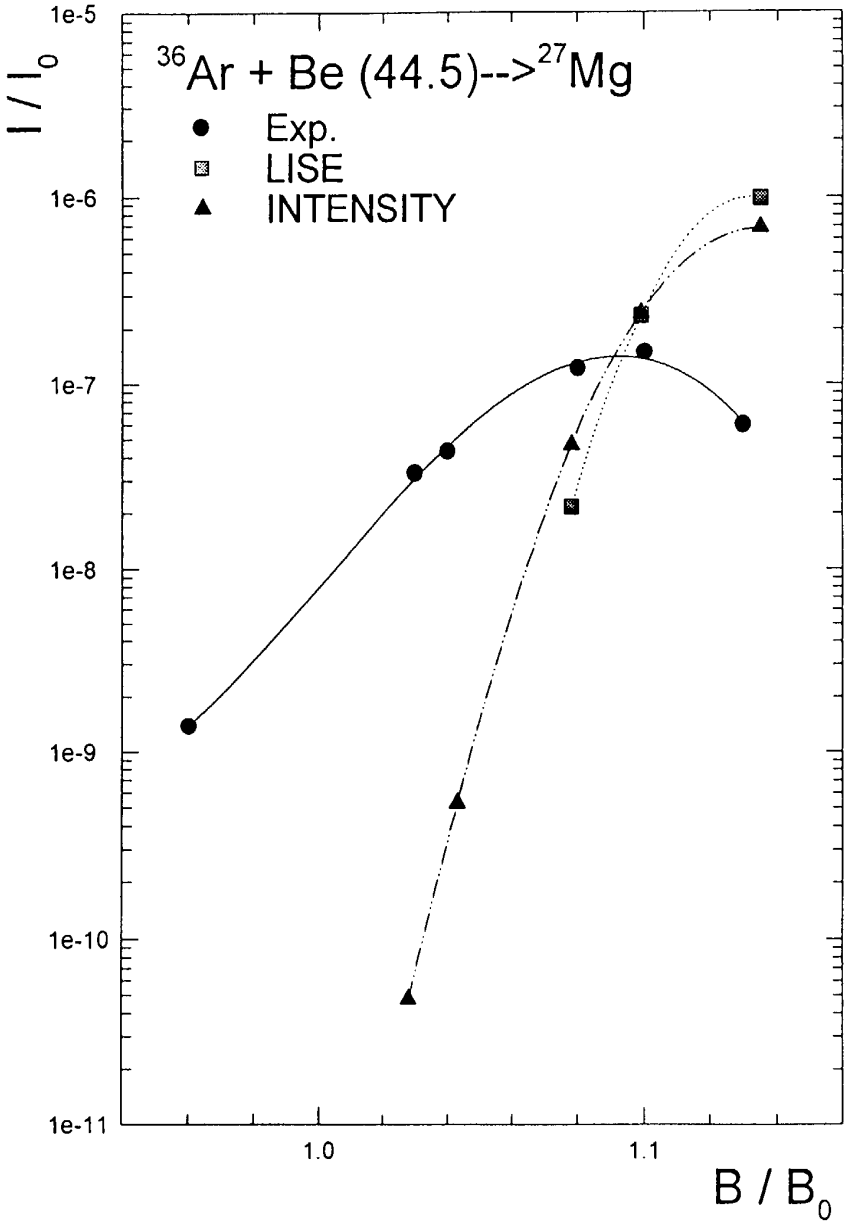

Fig. 15v

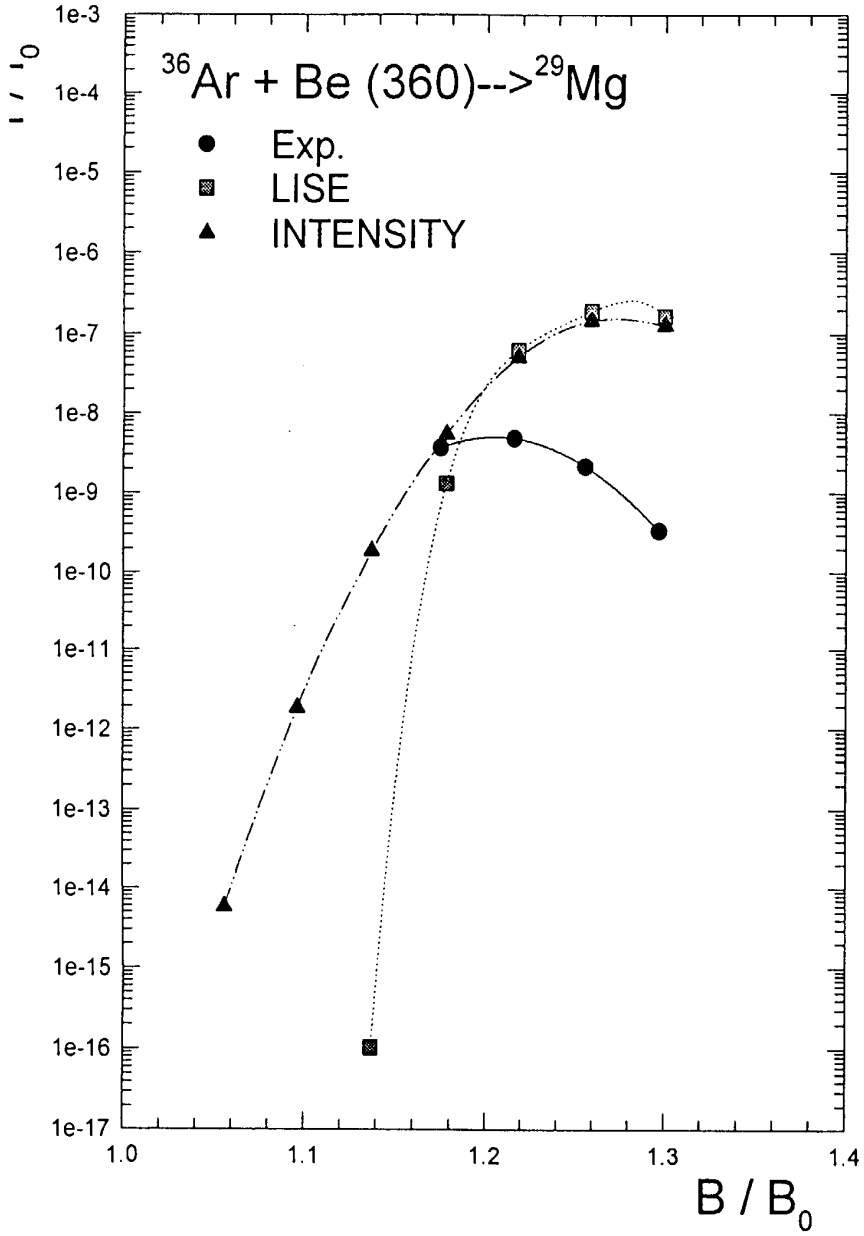

Fig. 15w

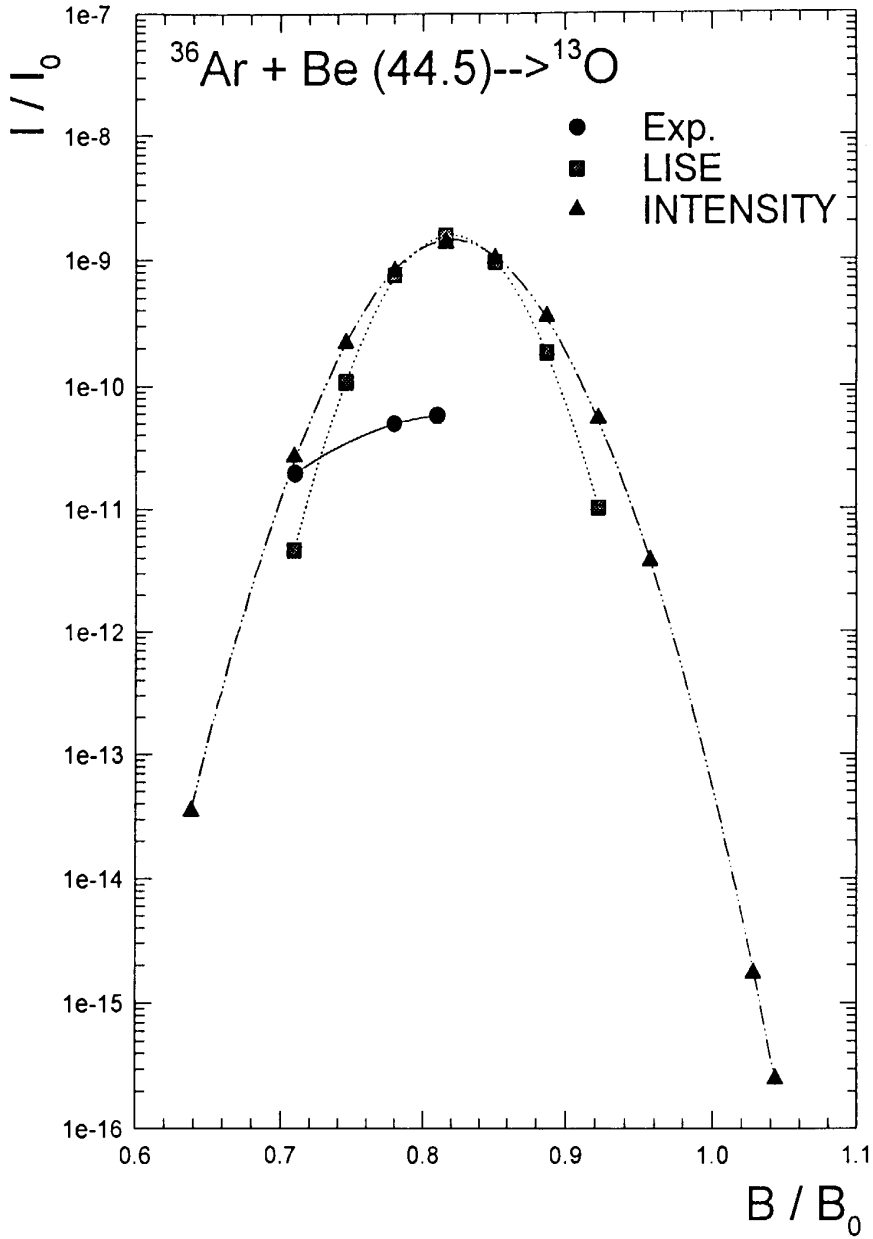

Fig. 15x

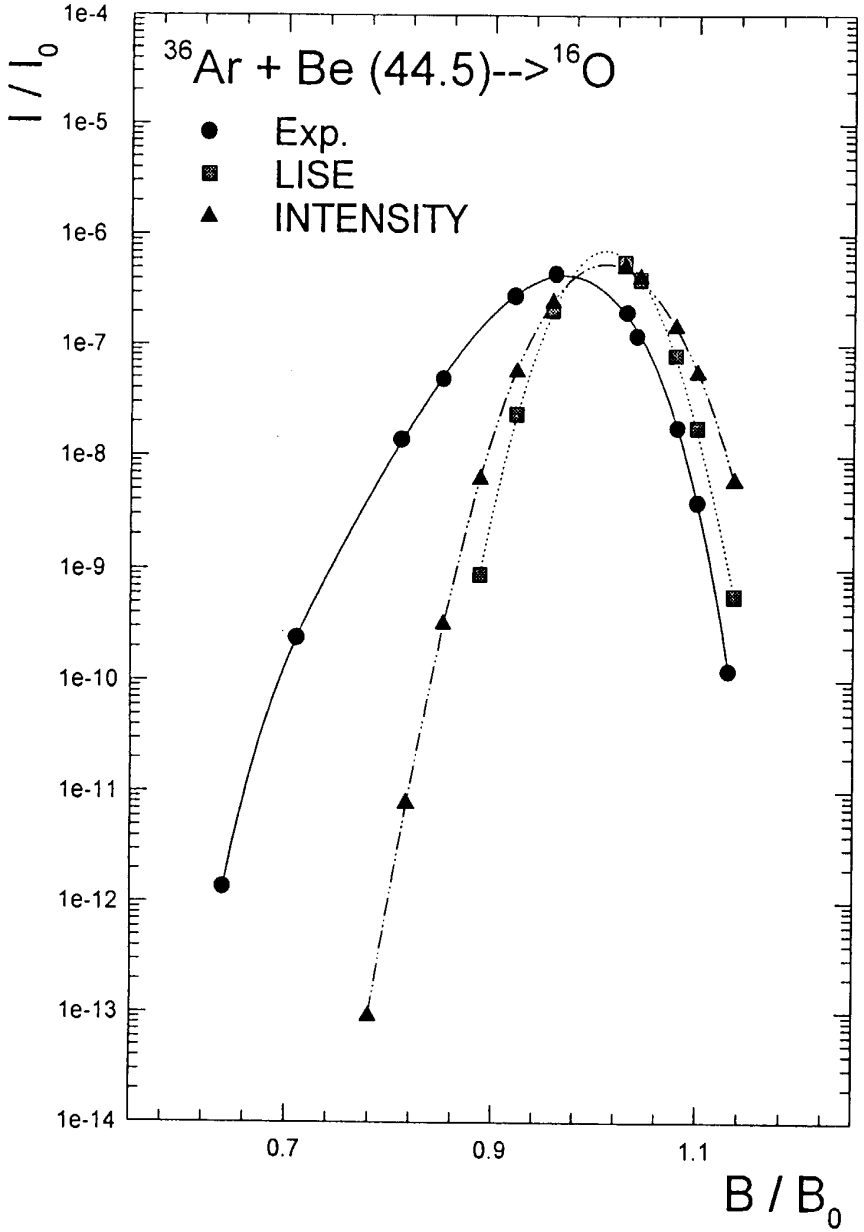

Fig. 15y

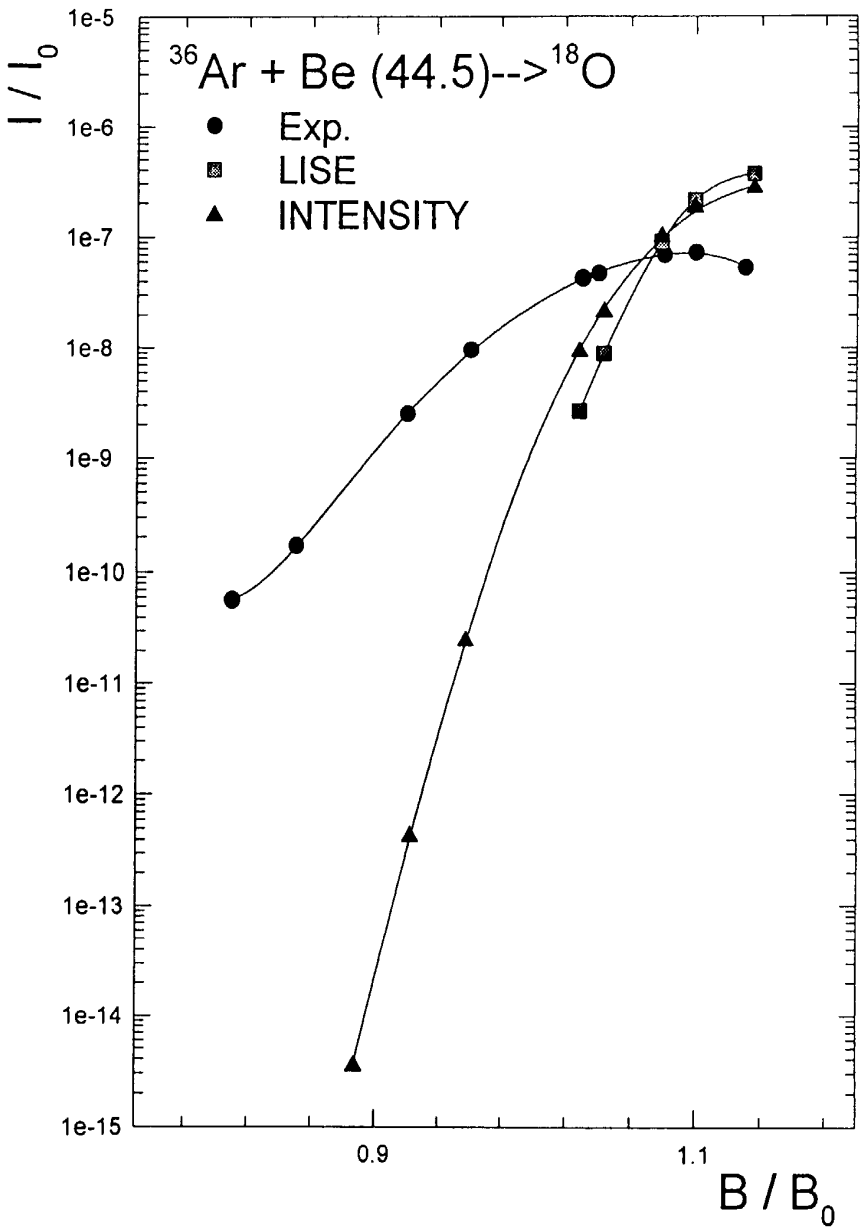

Fig. 15z

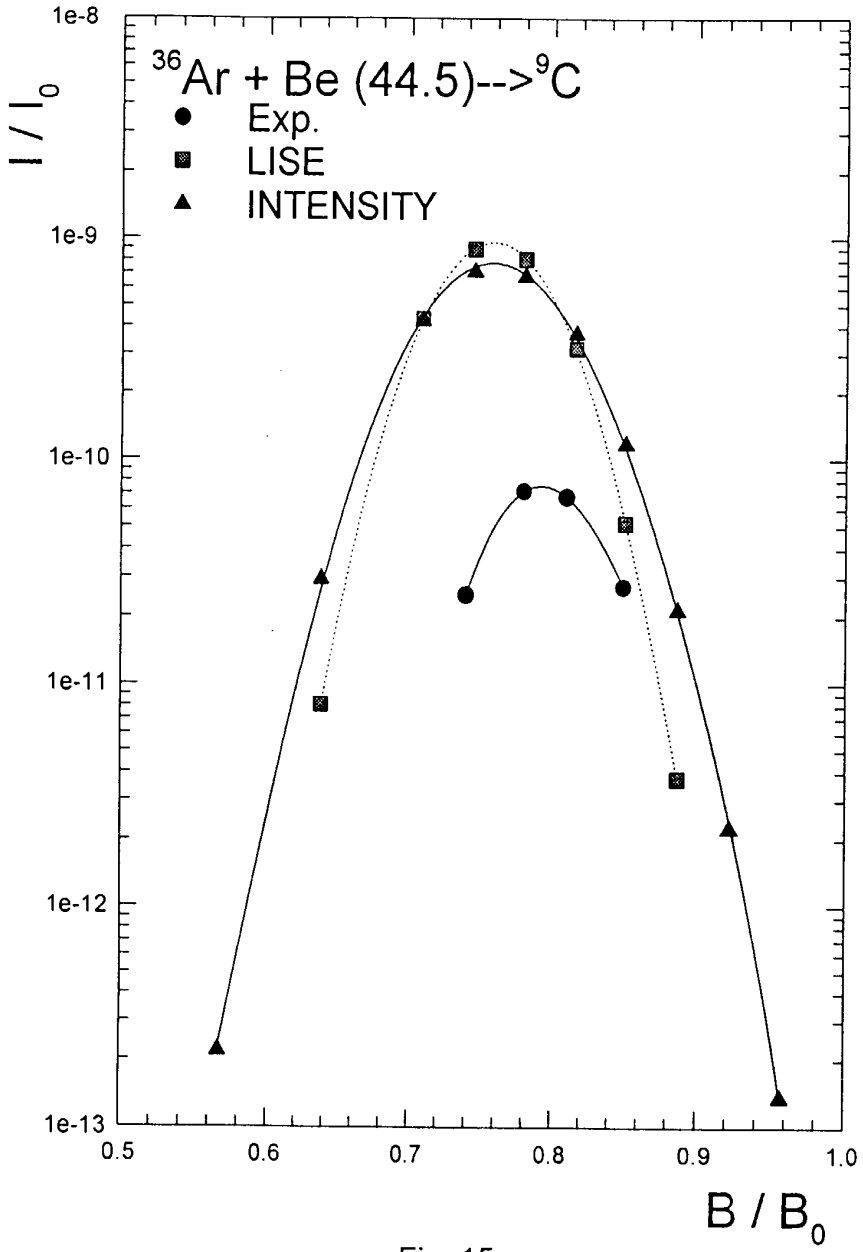

Fig. 15aa

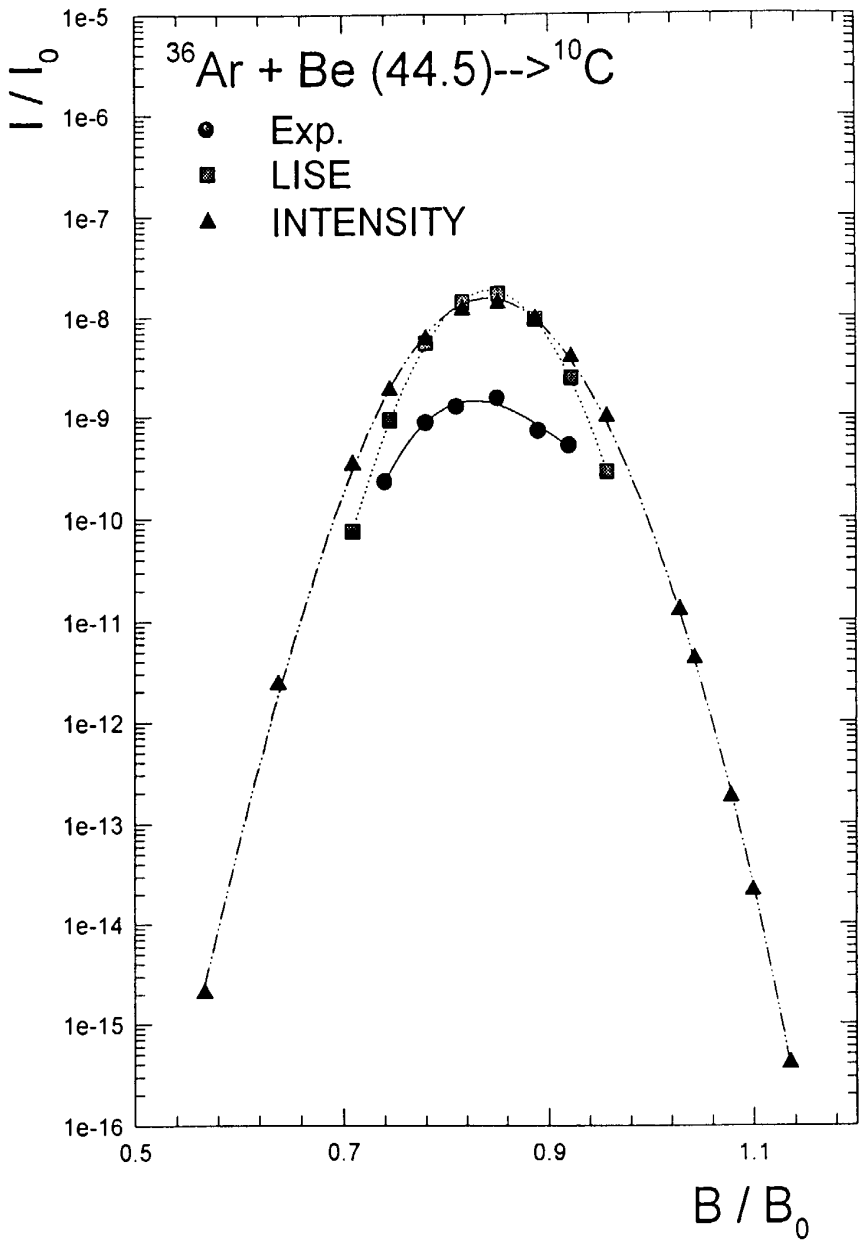

Fig. 15ab

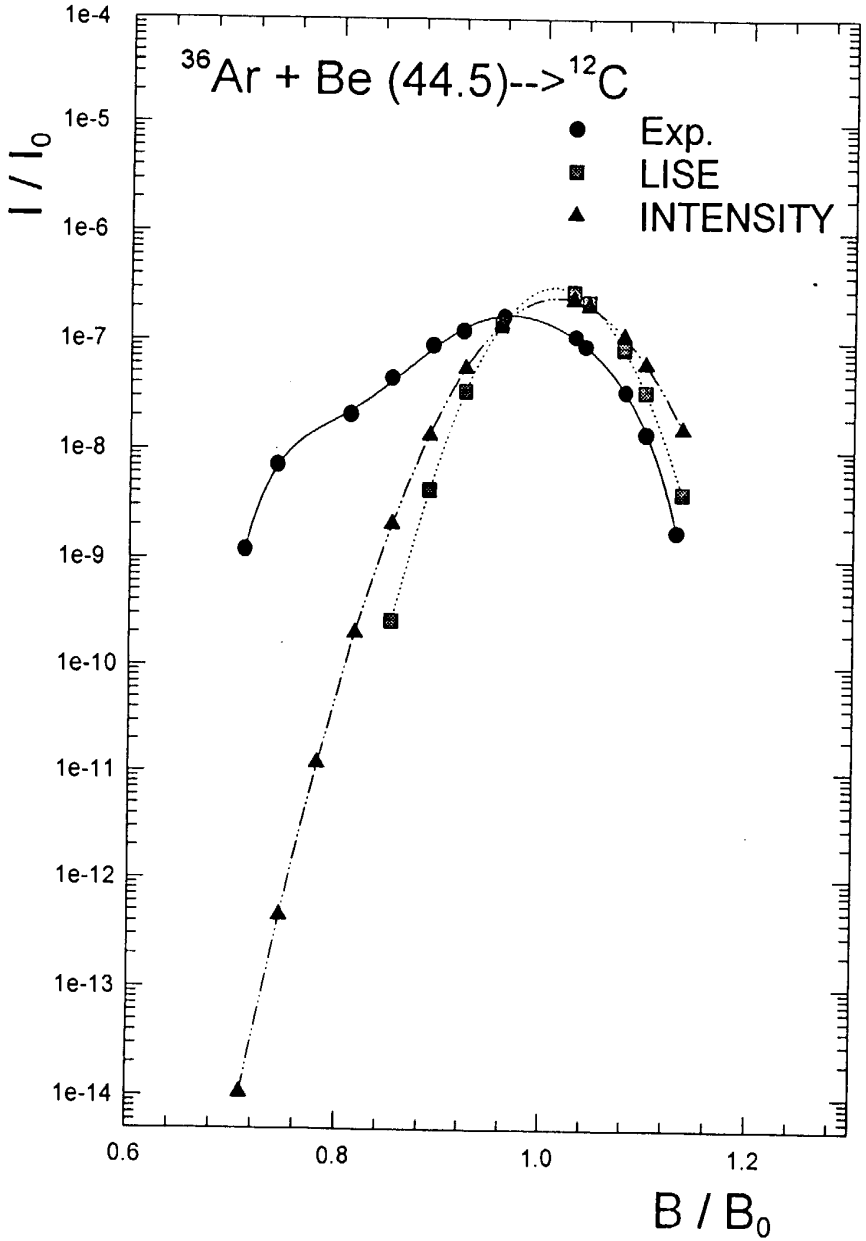

Fig. 15ac

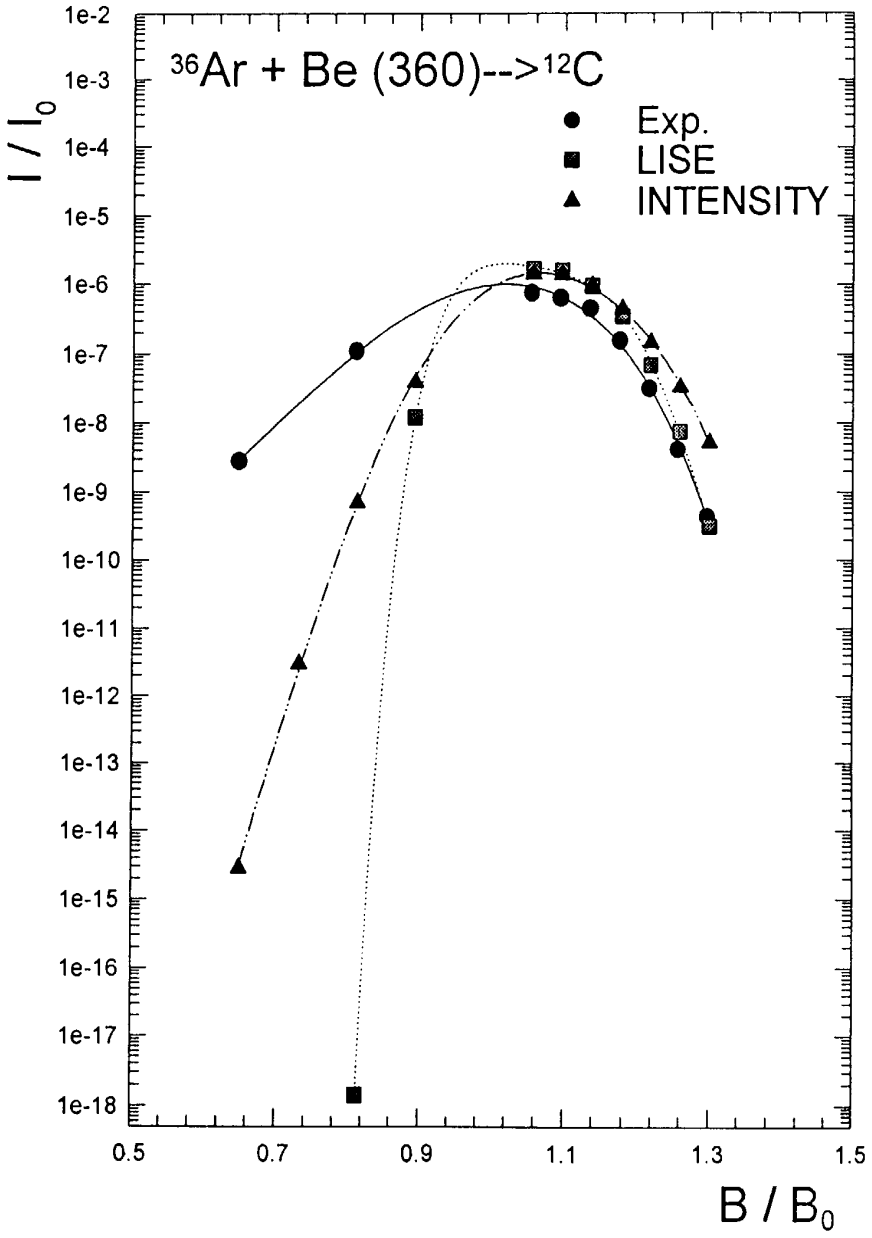

Fig. 15ad

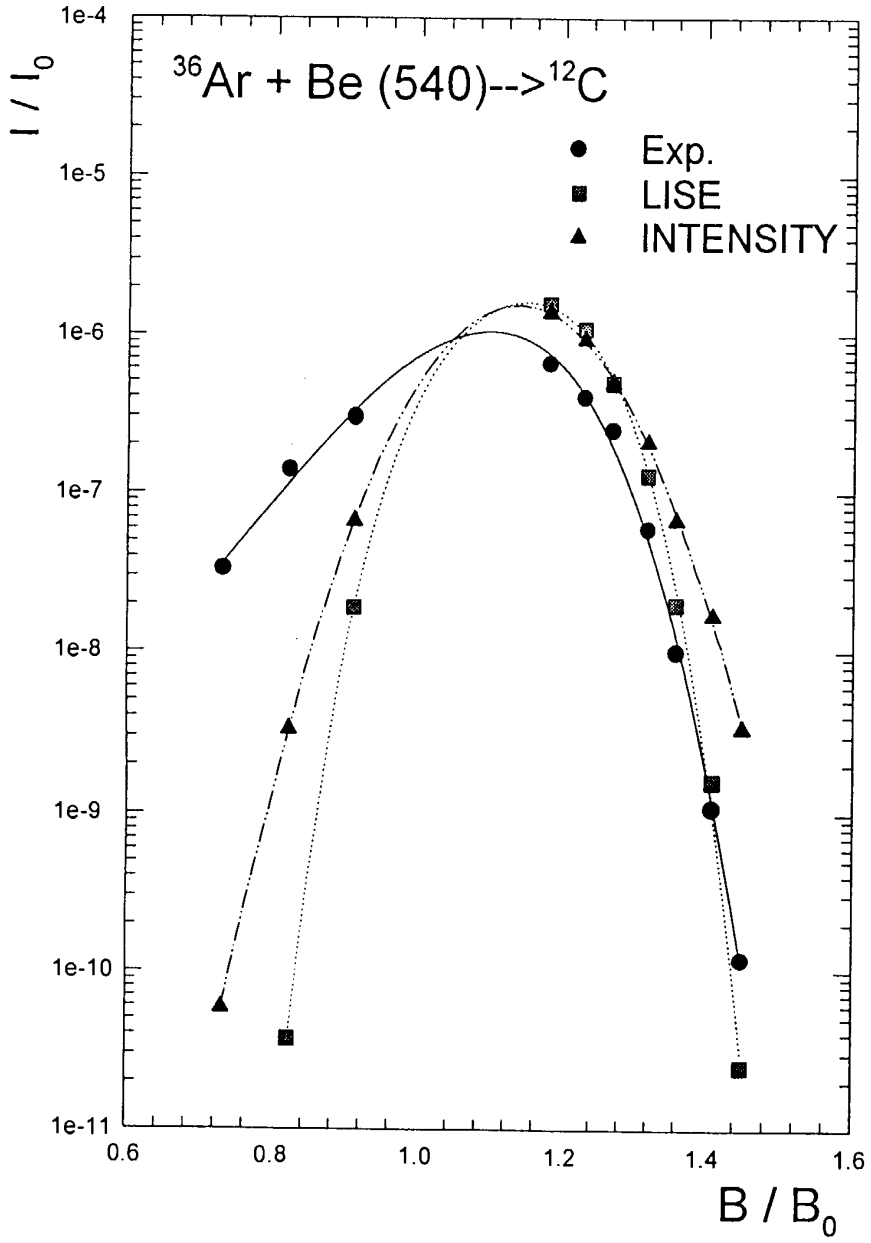

Fig. 15ae

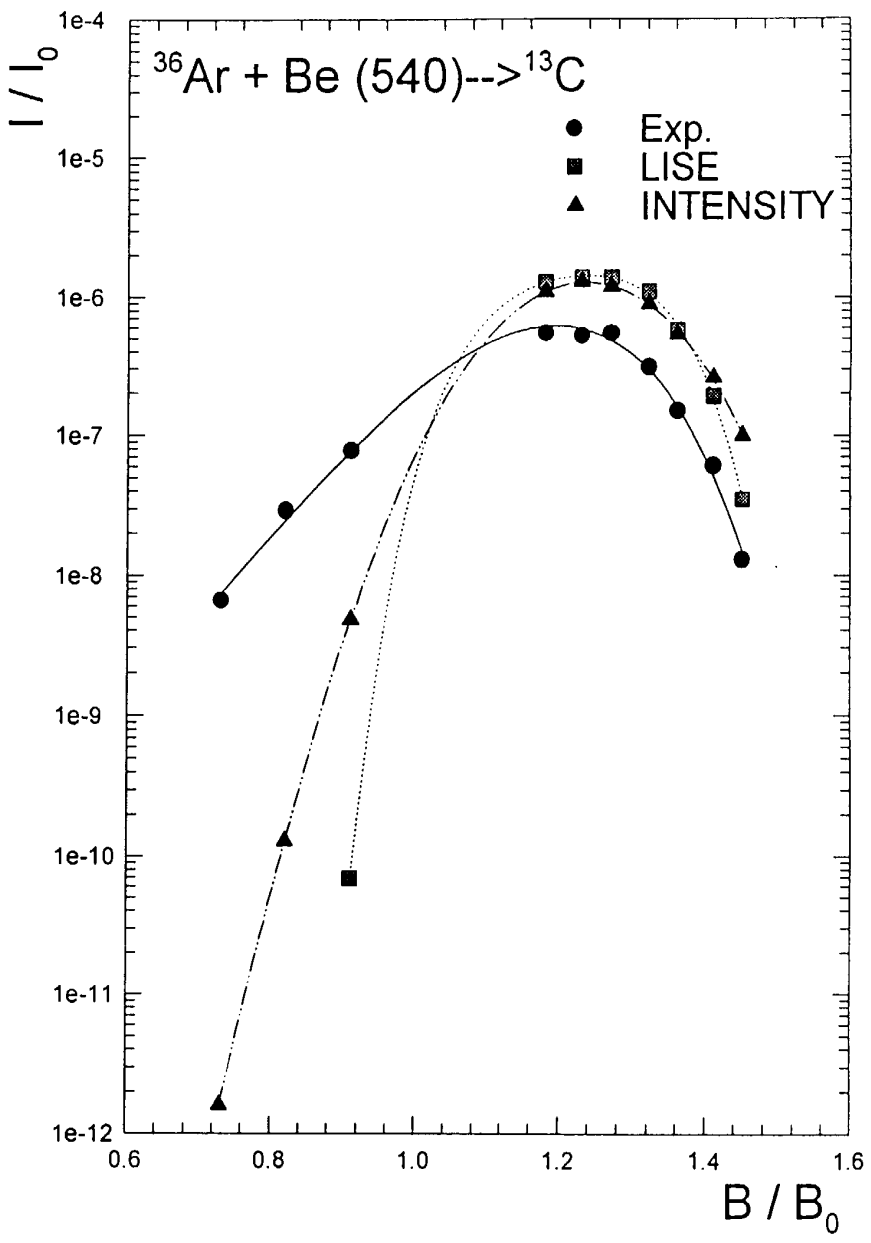

Fig. 15af